LONDON'S GLOBAL UNIVERSITY

Characterisation of ion exchange chromatography resins for therapeutic protein manufacture

by

Greta Jasulaityte

A thesis submitted for the degree of

Doctor of Engineering

in

The Department of Biochemical Engineering

UCL

August 2021

I, Greta Jasulaityte, hereby declare that the work presented in this thesis is my own. Where information has been derived from other sources, I can confirm that this has been indicated in the thesis.

Signature _____ Date _____

Acknowledgements

I am very grateful for the guidance and support provided by my supervisors Prof. Daniel Bracewell and Hans Johansson throughout the years. This project would not have been possible without the support from the Engineering and the Physical Sciences Research Council (EPSRC) and Purolite Life Sciences. I was blessed to be working with extremely responsive and knowledgeable individuals at Purolite. A special thanks must be said to Patrick Gilbert, Caroline Tinsley and Mark Hicks.

I would also like to thank the R&D team at Fujifilm Diosynth Biotechnologies. Quick response, input and advice by James Pullen and Jeff Keen were instrumental in the final results chapter of this thesis.

I would like to thank the whole department of Biochemical Engineering for providing a friendly environment and endless career development opportunities.

I would also like to thank my colleagues for their help, advice and support. Special thanks goes to my lab friends Anshul Sharma, Sushoban Bandyopadhyay, Chris Wayne, Michael Martinez and Mauricio Bufajer. Additional thanks goes to Elsa Noaks - my partner in crime, Chileab Redwood-Sawyerr - a shoulder to cry on, Chika Nweke - my mentor, and Tom Fanthom - my newly found joy. You all made my time at UCL so much more meaningful and enjoyable.

Finally, I would like to thank my family for encouraging me to actively seek for a brighter future, and Ash for being my absolute rock.

Abstract

This thesis, completed in collaboration with Purolite Life Sciences, aims to optimise agarose-based ion exchange chromatography resin design to address increased complexity of current feed materials: high titres and associated impurities.

Resins with different average particle sizes: 45, 65 and 90 µm, and ligand density: 0.05-0.28 mol/L, were designed and manufactured using a traditional stirred tank and a novel jetting process. Jetting method employing a porous membrane aimed to achieve a narrower particle size distribution than the alternative.

Resin designs were evaluated according to the key performance indicators: dynamic binding capacity (DBC), adsorption rate, lifetime, and resolution. DBC was performed at different flow rates with BSA feed, adsorption kinetics were observed with the confocal laser scanning microscope, whilst a fluorescent-dye assay was developed to measure aggregate accumulation in resins. Resolution studies were accomplished with ovalbumin, and monoclonal antibodies, IgG1 and IgG4.

Resins of 45 µm size and <0.10 mol/L ligand density, irrespective of resin manufacturing method, achieved the highest DBC at 125 cm/h flow rate, 50% faster protein adsorption rate, increased lifetime, and highest recovery in IgG1 and IgG4 separations. Matrix's performance was found to increase and then plateau with increasing ligand density. Whilst strong multipoint protein-ligand interactions caused by higher ligand density availability provided an increased retention time and improved ovalbumin isoform separation, steric hindrance effects were also a reason for poor protein recovery and reduced resins' lifetime. This was of particular importance for the unstable molecule IgG4: ligand density below 0.20 mol/L generated up to 20% higher yield at low buffer pH, whilst additional ligand resulted in peak splitting, oligomerisation and fouling. In contrast, IgG1 being more stable than IgG4 was not affected by these conditions.

This work demonstrates that selecting an appropriate combination of particle size and ligand density is crucial for optimal resin performance and throughput, and can be customised to suit unstable biopharmaceuticals' needs.

Impact statement

There is a considerable amount of pressure in the downstream processing stage due to increasing product titres in the upstream process development. With improvements in titres, the amount of impurities rises making chromatography step less efficient and robust leading to significant yield losses.

The work described in this thesis is hoped to be of immediate and future significance to both academic and industrial institutions employing traditional and continuous chromatography for intensified bioprocessing.

The knowledge gained whilst characterising the efficiency of various structural designs of agarose-based ion exchange resins on their performance will be of direct importance to resin manufacturers including the collaborating company Purolite Life Sciences. It will allow the companies to tailor resin design for both generic and specific processes encountered in the biological therapeutic field. The implementation of the suggestions such as particle size, particle size distribution and ligand density described in this work would have a positive impact on pharma and biotechnology companies that are directly involved in the biopharmaceutical manufacture allowing them to reduce production time and cost. Additionally, resins made with custom ligand densities for each product would allow to tailor the needs of unstable products by maximising step yield and reducing process related impurities such as higher molecular weight species. Consequently, the improvement in product purity, and reduction in production cost are expected to have an additional benefit in the overall therapeutic safety, and costs to the patients and national health clinics.

The development of a fluorescent dye-based aggregate detection assay in used chromatography columns is of particular importance to individuals and institutions doing early stage process development in both academia and beyond. This new analytical method allowing to measure and visualise the lifetime of chromatography

resins will aid in fouling process understanding enabling researchers to develop better cleaning conditions, and resin manufacturers – to enhance resin reusability. Extended resin lifetime will have a positive environmental impact whereby less waste will be generated.

The findings on antibody stability during the purification process provide additional knowledge for product discovery and design stages carried out in antibody-based therapeutic fields. It has been shown that ligand densities for chromatography matrices have to be carefully selected for different antibodies such as IgG1 and IgG4 that possess different stability properties in order to obtain the highest recovery and purity of the product.

Table of contents

List of figures

List of tables

List of abbreviations

AEX	Anion exchange
AAV	Adeno-associated virus
AFM	Atomic force microscope
ATR-FTIR	Attenuated total reflectance - Fourier transform infrared
BSA	Bovine serum albumin
CEX	Cation exchange
CIP	Clean-in-place
CLSM	Confocal laser scanning microscope
CV	Column volume
DBC	Dynamic binding capacity
DI	Deionized
DNA	Deoxyribonucleic acid
DOE	Design of experiments
FFD	Flow focusing device
FPLC	Fast protein liquid chromatography
HCP	Host cell protein
HETP	Height equivalent to a theoretical plate
HIC	Hydrophobic interactions chromatography
HMWS	High molecular weight species

HPLC	High performance liquid chromatography
IEX	Ion exchange
IgG	Immunoglobulin G
iSEC	Inverse size exclusion chromatography
LLD	Laser light diffraction
mAb	Monoclonal antibody
Mpa	Mega pascal
NaCl	Sodium chloride
NaOH	Sodium hydroxide
pI	Isoelectric point
PSD	Particle size distribution
qPCR	Quantitative polymerase chain reaction
RFU	Relative fluorescence units
RMSE	Root-mean-square error
RNA	Ribonucleic acid
RPM	Revolutions per minute
RSq	R-Squared
SBC	Static binding capacity
SD	Standard deviation
SEC	Size exclusion chromatography

SEM	Scanning electron microscope
TEM	Transmission electron microscope
TFF	Tangential flow filtration
UV	Ultraviolet

List of notation

R1	Ligand density (mol/L)
EP1	Consumption of silver nitrate at the first endpoint (mL)
C	Concentration of the solution (mol/L)
V_{sample}	Sample volume (mL)
h	Reduced plate height
d_p	Particle diameter (cm)
HETP	Height equivalent to the theoretical plate (cm)
$DBC_{10\%}$	Dynamic binding capacity at 10% breakthrough (g/L)
$V_{10\%}$	Retention volume at 10% breakthrough (mL)
V_0	Column void volume (mL)
V_c	Bed volume (mL)
C_{bound}	Bound protein concentration (mg/mL)
$C_{initial}$	Initial protein concentration (mg/mL)
$C_{unbound}$	Unbound protein concentration (mg/mL)
V_{resin}	Volume of resin slurry (mL)

List of publications

Original research papers

Jasulaityte, G, Johansson, HJ, Bracewell, DG, 2019. Chromatography process development aided by a dye-based assay. Journal of Chemical Technology & Biotechnology, 95(1): 132-141. (Relates to chapter 5)

Conference presentations

Jasulaityte, G, Gilbert, P, Johansson, HJ, Bracewell, DG, 2017. Particle size and ligand density effects on anion exchange chromatography for therapeutic protein manufacture. IChemE BESIG Novel Technologies & Young Researchers' Meeting, London, UK. (Relates to chapter 4)

Jasulaityte, G, Gilbert, P, Johansson, HJ, Bracewell, DG, 2018. Particle size and ligand density effects on anion exchange chromatography behaviour for therapeutic protein manufacture. 255th American Chemical Society Annual Meeting, division of Biochemical Technology, New Orleans, USA. (Relates to chapter 4)

Jasulaityte, G, Johansson, HJ, Bracewell, DG, 2019. Antibody variant ion-exchange separation and recovery at varying ligand densities. The 5th European Congress of Applied Biotechnology (ECAB 5), Florence, Italy. (Relates to chapter 6)

Jasulaityte, G, Johansson, HJ, Bracewell, DG, 2021. Ion exchange resin ligand density determines mAb stability and recovery. American Chemical Society, division of Biochemical Technology, Atlanta, USA. (Relates to chapter 6)

Introduction

Research aim

The aim of this thesis is to intensify the chromatography process and improve the purity of the target molecule through optimising the design of the resin particles facilitated by Purolite Life Sciences.

Objectives

- Design structurally different ion exchange chromatography resins of three particle sizes, three ligand densities, and manufacture them using two methods: jetted and conventional.
- Develop an assay that allows to detect resin fouling and estimates its lifetime.
- Characterise the performance of the resins to understand how different structural features affect their binding capacity, adsorption kinetics, lifetime and resolution capabilities under various process conditions including flow rate and feed concentration.
- Conclude which structural characteristics of resins are most beneficial for desired chromatography process stages and outcomes.

Thesis layout

Chapter one reviews the most relevant literature in the fields of biopharmaceutical market, agarose resin manufacture, desirable resin features and their characterisation methods.

Chapter two establishes materials and methods used for resin characterisation.

Chapter three is the first results chapter that describes the design and synthesis of agarose-based resins used for this work. Twelve types of resins are produced using

conventional and jetted manufacturing methods with varying ligand densities, particle sizes and particle size distributions. The mechanical strength and the quality of structural features are examined.

Chapter four, the second results chapter, addresses changes to protein adsorption kinetics due to varying resins' structural features: ligand density, particle size and particle size distribution. Dynamic binding capacity is determined at different process conditions, and intra-particle adsorption is observed with the help of a confocal microscope.

Chapter five, the third results chapter, considers the effect that structural resin characteristics and process conditions have on resin's lifetime. Traditional re-usability studies are performed, and a novel foulant detection assay is developed in order to confirm the results and provide additional information on specific foulant accumulation patterns.

Chapter six, the final results chapter, investigates the differences in resolution and separation efficiency as well as purity and stability that are provided by the jetted and non-jetted resins possessing different ligand densities. A model protein ovalbumin containing complex isoforms, and monoclonal antibodies IgG1 and IgG4 are used to identify the level of separation and stability.

Chapter seven summarises this thesis with an overview of the findings, and proposes future work.

1. Chapter: Literature review

1.1. Current outlook in monoclonal antibody manufacturing

1.1.1. Biopharmaceutical market

Biopharmaceutical market makes up 25% of the total pharmaceutical market with annual revenue of $275 billion in 2018 (Rader and Langer, 2018). More than a third of this revenue is generated by the monoclonal antibodies (Grilo and Mantalaris, 2019) making them important players in the market. The number of approved treatments is expected to increase as it has been for the past two decades (Kaplon et al., 2020). The antibody market will also be driven by the increasing number of next generation antibody products: bispecifics, antibody-fusion, antibody-drug conjugates, sugar-chain modified antibodies, low molecular weight antibodies, as well as biosimilar products (Shukla et al., 2017).

Antibodies are known to have high specificity and affinity for target antigens in addition to superior pharmacokinetics and low unwanted immunogenicity. All therapeutic monoclonal antibodies (mAbs) on the market belong to one of the immunoglobulin G (IgG) subclasses with IgG1 being the most common with 79% of the total share followed by IgG4 with 13% (Grilo and Mantalaris, 2019). The main structural differences amongst IgG1, IgG2, IgG3 and IgG4 are the number and location of interchain disulphide bonds as well as the length of the hinge region. These IgGs also have different affinity to Fc receptors found on the surface of protective cells such as monocytes and macrophages the choice of which would determine therapeutics' biological activity (Yu et al., 2020). Both IgG1- and IgG3-based therapeutics are known to be most effective in the Fc-mediated effector functions such as complement dependent and antibody-dependent cell-mediated cytotoxicity;

however, IgG3 is not used for therapeutic purposes due to its very long hinge region, polymorphism and short half-life leaving IgG1 the main choice. Some of the IgG1-based therapeutic products include Humira® (adalimumab), Rituximab (mabthera) and Herceptin (trastuzumab) (Yu et al., 2020).

1.1.2. Recombinant antibody manufacturing process

A traditional antibody purification process consists of a number of steps often divided into two sections: upstream and downstream. Upstream process considers the growth of host cultures such as *Escherichia coli*, *Saccharomyces cerevisiae* and Chinese hamster ovary cells from small flasks to large bioreactors. Once the desired cell density has been achieved, the harvesting and clarification steps take place. Centrifuges, homogenisers and depth filters are commonly used unit operations for host cell debris removal. Further purification of the product is achieved through downstream processing steps consisting of three chromatography columns and tangential flow filtration (TFF) prior to the fill and finish step. Chromatography aims to ensure a substantial reduction in the amount of virus-like particles, remaining host cell proteins and DNA, and other contaminants, resulting in high purity of the product. The importance of TFF is two-fold: it allows to exchange the target product into the final buffer and to concentrate the solution into the required dose.

1.1.3. Product- and process-related impurities

Purified monoclonal antibodies are heterogeneous in structure due to varying processing conditions and inherent instability. Structural changes to the product quality or failure to remove other contaminants can lead to compromised therapeutic protein’s efficacy and safety. The most commonly encountered and thus carefully monitored structural changes are aggregation, fragmentation, glycosylation, C- and

N-terminal modifications, oxidation, deamidation, protein conformation and glycation amongst others (Eon-Duval et al., 2012). Aggregation, for example, can occur at any stage during the process due to unfavourable temperature, buffer type and pH, protein concentration, and various physical stresses such as shearing, freezing, thawing or excessive stirring (Van Beers and Bardor, 2012). Similarly, fragmentation can also occur during both the upstream and downstream stages of the manufacturing if the proteolytic enzymes, which are present in the cell culture supernatant, cannot be neutralized early on and co-purify with the target molecule. In contrast, glycosylation is heavily dependent on the host cell line and upstream cell culture conditions meaning that differences in synthesized carbohydrate moieties could affect immunogenicity, biological activity and pharmacokinetics (Gramer, 2014). Therefore, once specific critical quality attributes are determined for each molecule, critical process parameters are established detailing acceptable process conditions such as temperature, pH, etc.

In addition to product-related impurities, there are process-related contaminants that include raw material-derived impurities, which have to be removed to an acceptable level in order to reduce cytotoxicity and immunogenicity (Eon-Duval et al., 2012). Raw materials such as chromatography resins, ultrafiltration membranes, tubing and hold containers can leach out during the bioprocess and contaminate the final product. Protein A leachables, for example, are off particular concern as they can have a mitogenic activity and other toxic effects. However, Protein A ligand clearance is usually robust due to multiple orthogonal downstream purification steps. Other control strategies include monitoring raw materials and their components, which are often conducted by their manufacturers.

Host cell specific contaminants include host cell proteins and DNA as well as viruses and endotoxins. Viruses are only found in the mammalian cells and usually require additional steps such as virus inactivation and virus filtration in order to significantly

reduce the presence of viruses. In contrast, endotoxins are native to bacterial cells, and can be cleared to a low level through traditional chromatography steps. Host cell proteins (HCPs) and DNA are released upon cell lysis and sometimes by secretion, and are usually removed through orthogonal chromatography steps. The presence of HCPs and DNA is influenced by the upstream conditions such as cell viability at harvest, culture duration, cell culture conditions and amino acid sequence of the target molecule. This indicates a clear relationship between the upstream and downstream processes: changes in one can lead to changes in the other.

1.1.4. Production bottleneck

There have been significant improvements in upstream processing (Chon and Zarbis-Papastoitsis, 2011), particularly in regards to product titre. Average mAb titre reported at clinical and commercial settings has reached 3.2 g/L (Rader and Langer, 2018), with a reported potential to reach >5 g/L (Shukla et al., 2017) from the initial <0.5 g/L 30 years ago (Langer and Rader, 2015). With higher titres, there are higher amounts of contaminants that challenge the current downstream processes (Wilson et al., 2019). Chromatography processes have not advanced at the same pace leading to unsatisfactory product purity, process robustness and yield. In turn, chromatography has become the biggest bottleneck in mAb processing.

1.1.5. Next generation mAb purifation

The industry has tried to alleviate the current chromatography bottleneck through either looking for new purification processes to replace the traditional column ones or via improvements to the base materials / structures (Cramer and Holstein, 2011; Roque et al., 2020). Different types of continuous processing such as periodic counter-current, counter-current tangential, simulated moving bed, cycling and

annular chromatography have emerged offering improved process productivity (Jungbauer, 2013). In addition, non-chromatography-based methods including precipitation, flocculation, crystallization and aqueous two-phase partitioning have also gained a lot of interest. Advances in chromatographic materials consider new types of ligands, membranes, nanofibers and monoliths.

The most established and commonly used chromatography matrix is composed of small porous beads in the micrometre range called resin. This solid phase takes an advantage of superior surface area that provides high binding capacity and exceptional protein resolution. Unfortunately, it suffers from high pressure at high flow rates leading to long cycle times. Materials such as membranes, monoliths and nanofibers that rely on convection rather than diffusion for target adsorption can overcome the drawbacks, and have been proposed for chromatographic separations. These matrices are particularly beneficial for large molecule separations including viruses and viral vectors due to wide pores and accessible channels. **Table 1-1** summarises and compares characteristics of all four materials and more details can be found in these references (Ghosh, 2002; Hardick et al., 2013; Rajamanickam et al., 2015). Nonetheless, bead-based resins remain the best materials for antibody capture and separation.

Table 1-1. Comparison of chromatographic matrices.

	Membranes	**Nanofibers**	**Monoliths**	**Resins**
Process steps*	Intermediate; Polishing	Capture; Polishing	Polishing; Analytical	Capture; Intermediate; Polishing; Analytical
Purpose*	Impurity removal	Impurity removal	Impurity removal; Molecule separation	Impurity removal; Molecule separation
Molecules*	Antibodies, viruses, virus-like particles	Antibodies, viral vectors, other macro-molecules	Nucleic acids, viruses, virus-like particles, proteins	Small proteins and antibodies
Features:				
• ***Flow rate***	High	High	Medium-high	Low
• ***Pressure drop***	Low	Low	Low-medium	High
• ***Binding capacity***	Low	Low-medium	Medium	High
• ***Mode of transport***	Convection	Convection	Convection	Diffusion
• ***Resolution***	Low	Low-medium	Medium	High
• ***Scalability***	Medium	Low	Medium	High
• ***Continuous processing***	No	Yes	No	Yes
• ***Reusability***	Single use	Single use	Reusable	Reusable
• ***Fouling***	Potential for premature fouling	Less prone to fouling	Potential for premature fouling, difficult to clean	Established cleaning procedures
• ***Other***	Poor flow distribution due to irregular pore structures	New technology		Very established technology

** Signifies most common items / activities*

1.2. Bead-based chromatography resin manufacture

Agarose is often chosen as the main resin matrix due to its intrinsic characteristics. Some of the agarose physiochemical properties include hydrophilicity, low non-specific binding, stability under alkaline conditions and efficient ligand functionalisation as outlined in **Table 1-2** (Carta and Jungbauer, 2010). These are highly important characteristics for high yield and purity of the product as well as resin lifetime.

Table 1-2. Types of base matrices for chromatography resins.

	Natural carbohydrate polymers	**Synthetic polymers**	**Inorganic polymers**
Examples	Agarose, cellulose, dextran, chitosan	Acrylic, acrylamido and vinyl co-polymers, poly(styrene-divinyl benzene) co-polymers, poly(methacrylate)	Silica, porous glass, zirconia, hydroxyapatite
Surface	Hydrophilic	Hydrophobic	Hydrophobic
Pore size	Smaller	Large pore sizes possible	Large pore sizes possible
Non-specific binding	Low	Moderate-high	Moderate-high
Ease of functionalization	Easy	Moderate-difficult	Moderate-difficult
Mechanical strength	Limited, requires chemical cross-linking	Good	Exceptional
Stability in harsh chemical conditions	Stable	Stable	Unstable in alkaline conditions

1.2.1. Resin structural characteristics

Resin design and its characteristics depend on the intended purpose, i.e. the purification stage: capture, intermediate or polishing. Capture step calls for a short processing time, and high capacity resin in order to deal with large volumes of reasonably crude protein solutions. Resins for the intermediate step are required to maintain high product yield in addition to high binding capacity. Polishing, the final chromatography step, relies on resins that can provide exceptional separation efficiency of closely related species.

Ideally, each chromatography step would be able to deliver all four elements: high speed, capacity, recovery and resolution. However, that would be very difficult to achieve. Good mass transfer and reduced cycle time at low pressure can be achieved through increased bead size and wide pores **(Table 1-3)**. In contrast, high capacity, good resolution and recovery can be attained with large surface area provided by small bead size, narrow bead size distribution, small pores, the choice of ligand and its optimum density. Regardless of the stage, resin particles also have to be mechanically stable in order to withstand manufacturing conditions and operating pressures of 3-4 bar. Good chemical stability, especially under alkaline conditions, is paramount for resin cleaning, sanitisation, and thus its operational lifetime.

The specificity of any chromatographic material is further determined by the choice of a ligand, an immobilised chain to a stationary phase that has high specificity towards the target molecule in the mobile phase, its amino acid sequence or other differentiating characteristics. Different types of ligands are used for affinity, ion exchange (IEX), and hydrophobic interaction (HIC) chromatography **(Table 1-4)**. In IEX chromatography, pH has a significant impact on the protonation behaviour of the ligands determining their operational ranges. Strong ion exchangers are charged the same throughout pH 2 to 10, whilst weak ion exchangers vary in their binding strength

and selectivity based on buffer pH. A large number of ligands present a good selection of options to suit different purification processes.

Table 1-3. Characteristics of chromatography resins and their impact on performance. Adapted from (Hagel et al., 2008).

Resin characteristic	**Impact**
Mechanical strength	Maximum operating velocity, throughput
Particle size	Maximum operating pressure, dynamic binding capacity, purity, resolution
Particle size distribution	Column packing efficiency, resolution
Pore size and pore size distribution	Dynamic binding capacity, maximum operating velocity, purity, resolution
Ligand type and density	Dynamic binding capacity, selectivity, resolution, recovery
Chemical stability	Lifespan, ease of SIP and CIP, ease of validation in between cycles

Table 1-4. Examples of ligands based on chromatography type.

		Strength	**Ligand**
Affinity			Proteins: A, G, L; Tags: His, FLAG, GST
HIC		In order of increasing hydrophobicity	Butyl, octyl, phenyl
IEX	• **Cation**	Weak	Carboxymethyl (CM), Carboxylate (COOH)
		Strong	Sulfopropyl (SP), Methyl sulfonate (S)
	• **Anion**	Weak	Diethylaminoethyl (DEAE)
		Strong	Quaternary aminoethyl (QAE), Quaternary ammonium (Q), Quaternary amine (QA)

1.2.2. Overview of resin production steps

Agarose has a high melting and a low cooling point, which is the basis of agarose-based resin manufacture **(Figure 1-1)**. Red seaweed (e.g. *Pterocladia capillacea*) is collected and processed in order to extract agarose. Emulsification process relies on heating agarose solution in oil to encourage droplet formation which solidify upon temperature reduction. The solid porous beads are then strengthened via crosslinking with, for example, epichlorohydrin or divinyl sulfone to enhance the mechanical strength that is inherently quite limited. The process of desired ligand functionalisation consists of several steps: bead washing to allow for solvent exchange and surface activation to enable ligand attachment.

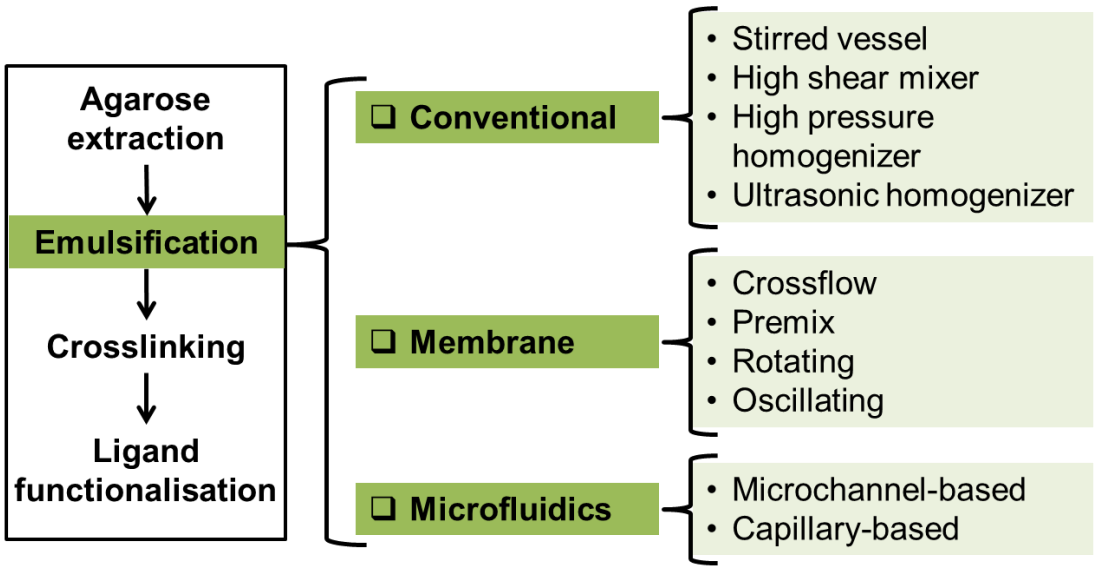

Figure 1-1. Agarose resin production process. Three main types of emulsification: conventional, membrane and microfluidics, which can be further sub-divided into categories based on the different instrumentation used.

1.2.3. Emulsification strategies

Emulsification step relies on a heterogeneous system of two immiscible liquid phases with one of them being dispersed and forming droplets in the other. Most common emulsions consist of water and oil, and require a supplementation of a chemical reagent called the emulsifier in order to avoid immediate recoalescence. Production of droplets in the colloidal particle size range needs a considerable amount of mechanical energy. Currently, there are three main resin emulsification methods utilising conventional batch, membrane and microfluidics technology **(Figure 1-1)**.

1.2.3.1. Conventional batch

The key advantage of this approach lies in its simplicity, robustness and scalability resulting in high production yields. It is also possible to manufacture different particle sizes with a single reactor, which is economically beneficial. Unfortunately, these reactors produce a wide range of particle sizes (Baker, 1993; Yan et al., 2009; Mu et al., 2005), leading to difficulties and differences in column packing, flow properties and operating pressures. As a result, the technique produces a large amount of fines, which could cause significant filter clogging and backpressure, and thus requires an additional step. Sieving is a time consuming process that is aimed at minimising particle size variation by excluding fines and coarse material.

Conventional emulsification offers a high particle size distribution due to its operating mechanism. The general idea of emulsification is to pour melted agarose into an oil and surfactant mixture, which is then stirred by either a propeller or a stirrer. Due to shear stress in the small space created by the rotor and the stator (i.e. reactor), droplets form of various size. The size of agarose beads depends on the type and speed of the rotor as well as the number of times agarose beads pass through it.

There are several types of rotor-stator mixers (Urban et al., 2006): stirred vessels, high-shear mixers (Zhang et al., 2012), and homogenisers: high pressure (Stang et al., 2001; Schultz et al., 2004) and ultrasonic (Canselier et al., 2002) **(Figure 1-2)**.

Stirred vessels are the most commonly utilised in industry. Precise design of the stirrers, geometries, baffles, and the use of surfactant and stabilisers makes the manufacturing very cost-effective and scalable (from 1 m^3 to 20 m^3 process vessels). Unfortunately, such vessels have a significant amount of dead space leading to wide particle size distribution. In contrast, high-shear mixers produce a smaller particle size range due to stator and rotor operating in very close proximity. Another difference between those is the speed at which they are spun. The high-shear mixer can develop higher speed and more efficient bead production resulting in unwanted shear levels, which could damage the beads.

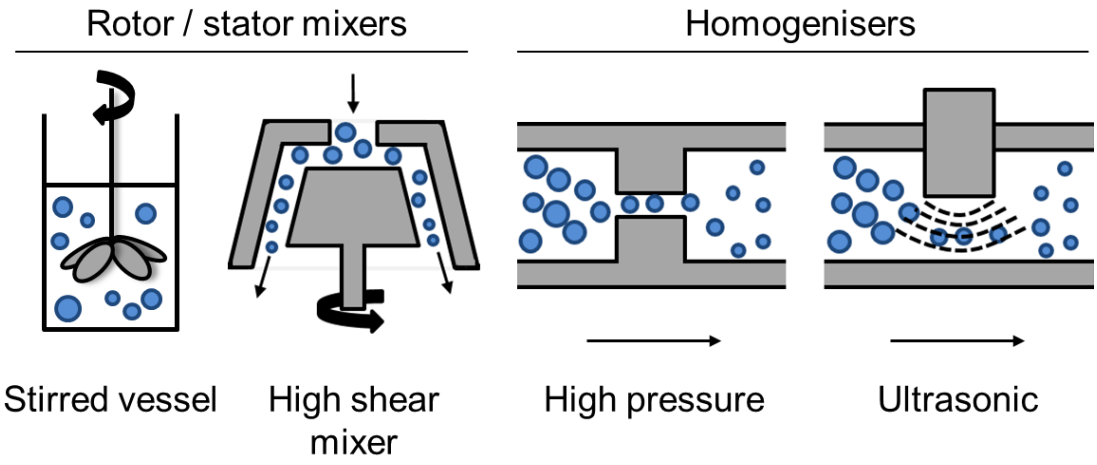

Figure 1-2. Conventional emulsification methods. Arrows indicate the direction of flow.

Similarly, two other techniques: high pressure and ultrasonic homogenisers create high product stress and wide bead size distribution range. Both homogenisers are mainly used for the laboratory scale applications because the cost of manufacturing and cost of goods increase significantly with the increasing scale. The least common high pressure system used for agarose bead production is spray-gelation (Bengtsson and Philipson, 1964; Egorov et al., 1970). It involves the use of numerous packed discs that allow the agarose phase to be squeezed through the nozzle of the sprayer. As droplets develop, they fall into a cold water-ether solution. Despite little information

about agarose bead production in the literature (Mu et al., 2005; Ioannidis et al., 2012), a number of patents have been registered in this field (e.g. Amersham Biosciences Ab, 2003; Millipore Corporation, 2010).

1.2.3.2. Membrane

Another emulsification method uses a porous membrane to generate beads of the chosen size. Having a history of use in food and biotechnology industries (Charcosset, 2006, 2009), this method has only recently been researched (Zhou et al., 2007, 2008, 2009; Yan et al., 2009; Zhao et al., 2014; Li et al., 2015) and introduced into agarose resin manufacturing by companies such as Dow, LANXESS and Purolite. There has been a growing interest in the membrane emulsification technique due to its key advantage – generation of monodisperse particles. The use of a membrane with a narrow pore size distribution allows for a more cost-effective, productive and reproducible resin manufacturing as the number of steps, specifically: washing and sieving of the beads, are eliminated. As a result, the amount of fines, which can clog filters and increase backpressure, is significantly reduced offering improved column packing efficiency and reproducibility. Better packing quality and improved flow properties are expected to provide a more efficient protein separation resulting in sharper and narrower elution peaks. This would be achieved through a reduction in varying solute's path length and velocity around and through the particles.

Membrane emulsification technique is similar to that of the conventional emulsification except it utilises a membrane instead of a stirrer **(Figure 1-3)**. A water phase containing dissolved agarose at high temperature is passed across a porous membrane forming droplets into the oil phase. An emulsifier can also be used to stabilise the droplets. The oil phase is then cooled down at the room or lower temperature whilst stirring to ensure a more uniform cooling temperature, and prevent from agglomeration. Once agarose particles are formed, they have to be washed

using ethanol or isopropyl alcohol to remove excess oil. Although commonly mentioned in the literature and generally more effective, ether as a washing reagent is not used in the industry due to safety concerns, which would increase capital outlay.

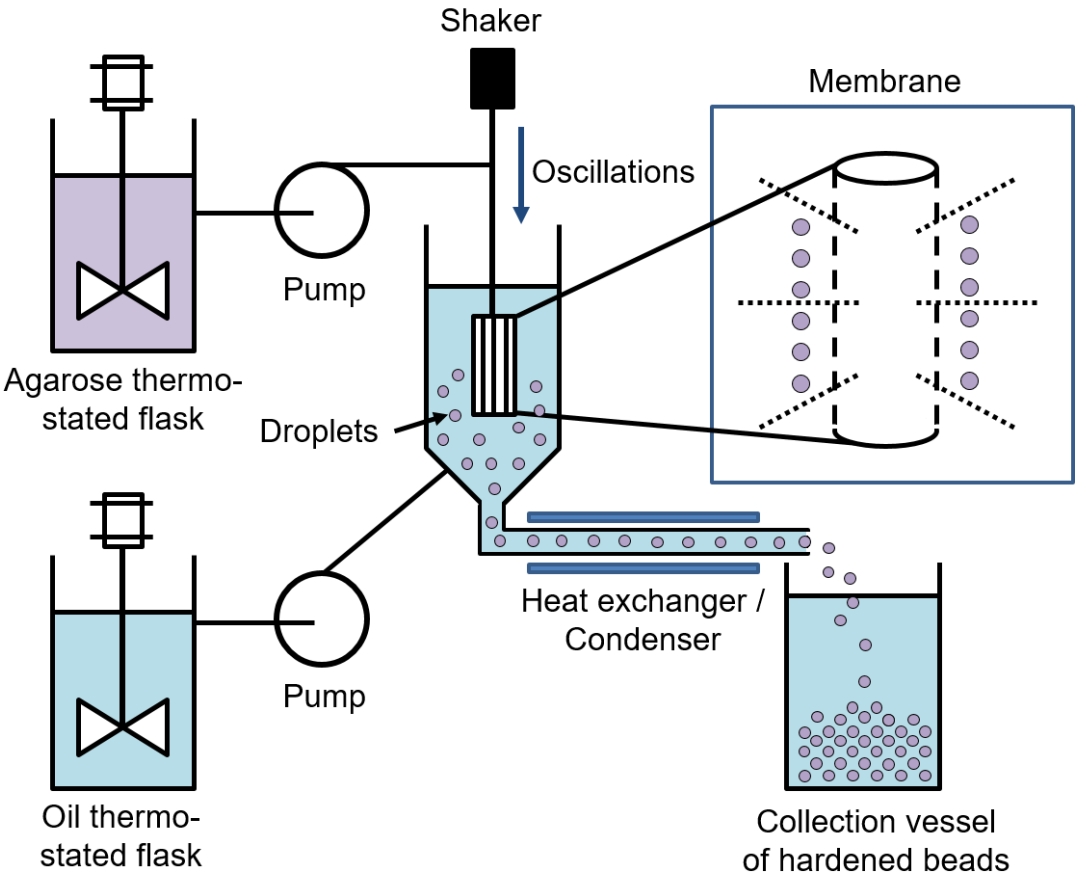

Figure 1-3. An overview of a membrane-based emulsification method – jetting.

Membrane emulsification can be divided into further subtypes: cross-flow (Gijsbertsen-Abrahamse et al., 2004), premix (Nazir et al., 2010), rotating (Li et al., 2015), and oscillating (Holdich et al., 2010) **(Figure 1-4)**. Cross-flow emulsification method relies on pushing melted agarose solution (to-be-dispersed phase) through the membrane into the continuous phase containing the oil and emulsifier. Unfortunately, this technique does not provide high yields due to low dispersed phase flux, and can only operate at low viscosities. Therefore, premix emulsification can be

used to improve it. Premix emulsification requires a preparation of the primary step: coarse emulsion via mixing, homogenisation or another wider pore membrane. The created coarse emulsion (large droplets) can be further reduced using transmembrane pressure to obtain a smaller size and narrower particle size distribution (Zhou et al., 2008). Rotating steel membrane has only been used in the production of very large beads of 220 µm, which are usually used in dairy applications, but does not require pre-processing (Li et al., 2015). In contrast, an oscillating membrane (otherwise known as jetting) has been patented for a continuous production of <100 µm porous agarose particles, and has been shown to reduce energy inputs and operating costs when compared to the conventional methods (Purolite Corporation, 2014).

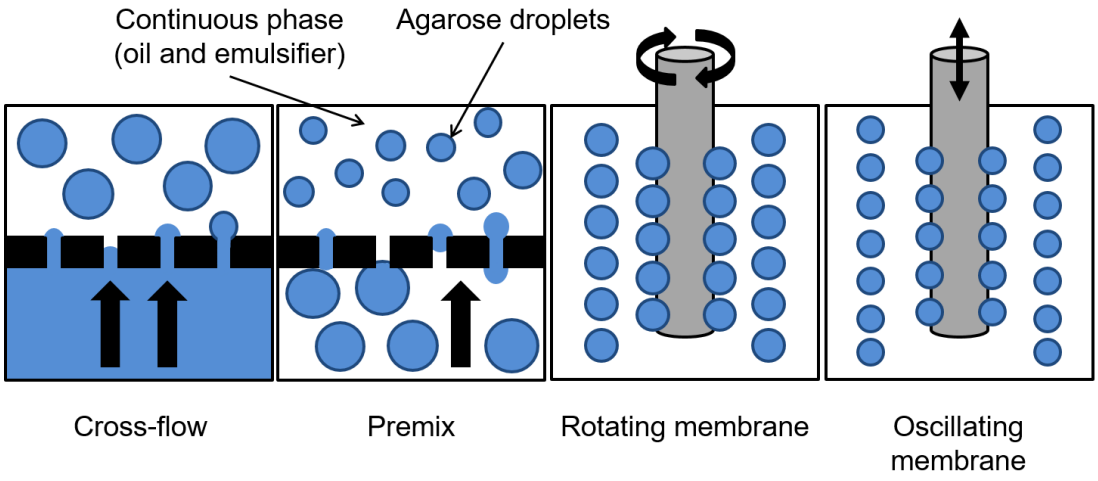

Figure 1-4. Types of membrane emulsification.

1.2.3.3. Microfluidics

Uniform agarose droplets can also be formed with the help of a scale-down approach. The method is attractive since only a small amount of raw materials is required. However, this means that micro-devices are mainly useful to look at different development factors and conditions rather than bead production at an industrial scale. Nevertheless, a company called Dolomite has developed very efficient and accurate

droplet generators, which are available on the market. The equipment is highly automated and easy to use allowing droplet generation of any desired size: from 1 to 100's µm. The speed of the oil or water flow as well as the pressure can be adjusted to give the desirable results. The company also developed a high-throughput version of these devices called Telos®. They claim that the system can create up to a tonne of droplets per month (Dolomite, 2017), and has already been successfully tested on agarose bead production (e.g. Dolomite, 2017; Grasso and Lintilhac, 2016; Shembekar et al., 2016).

Two main types of microfluidics-based approaches include microchannel- and capillary-based devices (Serra and Chang, 2008). These can be further sub-divided into terrace-like, T-junction, Y-junction and flow focusing (FFD) microchannel devices; also co-flow, cross-flow and FFD capillary devices **(Figure 1-5)**. More information about the improvements in the technology can also be found elsewhere (Mohanty and Purkait, 2012; Basova and Foret, 2014).

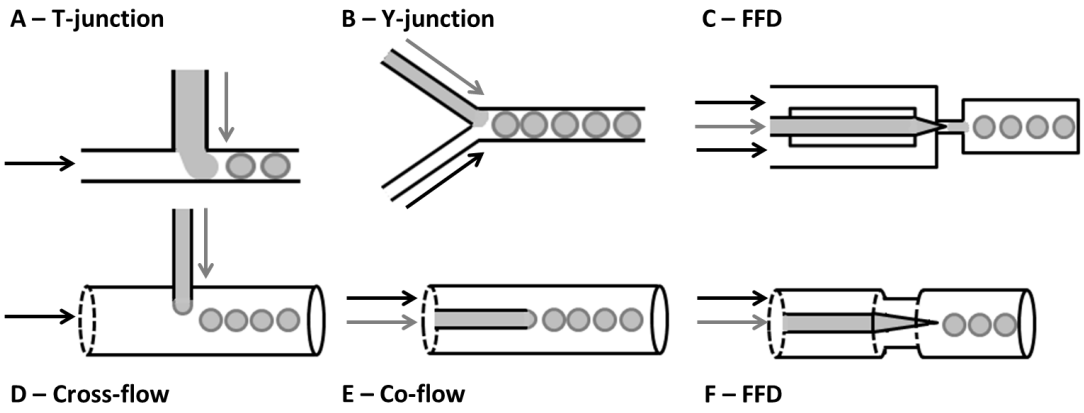

Figure 1-5. Microfluidics-based emulsification strategies. A, B and C are microchannel-based, whereas D, E and F are capillary-based devices. Black arrows represent the flow of continuous phase and grey ones the to-be-dispersed phase. FFD – flow focusing device. Adapted from Serra and Chang, 2008.

1.2.3.4. Summary of the techniques

The most important factors concerning resin manufacturing include potential to scale up and to implement a continuous process, low material consumption and low overall cost. The quality of the resin is another serious consideration. All three emulsification methods are comparable in terms of mechanical and structural features of the resin as agarose is the main component and other process conditions can be adjusted. The main difference is the particle size reproducibility that can be achieved. The most uniform particles are made in microfluidics devices followed by the membrane-based approach and conventional methods **(Table 1-5)**. Unfortunately, the former cannot be scaled up, whilst the latter cannot ensure lot-to-lot reproducibility. In addition, rotor / stator mixers have a large footprint since the production requires a threefold excess of starting material (Millipore Corporation, 2010). Therefore, membrane-based manufacturing method is currently of most interest as it has the desirable features: ease of scalability, production of monodisperse particles, and a small footprint.

Table 1-5. Comparison of emulsification methods.

	Conventional	**Membrane**	**Microfluidics**
Equipment	Rotor/stator mixers, homogenisers	Porous membrane	Microchip
Mode of operation	Batch	Continuous	Continuous
Particle size uniformity	Wide size distribution range	Narrow size distribution range	Uniform
Scale up	Yes, but not homogenisers	Yes	No
Reproducibility	Low	Medium	High
Cost of production	High	Medium	Low

1.2.4. Ligand functionalisation strategies

Ligand functionalisation is achieved through agarose activation and ligand coupling. Base activation is usually performed in a non-aqueous environment, and is therefore washed with solvents such as DMSO, acetone, methanol, ethanol, etc, in order to gradually eliminate water-based solutions. Agarose-based matrices are rich in hydroxyl groups that are activated by introducing electrophilic groups. The chosen ligand can then be coupled to the activated group. Ligand density and distribution on agarose beads depend on a) base activation conditions including extent of aqueous solvent exchange, and the type and concentration of the activating reagent, and b) ligand coupling parameters such as pH, temperature, length of reaction, amount of ligand, its size and type. Some of the parameters can be difficult to control and the evaluation of their efficiency can be challenging resulting in an unwanted lot-to-lot variation.

1.3. Agarose-based resin characterisation techniques

The characterisation of resin after its manufacture is of highest importance in order to reduce the lot-to-lot variation. Product structural quality and its consistency as well as the functional characteristics are determined. Particle size is the first factor to be measured whilst emulsification is taking place, followed by mechanical strength evaluation. Particles can also be examined for potential abnormalities such as cracking or deformations. Finally, adsorption kinetics, resolution, the degree of impurity clearance, and lifetime are evaluated. The most common agarose resin characterisation procedures will be discussed in this section as detailed in **Figure 1-6**.

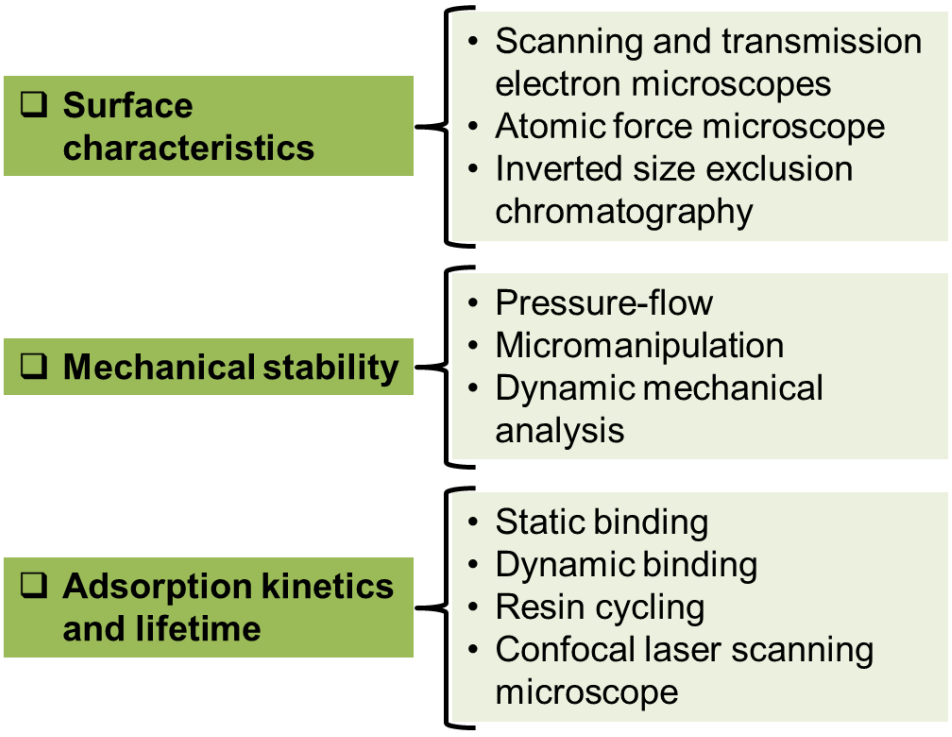

Figure 1-6. Agarose resin characterisation methods based on the three main desired resin qualities.

1.3.1. Surface area and particle size

The size of the particles depends on the manufacturing method and parameters used. Average particle size and distribution are primarily dictated by the implemented emulsification method: conventional, membrane- or microfluidics-based. Process parameters such as temperature, agarose concentration, rotor speed, and membrane pore size can also be adjusted for the desired particle size (Dolomite, 2015; Zhou et al., 2008; Vladisavljevic, 2015; Mu et al., 2005). The outcome of emulsification can be measured using specialised but easy to use equipment based on laser light diffraction (Mastersizer), electrical zone sensing (Coulter counter) or visible light (optical microscopes). More challenging techniques are required for pore size determination and involve electron and atomic force microscopes as well as size exclusion-based methods.

1.3.1.1. Scanning (SEM) and transmission (TEM) electron microscopes

Both electron microscopes can be used to visualise the surface of the particle: pore size and pore size distribution as well as particle size. While both SEM and TEM can be used to determine these features, SEM shows greater resolution and accuracy of agarose fibres and structural features (Lintern et al., 2016). The main disadvantages of both techniques, however, are the complexity of the microscopes and difficult sample preparation requiring complete water elimination. Drying of the sample often causes damage to the beads leading to fractures and changes to / loss of their overall shape making the image resolution challenging. Although four main types of drying techniques including air-, freeze- and critical-point-drying as well as cryo-sample preparation are available, only critical-point drying (Nweke et al., 2017b) and cryo-sample preparation (Bell and Santeufemio, 2006) have been shown to be effective at minimising damage to agarose structure.

1.3.1.2. Atomic force microscope (AFM)

Unlike electron microscopes, AFM is a non-invasive technique for imaging the internal pore structure. Agarose beads can be observed in their native slurry (solvent) environment without the need of drying. A number of successful experiments have been performed using this approach (e.g. Pernodet et al., 1997; Maaloum et al., 1998; Ioannidis et al., 2012). This microscope has also been used for silica beads to measure pore volume (Sörensen et al., 2008), which could potentially be used for agarose beads. Despite the great potential, AFM also has its drawbacks. Firstly, it is only effective for the outer surface of the particle as slicing wet resin is problematic, whilst electron microscopes can visualise internal structures. Secondly, AFM works by creating a contact between a sample and a sharp triangular tip, which moves quickly and with force through the sample to create a three -dimensional image. If the force is not adjusted or an alternative non-contact tip is not employed, soft surfaces such as agarose could therefore get damaged and result in a production of an inaccurate image (Paredes et al., 2003).

1.3.1.3. Inverse size exclusion chromatography (iSEC)

This method is also used to determine the pore size and distribution (e.g. DePhillips and Lenhoff, 2000; Goto and McCoy, 2000; Yao and Lenhoff, 2004) as well as pore accessibility (Stone et al., 2009) of agarose gels. It requires a prior selection of known molecular size markers (dextrans) that are run on the iSEC column to determine the molecular weight cut off. The analysis of the results is straightforward: retention times are indicative of the separation. Different size molecules will travel through respective pores and generate an elution profile indicating retention times, which can then be used for a calibration curve. Whilst this method allows to accurately determine pore size of the particles in their native state, the results can be limited by the chosen size of molecular markers.

1.3.2. Mechanical stability

Mechanical properties of the resin particles determine the maximum linear velocity and the resulting pressure that the column can be operated at. Agarose is known to be a relative soft gel that can compress and regain its shape until the maximum the maximum operating flow rate has been achieved after which resin is no longer functional. The particles can usually withstand higher operating pressures than the chromatography columns themselves; hence the pressure limit is 3-4 bar. Pressure-flow, micromanipulation and dynamic mechanical analysis are most commonly used methods to evaluate the mechanical stability of resins **(Figure 1-7)**.

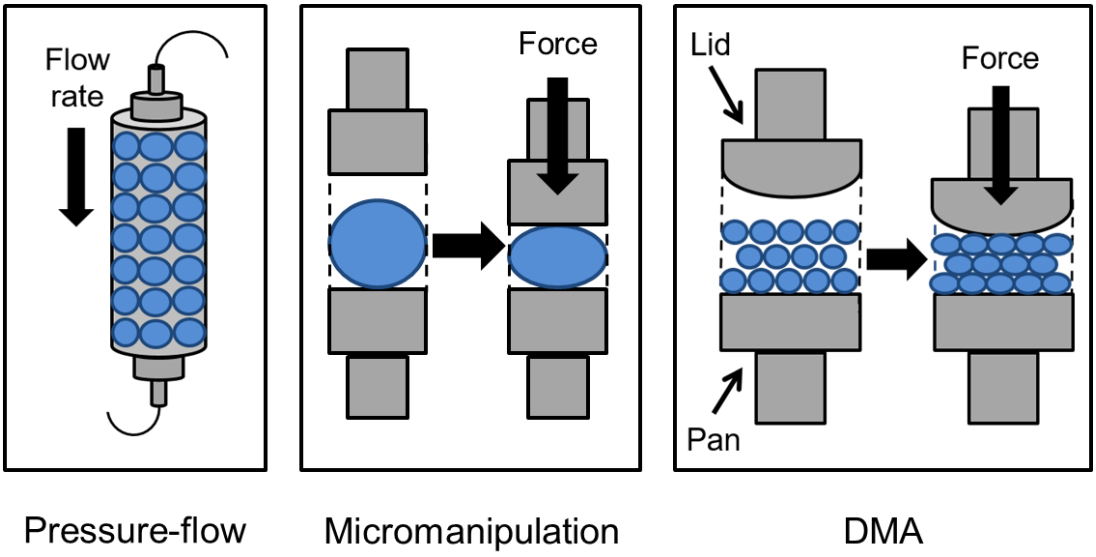

Figure 1-7. Methods for mechanical characterisation of resin.

1.3.2.1. Pressure flow

This is the most commonly employed method to measure the maximum operating pressure. The technique relies on a gradual increase of the flow rate through a packed column until the bed collapses, i.e. the pressure starts to rise uncontrollably without further increases in the flow rate. This technique is also useful when comparing, for example, new and aged (or fouled) resin samples. The fouled resins cannot withstand as high pressures as the new ones. The main disadvantage of the method is that it

requires large quantities of resin, good column packing and evaluation protocols as well as careful selection column parameters (i.e. width and height) that are representative of a large-scale chromatography process.

1.3.2.2. Micromanipulation

The technique involves compressing a single bead between two parallel micro-plates and measuring a compressive force. Whilst micromanipulation allows to examine mechanical properties of an individual bead without the need of column packing that saves resources and time, this method would provide inconsistent results for resins manufactured with conventional emulsification technology (Yan et al., 2009; Mu et al., 2005; Ioannidis et al., 2012). Wide particle size distribution would lead to differences in their strength; thereby, this method is more suitable for beads manufactured using membrane-based techniques, which offer a narrower bead size distribution.

1.3.2.3. Dynamic mechanical analysis (DMA)

This method has been used to test the viscoelastic features of a number of materials; however, only recently it has been tested on agarose beads (Nweke et al., 2017a). The results of this work suggested that the technique is comparable to the commonly used pressure flow method. The DMA machine consists of a lid and a small resin sample on top of a pan which is then compressed and the results are recorded in a time versus strain profile **(Figure 1-7)**. The quicker the lid reaches the pan, the less viscous and more deformed the sample is (potentially suggesting an old resin). At the same time, the percentage of the strain per minute increases levelling out once the pan has been reached or when the bed cannot be compressed any longer. This graph can be used to compare different types of resins and their mechanical stability. One of the obvious advantages of this method is that the small resin sample used is representative of laboratory scale experiments. Therefore, it is a time-efficient and cost-effective method in academic research, which has a potential to be utilised industrially.

1.3.3. Performance and chemical stability

Large surface area and good mass transfer determine the binding capacity, product resolution and yield as well as lifetime of the resin. The ability to maximize surface area improves resins' value in the market: smaller amount of resin and shorter processing times are required to capture the same amount of protein. Reusability of resin also depends on its chemical stability in various solvents such as sodium hydroxide, and is expected to have a lifespan of approximately 100 cycles.

1.3.3.1. Static binding capacity (SBC)

Also known as a batch uptake method, SBC provides information about the equilibrium state of the liquid and solid phases, and the speed of mass transfer under static flow conditions. The technique relies on known amount of solute (protein of interest) added into a known amount of adsorbent (resin) whilst mixing. Samples are then taken at set time intervals and the adsorbance is measured at 280 nm wavelength to determine the amount of unbound protein. The mass balance is determined and a graph usually representing a favourable Langmuir adsorption model is drawn depicting the speed of protein uptake and the maximum binding capacity. Whilst this method is very laborious and time-dependent, high throughput alternatives such as PreDictor™ plates could simplify the task. In addition, only a small amount of the feed material and chromatography resin is required.

1.3.3.2. Dynamic binding capacity (DBC)

Similar to the static binding capacity approach, DBC technique looks at the maximum binding capacity but under constant flow conditions. The method involves continuously supplying feed material onto a packed column and measuring the absorbance of flow through until the measurement reaches a plateau. Results are heavily specific to the chosen flow rate, thus several residence times ranging from 2 to 8 minutes are usually tested. This technique is straightforward and accurately depicts resins' performance under traditional process conditions, which can be scaled

down to 0.2 mL high throughput columns. An alternative approach such as biolayer interferometry has been developed by ForteBio suitable for high throughput method to analyse 200 samples in an hour (Do et al., 2008).

1.3.3.3. Confocal laser scanning microscopy (CLSM)

Confocal microscopes are used with various materials including chromatography resin particles (see a review by Hubbuch and Kula, 2008). Single particle visualisation under static flow conditions has been possible since 1996 (Kim et al., 1996) with many examples following later (Ljunglöf and Hjorth, 1996; Ljunglöf and Thömmes, 1998; Linden et al., 1999; Hubbuch et al., 2003a; Harinarayan et al., 2006). The major drawback of this approach was the inability to observe the same particles and protein uptake changes under dynamic flow conditions. This led to a development of a scale down model, a miniature chromatography column that could contain 20 µL of packed resin, and visualise intra-particle protein uptake in real time (Hubbuch et al., 2002; Dziennik et al., 2003; Hubbuch et al., 2003b; Siu et al., 2006; Yang et al., 2008; Yang and Sun, 2008; Close et al., 2013). The intensity of the bound fluorescently-labelled proteins could be measured and converted to the amount of bound protein (Hubbuch et al., 2002). This technique has been used to study general protein uptake behaviour (Dziennik et al., 2003; Yang et al., 2008; Yang and Sun, 2008) and resin lifetime (Siu et al., 2006; Close et al., 2013).

Confocal microscopy provides essential knowledge about adsorption kinetics if performed correctly. The challenges of this technique revolve around the type and concentration of the fluorescent dye, photobleaching and reabsorption amongst others reviewed by Hubbuch et al. (2008). Fluorescent dyes can interfere with the shape and activity of the labelled protein leading to misleading results and signifying the importance of evaluating several options. In addition, excessive amount of the labelled protein can cause detection issues, thus the right ratio such as 1:100 is recommended. In contrast, fluorophore bleaching would result in low signal readings

if the samples were not well protected from the light or laser intensity was set too high. Reabsorption is another serious problem that can be encountered and would result in a false appearing low signal pattern as some of the emitted light is reabsorbed by the adjacent molecules. The likelihood of this pattern increases with increasing concentration of dye-labelled molecules. Similarly, fluorescence intensity can be reduced if the light path is obstructed as a result of particles being tightly packed or air bubbles being present in the sample.

1.3.3.4. Resin lifetime

The lifespan and alkaline stability are important parameters that determine the number of cycles that can be performed with the same packed column. Chemical stability dictates which reagents can be used during the purification process as well as the cleaning and storage steps, and can be easily evaluated via the incubation experiments. Resins' re-usability calls for lengthy studies that are performed whilst running tens of cycles often with a clarified cell culture spiked with the protein of interest. With increasing number of cycles, the resins' binding capacity decreases accompanied with increasing column pressure as some of the feed material stays bound to the column. Various cleaning regimes can be explored in order to obtain the most effective resin procedure.

1.4. Concluding remarks

This chapter focused on the importance of antibody-based products in the pharmaceutical industry and their purification strategies. Downstream processing was found to be the main bottleneck limiting production yield and purity that could be alleviated through innovation in the chromatography process step itself or improvements in the raw materials. Novel materials including nanofibers, monoliths and membranes have been investigated to replace the traditional agarose-based

resins. The alternatives, however, were deemed less effective for the antibody purification as they were more suited towards the products of larger molecular weight such as viruses. Therefore, improvements in agarose-based resin manufacture became the main focus.

The main advantage of agarose-based resins is their large surface area that can provide high dynamic binding capacity. In order to achieve this, structural features such as particle size and distribution, pore size and distribution, tortuosity, and ligand type and density are the key elements for the optimum product adsorption kinetics and separation. The design of the particles is heavily dependent on the emulsification process, in which agarose is melted and cooled down to form droplets in a traditional stirred tank or novel membrane process. Particle size and distribution depend on the method used: stirred tanks generate a larger distribution of particle sizes, whereas membrane emulsification has a tighter control of the size making them monodisperse. The next steps of the production process consist of crosslinking to improve the mechanical strength, and functionalisation of ligands to determine molecule selectivity and binding capacity. All these steps can be altered to achieve the desired chromatography resin features.

Lot-to-lot resin variability is commonly encountered, and in order to avoid it, extensive effort is made to characterise the manufactured product. Surface area and particle size can be easily measured using microscopy techniques, whilst performance and chemical stability can be evaluated through subjecting resins to various feed materials and multiple bind-to-elute cycles. Resin production and characterisation are key to achieving consistent and reproducible recovery and separation of the target product.

1.5. Aim of the thesis

The aim of this thesis is to intensify the chromatography process and improve the purity of the target molecule through optimising the design of the resin particles facilitated by Purolite Life Sciences. A variety of objectives are established to fulfil the desired aim:

Chapter 3 – Resin structural feature assessment

In order to compare the effects of different manufacturing approaches, resins of various particle sizes and particle size distributions were made using the traditional batch and novel membrane emulsification methods. Structural feature consistency is determined with the help of SEM and CLSM as well as laser light diffraction, whilst mechanical stability is established through pressure-flow studies. Three densities of ligands with the aim of 0.08, 0.16 and 0.24 mol/L are functionalised to all beads in order to create a 4 x 3 matrix.

Chapter 4 – Resin adsorption kinetics

Resin performance is a key indicator of its suitability for intensive processing. Dynamic binding capacity and real-time protein uptake rate are determined for all resins (4 x 3 matrix) at different linear velocities ranging from 37 to 380 cm/h. A scale-down chromatography model is used with CLSM to visualise bovine serum albumin uptake rate at different concentrations.

Chapter 5 – Resin lifetime

Lifetime is another important measure of resins ability to withstand being exposed to multiple chromatography cycles. Due to a limited number of methods available to determine resin reusability, a novel detection technique was developed. A fluorescent dye was used to visualise with CLSM and measure with a fluorescent dye reader the remaining bound protein on and inside the particles. Fouling patterns caused by

structural resin features, bead positioning inside the column and cleaning conditions were evaluated.

Chapter 6 – Resin resolution capabilities

The knowledge gained in Chapters 4 and 5 allowed to choose the manufacturing method, average particle size, and ligand densities to be explored in the next set of resolution experiments. In this chapter, ovalbumin isoform and monoclonal antibody separation was performed to gain a detailed understanding of the effects of structural resin features and process conditions on protein resolution, recovery and purity.

2. Chapter: Materials and methods

2.1. Materials

2.1.1. Chemicals

Citric acid, L-arginine, silver nitrate, sodium hydrogen carbonate, sodium hydroxide, sodium nitrate, sodium acetate, sodium citrate (Fisher Scientific, Loughborough, UK), hydrochloric acid (36%, SciChem, Bilston, UK), sodium chloride, sodium phosphate (Merck Chemicals, Chilworth, UK), Tris (Promega, Madison, USA), sodium borate (VWR, Lutterworth, UK).

2.1.2. Proteins and fluorescent dyes

Lipid-free bovine serum albumin (BSA, Fraction V, Sigma-Aldrich, Gillingham, UK), Texas Red®-labelled BSA (Fisher Scientific, Loughborough, UK), Proteostat® dye (Enzo Life Sciences, Exeter, England), hen egg albumin or “ovalbumin” (Sigma Aldrich, Gillingham, UK), monoclonal antibodies IgG1 and IgG4 were kindly provided by Fujifilm Diosynth Biotechnologies, Billingham, UK.

2.1.3. Chromatography matrices

Praesto Q and Praesto SP were manufactured by Purolite Life Sciences, Llantrisant, Wales. MabSelect SuRe™ was purchased from GE Healthcare, Uppsala, Sweden. CIMac™ QA and CIMac™ COOH monolith columns were bought from BIA Separations, Ajdovscina, Slovenia. ACQUITY UPLC Protein BEH SEC 4.6 x 150 mm, 1.7 µm size exclusion column and ACQUITY UPLC Protein BEH SEC guard column were from Waters Corporation, MA, United States.

2.2. Equipment for chromatographic separations

Protein separations with fast protein liquid chromatography system ÄKTA™ Pure 150 were performed with Protein A, AEX or CEX resins packed in Tricorn 5/50, Tricorn 5/100 or XK16 (all equipment GE Healthcare, Uppsala, Sweden). Analytical high-performance liquid chromatography system Agilent 1260 Infinity (Agilent, Santa Clara, US) was used with the monolith and size exclusion columns. UNICORN™ 6 software allowed to determine column packing efficiency, peak area and peak percentages on ÄKTA™, whilst ChemStation software was used for the peak analysis in the Agilent system.

2.3. Methods

2.3.1. Agarose resin manufacture

Praesto Q agarose resins of three average sizes: 45, 65 and 90 µm, also known as Q45, Q65 and Q90, respectively, were manufactured in a stirred tank using a traditional emulsification method. The next set of 45 µm size beads were produced using a novel membrane emulsification method called jetting (developed by Purolite, Llantrisant, Wales). This technique allowed for a continuous production of uniform beads, thereby reducing the broad bead size distribution encountered with traditional emulsification methods.

Particle size distribution was determined using Mastersizer 3000 (Malvern Panalytical, Malvern, UK) that utilized laser light diffraction to measure particles from 10 nm to 3.5 mm making it suitable for agarose chromatography resins. Hydro SV liquid dispersion unit was used to accommodate small bead samples and to allow for 10 – 20% obscuration. Five measurements of each sample were taken in ethanol with the refractive index of 1.36 whilst being stirred at 1500 rpm. Refractive index for agarose was set at 1.40 and absorption at 0.

2.3.2. Structural resin characterisation

2.3.2.1. Bead surface imaging and evaluation

Surface imaging is often challenging as the beads are prone to collapsing upon desiccation. Therefore, resins were dehydrated through a stepwise increase of ethanol from 20 to 100% in order to prepare samples for critical point drying (Nweke et al, 2017). Ethanol slowly displaced water whilst maintaining the airy agarose structure. Particles were coated with gold and palladium prior to imaging. The materials and equipment including critical point drier, ion beam coater and scanning electron microscope (SEM) used here were exactly the same as described by Nweke et al (2017). Images were taken at 10.0 µA and 2.0 kV accelerating voltage.

Images taken at 100x magnification were analysed with ImageJ software to gain an insight into particle size distribution **(Figure 2-1)**. The scale was set for each image based on the metadata file from the SEM followed by the image inversion function. 'Find edges' button highlighted the circumference of the beads, and threshold selection allowed to distinguish them better from the background. Images not containing touching particles could be analysed immediately, whilst the ones with closely interacting beads had to go through two additional steps: 'fill holes' and 'watershed'. Watershed function allowed to separate the interacting beads, whereas fill holes function highlighted the area of the particles to be separated. The software could then calculate the height and the width of the beads representing their diameter, and provide size distribution plots.

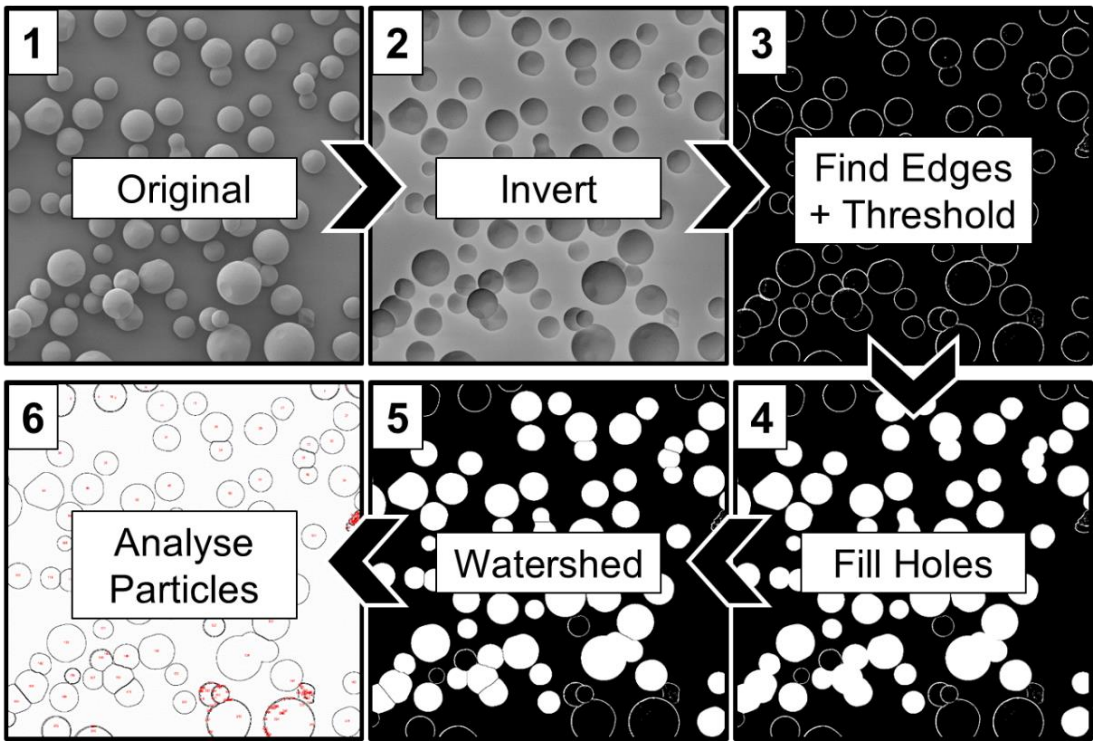

Figure 2-1. Particle size distribution analysis with ImageJ. SEM and CLSM images of 100x and 40x respective magnifications were used. Steps 1-6 represent required commands in ImageJ to measure particle diameters (width).

Images taken at 15,000x magnification were further analysed to estimate the pore count, average pore size and apparent porosity (Nweke, 2017). The steps taken to quantify the images were similar to those described above **(Figure 2-1)**. Here, however, the images were 'smoothened out' prior to their inversion **(Figure 2-2)**. Threshold was established and edges were found prior to 'analyze particles' function was selected. Pore count, average pore size, their diameter and apparent porosity were extrapolated from the summary box provided by the software. Average pore size was displayed in nm^2 and the diameter was approximated based on the area of a circle (πr^2) in nm. Apparent porosity reflected the percentage of pores in the image against the total fibrous network.

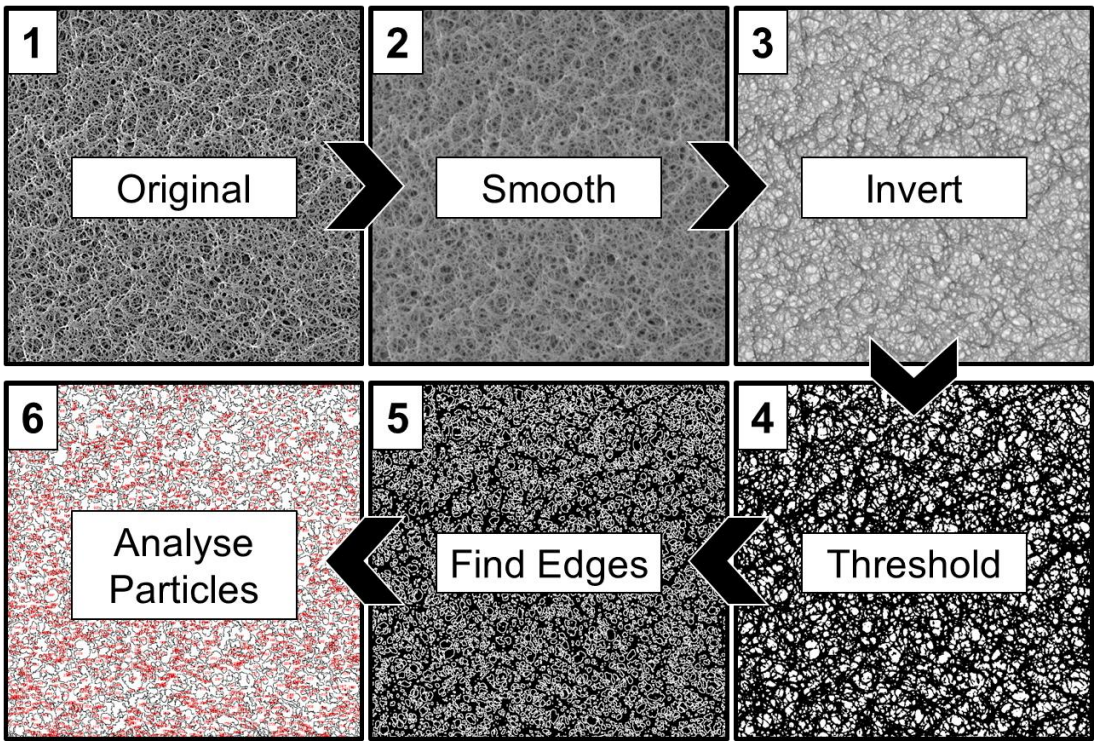

Figure 2-2. Pore analysis with ImageJ. SEM images of 15,000x magnification were analysed to gain measurement of pore count, average pore size and apparent porosity. Steps 1-6 represent required commands to quantify pore composition.

2.3.2.2. Quaternary ammonium functional group quantification

Ligand density for agarose resins was determined using 0.1 M silver nitrate. Five-millilitre silver nitrate burette and 848 Titrino Plus units (both Metrohm, Runcorn, UK) were used to measure ion exchange capacity. A small sample of resin was poured into a 1.9 mL glass filter funnel (plate 10 mm, stem 6 mm, porosity 3, VWR, Lutterworth, UK), which was placed in the thick rubber tubing. The excess liquid was pumped through to a Buchner flask to ensure 1.9 mL of dewatered resin. The resin was rinsed with deionized (DI) water into a 30 mL glass filter funnel (plate 20 mm, stem 9 mm, VWR). The resin particles were charged using 200 mL of 1:6 parts diluted hydrochloric acid (36%). Washing of the resin was performed with DI water until the filtrate tested neutral using pH paper. The resin was then suspended in 40 mL with DI water, and 1 g sodium nitrate and 0.2 g sodium hydrogen carbonate were added.

The mixture was stirred for more than 20 minutes. Once the sample and the equipment were set up, the electrode evaluated the ion exchange capacity using Equation 1:

$R1 = EP1 \times C \div V_{sample}$ Equation 1

R1 = ligand density (mol/L), EP1 = consumption of silver nitrate at the first endpoint (mL), C = concentration of the solution (mol/L), V_{sample} = sample volume, i.e. 1.9 mL.

2.3.3. Mechanical resin evaluation

The columns were packed using a pre-written method: flow rate increased gradually from 0.5 to 4 mL/min by 0.5 mL/min every 2 min. The packing cylinder was then removed and replaced by a 5 mm connector. The former packing method with an extended 20 min flow at 4 mL/min was carried out prior to lowering the adaptor to the compressed bed height of 5 ± 0.2 cm. Packing quality was determined using 5% acetone against water background. Reduced plate height (h) was calculated using Equation 2, where HETP was height equivalent to a theoretical plate and d_p was particle diameter, both in cm:

$h = HETP \div d_p$ Equation 2

Column performance parameters were deemed acceptable if they had 0.9 – 1.4 asymmetry, >4000 N/m plates per meter, and ≤4 reduced plate height (except for 45 µm beads ≤5).

Pressure-flow test was then performed. The flow rate was increased again from 0.5 mL/min with 0.5 mL/min increments to reach the maximum flow rate at which the column would collapse, i.e. reach critical velocity. At this point, the pressure would start rising rapidly without any further increases to flow rate. Small-scale 1 mL columns were used due to limited resin availability.

2.3.4. Resin performance evaluation

2.3.4.1. Dynamic binding capacity

Chromatography runs were performed with 1 mL (5 ± 0.2 cm height) columns. Stationary phase was equilibrated with 50 mM Tris, pH 8.5 buffer prior to the 200 mg lipid-free BSA load challenge at three velocities: 37, 50 and 125 cm/h. These flow rates represented residence times of 8, 6 and 2.4 minutes, respectively. Lipid-free BSA was chosen in order to eliminate fatty acid-caused resin fouling (Jin et al., 2010). All runs were performed in triplicate to determine the average capacity and a standard deviation of each resin type. Five column volumes (CV) of wash with the equilibration buffer and 10 CV of 0-100% gradient elution were performed. Elution buffer consisted of 50 mM sodium acetate and 1.5 M sodium chloride at pH 4.7.

Dynamic binding capacity calculations at 10% breakthrough were performed using Equation 3. Ultraviolet (UV) absorbance at 280 nm was measured and considered to be 100%. Therefore, $V_{10\%}$ was equal to the retention volume (mL) at 10% breakthrough. Actual BSA absorbance was measured in triplicate using a conventional spectrophotometer at 280 nm wavelength. The actual protein concentration in mg/mL ($C_{initial}$) was calculated using the Beer-Lambert law and extinction coefficient of 0.67 M/cm. The values of void volume (V_0, mL) and bed volume (V_c, mL) were calculated depending on the bed height and the column diameter. Columns were cleaned with 1 M sodium hydroxide with a contact time of 30 minutes.

$$DBC_{10\%} = (V_{10\%} - V_0) \times (C_{initial} \div V_c) \qquad \text{Equation 3}$$

2.3.4.2. Adsorption kinetics

Protein uptake rate in real time was visualised using confocal laser scanning microscopy (CLSM) Leica TCS SPEinv (Leica Microsystems, Mannheim, Germany) and a custom-made miniature flow cell **(Figure 2-3)**. A commercially available Texas Red®-labelled BSA was used in confocal microscopy in a recommended ratio of 1:100 (Hubbuch and Kula, 2008). Red fluorescent protein was not found to affect BSA binding or its conformation (Close et al., 2013), but in order to protect the fluorophores from photobleaching, samples were wrapped in aluminium foil and laser activity was set for a maximum of 10 seconds in 5-10 minute intervals. Microscopy parameters were maintained at 40x magnification with oil immersion, gain 900, intensity 40% (unless indicated otherwise), excitation wavelength 550 nm, and emission wavelength 600 nm.

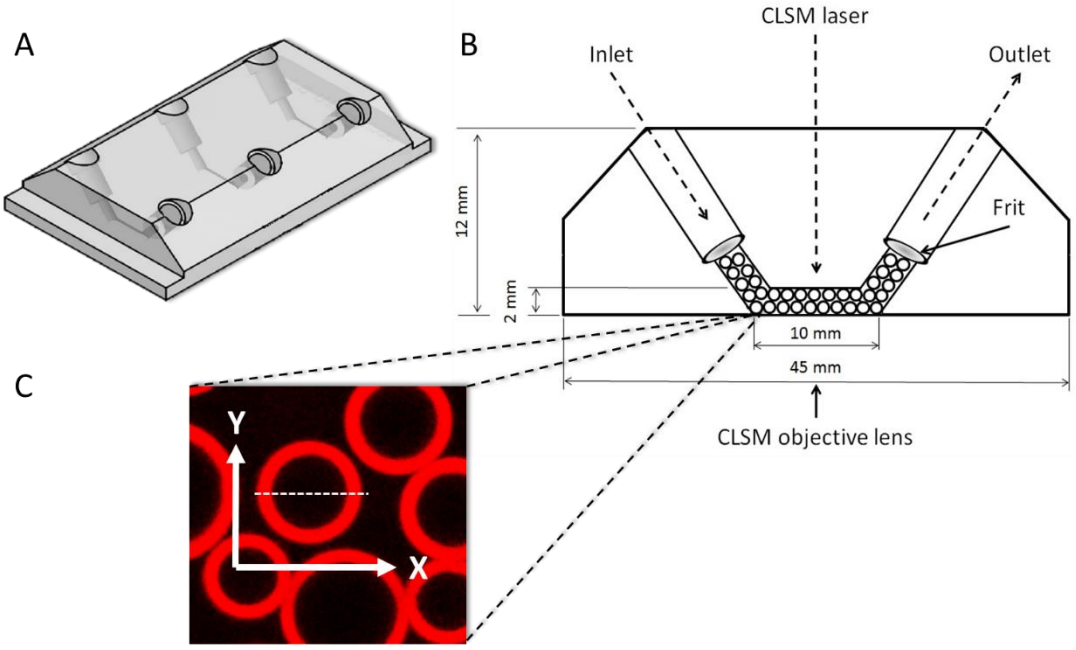

Figure 2-3. Flow cell design. A and B – flow cell, C – image taken by the CLSM, where X and Y axes represent the distance and fluorescence intensity. The image can be retrieved from the ImageJ software after the cross sectional area had been selected (dashed line).

The flow cell was packed with resin using a syringe supplied with roughly 50% slurry. Small frits were inserted to keep the beads in place. The packed column was then washed with 2 mL of water followed by 2 mL of chosen equilibration buffer. A flow rate of 2 mL/h (255 cm/h) or 3 mL/h (380 cm/h) was controlled by a syringe pump. Live images of the resin particles were taken through the x, y, and z planes whilst running 3, 5 or 10 g/L of Texas Red®-labelled BSA mixture through the column.

Images generated from the Leica Application Suite software, version 2.0 were analysed using ImageJ software. Once the area of interest had been selected (the cross section of the particle), the software was able to translate it to the fluorescence intensity profiles measured in relative fluorescence units over the radius. The intensity depended on the amount of protein bound to the particle and was measured in grey values, which in an 8-bit image ranged from 0 to 255 indicating the brightness of a pixel. Unfortunately, lower or higher values than 0 or 255, respectively, could not be identified and were considered as one of the two.

Raw images consisted of numerous peaks representing noise and other artefacts associated with the area of interest, which made it difficult to determine the true value. Therefore, all images were converted into binary images to analyse the data more accurately. Pixel values were separated into two segments: representing the area of interest and background. Auto threshold was selected as it seemed to be a reasonable reflection of the original image. Pixel values that were above or below the threshold were eliminated by the software. The next step was to identify the widest cross section area of the particle from the z-stack, which was done by simply measuring the width change in the set of images. A line across the particle was drawn to collect two measurements for five particles (n=10) to account for the uneven protein adsorption pattern.

Although particles of similar size were chosen, difficulties were encountered when comparing different bead size populations. It was unclear whether a certain distance travelled by the protein was of high or low value in regards to the total bead occupation. Therefore, a method addressing comparability between 45, 65 and 90 µm samples was found to be the percentage of the band spread in relation to the total bead radius. Averages and standard deviations of the samples were subsequently plotted.

In order to confirm that Texas Red®-labelled BSA performed in the same way as the unlabelled BSA, static binding capacity experiments were carried out. Equilibrated resin was added to the BSA solution whilst being mixed in a beaker, and samples were taken with a 1 mL syringe attached to a 0.22 µm filter every 5 seconds. The final sample volume was 50 mL (V_{sample}) with 4 mg/mL BSA ($C_{initial}$) and 10 mL of 30% resin slurry (V_{resin} = 3.3 mL). The unbound BSA samples ($C_{unbound}$) were measured in triplicate in a 96-well plate at 280 nm absorbance using Infinite® 200 PRO plate reader (Tecan, Mannedorf, Switzerland). Calculations for the bound BSA (C_{bound}) were performed using Equation 4.

$$C_{bound} = \frac{V_{sample} \times (C_{initial} - C_{unbound})}{V_{resin}} \qquad \text{Equation 4}$$

2.3.5. Resin lifetime evaluation and aggregate detection assay development

2.3.5.1. Controls for the dye assay

A number of controls including fresh resin sample, fresh resin with bound BSA, IgG1, and heat-denatured BSA were prepared in addition to the ones provided by the manufacturer: aggregated and lyophilised native lysozyme proteins as well as 1x assay buffer. Heat-denatured BSA sample was prepared by heating the protein at 65ºC for 35 min to form soluble aggregates.(Holm et al., 2007) Fresh resin with bound heat-denatured BSA and fresh BSA (both at 10 g/L concentration), and IgG1 samples were prepared using a miniature flow cell using conditions outlined in **Table 2-1**. The flow cell was packed with Praesto Q or SP slurry, washed with DI water, equilibrated with Tris or sodium citrate buffer, loaded with 30 mg of BSA or 6 mg of IgG1, respectively, and then washed again with the equilibration buffer to remove unbound protein. Treated resin was collected to be investigated with the fluorescent dye.

Table 2-1. Small-scale chromatography conditions.

	Feed material	**Equilibration and wash**	**Gradient elution (5 CV)**	**Strip (100%B, 15 CV)**	**CIP**
a)	Pure BSA	50 mM Tris, pH 8.5	+ 1.5 M NaCl, pH 4.7	Yes	1 M NaOH (30 min hold)
b)	Pure BSA	50 mM Tris, pH 8.5	+ 1.5 M NaCl, pH 4.7	Yes	No
c)	Pure BSA	50 mM Tris, pH 8.5	+ 1.5 M NaCl, pH 4.7	No	1 M NaOH (30 min hold)
d)	Pure BSA	50 mM Tris, pH 8.5	+ 1.5 M NaCl, pH 8.5	Yes	No
e)	IgG1 post Protein A	10 mM sodium citrate, pH 5	+ 0.5 M NaCl, pH 5	Yes	No

2.3.5.2. Sample preparation for imaging

Sample preparation and staining were performed as detailed in the Proteostat® product manual, in Costar 96-well black, clear bottom polystyrene plates (Fisher Scientific, Loughborough, UK). Each well contained 98 µL of 20% resin slurry sample in water, and 2 µL of Proteostat® dye; plates were incubated in the dark for a minimum of 20 min.

2.3.5.3. Fluorescence intensity measurement

Fluorescence intensity was measured using Tecan Safire2™ system (Tecan, Mannedorf, Switzerland) with 30 seconds of orbital shaking prior to excitation at 550 nm wavelength, and emission at 600 nm wavelength. Samples were prepared in triplicate.

2.3.5.4. Fluorescence visualisation with CLSM

Leica TCS SPE inverted confocal microscopy was used to visualise particular areas of fluorescence (aggregation) in resin samples. Microscopy settings were the same as discussed ealier but image quality was increased to 1024x1024 and pinhole was set up to 2. The usual flat or round bottom microscope slides failed to provide good quality images. Therefore, the flow cell was used to contain and provide hydrated environment for resin during imaging (other designs such as 96-well plates could be used with compatible microscopes). At least three images of each sample were taken, but only the most representative ones are shown.

2.3.6. Product separation evaluation

2.3.6.1. Ovalbumin isoform separation with AEX

Two milligrams of ovalbumin were loaded onto the equilibrated 1 mL AEX column (50 mM Tris, pH 9) and eluted via a salt gradient from 100 to 300 mM over 50 CV at 0.5 mL/min flow rate. Fractions of 5 mL were collected and further analysed on an AEX monolith column.

CIMac™ QA monolith column was equilibrated with the same buffer, and 100 µL of ovalbumin fractions were injected. Elution step consisted of the salt gradient from 100 to 275 mM over 20 minutes. Runs were performed at 1 mL/min.

2.3.6.2. Monoclonal antibody separation with CEX

A monoclonal antibody (mAb) mixture consisting of IgG1 and IgG4 was purified using an XK16, 10 cm height Protein A column prior to the polishing steps. The resin was equilibrated with 20 mM sodium phosphate, 150 mM sodium chloride, pH 7.4 buffer, and the product was eluted with 100 mM sodium citrate, pH 3.4 buffer. Eluate was subsequently adjusted to pH 5.5 with 1 M Tris, pH 9 to avoid precipitation.

The mAb solution was buffer exchanged into either 10 mM sodium citrate or 20 mM sodium acetate of pH 4.5, 5.0 or 5.5. Vivaspin® 20, 30,000 MWCO, PES spin columns (Sartorius, Goettingen, Germany) were centrifuged at 6,000 x g for 10 min for 7x buffer exchange. Conditioned feed was then loaded to the 10 ± 0.2 cm height columns packed with jetted Praesto SP resins. Product was eluted with a salt gradient from 100 to 500 mM at 244 cm/h. The runs were performed in triplicate, and 2 mg of buffer exchanged mAb solution was loaded.

2.3.7. Purified product characterisation

2.3.7.1. Product size

Ultra performance liquid chromatography and a size exclusion column were used to measure the composition of the samples, i.e. monomer and aggregate forms. Analysis was conducted at 0.2 mL/min using mobile phase formulated of 100 mM sodium phosphate and 100 mM sodium chloride at pH 7.0. The column was equilibrated with 5 CVs prior to the 20 µL sample injections, which had been centrifuged at 18,000 g for 10 min. Proteins were quantified using a wavelength absorbance at 280 nm with a reference at 550 nm.

2.3.7.2. Charge variants

Charged mAb species were analysed with a weak 0.1 mL CIMac™ COOH monolith column. An increasing pH gradient from 3.6 to 9.4 was achieved over 30 min with the buffer consisting of 10 mM borate, 10 mM citrate and 10 mM phosphate. Process flow rate was 1 mL/min.

2.3.7.3. Product stability

Thermal stability of IgG1 and IgG4 was determined based on the static light scattering at 266 nm with the UNit (Unchained Labs, Gent, Belgium). The temperature was gradually increased from 20ºC to 90ºC with 0.5ºC increments. Aggregation temperature was determined by the UNit software.

3. Chapter: Resin structural feature assessment

In the design of ion exchange resins, overall performance is determined by a selection of resin properties: resin particle size dictates pressure drop, particle size distribution affects column packing efficiency and ligand density influences selectivity. In order to understand how these features work together in influencing dynamic binding capacity, protein uptake rate, resolution and lifetime, an array of resins was fabricated. Anion exchange resins of 45, 65 and 90 µm average particle size were manufactured using a traditional batch emulsification method, whilst an additional set of 45 µm resins in uniform particle size was produced using a jetting technique. Additionally, varying amounts of ligand were functionalised onto the beads. Even though orthogonal particle size evaluation methods including SEM and CLSM microscopies as well as DLS reported some inconsistencies, they generally agreed that jetted resins had a 5-10 µm lower average particle size than non-jetted resins, and similar variation in particle size distribution. As a result, column packing efficiency and pressure-flow studies revealed insignificant differences between the two. However, the pore sizes and porosities were comparable amongst all resins.

3.1. Introduction

Performance of ion exchange chromatography resins is determined by their dynamic binding capacity, mass transfer, selectivity, lifetime as well as chemical and physical stability. In order to address as many characteristics as possible, manufacturers have come up with different materials and formats, including beads, monoliths, membranes and nanofibers with further variations in pore size and functionalised group length.

Despite many alternatives, resin beads are still most commonly used due to their superior capacity and selectivity. This can often be achieved through a large surface area provided by a small particle size, narrow pores and a high number of functionalised groups.

Particle size in preparative chromatography resins has been of particular consideration with respect to flow rate. Larger particles of around 90 µm are traditionally used for the first capture step as they can withstand high flow rates, thereby allowing faster processing of large volumes of crude feed material. Smaller particles of 30-50 µm are best utilised in the last stage of chromatography, namely, the polishing step, in which the volume of the feed and the importance of flow rate are lower. This step demands precise separation of closely related protein isoforms or impurities from the main product.

The quality of protein separation, or resolution, depends on efficient column packing and small particle size. High performance liquid chromatography (HPLC) utilises very small particles such as 2-5 µm in order to generate very accurate analytical results. Preparative chromatography, however, could not adopt such small particles as the pressure drop would be too extreme for the hardware. Instead, considerable effort is put in to designing robust column packing procedures, which can provide desirable column efficiency characteristics, namely: >4000 plates per metre, asymmetry of 1,

<5 reduced plate height and the lowest possible height equivalent to the theoretical plate (HETP) value.

There have also been reports suggesting that narrow particle size distribution (PSD) with the deviation from the mean being smaller than 40% may have a positive effect on the HETP value (Naefe and Halász, 1972; Han et al., 1985; Gritti et al., 2011; Liekens et al., 2011; Horváth et al., 2014). Depending on the particle size and the percentage of particle size distribution, it could have a positive, minor or negative influence on HETP. Small particles of 2-5 µm produced insignificant differences on HETP value (Nakanishi et al., 1978; Dewaele and Verzele, 1983; Athalye et al., 1992), whilst larger particles saw an increase in HETP due to significant variance (>40%) in PSD (Naefe and Halász, 1972; Gritti et al., 2011; Liekens et al., 2011; Horváth et al., 2014; Li et al., 2015). HETP value is linked to the column's ability to provide efficient separation. Therefore, there is supporting evidence to suggest that protein resolution could be enhanced if the PSD was reduced.

The control of agarose particle size distribution is not a simple task. Batch emulsification process, which generates a broad particle size distribution, is the most commonly used method for agarose bead manufacturing. Production of huge volumes of resin requires a large stirred tank, similar to that typically used in upstream processing. Although various microfluidics devices could create uniform particle sizes, they have not been able to compete with the stirred tanks in doing so at a large scale. Recently, a more controlled manufacturing process called jetting was developed by Purolite Life Sciences. Jetting relies on a vibrating membrane with uniform pores to produce uniform particle sizes with a narrow PSD.

The next steps in resin manufacture involve the functionalisation of desired ligands. Ligand density has been extensively studied to determine the role it plays in resin binding capacity, resolution, product recovery and impurity clearance. The majority of the publications found that static and dynamic binding capacities could be altered

through changes in ligand density, whereby higher ligand density could achieve higher capacities (Wu and Walters, 1992; Ghose et al., 2007; Langford et al., 2007; Hardin et al., 2009; Wrzosek et al., 2009; Dismer and Hubbuch, 2010; Franke et al., 2010; Huang et al., 2010; Fogle and Persson, 2012; Fogle et al., 2012; Lu et al., 2012b; a; Steinebach et al., 2017; Wang et al., 2019). A prolonged retention time has been another cause of high ligand density, which would sometimes reverse the order of the eluted proteins (Wu and Walters, 1992) or improve the resolution of antibody charged variants and aggregates (Fogle et al., 2012; Fogle and Persson, 2012) as well as other proteins (Kopaciewicz et al., 1985; DePhillips and Lenhoff, 2001; Huang et al., 2006, 2010; Dismer and Hubbuch, 2010; Lang et al., 2015). However, high ligand density was found to contribute towards the reduction in product recovery, in some cases leading to aggregation (Kopaciewicz et al., 1985; Pessela et al., 2004; Huang et al., 2006; McCue et al., 2009; Huang et al., 2010). Interestingly, no effects on host-cell protein or high molecular weight clearance due to changes in ligand density have been observed (Fogle et al., 2012; Fogle and Persson, 2012).

Nevertheless, there is no clear consensus on the optimum particle size, particle size distribution or ligand density by themselves or let alone together. In fact, many studies are controversial in terms of how significant the outcomes could be. Therefore, I have decided to explore the interactions of the three factors together.

Aim

The aim of this chapter is to ensure that these agarose resins have been manufactured in line with the chosen bead size and ligand density parameters whilst maintaining the same structural pore characteristics.

Objectives

- Utilise batch-emulsification and jetting to produce agarose beads varying in particle size distribution.
- Manufacture and measure resins with average bead sizes: 45 µm, 65 µm and 90 µm and varying ligand densities: 0.08 - 0.28 mol/L.
- Evaluate pore structures using microscopy and laser light diffraction techniques.
- Evaluate and compare column packing efficiency as well as pressure-flow characteristics for batch-emulsified and jetted resins.

3.2. Results and Discussion

A selection of resins containing average particle sizes of 45 μm, 65 μm and 90 μm, i.e. Q45, Q65 and Q90 respectively, with corresponding “low”, “medium” and “high” ligand densities, were manufactured in a traditional batch emulsification process. Additional 45 μm resins with representative ligand densities were fabricated by jetting. Several methods were used to measure particle size distribution and validate average particle size: laser light diffraction using the Mastersizer 3000, scanning electron microscopy (SEM) and confocal laser scanning microscopy (CLSM). Particle size distribution was of particular importance for the jetted Q45 resin as it was expected to have a narrower PSD than the non-jetted Q45 resin. The inner composition of the particles was examined with SEM to assure that the only potential mass transfer and capacity differences amongst the resins were due to varying PSD, average particle size or ligand density and not due to differences in pore size.

3.2.1. Particle size distribution

Laser light diffraction (LLD) and optical imaging techniques produce different types of particle size distribution plots: volume- and number-based, respectively. Conversions from one type to another can introduce significant errors, especially if the number of particles in a sample is below 400 (Bowen, 2002). Therefore, to better characterise the anion exchange resins, both types of graphs were presented in this section.

Average particle size (d_{50v}) by LLD was 1.2-1.4 times higher than anticipated: 64, 82 and 110 μm instead of 45, 65 and 90 μm, respectively, for the non-jetted resins **(Figure 3-1, Table 3-1)**. In contrast, the jetted resin had the average size of 50 μm, which was close to the expected 45 μm value but could indicate that the true value was around 35-40 μm.

LLD is known to provide higher average particle size values due to strong sensitivity towards particles of larger volume (even if the count is smaller) compared to the number-based techniques. In addition, it has been noticed that different instrument models and even software may give contrasting average particle sizes due to differences in the algorithms used for normalization (Burgess et al., 2004). Mastersizer 2000 was used by Purolite Life Sciences when manufacturing resins, which is an older version with a different detector layout than Mastersizer 3000, and thus was likely to generate slightly different results.

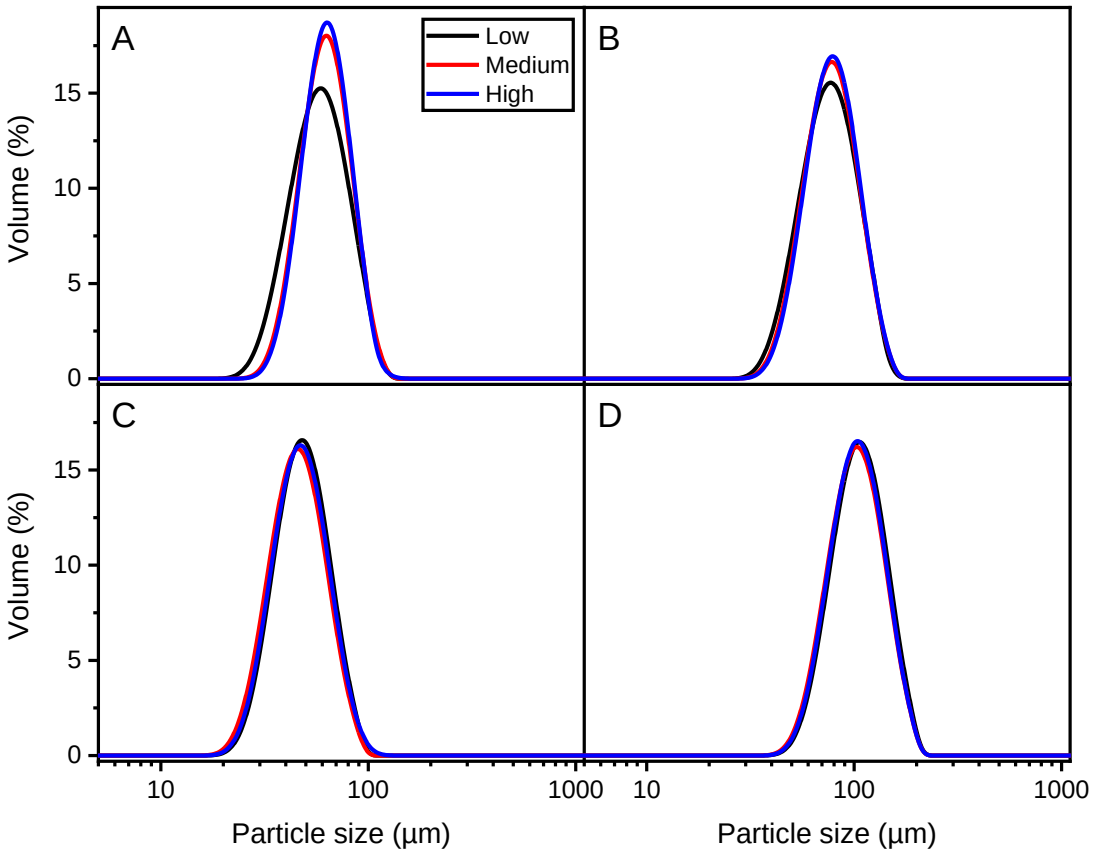

Figure 3-1. Particle size distribution measured with laser light diffraction. A – Q45, B – Q65, C – Q45 jetted and D – Q90 resins with low, medium and high ligand densities were evaluated with Mastersizer 3000. Five measurements of each sample in 20% ethanol were taken by the instrument with 10-20% obscuration whilst being stirred at 1500 rpm.

Optical microscopy was employed to act as an orthogonal technique providing additional insight into the average particle size determination. Images produced at 40x and 100x magnification with CLSM and SEM, respectively, were analysed with ImageJ software to generate distribution graphs and averages for all bead sizes. Despite potential particle shrinkage during the critical point drying, SEM provided similar values to those indicated by the manufacturer: 50 µm and 45 µm for the non-jetted and jetted resins, respectively **(Figure 3-2, Figure 3-3)**. Similarly, CLSM images depicted 45 µm and 41 µm average sizes for the same resins **(Figure 3-4)**. Both optical techniques provided a lower average particle size than the LLD, but all three of them agreed that the jetted resins possessed overall smaller average particle size than the non-jetted resins **(Table 3-1)**.

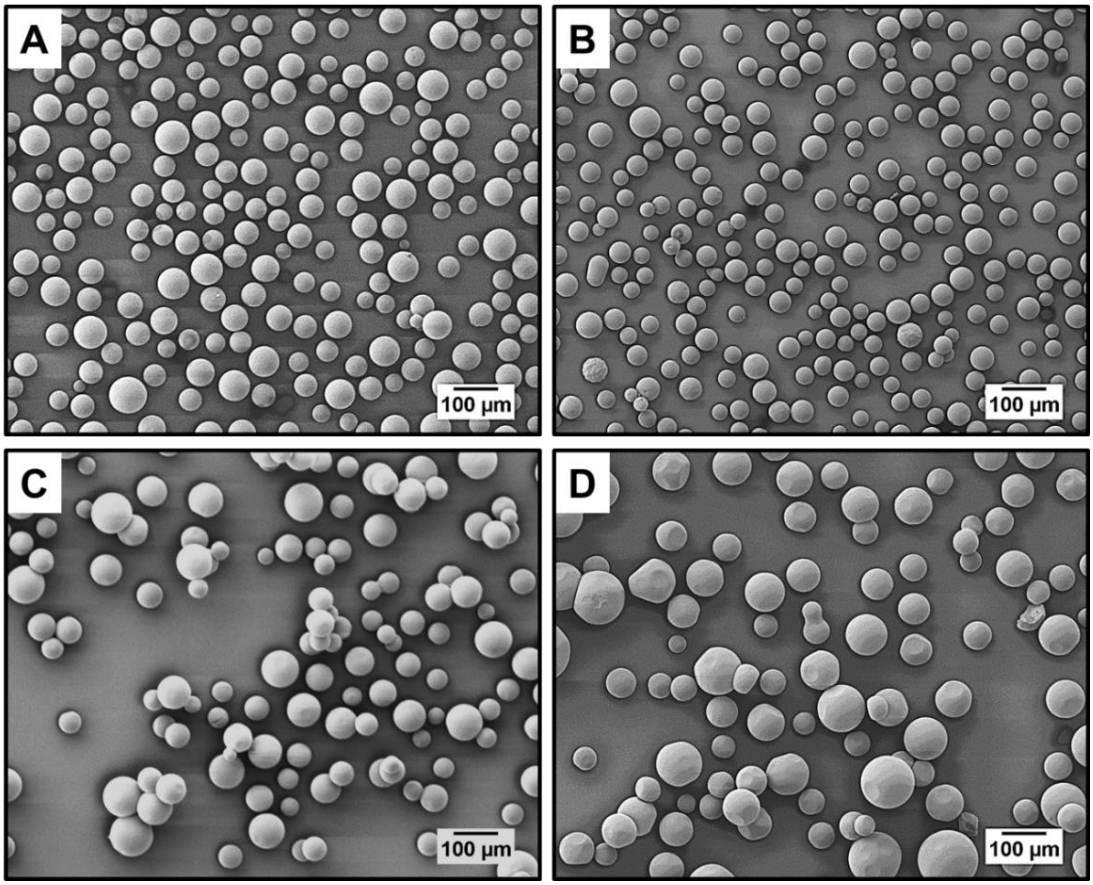

Figure 3-2. SEM images of AEX resins at 100x magnification. A – Q45, B – Q45 jetted, C – Q65, D – Q90 resins. Samples were critical point dried prior to gold/palladium coating and imaged at 2.0 kV accelerating voltage.

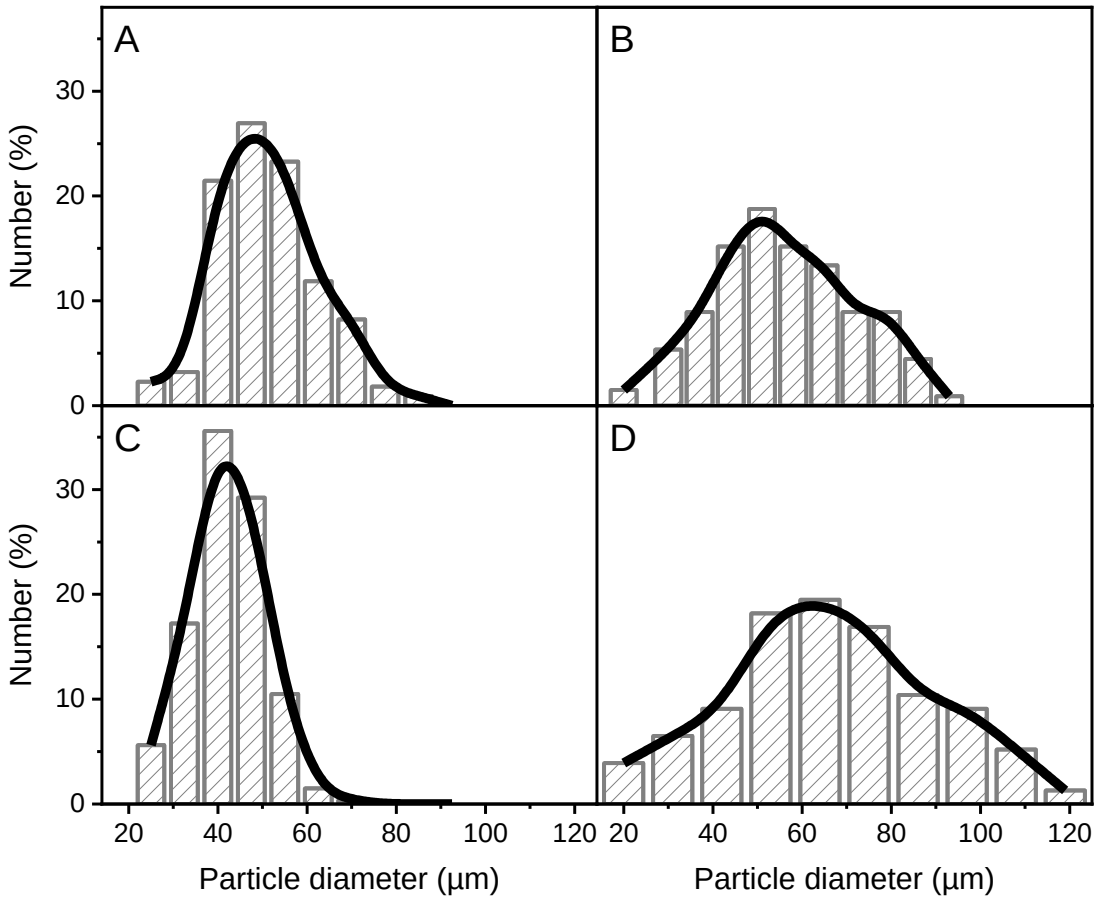

Figure 3-3. Particle size distribution analysis with ImageJ based on SEM images. Evaluation of A – Q45, B – Q65, C – Q45 jetted and D – Q90 resins imaged at 100x magnification. Appropriate image threshold was established prior to automated particle area selection and calculation by ImageJ. Results were then grouped into 10 sections represented as bars, and particle count was converted to percentage of the total. Line graphs show a general trend.

Particle size distribution range for the 45 µm resins was comparable when analysed with SEM and DLS methods **(Table 3-1)**. Relative standard deviation (RSD) was calculated for the number-based, whilst particle size distribution was expressed in span ($(d_{v90} – d_{v10})/d_{v50}$) for the volume-based measurements. Both jetted and non-jetted resins had an RSD of ± 17.8 and 18.0%, and a span value of 0.755 and 0.757, respectively. However, CLSM results provided a contrasting RSD value of ± 26.7%

for the non-jetted resin making the difference between the two resins significant. Since two orthogonal techniques showed similar results, it is likely that a small sample size used during CLSM resulted in a less accurate number.

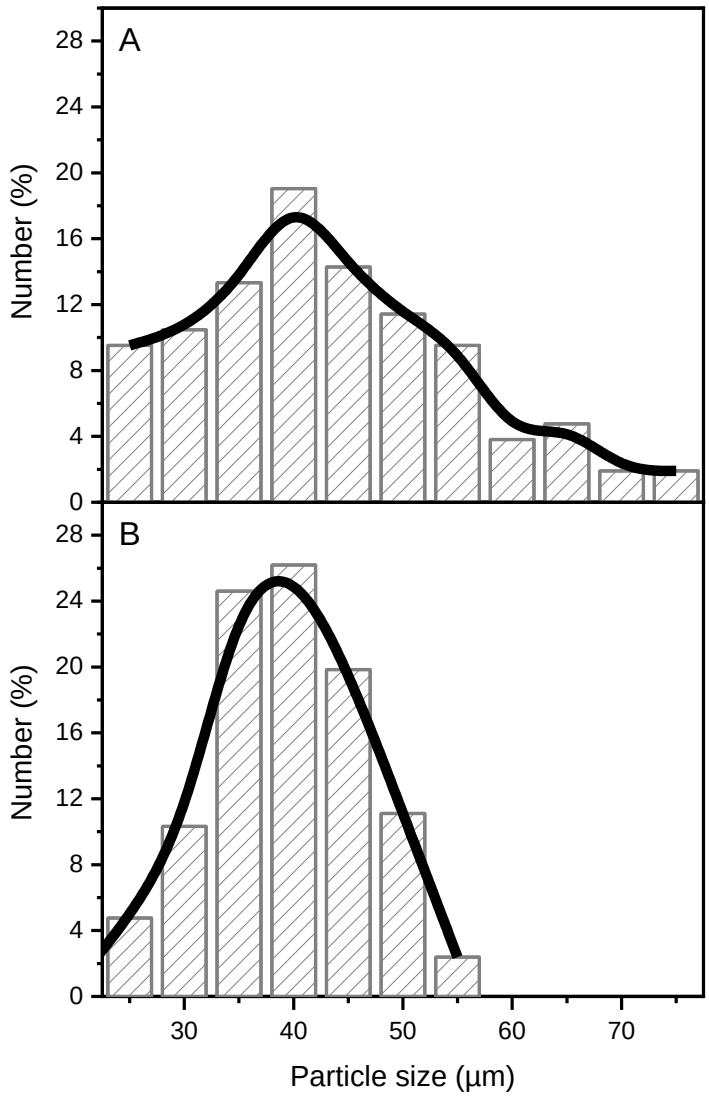

Figure 3-4. Particle size distribution analysis with ImageJ based on CLSM images. A – 45 µm and B – 45 µm jetted resins imaged at 40x magnification. Results were grouped into 7 sections represented as bars, and particle count was converted to percentage of the total. Line graphs show a general trend.

Unfortunately, the CLSM method could not be used for the Q65 and Q90 resins due to the same reason – a small sample size. Despite that, it was evident from the SEM image analysis that the Q65 and Q90 had the widest particle size distribution compared to the Q45 resins **(Figure 3-3, Table 3-1)**. Smaller particles manufactured for a polishing step are known to have a narrower PSD in order to provide higher selectivity and resolution than the larger particles used for the capture step (Staby and Jensen, 2001; Staby et al., 2004, 2005, 2006, 2007).

Table 3-1. Determination of average particle size and distribution.

Expected average particle size (µm)	**Method**				
	SEM		CLSM		LLD
	Particle size (µm) ± RSD (%)	Sample size	Particle size (µm) ± RSD (%)	Sample size	Particle size (µm); Span value
45	50 ± 18.0	218	45 ± 26.7	105	64; 0.757
45 (jetted)	45 ± 17.8	265	41 ± 17.1	126	50; 0.755
65	60 ± 25.0	112	-	-	82; 0.774
90	73 ± 23.3	82	-	-	110; 0.768

Optical and light diffraction methods that quantify the average particle size of the sample were in disagreement: the former underestimated, whilst the latter overestimated the results. This conclusion is not completely surprising as laser diffraction detects larger beads more readily since they contain a significant volume, whilst number-based methods tend to identify smaller beads in any given sample. In order to achieve a more representative estimate, the sample size and replicate number would have to be increased for the optical method and laser diffraction methods, respectively. Nonetheless, it was evident that the jetted resin had on average lower average particle size with a potential difference of 5-10 µm when compared to the non-jetted resin, whilst no significant variation was observed in their size distribution range.

3.2.2. Pore features

Scanning electron microscopy (SEM) was utilised to confirm that all resins had the same pore structure **(Figure 3-5)**. Pictures were analysed using ImageJ software to obtain quantitative data for the comparison purposes. Particle pore count was determined as 3000, apparent porosity as 65%, and average pore size ranged from 5000 to 6000 nm^2 indicating that the average pore diameter was about 80 nm **(Figure 3-6)**. The latter result was in agreement with previous publications, in which average pore diameter was found to be below 100 nm (Ioannidis, 2009; Nweke, 2017). Overall, the four anion exchange resins were similar in terms of their structural composition.

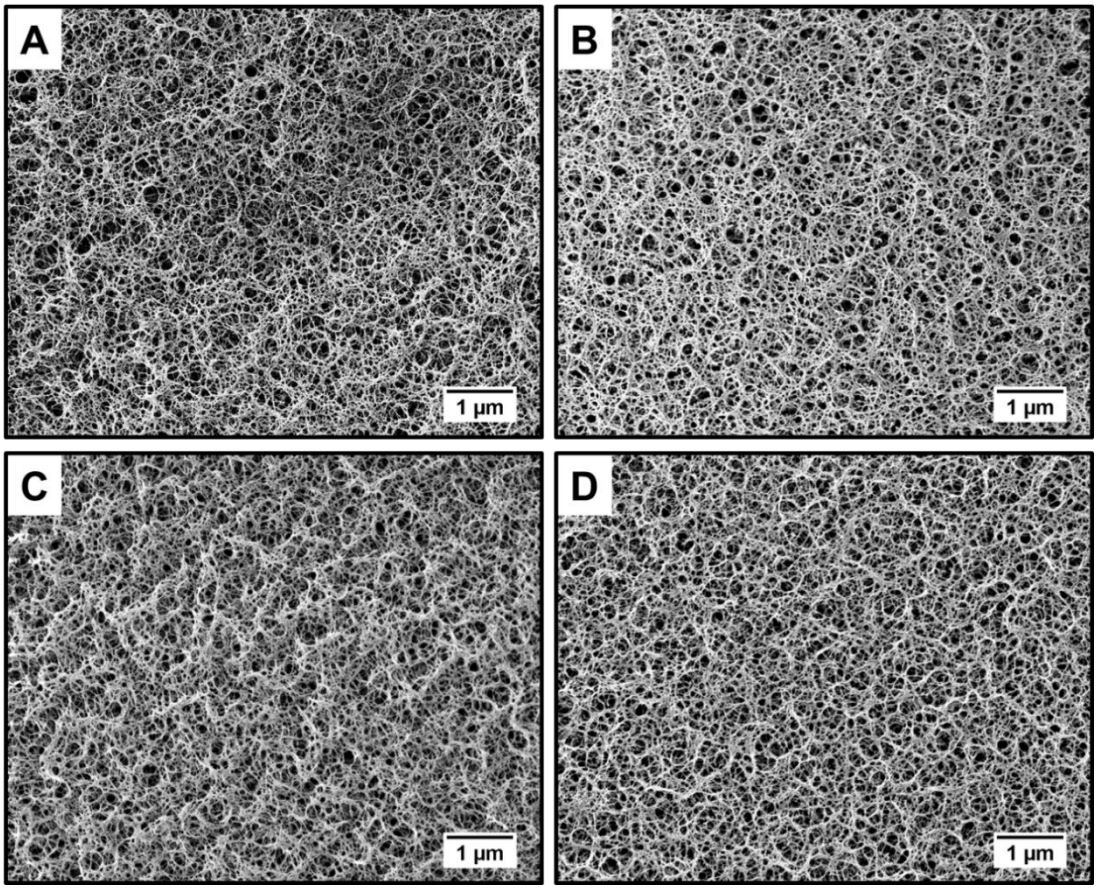

Figure 3-5. AEX resin pore structure by SEM at 15,000x magnification. Images of A – Q45, B – Q45 jetted, C – Q65, D – Q90 resins. Samples were critical point dried prior to gold/palladium coating and imaged at 2.0 kV accelerating voltage.

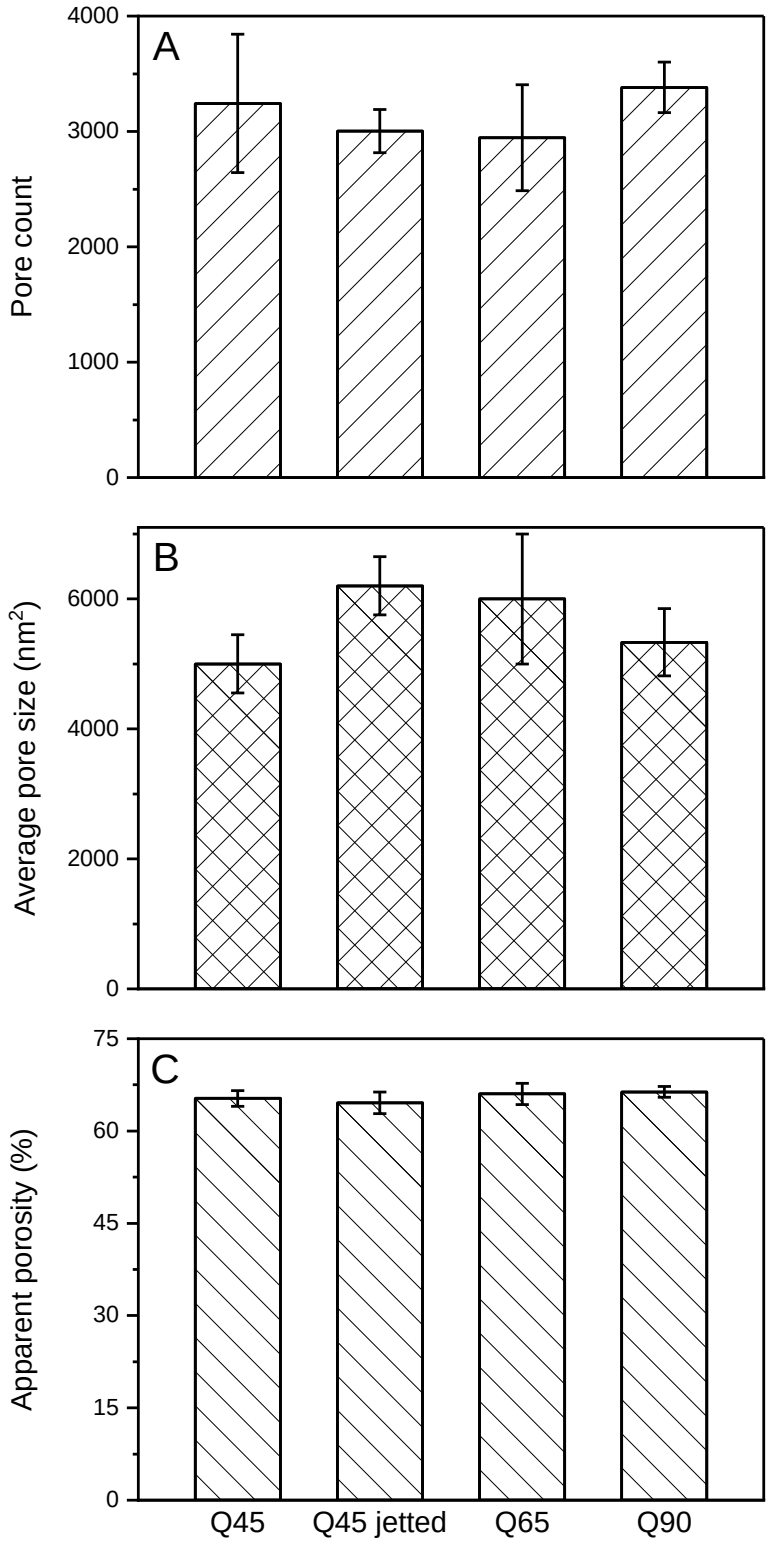

Figure 3-6. Pore structure analysis based on SEM images at 15,000x magnification. A – Pore count, B – average pore size and C – apparent porosity were estimated by ImageJ software. Images were “smoothened out” and inverted prior to threshold adjustment. The edges of all pores were then selected and analysed. Averages of three images with ± 1SD are shown.

3.2.3. Ligand density

Different ligand amounts were functionalised onto the AEX resins. Although it was aimed at maintaining comparable ligand densities to form groups of “low”, “medium” and “high”, this was not always possible **(Table 3-2)**. Q45 jetted resin was the biggest outlier with 18-42% higher ligand densities than its non-jetted counterpart. The Q90 resins also contained more ligand for the “low” and “medium” ligand densities than the Q45 and Q65 resins. The control of functionalised ligand amount and its uniform distribution throughout the particle is very difficult because it depends on a number of factors such as temperature of the reaction and scale of the reactor, which can result in lot-to-lot variation. The remaining samples could be otherwise directly comparable.

Table 3-2. Anion exchange resin capacity.

Resin	**Ligand density (mol/L)**		
	Low	Medium	High
Q45	0.08[1]	0.16[1]	0.24[1]
Q45 jetted	0.11	0.22	0.28
Q65	0.08	0.16	0.25
Q90	0.10	0.18	0.24

[1] *Averages gained from two repeats of the experiment; no further repeats were performed as the standard deviation was below ± 0.003 and the technique was proven to be reproducible.*

3.2.4. Column packing evaluation

Column packing efficiency was determined for all bead sizes prior to each experiment but only the jetted and non-jetted Q45 resins were analysed in more detail **(Figure 3-7)**. It was expected that narrow particle size distribution would be most advantageous in achieving better packing efficiency and thus resolution (Naefe and Halász, 1972; Han et al., 1985; Wahome et al., 2008; Gritti et al., 2011; Liekens et al., 2011; Horváth et al., 2014). Overall, asymmetry between 1.0 and 1.5, plate number above 4500 and reduced plate height below 5 were achieved for both resins **(Figure 3-8)**. Although plate number was more reproducible for the jetted rather than non-jetted resins, both performed in a similar manner offering only minor potential differences in protein separations. Average particle size variation for both samples was also not significant enough to make a difference as discussed in previous reports, whereby generally >40% variation was required to have a significant impact on HETP (Naefe and Halász, 1972; Gritti et al., 2011; Liekens et al., 2011). A more extensive study such as HETP versus linear velocity might be required to conclude whether there were any significant differences.

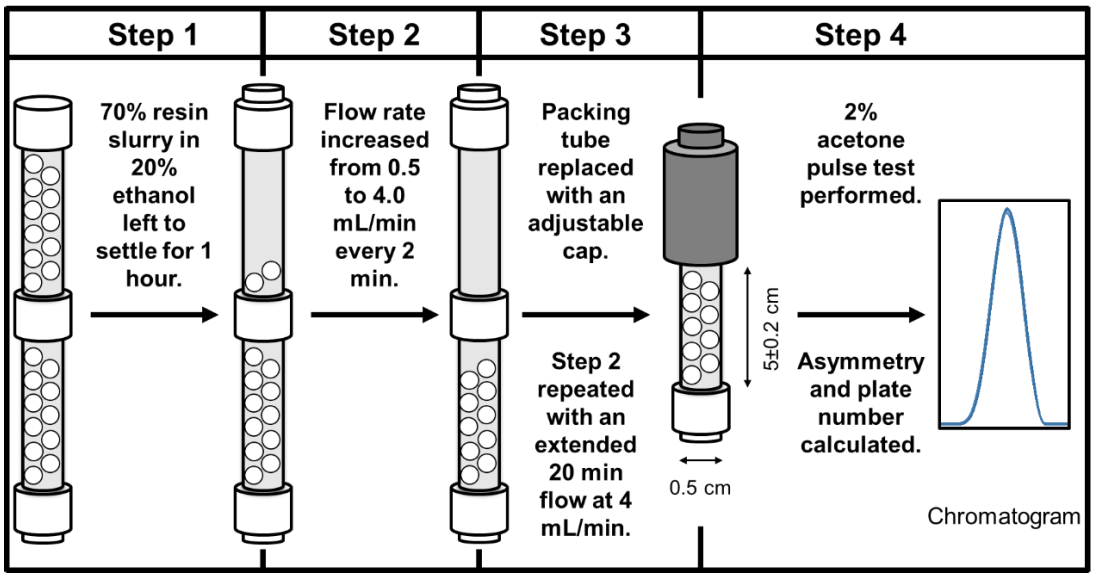

Figure 3-7. An overview of column packing method and analysis.

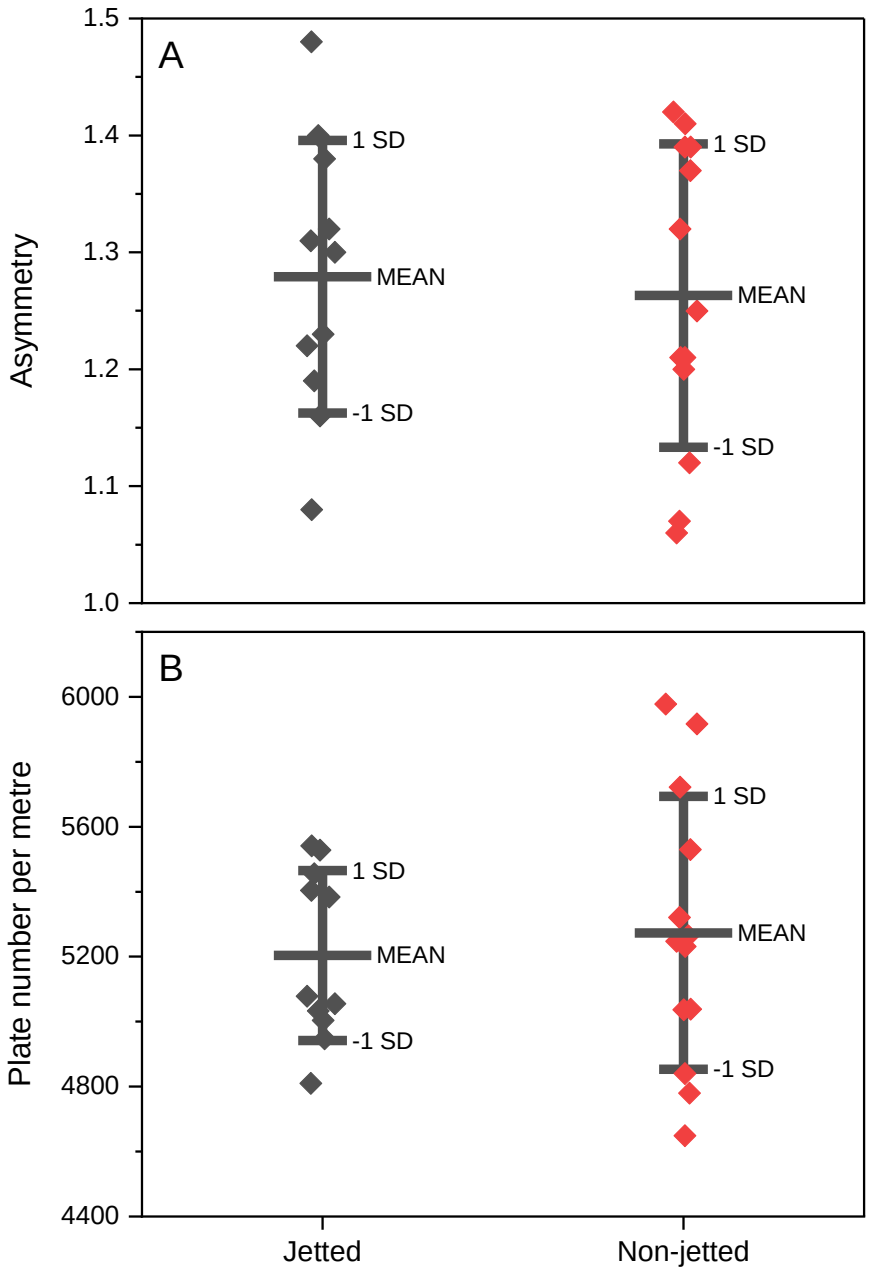

Figure 3-8. Column packing evaluation of jetted and non-jetted Q45 resins. Mean values with ± 1SD of A – asymmetry and B – number of plates per metre are shown. Tricorn 5/50 columns and 2% acetone pulse were used to test column packing efficiency. Two-sample *t*-test performed on OriginPro® 2020 did not reveal any significant differences between the two sets of data.

3.2.5. Pressure-flow characteristics

Pressure-flow experiments were conducted to evaluate mechanical particle strength as past publications had shown that wider particle size distribution could cause higher back pressure (Dewaele and Verzele, 1983; Liekens et al., 2011; Henry, 2014). Traditionally, columns of at least 26 mm in diameter are used to reflect pressure behaviour in large scale reactors where column walls fail to provide support leading to accelerated particle compression (Stickel and Fotopoulos, 2001). Bed height of at least 15 cm is also considered to be more representative of a large scale process as it sustains lower critical velocity (Tran et al., 2007). However, the experiments performed here used small scale columns of 5 mm in diameter and 5 cm in height due to limited resin supply.

Results showed that jetted and non-jetted resins could withstand high flow rates of up to 1800 cm/h resulting in 0.45 MPa pressure **(Figure 3-9)**. The pressure started to rise dramatically after flow rates exceeded 1900 cm/h and 2100 cm/h with the jetted and non-jetted resins, respectively. Based on SEM results, average pore size of jetted resins was larger averaging to 6100 nm^2, whilst non-jetted resins had a pore size of around 5000 nm^2 **(Figure 3-6)**. In addition, there were differences in average particle sizes: jetted resin had a 5-10 µm lower average particle size compared to the non-jetted resin as determined by orthogonal techniques **(Table 3-1)**. Average particle size may have had a slightly contribution to the overall flow properties. Nonetheless, both resins managed to achieve high comparable linear velocities due to short bed height and significant wall support effects that would not be present for larger scale columns.

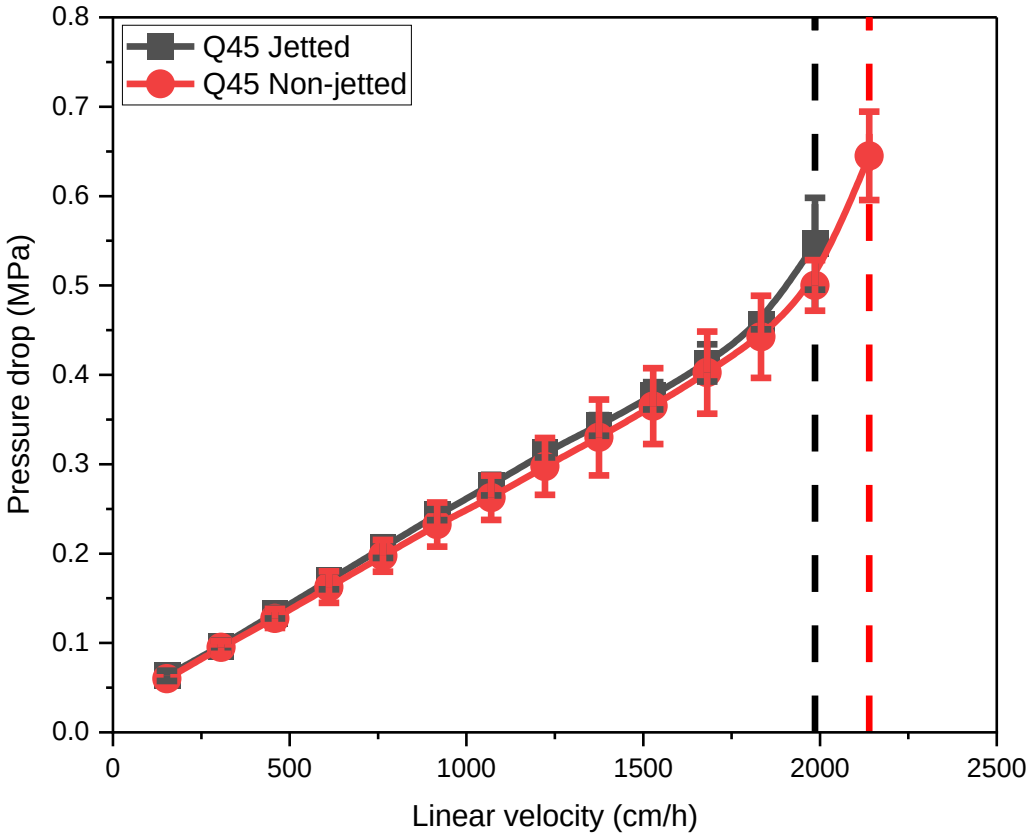

Figure 3-9. Pressure-flow plots of jetted and non-jetted Q45 agarose resins. The flow rate was increased gradually to 7 mL/min (2140 cm/h) until the bed compressed and pressure started rising dramatically (dotted line). Tricorn 5/50 columns with 5 mm diameter and 5 cm height were used. Averages with ± 1SD of three experiments per Q45 resin are shown.

3.3. Conclusions

The aim of this chapter was to evaluate and compare the physical features of the resins that had been manufactured for this project by the collaborating company Purolite Life Sciences. Resin design focused on the differences in terms of average particle size (Q45, Q65 and Q90), particle size distribution (batch-emulsified versus jetted) and ligand density (0.08 - 0.28 mol/L) whilst keeping pore size and porosity the same. The results confirmed that these differences had been achieved whilst maintaining comparable pore design.

- Orthogonal techniques such as microscopy and light diffraction are desirable when determining the average particle size and size distribution. Jetted resins possessed a 5-10 µm lower average particle size than the non-jetted resins.
- Resin lot-to-lot variation was present due to difficulties in controlling the amount of functionalised ligand on bead surfaces.
- Column packing efficiency and pressure-flow experiments depicted minor differences between the jetted and non-jetted resins possibly due to insignificant variations in their average particle size and distribution.

4. Chapter: Resin adsorption kinetics

Dynamic binding capacity is one of the major determinants of the chromatography matrix performance. The ability of matrix to bind high amounts of product can be optimised through alterations in resin particle size, pore size and ligand density all of which affect the total surface and, thus, the interaction area. Process conditions including linear velocity and feed composition determine the rate at which protein can be bound before reaching breakthrough. However, there is a lack of understanding of how various resin features interact together under these processing conditions. Therefore, a series of experiments were devised to understand the combined influence on dynamic binding capacity and protein uptake rate. An array of 12 particle types with Q45, Q65, Q90 and jetted Q45 resins containing 0.08-0.28 mol/L ligand density was generated and studied using bovine serum albumin (BSA) in chromatographic separations and with confocal laser scanning microscopy (CLSM). The use of smaller particles of 45 µm led to 25% higher DBC and 40% faster protein uptake rate than the larger particles of 90 µm. An optimum ligand density was identified for each particle size, generally <0.18 mol/L being the most beneficial for DBC. Additional ligand resulted in the reduction in DBC and BSA adsorption rate, particularly at higher flow rates of ≥125 cm/h. In addition, CLSM revealed that resins possessing a bigger size and a higher ligand density suffered from impaired mass transfer effects due to long diffusion paths and steric hindrance, respectively. The results demonstrate that selecting the appropriate combination of ligand density, particle size and flow rate is crucial for optimal resin design and performance.

4.1. Introduction

One of the key ion exchange chromatography matrix performance indicators is its ability to efficiently adsorb the molecule of interest. Static and dynamic binding capacities are measured to determine the maximum and optimum load ratios under the static and dynamic flow conditions, respectively. Dynamic binding capacity (DBC) is heavily dependent upon the structural features of the resin including its particle size, ligand type and density, pore size, porosity and tortuosity. Good mass transfer properties can be ensured through wider pores and improved porosity and tortuosity. Fast adsorption rates can be achieved by increasing charged surface area through a reduction in particles size and an increase in the number of functionalised ligands.

The impact of ligand density has been a serious debate amongst researchers. Whilst some scientists believe that ligand density has insignificant effects, the majority of the publications found that static and dynamic binding capacities would increase with increasing ligand density until reaching a certain point after which the capacity would either stabilise or decline (Wu and Walters, 1992; Ghose et al., 2007; Langford et al., 2007; Hardin et al., 2009; Wrzosek et al., 2009; Dismer and Hubbuch, 2010; Franke et al., 2010; Huang et al., 2010; Fogle and Persson, 2012; Fogle et al., 2012; Lu et al., 2012b; a; Steinebach et al., 2017; Wang et al., 2019). The decline in DBC has been heavily attributed to the steric hindrance or electrostatic repulsion effects particularly seen for the resins with grafted polymer ligands. The electrostatic repulsion effects could be reversed through an increase in buffer ionic strength and adjustments to pH. Poor selection of buffer molarity and pH may lead to either weekly or very strongly bound protein resulting in unsatisfactory recovery.

Process parameters such as flow rate play a significant role in DBC. Higher flow rate would lead to lower DBC compared to the conditions using reduced flow velocity as binding capacity is negatively affected by the short time that molecule has to travel

through the pores to reach the ligand. In addition, product of interest will start to break through sooner under high feed concentration and / or high flow rate conditions making additional feed application disadvantageous. It is common to select the feed load ratio that reflects 1-10% breakthrough of the total dynamic binding capacity as the equilibrium state in terms of bound protein cannot be reached.

Fast protein adsorption rate and good mass transfer properties of the chromatography matrix are crucial to maximise the dynamic binding capacity before the breakthrough. Adsorption kinetics describe the rate at which molecules in the mobile phase can be adsorbed to the chromatographic stationary phase. The rate of adsorption is controlled through external mass transfer, pore diffusion and solid diffusion transport resistances. External mass transfer concerns molecule's ability to travel across the stagnant layer of liquid surrounding the particle due to concentration differences between the mobile phase and the surface of the particle. Having passed the stagnant film, the molecule moves through the pores without interacting with the pore wall or functionalised ligands. Such pore diffusion is driven by the protein concentration gradient in the pore liquid with the rate being elevated in the presence of large uniform pores and well connected channels. The molecule can then adsorb and move along the exposed ligands in the solid diffusion transport mode, in which homogeneous diffusion model describes charged protein's movement along the oppositely charged ion exchange matrix layer. Pore diffusion driven adsorption is usually dominated over the homogeneous diffusion as molecule movement in the solid phase is often more restricted. However, the opposite can also be true in the cases where the adsorbed-phase concentration gradient is very high.

Pore diffusion model or otherwise known as intra-particle protein uptake rate model can be observed and measured using confocal laser scanning microscopy (CLSM). This can be performed in a finite bath experimental set up, whereby a sample of chromatography matrix is incubated with a fluorescently labelled protein in static

conditions, or, conversely, resin can be packed in a miniature flow cell that replicates the design of a chromatography column in a dynamic flow setting (Hubbuch et al., 2002; Dziennik et al., 2003; Close et al., 2013). The use of the miniature chromatography column allows to monitor protein adsorption rate within specific particles in real time, and to calculate the amount of bound protein in relation to the radius of the particle.

Aim

The aim of this Chapter was to investigate and determine which structural resin features or a combination of: average particle size, particle size distribution and ligand density, play the key role in protein adsorption kinetics.

Objectives

- Evaluate Q45, Q45 jetted, Q65 and Q90 resins containing varying ligand densities for their dynamic binding capacity with BSA protein at different linear velocities including 37, 50 and 125 cm/h.
- Observe and measure the intra-particle protein uptake rate at varying flow rates and feed concentrations with a miniature flow cell and confocal laser scanning microscope.
- Conclude and recommend the structural parameters of resins with the most significance.

4.2. Results and Discussion

4.2.1. Dynamic binding capacity

Dynamic binding capacity studies were performed in order to determine ligand density effects on protein adsorption kinetics. BSA solution was loaded onto the AEX columns at three flow velocities equal to 37, 50 and 125 cm/h. Dynamic binding capacity at 10% breakthrough was then calculated for all resin types.

4.2.1.1. Smaller beads provide higher capacity

The results revealed that smaller average particle size provided higher capacity, whilst the use of larger particles resulted in reduced dynamic binding capacity. Q45 resins generated DBC of up to 100 g/L, whilst Q65 and Q90 resins achieved 80 g/L and 75 g/L, respectively **(Figure 4-1)**. This data agrees with the studies performed with affinity (Carlsson et al., 1994; Ljunglöf and Hjorth, 1996; Hahn et al., 2003, 2005; Baur et al., 2018), size exclusion (Persson et al., 2006) and ion exchange resins (Franke et al., 2010), whereby the adoption of smaller beads improved the DBC resulting in steeper breakthrough curves for both batch and continuous chromatography set ups. Smaller particle size allowed for a faster pore diffusivity, better mass transfer and utilization of the internal bead volume due to shorter path length.

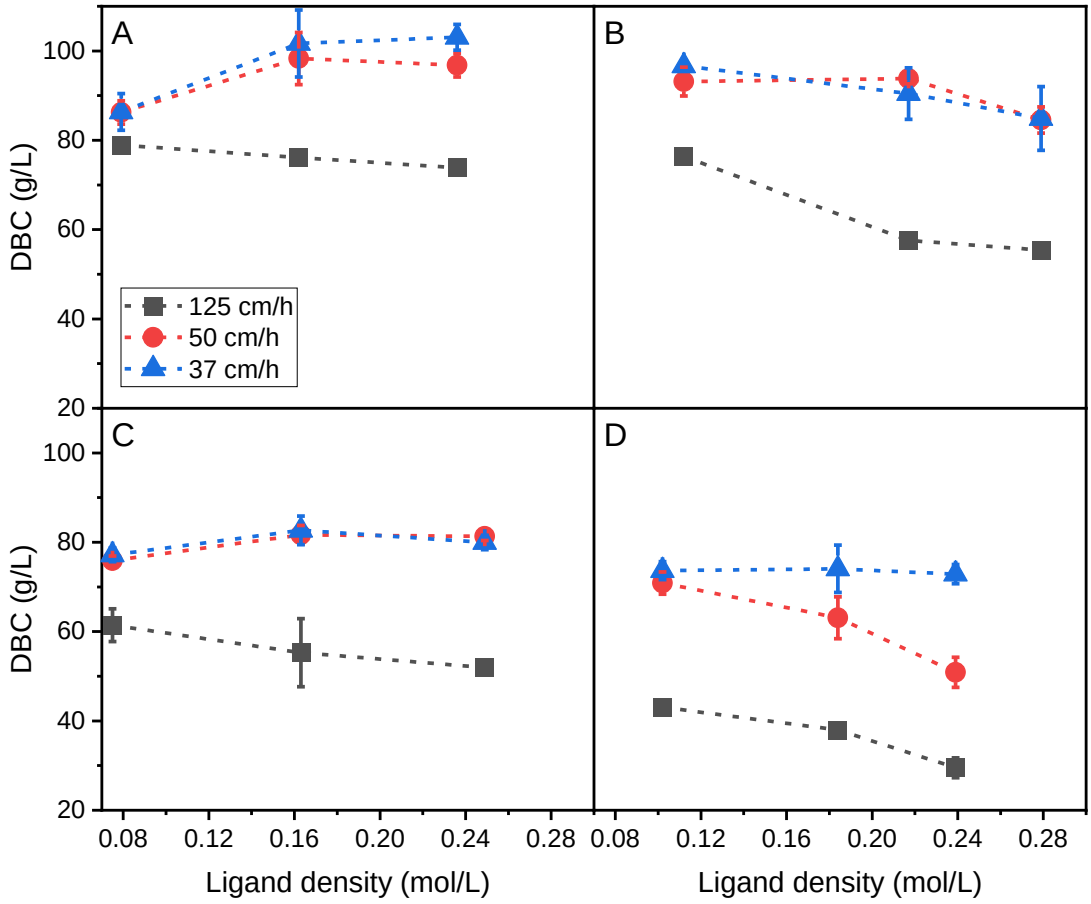

Figure 4-1. Dynamic binding capacity according to ligand density. A – Q45, B – Q45 jetted, C – Q65 and D – Q90 AEX resin. Triplicate runs were performed at each flow rate to generate averages with ± 1SD. Experiments were carried out with 200 mg BSA solution and 5 cm height, 1 mL column. Dotted line guides the reader's eye through data rather than expresses dependence between variables.

4.2.1.1. Optimum ligand density for each bead size

The effect of ligand density on dynamic binding capacity was particle size specific. In the case of non-jetted Q45 resins, DBC improved by 17% as ligand density increased from 0.08 to 0.16 mol/L but plateaued thereafter with 37 and 50 cm/h flow rates **(Figure 4-1 A)**. Q65 resins revealed a different pattern in which all ligand densities generated a similar dynamic binding capacity with the same flow rates **(Figure 4-1 C)**. An opposite pattern was seen for the Q90 resins as the capacity decreased with increasing ligand density **(Figure 4-1 D)**. Different combinations of particle size and ligand density had a diverse effect on the dynamic binding capacity.

Ligand density effects on DBC seen in this work are in agreement with previous publications. The majority of the reports discuss two trends: (i) an increase in DBC with increasing ligand density and (ii) a plateau or reduction in DBC with further boost in ligand density (Wu and Walters, 1992; Ghose et al., 2007; Langford et al., 2007; Hardin et al., 2009; Wrzosek et al., 2009; Dismer and Hubbuch, 2010; Franke et al., 2010; Huang et al., 2010; Fogle and Persson, 2012; Fogle et al., 2012; Lu et al., 2012b; a; Steinebach et al., 2017; Wang et al., 2019). Although differences amongst this work and other reports is unavoidable due to variation in ligand densities and their distribution, average particle and pore sizes, type of resin and flow rates used, the common consensus is similar: an optimum ligand density can often be established.

Optimum ligand density is considered to be a point at which the total surface area of the particle has been fully utilised and there is no space for additional protein to bind. In theory, when ligand density is low, a single protein is expected to bind to several ligands if the distance between the two is bigger than the size of the protein (Wu and Walters, 1992; Langford et al., 2007; Hardin et al., 2009; Lu et al., 2012b; Steinebach et al., 2017). Even though it would provide good pore and ligand accessibility, the ligand density would become a limiting factor for DBC. However, when the ligand density is higher than the optimum, a single protein is bound by more ligands than required making them inaccessible by other proteins and resulting in early breakthrough (Wu and Walters, 1992; Langford et al., 2007; Hardin et al., 2009; Huang et al., 2010; Fogle et al., 2012; Steinebach et al., 2017). This effect seems to be further amplified with an increase in bead diameter and flow rate, whereby lower ligand density becomes more beneficial **(Figure 4-1)**.

Reduction in DBC after reaching the optimum point can be explained two-way: presence of steric hindrance or electrostatic repulsion (Harinarayan et al., 2006; Ghose et al., 2007; Wrzosek et al., 2009; Franke et al., 2010; Lu et al., 2012b; a; Wang et al., 2019). It is possible that at high ligand concentration the protein is strongly attracted and bound to the charged surface of the particle restricting further pore diffusion, reducing pore accessibility and causing crowding around the outer particle layer. Otherwise, electrostatic repulsion could result from a dense surface area coverage by a protein due to elevated overall negative charge. An increase in conductivity could be useful in this situation as it has been found to reduce electrostatic repulsion and improve binding capacity (Harinarayan et al., 2006; Hardin et al., 2009; Wrzosek et al., 2009).

4.2.1.2. Impact of flow rate

The highest flow rate of 125 cm/h provided the lowest capacity, whilst the reduction in flow rate to 37 cm/h had the most positive impact on DBC **(Figure 4-1)**. In fact, the capacity was improved almost double for Q90 and jetted Q45 resins **(Figure 4-1 B, D)**. Low flow rate is known to positively influence dynamic binding capacity due to prolonged contact time between mobile and stationary phases, but has a negative impact on process productivity (Hahn et al., 2003, 2005; Dziennik et al., 2005; Yao and Lenhoff, 2006; Langford et al., 2007; Franke et al., 2010; Baur et al., 2018). As seen from this work, the latter can be improved since the difference in DBC generated by 37 cm/h and 50 cm/h velocities was insignificant suggesting that near equilibrium capacity could be reached at a slightly higher flow rate. In the case of non-jetted Q45 resin with low ligand density, even 125 cm/h flow rate could provide comparable near-equilibrium results **(Figure 4-1 A)**. This represents good mass transfer and ligand accessibility at low ligand supply.

4.2.1.3. Combined parameter effects

The results above depict the effects of single variables: particle size, ligand density and linear velocity. In order to understand the combined effects and their significance for DBC, JMP statistical software was implemented. A full factorial design of experiments model resulted in 27 combinations that covered the 3x3x3 matrix and produced a very good model fit with the predicted root-mean-square error (RMSE) of 3.88 and R-Squared (RSq) of 0.98 **(Figure 4-2)**.

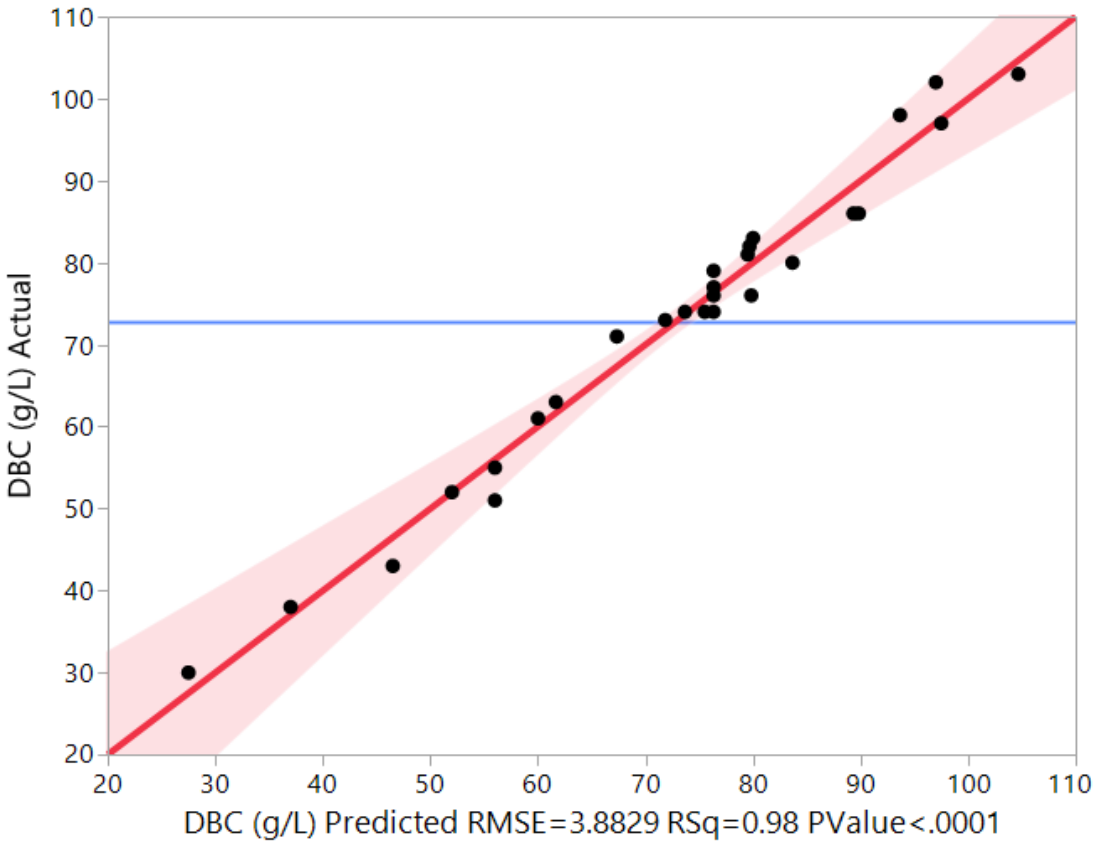

Figure 4-2. JMP model accuracy: predicted values versus actual values. Full factorial DoE was fitted with the Standard Least Squares regression model.

Statistical analysis and predictions by JMP software concluded that particle size and linear velocity were the most significant parameters that influenced DBC **(Table 4-1)**. Combined effects of two parameters: particle size and ligand density, linear velocity and ligand density as well as particle size and ligand density, were also deemed significant with the p-value below 0.05. Ligand density alone, however, did not have a significant effect on DBC as the results heavily depended on the particle size **(Figure 4-3)**.

Table 4-1. Statistical analysis of single and combined effects on DBC.

Term	**P-Value**
Particle size (µm)	<0.0001
Linear velocity (cm/h)	<0.0001
Particle size (µm)*Ligand density (mol/L)	0.0021
Ligand density (mol/L)*Linear velocity (cm/h)	0.0084
Particle size (µm)*Linear velocity (cm/h)	0.0125
Particle size (µm)*Ligand density (mol/L)*Linear velocity (cm/h)	0.1191
Ligand density (mol/L)	0.4026

The model identified that the highest DBC can be achieved with the lowest particle size of 45 µm, lowest linear velocity of 37 cm/h and the highest ligand density of 0.24 mol/L and above **(Figure 4-3)**. Flow rate patterns for different particle sizes followed the same trend as for the 45 µm resin shown in **Figure 4-3 A**. The effects of ligand density depended on the particle size. If ligand density was increased from 0.08 to 0.24 mol/L, a 15% increase in DBC could be achieved for 45 µm resins **(Figure 4-3 A)**, <5% increase would be seen for 65 µm beads **(Figure 4-3 B)**, and 3% decrease for the 90 µm resins **(Figure 4-3 C)**. The positive effect of ligand density on DBC was found to surge with the decreases in particle size.

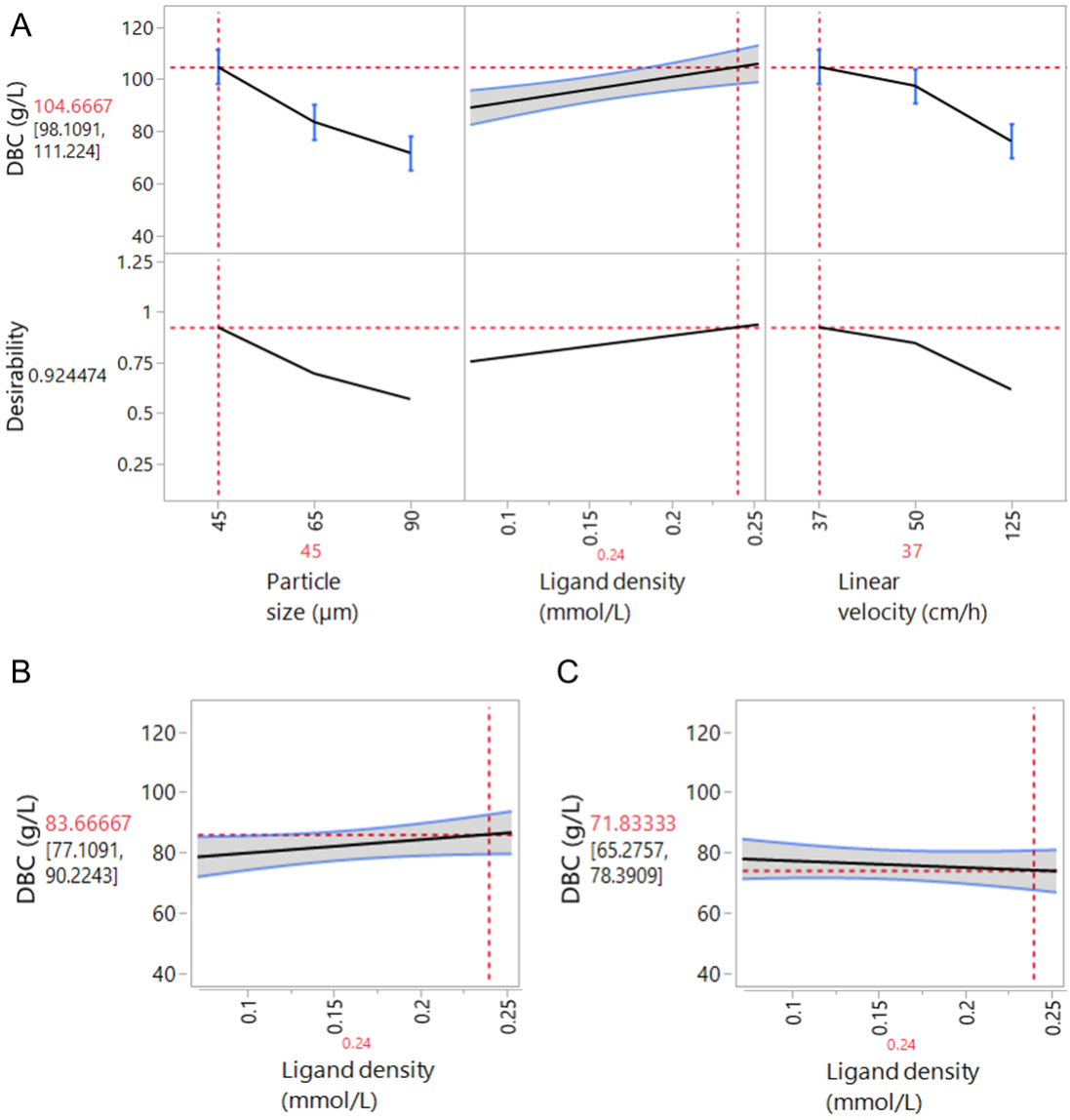

Figure 4-3. JMP prediction profile for DBC. A – chosen parameters by the model to achieve the highest DBC, B – predicted effects of ligand density on DBC for 65 µm particles, C – predicted effects of ligand density on DBC for 90 µm particles. Full factorial DoE was fitted with the Standard Least Squares regression model. Desirability was set between 0 and 1 indicating the least and most wanted outcomes, respectively. Particle size and linear velocity parameters were considered categorical, whereas ligand density was a continuous factor.

4.2.1.4. Impact of narrow particle size distribution

Narrow particle size distribution did not have a significant effect on DBC as both jetted and non-jetted resins captured between 95 and 100 g/L of BSA **(Figure 4-1 A, B)**. The highest DBC was achieved with 0.11 mol/L and 0.16 mol/L ligand densities for jetted and non-jetted resins, respectively. It is likely that if a wider range of ligand densities was studied with jetted resins, the pattern of DBC would be similar to that of non-jetted resins: an initial increase would be followed by a plateau and a reduction in capacity. In addition, the highest flow rate of 125 cm/h was the least beneficial for the jetted resin with ligand densities above 0.20 mol/L as it resulted in 30% reduction in DBC. The effect was not significant for the non-jetted resin causing only a 6% drop. Both flow rates of 37 and 50 cm/h showed comparable results. Overall, no particular differences were observed between the two resin types.

Product cycling experiments were performed in order to understand whether narrow or wide particle size distribution had any effect on fouling. Flow rate of 75 cm/h corresponding to 4 min. of residence time was used to carry out 7 consecutive runs. An additional jetted Q45 resin with 0.10 mol/L ligand density was included as an extra point. This set of experiments revealed that ligand density had a more significant effect on DBC than the particle size distribution **(Figure 4-4)**. Dynamic binding capacity remained stable at >80 g/L for resins with ligand densities below 0.16 mol/L. As ligand number was increased above 0.16 mol/L, the DBC started to drop after the second cycle resulting in >90% loss in capacity by the 7^{th} cycle. It was clear that the difference between these jetted and non-jetted resins was not significant enough to indicate the importance of particle size distribution or their average particle size in fouling.

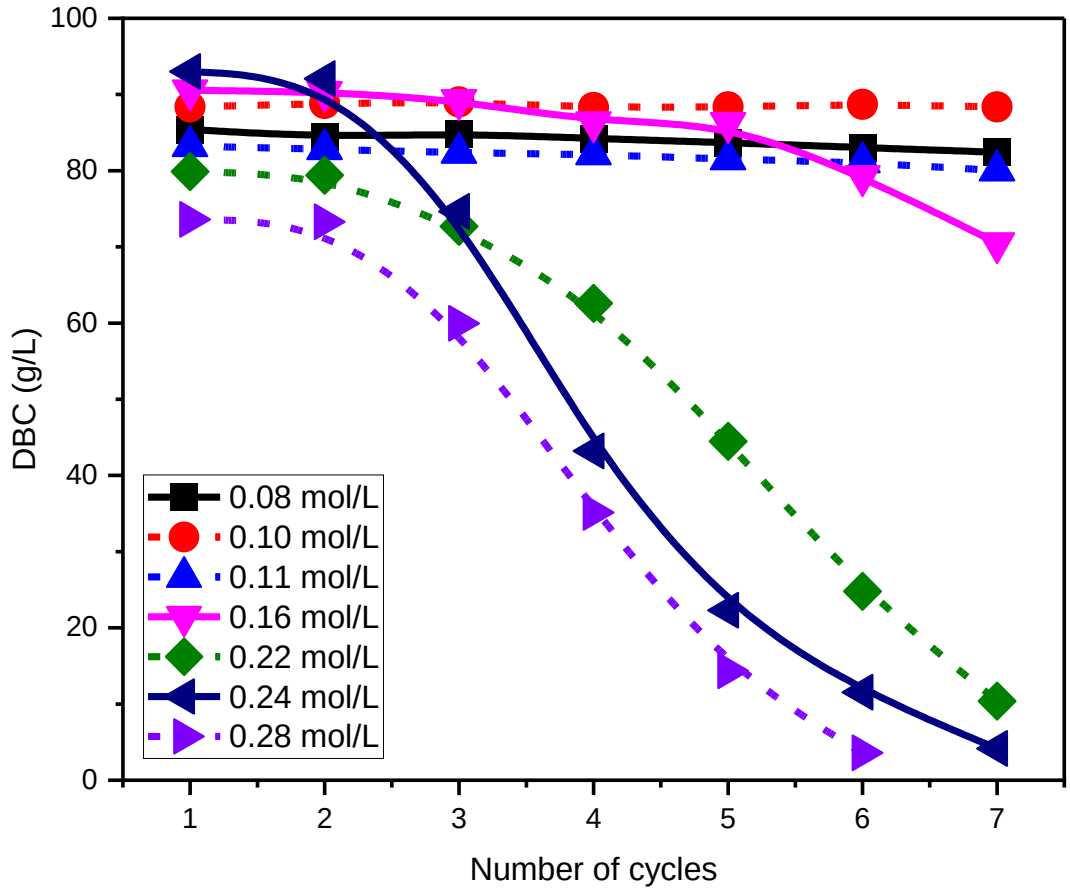

Figure 4-4. Resin lifetime study over 7 consecutive cycles. Experiments were performed at 75 cm/h using both non-jetted (straight line) and jetted (dashed line) Q45 resins with different ligand densities. Total BSA load was 200 mg per cycle, equilibration buffer was 50 mM Tris, pH 8.5 and elution buffer was 50 mM Tris, 1.5 M NaCl, pH 8.5. CIP was performed after each cycle using 1 M NaOH with a hold for 30 min. Columns of 5 cm height, 1 mL were used.

4.2.1.5. Dynamic binding capacity: Summary

Particle size, ligand density and flow rate were found to have a significant effect on the dynamic binding capacity, whilst narrow particle size distribution did not. Q45 resin with the smallest beads provided the highest binding capacity, whereas Q90 resin with the largest beads resulted in ≥30% reduction in DBC **(Figure 4-1)**. Optimum ligand density could be identified for each bead size and was generally <0.20 mol/L. Presence of additional ligand resulted in either the same or reduced capacity due to possible steric hindrance or electrostatic repulsion effects. Flow velocity of 50 cm/h (or 6 min residence time) was found to provide the highest, near-equilibrium capacity for all resins. In contrast, higher flow rate of 125 cm/h (or 2.4 min residence time) resulted in the lowest binding capacity throughout. The main advantage of using resin with low ligand density would be the high binding capacity achieved at high flow rates such as 125 cm/h, whilst the reason for using resin with high ligand density would be to achieve even higher DBC but at lower flow rates.

4.2.2. Protein uptake rate with confocal microscopy

Dynamic binding capacity studies revealed that excess ligand density was a cause of reduction in capacity **(Figure 4-1)**. Previous reports have suggested that this may be a result of protein crowding or electrostatic repulsion effects occurring on the surface of the particles (Harinarayan et al., 2006; Ghose et al., 2007; Wrzosek et al., 2009; Franke et al., 2010; Lu et al., 2012b; a; Wang et al., 2019). The most commonly used method to test these hypotheses is to observe intra-particle protein uptake using confocal laser scanning microscopy and a miniature chromatography flow cell (Hubbuch and Kula, 2008). This technique allows to visualise fluorescently labelled protein uptake at a single bead level under the constant flow conditions. A series of experiments included Q45, Q65, Q90 and jetted Q45 resins that were used under different process conditions such as flow rate and feed concentration were set up. Protein uptake rate was expected to slow down with the increase in ligand density if the crowding effects played a role.

4.2.2.1. Confocal microscopy set up

One of the major concerns in the experimental set up was the ability of fluorescently labelled protein to behave in the same way as the unlabelled protein. A commonly used strategy to understand the behaviour of both proteins is to measure the amount of free protein in solution that resin can bind in static conditions over time. Here, static binding capacity experiments showed that both Texas Red-labelled and unlabelled BSA solutions gave rise to overlapping protein uptake curves **(Figure 4-5)**. Consequently, this confirmed that the protein-dye conjugate and resin interactions in the miniature flow cell would be representative of those with the non-labelled protein.

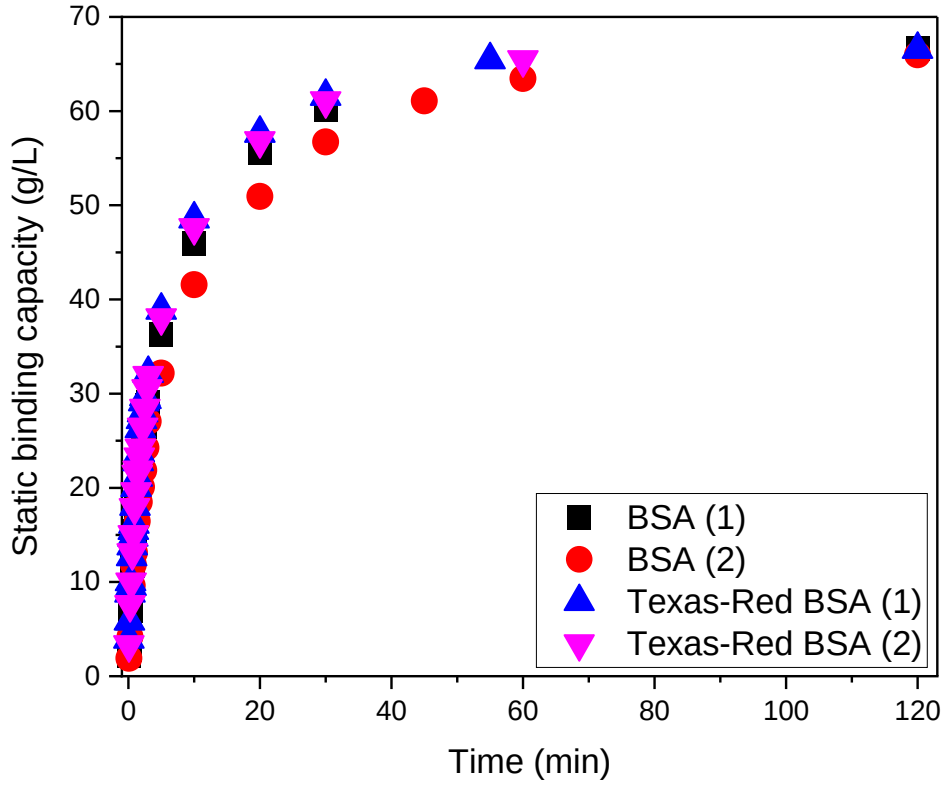

Figure 4-5. Static binding capacity comparison of the Texas Red-labelled and unlabelled BSA solution. Numbers 1 and 2 represent different replicates for each protein solution. Equilibration buffer was 50 mM Tris at pH 8.5. The unbound protein was measured in triplicate at 280 nm absorbance.

4.2.2.2. Smaller beads provide faster protein uptake rate

The first set of data performed with 3 g/L and 10 g/L of BSA at 380 cm/h flow rate revealed that protein uptake rate was dependent on particle size **(Figure 4-6, Appendix A: Figure 0, Figure 1, Figure 4)**. Fastest protein uptake rate was seen for the smallest beads of Q45, whilst lowest uptake rate was noticed for the larger beads of Q65 and Q90 **(Figure 4-6, Figure 4-7)**. The Q45 resins reached 100% saturation within approximately 15 minutes, whereas only about 40% saturation was evident for the Q65 and Q90 resins with 10 g/L BSA feed **(Figure 4-7 D-F)**. When the feed concentration was reduced to 3 g/L, Q45 resins were completely saturated within 100

minutes **(Figure 4-7 A)**. In contrast, the Q65 and Q90 resins saw a shallow protein uptake curve with a potential to plateau, and reached a maximum of 40% saturation within the same period of time **(Figure 4-7 B-C)**. The results are in good agreement with the earlier DBC data, whereby Q45 resins provided highest capacity at 125 cm/h flow rate; on average 80 g/L, 60 g/L and 40 g/L for Q45, Q65 and Q90, respectively **(Figure 4-1)**.

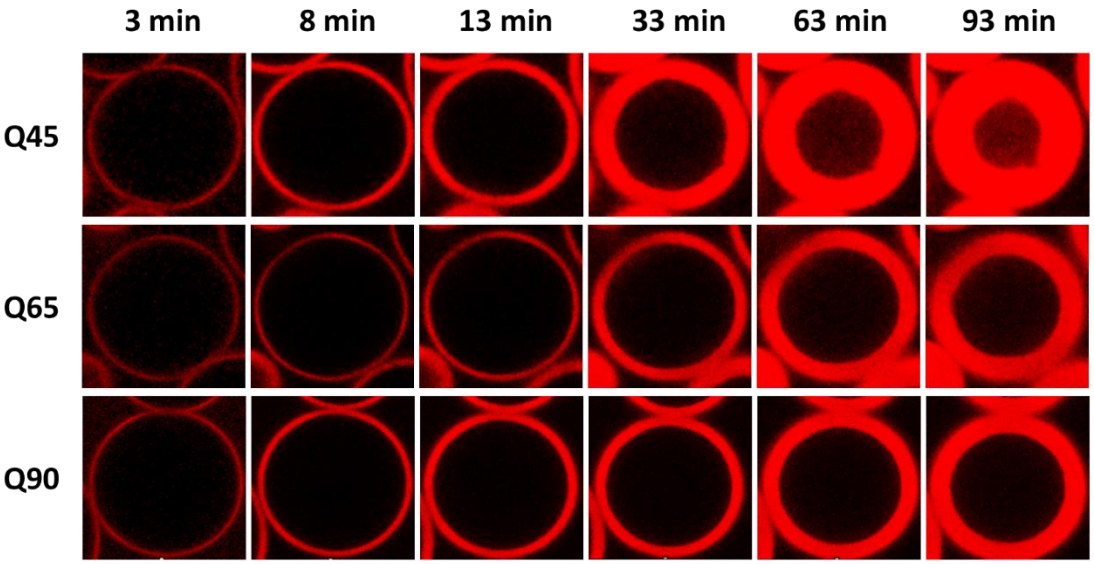

Figure 4-6. CLSM images of Texas Red-labelled BSA uptake for different particle sizes. AEX resins with high ligand density and 3 g/L of feed were used. Resins were packed in a flow cell and equilibrated with 50 mM Tris, pH 8.5 at 380 cm/h flow. Total of 5 particles each were analysed and the most representative profiles are shown. Excitation and emission wavelengths were 550 and 600 nm, respectively. Other microscopy parameters: 40x magnification lens with oil immersion, 40% laser intensity and 512x512 image resolution.

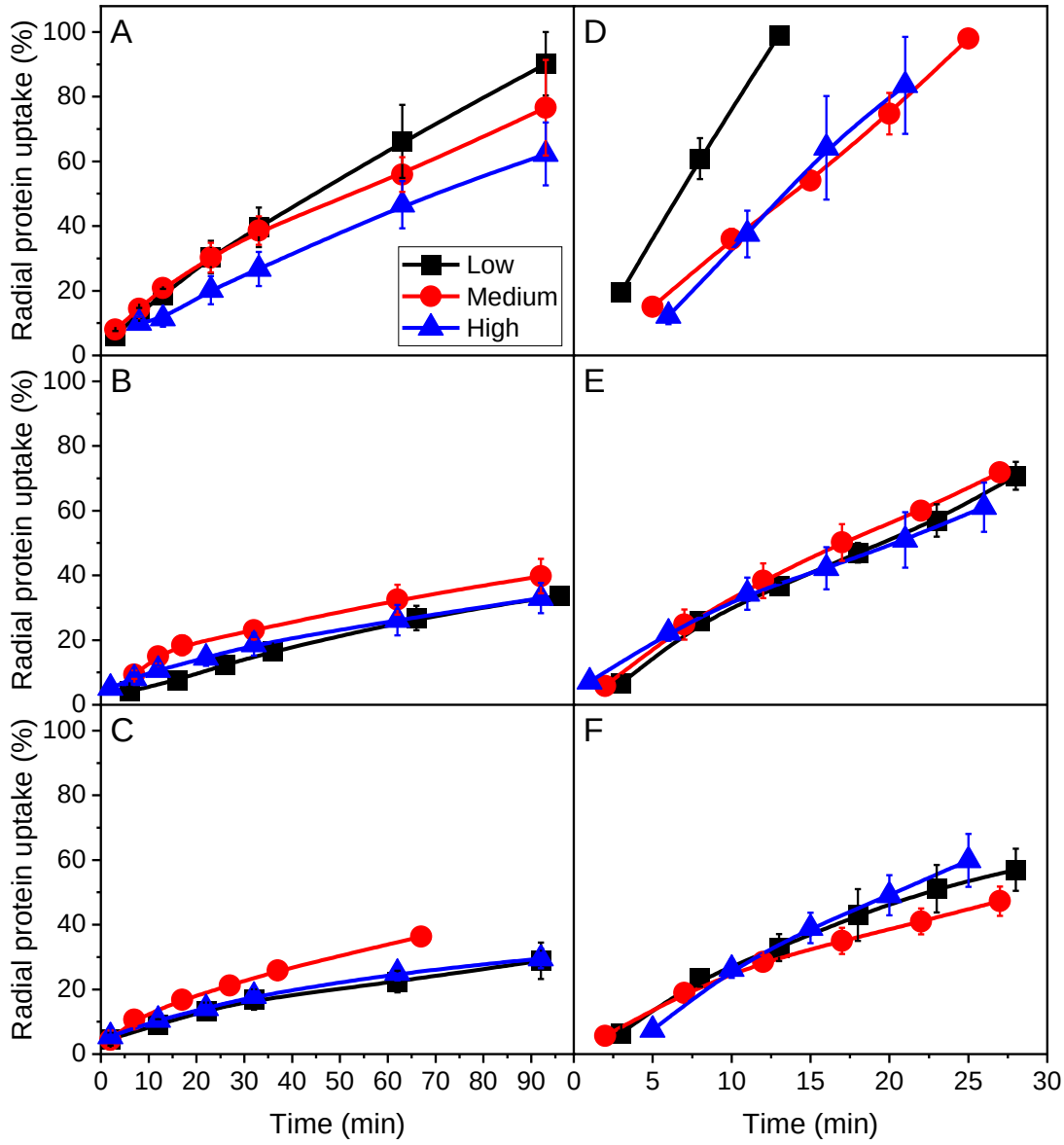

Figure 4-7. Quantitative analysis of protein uptake rate for different bead sizes with 3 g/L and 10 g/L feed conc. A and D – Q45, B and E – Q65 and C and F – Q90 resins with low, medium and high ligand densities. Figures A-C represent 3 g/L feed conc., whilst D-F show results of 10 g/L BSA uptake rate. CLSM experiments were performed with Texas Red-labelled BSA solution at 380 cm/h flow rate following equilibration with 50 mM Tris, pH 8.5. Images were analysed with ImageJ software. A total of 5 beads were selected for protein uptake band spreading through the radius and averaged based on particle size to give the percentage saturation. Averages with ± 1SD error bars are shown.

Comparable results and conclusions that larger beads require longer incubation time for improved uptake rate have been described elsewhere (Ljunglöf and Hjorth, 1996). A surface diffusion model also suggested that particles of 40 µm could be fully saturated within 30 min, whilst larger ones would require more time (Zhou et al., 2006). This was due to longer diffusional length inside the pores of the larger particles (the effective pore diffusivity being dependent on the square particle diameter) and reduced ligand access as a result of convective flow (Wahome et al., 2008; Baur et al., 2018).

4.2.2.3. Optimum ligand density for each bead size

Protein uptake rate for Q45 resins in a flow cell was ligand density dependent. Low ligand density resin together with 10 g/L feed provided significantly faster protein uptake rate resulting in 100% bead saturation within only 13 minutes which was a two-fold improvement compared to the highest ligand density **(Figure 4-7 D)**. Low ligand number was also more beneficial with the 3 g/L BSA as it resulted in 15% and 30% higher bead saturation than with the medium and high ligand densities, respectively **(Figure 4-7 A)**.

Protein uptake rate for both Q65 and Q90 resins did not seem to be highly affected by the differences in ligand density. Particle saturation for these resins was generally <50% after 20 minutes with 10 g/L BSA and <20% with 3 g/L feed **(Figure 4-7 B-C, E-F)**. The results were slightly different to those obtained in the DBC study, whereby at high flow rate binding capacity reduced by 20% and 30% for Q65 and Q90 resins, respectively, with increasing ligand density, whereas protein uptake rate was reduced by 10% and 20% with 10 g/L BSA feed under 380 cm/h flow. It is possible that the flow rates above 125 cm/h would restrict the utilisation of the full particle volume and would therefore generate comparable capacity as contact time rather than ligand density would become a limiting factor.

4.2.2.4. Impact of particle size distribution

Protein uptake rate for the jetted Q45 resins also revealed similar results whereby particle saturation could be achieved quicker with the low ligand density resins. The 0.11 mol/L ligand density resin achieved >80% bead saturation within 18 minutes, whilst 0.22 mol/L and 0.28 mol/L ligand density resins achieved <60% saturation within the same time **(Figure 4-8)**. This is in a good agreement with the DBC data, whereby the capacity decreased by 30% with increasing ligand density at the highest flow rate **(Figure 4-1 B)**. Both experimental studies confirmed the same trend: As ligand density increased above the optimum, binding capacity and protein uptake rate decreased and plateaued.

However, both the DBC and protein uptake rate studies showed that the role of particle size distribution was irrelevant. This was expected because good flow cell packing could not be ensured and single beads could only be observed rather than the overall column performance. Despite that, it was evident that protein uptake was particularly ligand density dependent for the Q45 resins **(Figure 4-8)**. Protein adsorption rate increased significantly for resins containing low ligand density, which was evident from a steep linear curve. In contrast, the BSA uptake curve started to flatten as the ligand number increased. This provided evidence to support the hypothesis that the use of excess amount of ligand would result in poor mass transfer.

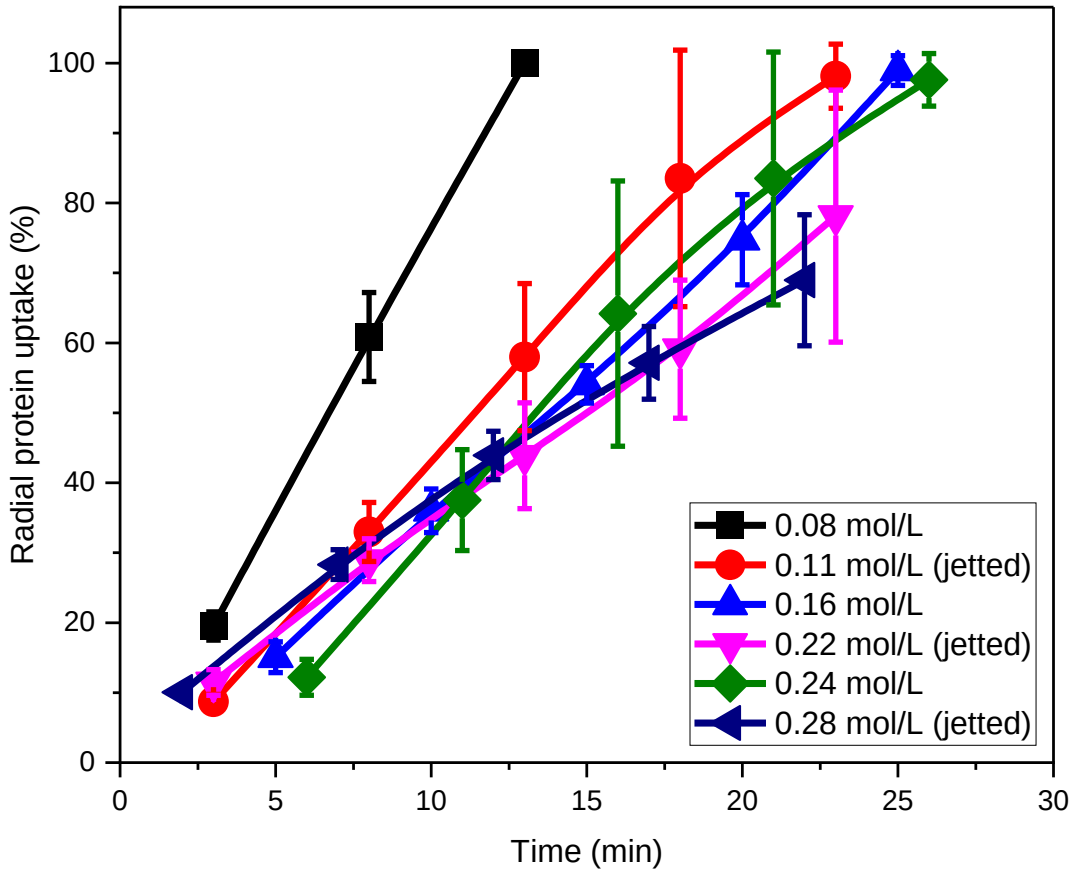

Figure 4-8. Comparison of Q45 jetted and non-jetted resins' BSA uptake rate. CLSM experiments were performed with 10 g/L Texas Red-labelled BSA solution (1:100 ratio) at 380 cm/h flow rate following equilibration with 50 mM Tris, pH 8.5. Excitation and emission wavelengths were 550 and 600 nm, respectively. Other microscopy parameters: 40x magnification lens with oil immersion and 40% laser intensity. Images were analysed with ImageJ software. A total of 5 beads were selected for protein uptake band spreading through the radius and averaged based on particle size to give the percentage saturation. Averages with ± 1SD error bars are shown.

4.2.2.5. Feed concentration determines diffusion model

In order to fully understand whether the reduced protein uptake rate at high ligand density was caused by electrostatic repulsion or pore crowding, we devised a set of experiments with additional feed concentrations and flow rate conditions. Feed concentrations of 3, 5 and 10 g/L as well as flow velocities of 255 and 380 cm/h were explored with three ligand densities of non-jetted Q45 resins via confocal microscopy **(Figure 4-9, Appendix A: Figure 4, Figure 5, Figure 6)**.

Low ligand density resin provided highest protein adsorption rates with all conditions tested **(Figure 4-9 A)**. For example, using a feed concentration of 5 g/L at 255 cm/h it took low ligand density resin 55 min to saturate the beads, whereas it required 65 min and 75 min for medium and high ligand density resins, respectively. This can be related to the DBC runs and predicted that breakthrough would start earlier for the higher than the lower ligand density resin if the residence time was 1 min. It therefore further aids the hypothesis that higher ligand density could restrict protein uptake.

The results showed that feed concentration also dictated the uptake rate. It was found that higher BSA concentration led to faster uptake rates for all ligand densities suggesting that the adsorption process was diffusion-driven. A very clear distinction could be seen for the lowest ligand density resin, whereby it took 15 minutes for a full saturation with 10 g/L feed and on average 60 min and 90 min for the 5 g/L and 3 g/L BSA, respectively **(Figure 4-9 A)**.

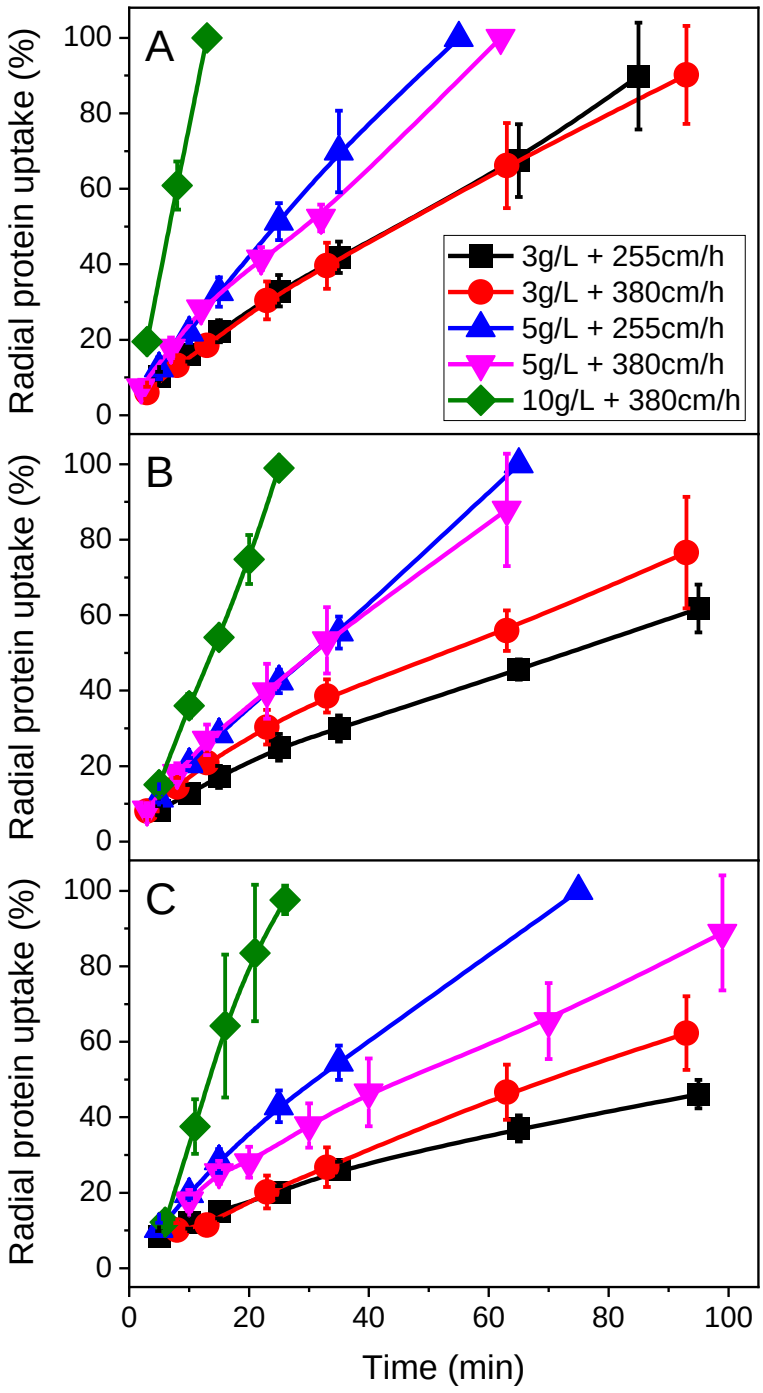

Figure 4-9. Protein uptake rate with varying feed and flow conditions. A – low, B – medium and C – high ligand density containing non-jetted Q45 resins. Feed concentrations of 3, 5 or 10 g/L were supplied at either 255 cm/h or 380 cm/h in a flow cell following equilibration with 50 mM Tris, pH 8.5. Texas Red-labelled BSA solution was made in a ratio of 1:100. Excitation and emission wavelengths were 550 and 600 nm, respectively. Other microscopy parameters: 40x magnification lens with oil immersion and 40% laser intensity. A total of 5 beads were selected for protein uptake band spreading through the radius and averaged based on particle size to give the percentage saturation. Averages with ± 1SD error bars are shown.

The differences in protein uptake rate due different feed concentrations could be visually observed. **Figure 4-10** displays a slow-moving self-sharpening front representing a “shrinking core model” due to significant pore diffusion effects at 3 g/L BSA **(Appendix A: Figure 2)**, whilst **Figure 4-11** reveals a fast-moving diffuse pattern resembling homogeneous or solid diffusion model at 10 g/L feed concentration **(Appendix A: Figure 3)**. Effective adsorbed-phase diffusivity (D_s) value is known to become higher than that of the effective pore diffusivity (D_e) if the driving force, i.e. the concentration gradient in the adsorbed phase (∇q), was significant. This is often expected from the adsorbers with high capacity.

Both models have been previously observed with the help of confocal microscopy. The shrinking core model could be seen at lower ionic strength, whilst the homogenous diffusion profile would be visible at a slightly higher ionic strength (Linden et al., 2002; Hubbuch et al., 2002, 2003a; b; Dziennik et al., 2003, 2005; Harinarayan et al., 2006; Langford et al., 2007). The latter condition was speculated to loosen the protein-ligand interactions, reduce any potential electrostatic repulsion effects and, thus, improve protein adsorption rate. If the reduction in protein uptake rate and DBC for high ligand density resins were a result of electrostatic repulsion effects, changes to conductivity would enable to provide more insight.

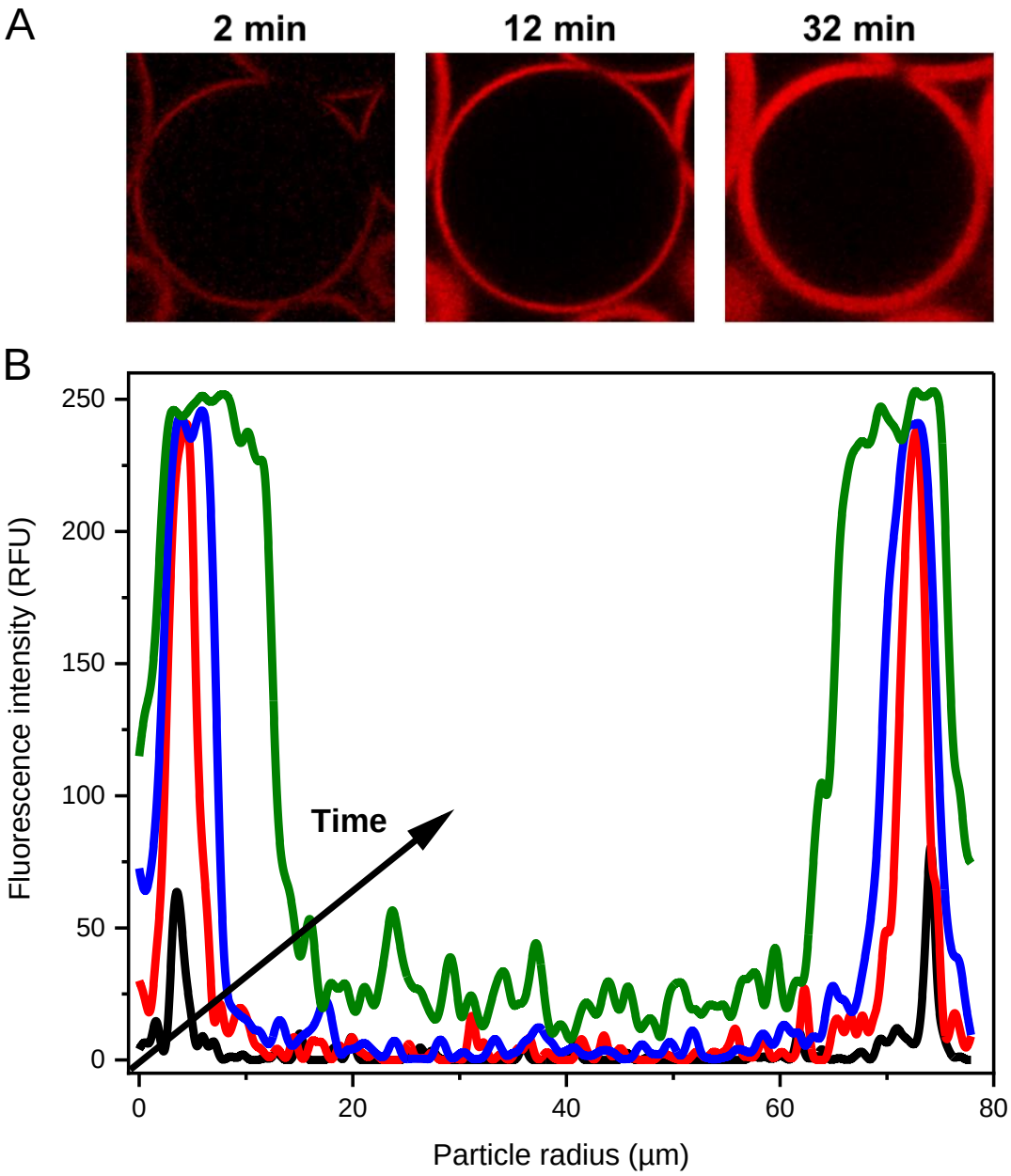

Figure 4-10. Shrinking core model visualised with CLSM. A – shows the same particle being imaged over the course of time at 380 cm/h flow velocity. Texas Red-labelled BSA solution of 3 g/L was continuously supplied with a syringe pump after equilibration with 50 mM Tris, pH 8.5. Q65 resin with low ligand density is shown as an example. B – depicts numerical data extracted from ImageJ software following the analysis of the top images. Fluorescence intensity is represented in relative fluorescence units (RFU) with maximum being 255. Black arrow shows a change in fluorescence intensity profile with increasing time.

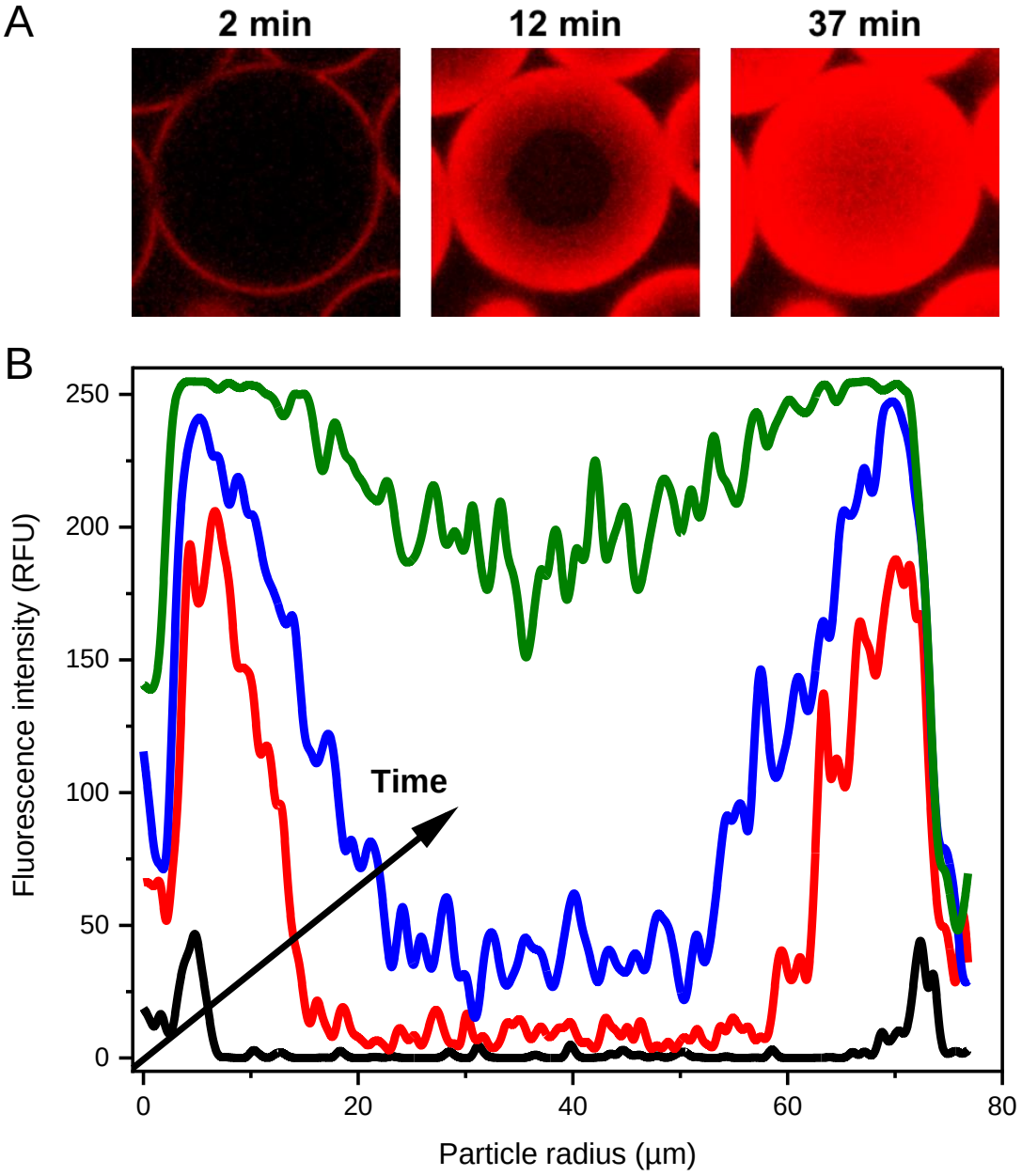

Figure 4-11. Diffuse model visualised with CLSM. A – shows the same particle being imaged over the course of time at 380 cm/h flow velocity. Texas Red-labelled BSA solution of 10 g/L was continuously supplied with a syringe pump after equilibration with 50 mM Tris, pH 8.5. Q65 resin with low ligand density is shown as an example. B – depicts numerical data extracted from ImageJ software following the analysis of the top images. Fluorescence intensity is represented in relative fluorescence units (RFU) with a maximum being 255. Black arrow shows the change in fluorescence intensity profile with increasing time.

4.2.2.6. High flow rate limits protein uptake rate

The effect of flow rate was twofold: it could either improve or restrict the protein uptake rate. Higher flow velocity of 380 cm/h caused a reduction in protein uptake rate when using 5 g/L feed concentration, whereas the same flow was proven beneficial for the 3 g/L conc. **(Figure 4-9)**. The opposite was also true, whereby 255 cm/h linear flow resulted in higher uptake rate for the 5 g/L BSA solution but lower uptake rate for the 3 g/L. The effects were more pronounced for the medium and high ligand density resins **(Figure 4-9 B-C)**. This suggested that higher flow rate was required for lower feed concentration to overcome the diffusion-limited reaction, whilst lower flow rate was beneficial for the mass transfer-limited reaction at high feed concentration. The DBC results closely resembled those of 5 g/L (and possibly 10 g/L although data not available) seen in the CLSM findings as lower flow rate was required to achieve higher dynamic binding capacity.

4.2.2.7. Hypothesis

Steric hindrance was hypothesized to be the cause of the reduction in both protein uptake rate and dynamic binding capacity. Confocal microscopy revealed that protein adsorption was predominantly influenced by homogeneous (or solid) diffusion forces at 10 g/L feed concentration. Since homogeneous diffusion relies on molecules jumping between adsorption sites, high ligand density may have caused the protein to stall and move slower as the electrostatic interactions were stronger. This in turn could have caused crowding (but not complete blockage) at the entrance to the pores. The uptake could be accelerated through the reduction of flow rate as seen from both DBC and CLSM experiments **(Figure 4-1, Figure 4-9)**.

4.2.2.8. Protein uptake rate: Summary

Confocal laser scanning microscopy revealed that protein uptake rate was dependent on four factors: average particle size, ligand density, feed concentration and flow rate. Smaller particles, low ligand density, high feed concentration and reduced flow rate were all found to provide fast protein uptake rate within the conditions studied. Two distinct models including the shrinking core and homogeneous diffusion could be observed when using 3 g/L and 10 g/L BSA, respectively. As a result, low flow rate was required for high feed concentration, whilst accelerated flow rate was beneficial for the low feed concentration in order to reduce steric hindrance effects in resins with high ligand density.

4.3. Conclusions

The aim of this chapter was to evaluate which physical particle characteristics were important and could be used to improve the chromatography resin design. Average particle size, particle size distribution and functionalised ligand density were the key features that were examined in this work.

- Average particle size: Smaller particle size generated high dynamic binding capacity, fast protein uptake rate and improved resin lifetime due to shorter diffusion path lengths inside the pores. In contrast, the opposite was true for the larger particles.
- Particle size distribution: Jetted and non-jetted resins revealed similar findings in all conditions tested meaning that the differences between the two types might not be significant enough.
- Ligand density: Low ligand density provided high binding capacity at high flow rate (125 cm/h), fast protein uptake rate and improved resin lifetime. However, the use of high ligand density resulted in higher binding capacity at low flow rates (37-50 cm/h). It also caused lower protein uptake rate and reduced resin longevity due to strong multipoint protein-ligand interactions and steric hindrance effects.

5. Chapter: Resin lifetime and novel aggregate detection assay development

The lifetime of chromatography resins averages between 10-300 cycles for the manufacture of a therapeutic protein. Developing and establishing the robustness of the method for each separation process represents a significant challenge, and is subject to extensive regulatory oversight. Here, we present a novel fluorescence-based assay for residual aggregated proteins to aid the evaluation of the extent of resin regeneration. The versatility of this method was demonstrated by using strong anion and cation exchange agarose resins Praesto Q and SP in conjunction with bovine serum albumin and monoclonal antibody feed materials. The assay entailed applying a molecular rotor dye to a sample of free resin, and measuring the fluorescence intensity using a plate reader or visualising under confocal laser scanning microscope to gain a more detailed understanding. Following five consecutive chromatography cycles, both methods revealed a 10-fold increase in fluorescence intensity along with a proportional reduction in dynamic binding capacity. Furthermore, the use of the assay suggested that fouling was dependent on particle size, bead channel structure, ligand density, spatial bead positioning in the column, and cleaning conditions. This chapter presents a simple assay suitable for use in resin lifetime studies to enhance process understanding.

5.1. Introduction

Resin reuse over multiple cycles causes a reduction in dynamic binding capacity, product yield and purity resulting in higher production costs or complete lot failures. The deterioration of chromatography resin occurs due to accumulation of remaining biological material such as host cell proteins and DNA, exposure to harsh buffers and mechanical compression (Nweke et al., 2018). Control and maintenance of resin performance is especially important for the repeat manufacture of biological products, where costs and regulatory standards are high (Sofer and Yourkin, 2007).

Levels of fouling caused by biological material can be reduced by tangential or dead-end depth filtration prior to column chromatography, in addition to selecting appropriate cleaning and storage procedures for chromatographic operations. It is essential to establish and validate an effective cleaning protocol during process development, which is generally achieved in several phases. Phase one involves screening a large number of cleaning protocols whilst running them in parallel using scale-down high-throughput approach (Grönberg et al., 2011; Elich et al., 2016). In phase two, the most effective protocols from the initial phase are identified and tested at a larger scale before a manufacturing run (Rathore and Sofer, 2005a; b). Correctly chosen protocol will allow to significantly increase resin lifetime, and reduce the overall production cost.

The deterioration of resin performance can be evaluated by monitoring critical quality attributes of the eluate through employing a number of analytical methods such as gel electrophoresis, turbidity and absorbance readings. The use of standard gel electrophoresis technique has advanced into miniaturized devices (lab-on-a-chip), which can determine the amount of DNA, RNA and protein (Bousse et al., 2001). Turbidity measurements taken at 320 nm can be used to analyse the clearance of high molecular weight species (HMWS) and host cell impurities (Yigzaw et al., 2006;

Iskra et al., 2013; Gagnon et al., 2014; Elich et al., 2016), whereas absorbance measurements at 280 nm can indicate the presence of the desired protein in the flow through, elution and strip steps (Bergander et al., 2008). The amount of detected host cell DNA and protein indicates the effectiveness of the cleaning-in-place (CIP) and, by extension, the degree of fouling.

Alternative techniques for monitoring the extent of fouling rely on more complex analytical set-ups. Fourier transform infrared spectroscopy with attenuated total reflection sensor (ATR-FTIR) can monitor protein contaminant build up and Protein A ligand leaching, as well as predict dynamic binding capacity, which would be highly beneficial for usage *in situ* with small scale columns (Boulet-Audet et al., 2015, 2016). However, since the ATR technique can accurately measure only a layer of several micrometres, a mechanical bead compressor and a custom container are required, neither of which are compatible with the current automated liquid handling systems.

To understand the impact of repeated cycles on a chromatography resin, microscopy-based techniques can be used to produce highly detailed images, providing insight into the extent and location of residual impurities. Scanning and transmission electron microscopes can reveal morphological changes to the bead surface under poor cleaning conditions (Angelo et al., 2013, 2016; Close et al., 2013; Corbett et al., 2013; Elich et al., 2016; Zhang et al., 2016a; b). However, dry samples are a prerequisite for most forms of electron microscopy imaging, which can compromise the bead structure (Nweke et al., 2017b). In contrast, confocal microscopy enables the resin to remain hydrated, eliminating concerns about the impact of drying processes, and thereby facilitating studies on foulant distribution throughout the entire bead with the help of fluorescently tagged proteins (e.g.,(Siu et al., 2006; Close et al., 2013)).

A non-invasive, fluorescence-based technique developed by Pathak and Rathore allowed monitoring of fouling in real time using PreDictor™ plates without additional protein tags (Pathak et al., 2017; Pathak and Rathore, 2017). The basis of this approach relied on differential amounts of tyrosine and phenylalanine residues in Protein A resin that absorbed at 303 nm, compared to the higher concentrations of tryptophan in foulants, which caused a shift in the absorbance spectra to 340 nm. This method demonstrated the capacity to monitor ligand leaching in addition to foulant accumulation. However, applicability of this technique has yet to be fully established, since testing has been confined to only a single type of resin.

In this study, I propose a sensitive and quick fluorescent dye-based method specific to aggregated proteins in the sample that can be used either in conjunction with automated liquid handling systems integrated with plate-based measurement of fluorescence or with confocal microscopy. The method employs a commercially available fluorescent dye PROTEOSTAT® that ceases its free rotation around a single bond, and fluoresces upon binding to protein aggregates. The dye provides a much greater sensitivity towards a broader variety of proteins and conditions compared to its early prototype Thioflavin T. It was developed to have minimal activity in the presence of monomers but displays a 20 to 90-fold increase in fluorescence upon binding to cross-β spine structures (Shen et al., 2011) that are indicative of aggregates (Nelson et al., 2005; Holm et al., 2007; Borzova et al., 2016). This is to our knowledge the first time this dye technology has been used to examine aggregates in separation materials.

Aim

Develop and evaluate a dye-based assay for an in-column foulant detection.

Objectives

- Establish positive and negative controls in order to determine the selectivity of the dye.
- Evaluate its sensitivity based on multiple chromatography cycles, cleaning regimes and positioning in the column.
- Set up a quantitative assay to measure the level of fluorescence at a resin slurry sample level.
- Set up a qualitative assay to visualise and determine dye's specificity at a bead level.
- Confirm the dye's sensitivity to resins with structural differences including particle size, size distribution and ligand density.

5.2. Results and Discussion

5.2.1. Reduction in DBC indicates fouling

Whilst performing DBC studies described in Chapter 4, it was noticed that depending on ligand density and flow rate the binding capacity would drop significantly after several runs, and a new column would have to be packed again. An example of such reduction in DBC is shown in **Figure 5-1**. The drop in capacity was hypothesized to be a result of accumulation of irreversibly bound protein, which resulted in resin fouling.

5.2.1.1. High flow rate causes a small change in DBC

The percentage loss in capacity increased with decreasing flow velocity, i.e. increasing residence time **(Figure 5-1)**. Three consecutive runs at 125 cm/h showed little change in DBC (<15%) for all bead sizes and ligand densities, whereas runs at 50 cm/h and 37 cm/h saw an average reduction in capacity by 24% and 34%, respectively **(Table 5-1)**. The gradual decline in capacity suggested an increase in residual protein accumulation inside the columns, the level of which was strongly affected by the flow rate.

In Chapter 4, lower flow rate was found to provide higher DBC due to a longer residence time and thus better resin utilization, whilst higher flow rate would not allow for a full particle saturation due to a shorter residence time and would result in lower DBC **(Figure 4-1, Chapter 4)**. A complete particle saturation could become an obstacle for the more viscous cleaning solutions such as sodium hydroxide trying to get through the core. In fact, prolonged tailing peaks of unbound protein were noticed after cycles had been subjected to 1.5 M NaCl strip and 1 M NaOH CIP steps (data

not shown). In contrast, when runs were performed at 125 cm/h and less protein was bound, no tailing peaks could be observed due to an effective protein removal.

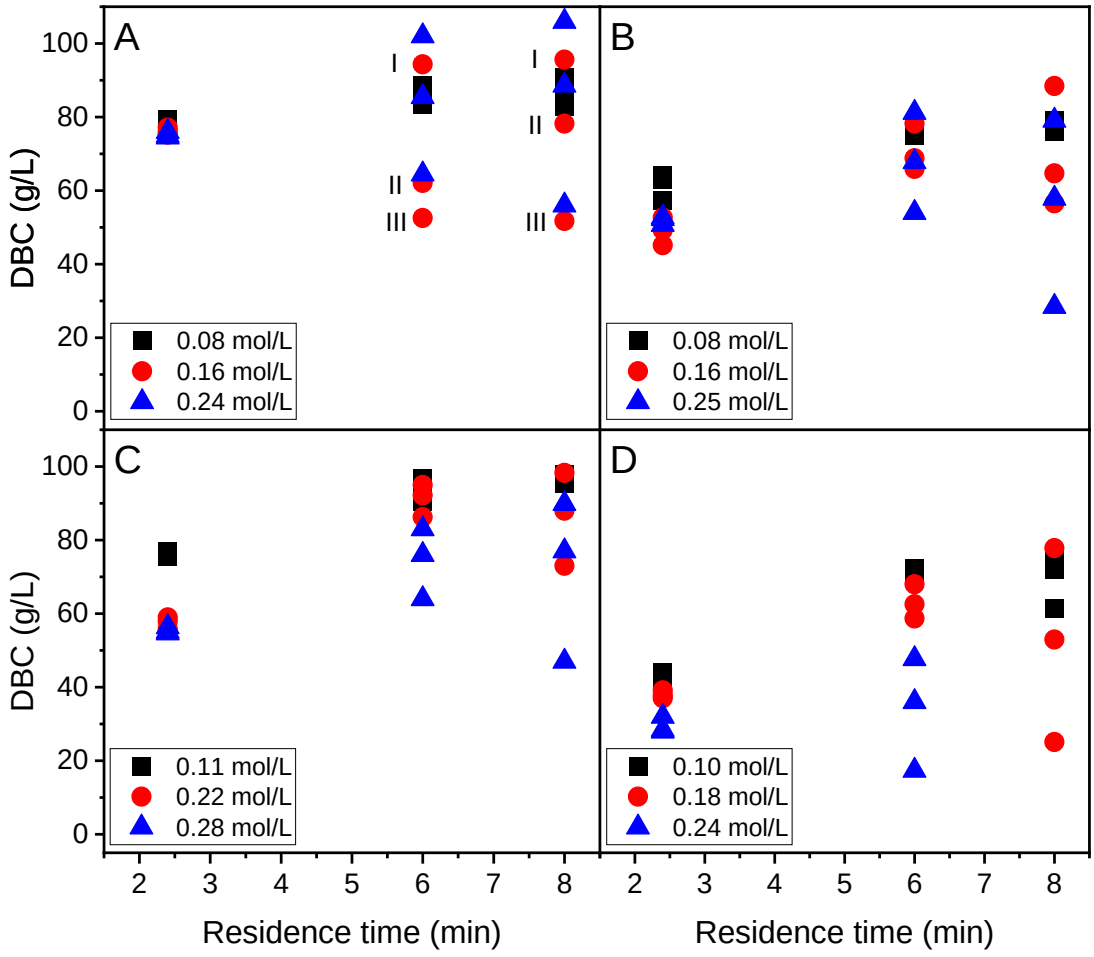

Figure 5-1. Resin lifetime study based on changes in DBC. A – non-jetted Q45, B – Q65, C – jetted Q45, and D – Q90 resins with low, medium and high ligand densities. Total BSA load was 200 mg per cycle, and three consecutive runs were performed at 125 cm/h (2.4 min residence time), 50 cm/h (6 min res. time) and 37 cm/h (8 min res. time). Equilibration buffer was 50 mM Tris, pH 8.5 and elution buffer was 50 mM sodium acetate, 1.5 M NaCl, pH 4.7. CIP was performed after each cycle using 1 M NaOH for 30 min. Columns of 5 cm height, 1 mL were used. Roman numbers on graph A represent a change in capacity after the first (I), second (II) and third (III) runs, and is applicable for all graphs. Note: Experiments at 37 cm/h flow rate with Q90 and 0.24 mol/L ligand density were not carried out as the column was excessively fouled after runs at 50 cm/h.

5.2.1.2. High ligand density causes a large drop in DBC

High ligand density was found to be another cause of considerable reduction in resin lifetime. The higher the ligand density, the bigger the drop was seen in DBC. Resins containing lowest ligand densities (0.08-0.11 mol/L) produced little to no change in DBC (mostly <10%) irrespective of bead size and flow rate **(Figure 5-1 and Table 5-1)**. Accordingly, medium ligand density resins had generally smaller changes in DBC compared to the highest ligand density resins **(Table 5-1)**. For example, medium ligand density containing Q65 resin saw a 35% reduction in capacity, whilst its high ligand density counterpart had a notable 65% reduction at 37 cm/h flow rate.

Table 5-1. Reduction in DBC over consecutive runs at varying residence time.

Resin	**Ligand density (mol/L)**	**DBC reduction at different residence times (%)**		
		2.4 min (125 cm/h flow)	6 min (50 cm/h flow)	8 min (37 cm/h flow)
Q45	0.08	1	7	9
	0.16	3	44	46
	0.24	3	37	47
Q45 jetted	0.11	3	7	3
	0.22	3	9	26
	0.28	2	23	48
Q65	0.08	10	3	4
	0.16	7	15	35
	0.25	2	33	65
Q90	0.10	3	1	20
	0.18	3	13	68
	0.24	12	65	No data

As suggested in Chapter 4, higher ligand density would provide a bigger number of protein-ligand attachment points, and thus form stronger ionic bonds. In contrast, lower ligand density could make a smaller number of connections to a lesser number of proteins provided that ligands were distributed evenly throughout the surface area. Therefore, an improvement in protein recovery with the reduction in ligand density would be expected, and has been described elsewhere (Kopaciewicz et al., 1985; Pessela et al., 2004; Huang et al., 2006; McCue et al., 2009; Huang et al., 2010).

5.2.1.3. Narrow PSD provides insignificant differences in DBC

Particle size distribution did not seem to play a statistically significant role in fouling. The results showed that both low ligand density containing jetted and non-jetted resins used at 125 cm/h did not exceed 10% in DBC reduction, and behaved very similarly **(Figure 5-1, Table 5-1)**. Medium and high ligand density containing non-jetted resins generated from 37% to 47% reduction at 50 cm/h and 37 cm/h flow rates, which was generally higher than that for the jetted resins **(Table 5-1)**. The jetted resin produced from 9% to 26% reduction in DBC capacity with the highest one being 48% at 37 cm/h (0.28 mol/L ligand density).

5.2.2. Analytical aggregate detection assay development

In order to confirm that the drop in the dynamic binding capacity was indeed caused by fouling, visual detection techniques had to be employed. A red fluorescent dye Proteostat, which emits light only upon binding to aggregated proteins, was used to develop a novel foulant detection assay. Used and cleaned 1 mL columns were unpacked prior to the Proteostat dye addition and incubation for 20 min **(Figure 5-2)**. The dye-resin sample was then transferred either to a 96-well plate to generate quantitative data or to a miniature flow cell to produce visual information with CLSM.

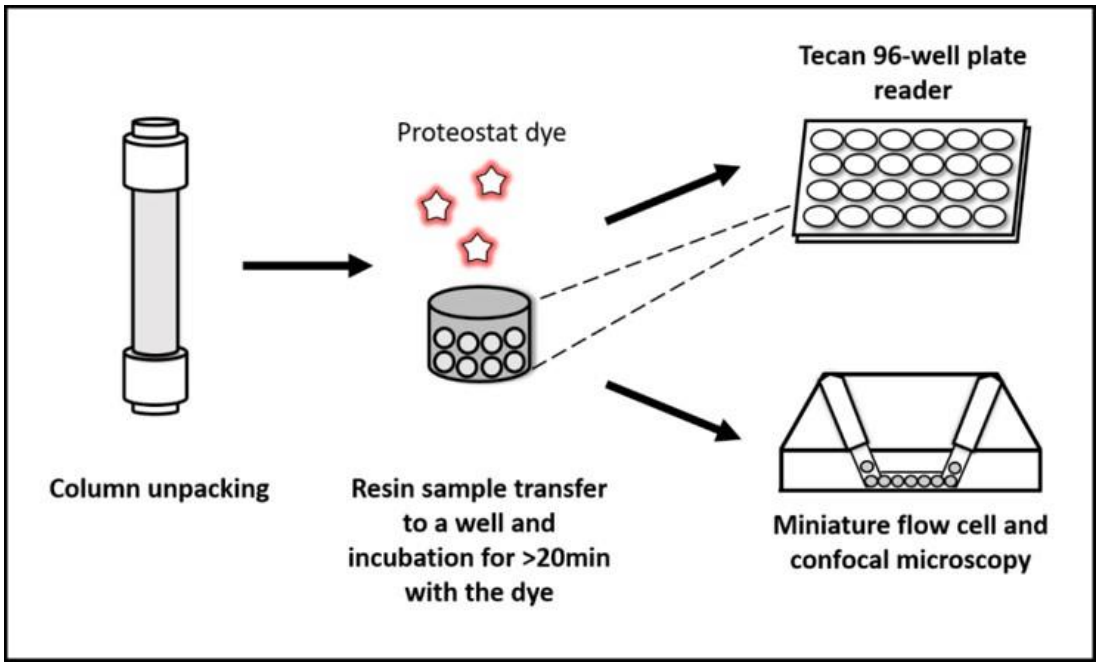

Figure 5-2. Proteostat dye assay.

5.2.2.1. Fluorescent dye interacts with native proteins

Proteostat dye, to our knowledge, has not been combined with chromatography resins or indeed any separation materials, and therefore required a number of controls to be evaluated to ensure resin-dye or monomer-dye interactions would not interfere with the assay. Initial negative controls included fresh resin, fresh BSA and IgG1, bound BSA and IgG1, in addition to positive controls of fresh and bound heat-denatured BSA. Fresh agarose media Praesto Q and SP were shown to lack interactions with the dye leading to basal levels of fluorescence as expected **(Figure 5-3 i)**. In contrast, despite possessing an all α-helix structure (Carter et al., 1989), bound BSA interacted with the dye producing a fluorescent ring pattern **(Figure 5-3 iii)**. Similarly, outer ring patterns were visible for the bound IgG1 control, although more beads displayed fluorescence throughout the core **(Figure 5-3 vi)**. Fluorescence readings for bound BSA and IgG1 were 5 to 6-fold higher than those for the proteins alone **(Figure 5-4)**.

BSA is known to form dimers, trimers, and other oligomers, which are often seen in commercial BSA solutions when analysed on a size exclusion chromatography column (Wen et al., 1996). These protein conformations can cause the dye to bind as it has an affinity for β-sheets that are present in dimers. A recent study with an early prototype Thioflavin T revealed that the dye exhibits a 6-fold higher affinity towards BSA dimers than monomers (Rovnyagina et al., 2018). Conversely, there is evidence to suggest that the dye can bind to specific parts of monomers, non-β-sheet cavities (Groenning et al., 2007a; b; Sen et al., 2009), and therefore fails to distinguish between different protein conformations (Oshinbolu et al., 2018).

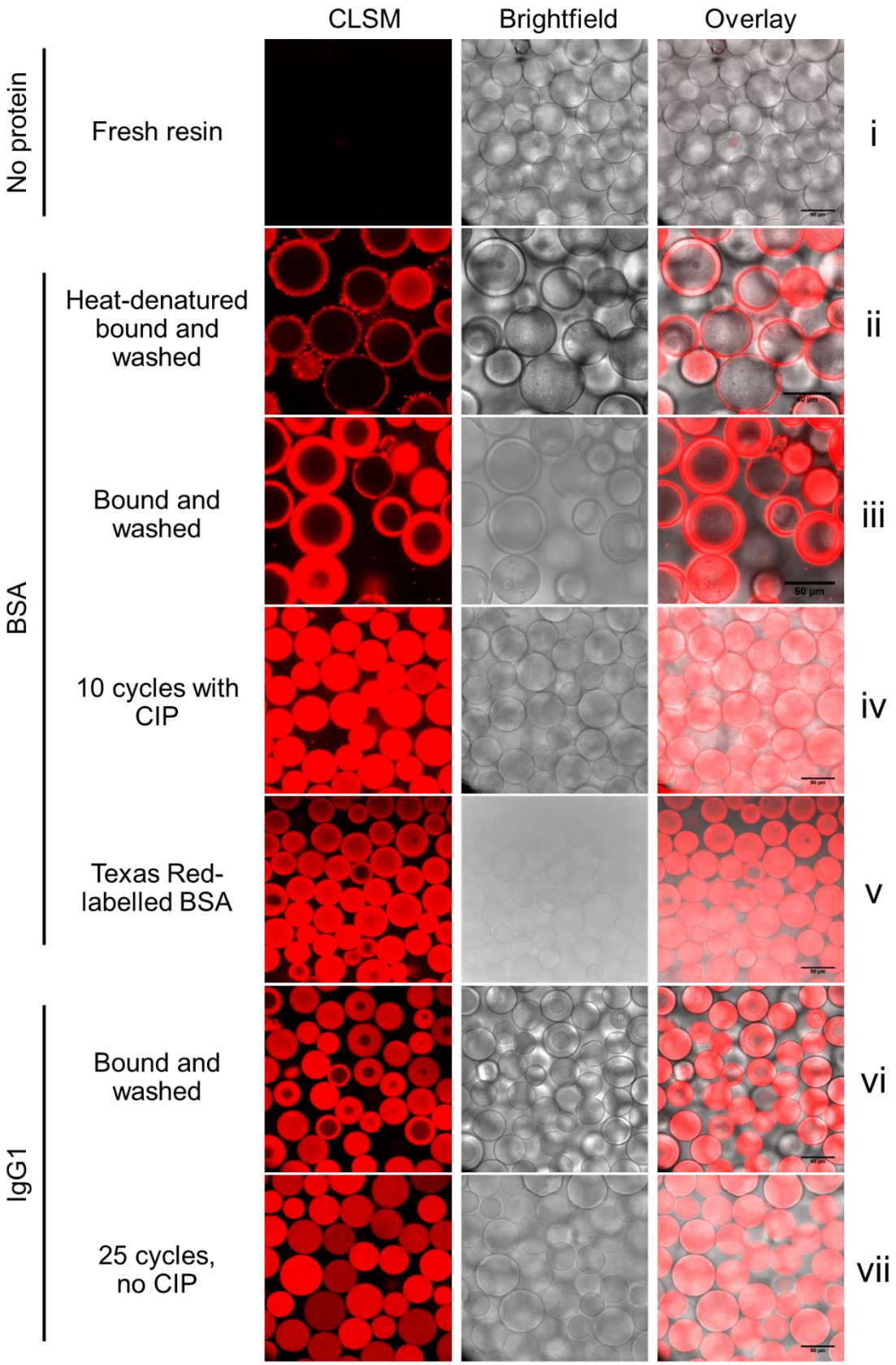

Figure 5-3. Controls for the dye assay using CLSM. CLSM images of fluorescence, transmitted light, and their overlay are presented. At least three images were taken, and one representative example is shown.

Figure 5-3 (continued). Laser intensity was 40%, excitation was 550 nm and emission was 600 nm for all samples. Images (**ii**) and (**iii**) show a smaller section of a larger image for a clearer representation. Samples for images (**ii**), (**iii**) and (**iv**) were obtained using the Proteostat dye, whereas sample (**v**) was imaged live using Texas Red labelled BSA. Heat-denatured sample (**ii**) was produced after heating BSA at 65ºC for 35 min. Equilibration buffer used for samples (**iii**), (**iv**) and (**v**) was 50 mM Tris at pH 8.5, and elution buffer for sample (**iv**) contained additional 1.5 M NaCl followed by a 1 M NaOH clean. Similarly, equilibration buffer for samples (**vi**) and (**vii**) was 10 mM sodium citrate at pH 5, and elution buffer for sample (**vii**) contained 0.5 M NaCl and no CIP.

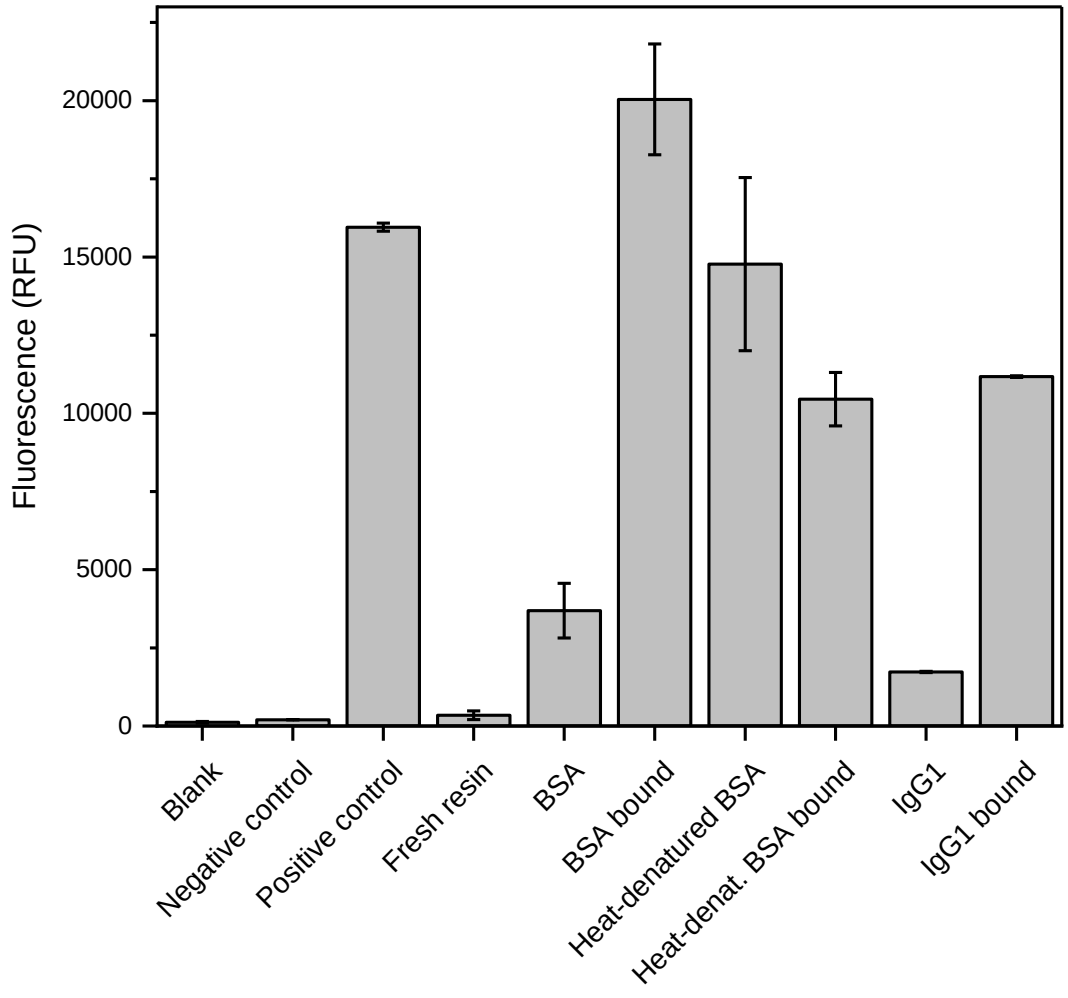

Figure 5-4. Fluorescence intensity readings for controls. Proteostat dye was added to a sample of resin that has been used for 10 cycles with BSA. Excitation wavelength was 550 nm and emission wavelength was 600 nm when using with Tecan 96-well plate reader. Samples were prepared in triplicate; averages with ± 1SD are shown.

To understand which mechanism prevailed in this work, several different approaches were undertaken. Firstly, BSA solution and IgG1 were loaded onto a size exclusion column, whereby chromatograms displayed 10% and 7% HMWS, respectively **(Figure 5-5)**. However, the presence of such interactions was not sufficient to explain the ring pattern seen for both BSA and IgG1 **(Figure 5-3 iii, vi)**, and high fluorescence readings **(Figure 5-4)**.

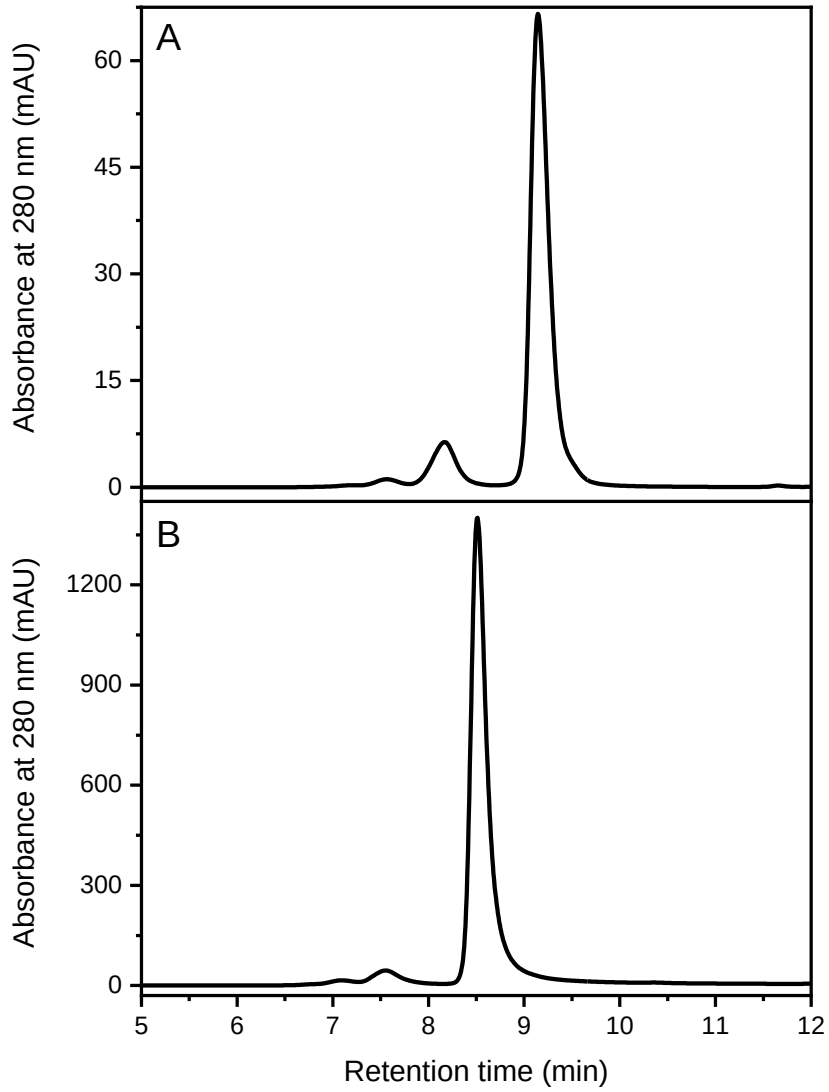

Figure 5-5. Determination of high molecular weight components in the feed with SEC-HPLC. Chromatograms of A – pure lipid-free BSA and B – post-Protein A purified IgG1 showing large main peaks and smaller HMWS. Running buffer made up of 100 mM sodium phosphate and 100 mM sodium chloride at pH 7 was run at 0.1 mL/min through a TSK UP SW3000 column.

Next, it had to be ensured that the ring pattern was not a result of incomplete bead saturation via an implementation of another dye. Texas Red-labelled BSA was mixed with fresh BSA in a 1:100 ratio (Hubbuch and Kula, 2008), and 10 g/L of the mixture was loaded onto the flow cell using the same feed and time conditions as the Proteostat dye experiments. Real time confocal microscopy confirmed a complete bead core saturation with Texas Red-labelled BSA after 30 min **(Figure 5-3 v)**, which equated to 30 mg of material, rejecting the 'incomplete bead saturation' hypothesis, and suggesting that species other than intact monomers were the cause of the ring structure. Another logical reason for ring formation had been suggested to be a large protein size and small resin pores (Matlschweiger et al., 2019). However, here an appropriate resin pore size was selected as live protein uptake as well as static binding capacity results confirmed much higher levels of protein absorption **(Figure 4-5, Chapter 4)**, and therefore could not be used as a hypothesis.

Native protein-dye interactions could be attributed to partial protein unfolding and/or aggregation upon binding to ligands, since the fluorescence readings were significantly higher than those for both non-bound protein solutions **(Figure 5-4)**. Whilst BSA has been shown to exhibit this behaviour only at low pH's of 3.0 to 4.5 (Gospodarek et al., 2014), there has been substantial evidence to support such ligand interactions with antibodies (Gillespie et al., 2012a; Luo et al., 2014; Guo et al., 2014, 2016; Guo and Carta, 2014, 2015). Process conditions such as pH and salt were found cause on-column protein unfolding and aggregation. Such factors may be applicable to the IgG1 used in this study **(Figure 5-3 vi)**, since this particular antibody contained high levels of charge variants. Changes to protein conformation upon binding may be enough to partially block resin pores impairing further protein uptake, thus creating rings of accumulated protein. Alternatively, charge-based structural changes may induce stronger or even irreversible binding to resin. Therefore, the hypothesis was that the Proteostat dye interaction with bound native BSA and IgG1

could be explained as both presence of dimers and conformational changes to the protein structure upon adsorption.

5.2.2.2. Heat-denatured protein blocks bead channels

Heat-denatured BSA and Proteostat dye interaction was anticipated as thermal stress above 65ºC causes a decrease in α-helices while increasing β-sheet formation, resulting in aggregation (Clark et al., 1981). This sample revealed an alternate fluorescence profile, whereby protein was primarily distributed on the surface of the bead with round, aggregate-like structures **(Figure 5-3 ii)** instead of thick rings observed for native BSA **(Figure 5-3 iii)**. These aggregate-like structures may have occluded the resin pores preventing further protein uptake, as observed by limited permeation of the dye. Similar structures, primarily deposited on the resin surface with protruding protein aggregates and interacting with other beads, have also been visualised with scanning electron microscopy (Close et al., 2013; Elich et al., 2016; Pathak et al., 2018). Additionally, fluorescence measurements in a plate reader demonstrated approximately 4-fold higher levels of fluorescence when using heat-denatured instead of native BSA solution, which was comparable to the manufacturer's positive (aggregated lysozyme) control **(Figure 5-4)**. In contrast, the fluorescence intensity for the bound protein was 1.4-fold lower than for the non-bound protein solution. This was possibly a result of heat-denatured protein not being able to move through to the core of the bead and eluting prematurely, as aggregate-like structures blocked the entrance **(Figure 5-3 ii)**.

5.2.2.3. Dye has a high affinity to deliberately fouled resins

Having demonstrated sufficient sensitivity and selectivity from the initial controls, fouled resin samples were prepared. 1 mL columns were packed, and 10 cycles of BSA and 25 cycles of IgG1 were run with loadings of 200 mg and 1 mg per cycle, respectively. Equilibration was performed with 50 mM Tris at pH 8.5, and BSA was eluted with 50 mM Tris, 1.5 M NaCl at pH 4.7 over 15 column volumes followed by a CIP cycle with 10 CV of 1 M NaOH. Equilibration buffer for the IgG1 runs was 10 mM sodium citrate at pH 5, and elution buffer had additional 0.5 M of NaCl. CIP was not performed for the IgG1 cycles as the elution step seemed to sufficiently remove small amounts of bound protein. Following the runs, the columns were unpacked and the fluorescence intensity was measured by applying the dye onto the samples.

Confocal microscopy images revealed that both residual BSA and IgG1 molecules occupied resin following the strip and elution steps, respectively **(Figure 5-3 iv and vii)**. This confirmed that the fluorescent dye had high affinity towards the remaining aggregated proteins inside chromatography beads.

5.2.3. Assay validation: Case 1

5.2.3.1. Strip and CIP steps are crucial in resin regeneration

To further evaluate the selectivity of the dye as well as to understand what caused fouling, effects of different cleaning solutions were investigated. The routine cleaning procedure for an IEX resin consists of a high salt concentration strip followed by a 1M NaOH solution, and therefore variations of this method were selected. Consecutive DBC runs were performed using three different flow rates: 125 cm/h for the first 4 consecutive runs, 50 cm/h for the next three, and 37 cm/h for the final three, followed by a selected cleaning regime after each cycle **(Figure 5-6, Table 2-1 in Chapter 2)**.

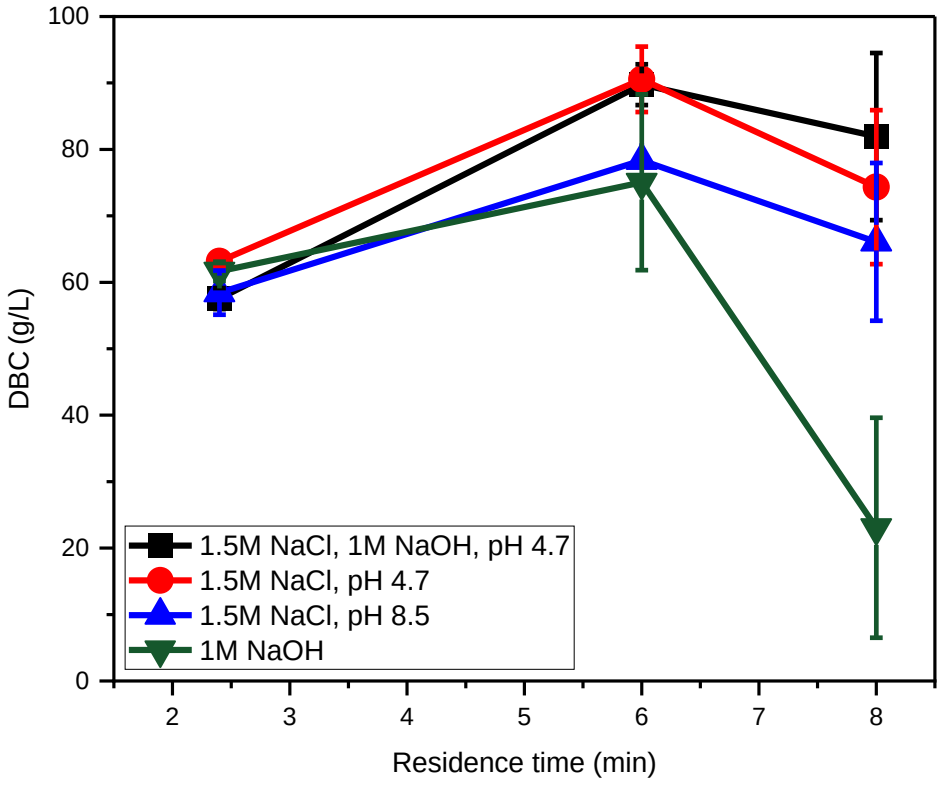

Figure 5-6. Change in DBC with various CIP conditions. DBC after 10 cycles with Q45 resin containing medium ligand density using 200 mg of pure BSA at different flow rates. Four cleaning regimes were chosen: (1) strip with 1.5 M NaCl at pH 4.7 followed by 1 M NaOH CIP; (2) strip with 1.5 M NaCl at pH 4.7, no CIP; (3) strip with 1.5 M NaCl at pH 8.5, no CIP; (4) no strip, only 1 M NaOH CIP. Averages with ± 1SD were calculated for four, three and three consecutive runs. Columns of 5 cm height, 1 mL were used.

After ten DBC runs with fresh BSA, the upper resin fraction in the column (1.7 cm) was collected, and the degree of fluorescence was quantified using a plate reader before visualisation under confocal microscopy. Both techniques revealed that using a cleaning regime consisting exclusively of 1 M NaOH (without a strip step) would result in the highest level of fluorescence up to 29,000 RFU indicating the highest degree of fouling compared to other conditions with 6,000 RFU **(Figure 5-7, Figure 5-8)**. This was also in agreement with a 5-fold reduction in DBC for the 1 M NaOH condition after 10 cycles **(Figure 5-6)**.

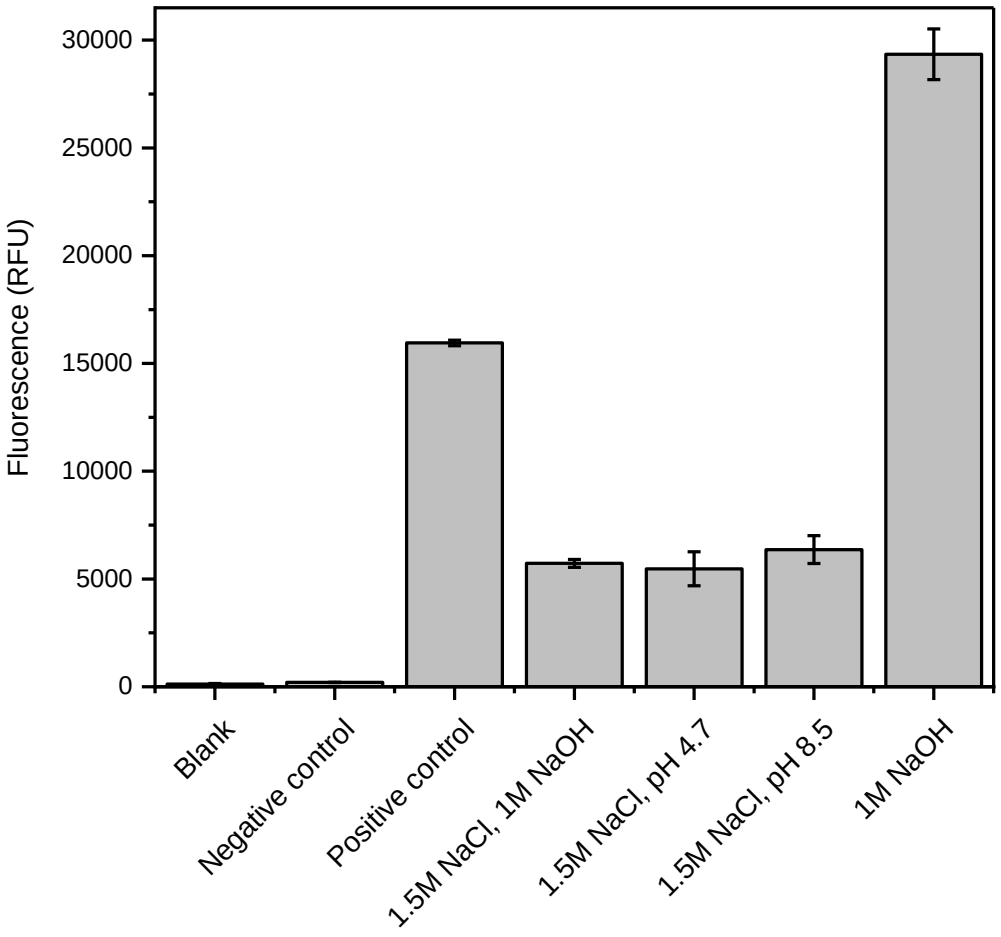

Figure 5-7. Fluorescence measurements for various CIP conditions. Proteostat dye was added to a sample of resin processed over 10 cycles with 200 mg BSA. Blank, negative and positive controls were provided by the manufacturer. Excitation and emission wavelengths were 550 nm and 600 nm, respectively, and used with Tecan 96-well plate reader. Samples prepared in triplicate; averages with ± 1SD are shown.

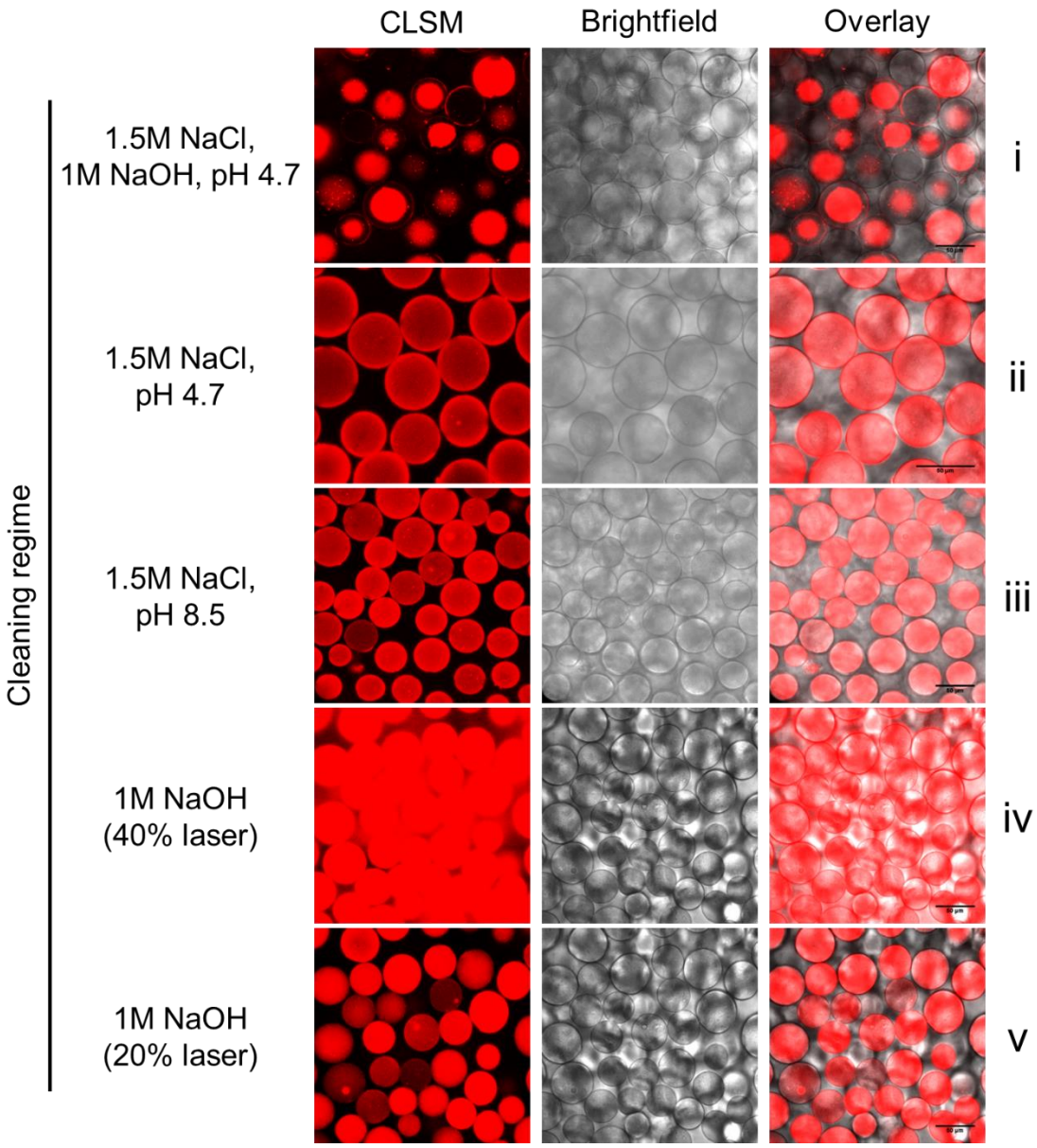

Figure 5-8. CLSM images of resins after exposure to different CIP conditions. Proteostat dye was added to a sample of resin that has been used for 10 cycles with 200 mg BSA, and then imaged with CLSM. Images produced with transmitted light and an overlay of the two are shown for comparison purposes. At least three images were taken and one representative example is shown. CLSM excitation wavelength was 550 nm, emission wavelength was 600 nm, and laser intensity was 40% unless specified otherwise.

The maximum DBC at 10% breakthrough was found to be around 60 g/L, 95 g/L and 98 g/L for 2.4 min, 6 min and 8 min residence time, respectively. Based on the reduction in binding capacity and equivalent increase in total fluorescence, it was estimated that acceptable fluorescence levels would be up to 20,000 RFU, which would equate to 60 g/L DBC. Upon reaching >30,000 RFU (or <40 g/L DBC), the sensitivity of the assay plateaued exceeding its detection limits for high levels of aggregates. Nevertheless, plate reader measurements suggested that strip step was crucial for column CIP, whereas a sodium hydroxide step alone was insufficient, and led to a dramatic loss in binding capacity. These results support previous findings, whereby both NaOH and NaCl were required to provide appropriate clearance of host cell impurities (Siu et al., 2006, 2007).

Quantitative fluorescence measurements indicated no significant differences amongst the three salt buffer conditions **(Figure 5-7)**, whereas confocal microscopy revealed variation in fluorescence amongst individual beads **(Figure 5-8)**. This was particularly visible in images **(i)** and **(ii)**, where not all beads were uniformly fluorescent. Image **(i)** revealed uneven foulant accumulation inside and outside of the bead core, whilst images **(ii)** and **(iii)** showed homogenous foulant distribution. In addition, images **(iv)** and **(v)** were taken of the same sample but imaged under different laser intensities: 40 and 20 per cent, respectively, but showed a heterogeneous foulant distribution pattern. High levels of protein aggregation caused by a 1 M NaOH clean were expected to affect more or less all beads equally; however, numerous beads exhibited very low levels of fluorescence at 20% laser intensity **(Figure 5-8 v)**. I hypothesized that this could be a result of the sampling of a mixed population of beads from the column, which would contain populations from both axial and radial dimensions within the column.

5.2.3.2. Fouling heterogeneity is present at column level

Data from initial fouling experiments revealed a non-uniform fluorescence pattern amongst the beads requiring further studies to identify the cause of these variations. It was hypothesised that this variation could have been a result of bead positioning in the column (Zhang et al., 2016b; a). Logically, the upper part of the column, which is subject to exposure to the highest protein loading, would contain the most extensive levels of residual aggregated protein when compared to the lower end of the column. Therefore, the columns were dissected into five parts: top filter, top, middle, bottom, and bottom filter, following DBC runs with one cleaning regime: 15 CV gradient strip with 50 mM Tris, 1.5 M NaCl at pH 8.5, and 10 CV CIP with 1 M NaOH plus 30 min hold **(Figure 5-9)**. Additional IgG1 fouling runs were then performed: 1 mg of IgG1 was loaded for each cycle followed by a 30 CV gradient elution with 10 mM citrate, 0.5 M NaCl, pH 5, and no CIP **(Table 2-1 e, Chapter 2)**.

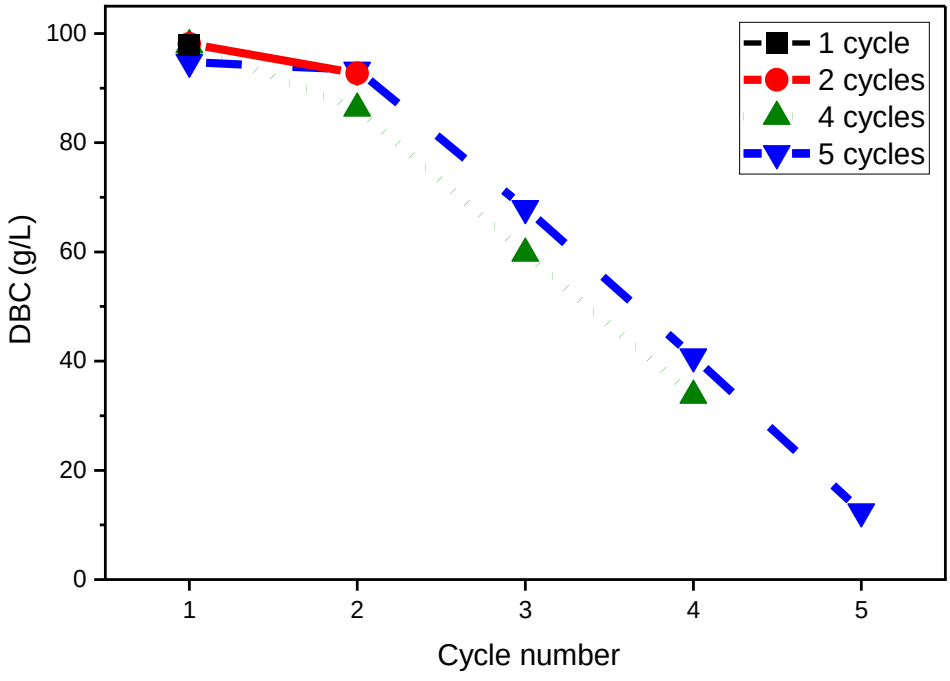

Figure 5-9. Column fouling patterns over 5 chromatography cycles. DBC runs at 10% breakthrough were performed at 50 cm/h with 200 mg of BSA per cycle. Strip involved a high molarity salt buffer, whilst CIP had 1 M NaOH with 30 min hold. Resin was separated into sections such as top, middle, bottom, etc., after each number of cycles (i.e., 1, 2, 4 and 5) to be stained with the Proteostat dye.

The amount of residual aggregated protein was found to increase with cycle number as seen from the decline in DBC and an increase in fluorescence intensity **(Figure 5-9, Figure 5-10)**. The chosen experimental flow rate of 50 cm/h, which was equal to 6 minutes of residence time, and high BSA load of 200 mg provided maximum bead saturation resulting in severe levels of fouling. Due to the long residence time, dynamic binding capacity dropped from 100 g/L to a mere 10 g/L only after five chromatography cycles **(Figure 5-9)**. Whilst this was not representative of a typical number of chromatography cycles, the dye was sensitive enough to differentiate between severe fouling conditions, and thus would be suitable for less pronounced cases. In contrast, experiments run at a higher flow rate of 125 cm/h (providing 2.4 minutes of residence time) resulted in no decrease in DBC, and undetectable fluorescence under confocal microscopy after 15 cycles (results not shown). Consequently, due to time constraints, the latter experimental conditions were discontinued, and the more extreme fouling case was studied as a proof of concept.

Fouling was found to begin in the upper part of the column and continue through to the lower part as the number of cycles increased **(Figure 5-10, Figure 5-11)**. The most upper part of the column exhibited highest fluorescence intensity of 900 RFU during the first cycle followed by a gradual increase in fluorescence of up to 7,900 RFU over the following 2-4 cycles. It culminated with the lowest filter section being still reasonably foulant-free after the final 5^{th} cycle with only 5,000 RFU **(Figure 5-10)**. Fluorescence data from plate reader measurements and confocal microscopy were concordant with the overall DBC calculations, whereby reduction in capacity was representative of the residual protein accumulation in the upper parts of the column.

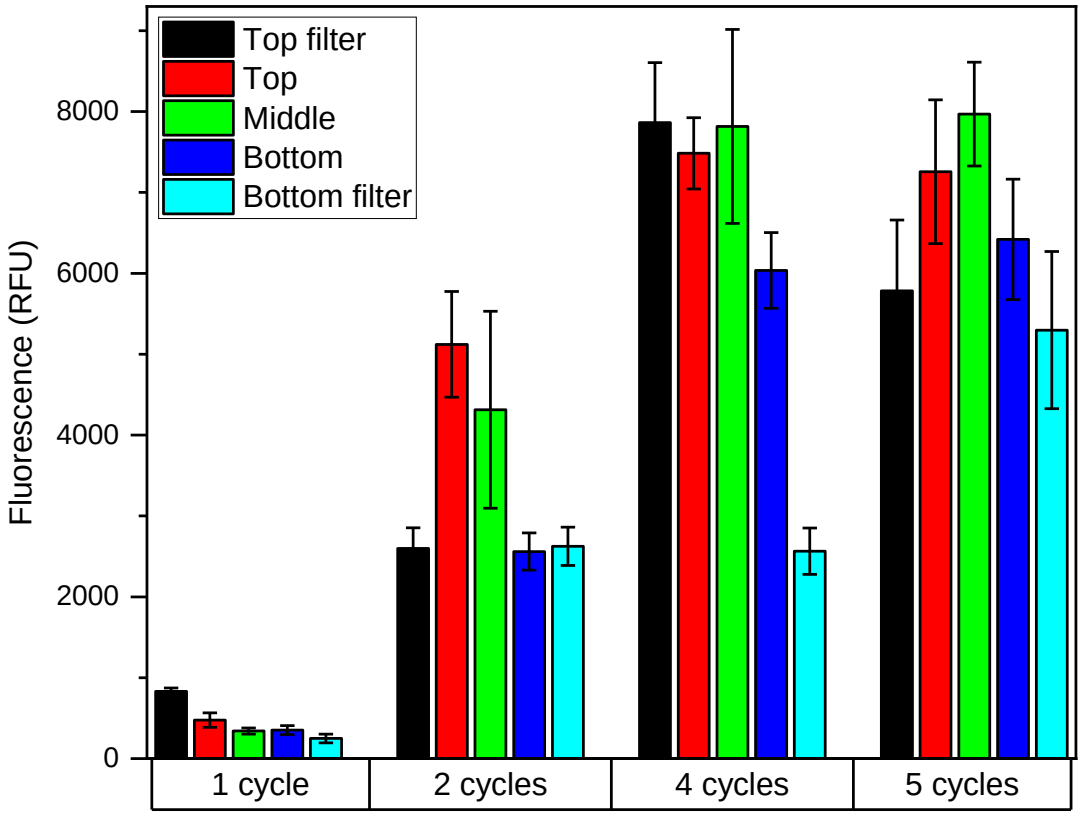

Figure 5-10. Fluorescence intensity measurements of columns after cycles 1-5. Once DBC runs with BSA were performed and resin was separated into sections such as top, middle, bottom, etc., after each number of cycles (i.e., 1, 2, 4 and 5), it was subjected to an incubation with the Proteostat dye for 20 min. The samples were then quantified using a 96-well plate Tecan reader: Excitation wavelength was 550 nm, emission wavelength was 600 nm. Samples were prepared in triplicate, and averages with ± 1SD are shown. Columns of 5 cm height, 1 mL were used. “Top filter” and “bottom filter” reflected 0.2 cm height, whilst “top”, “middle” and “bottom” each had 1.5 cm height.

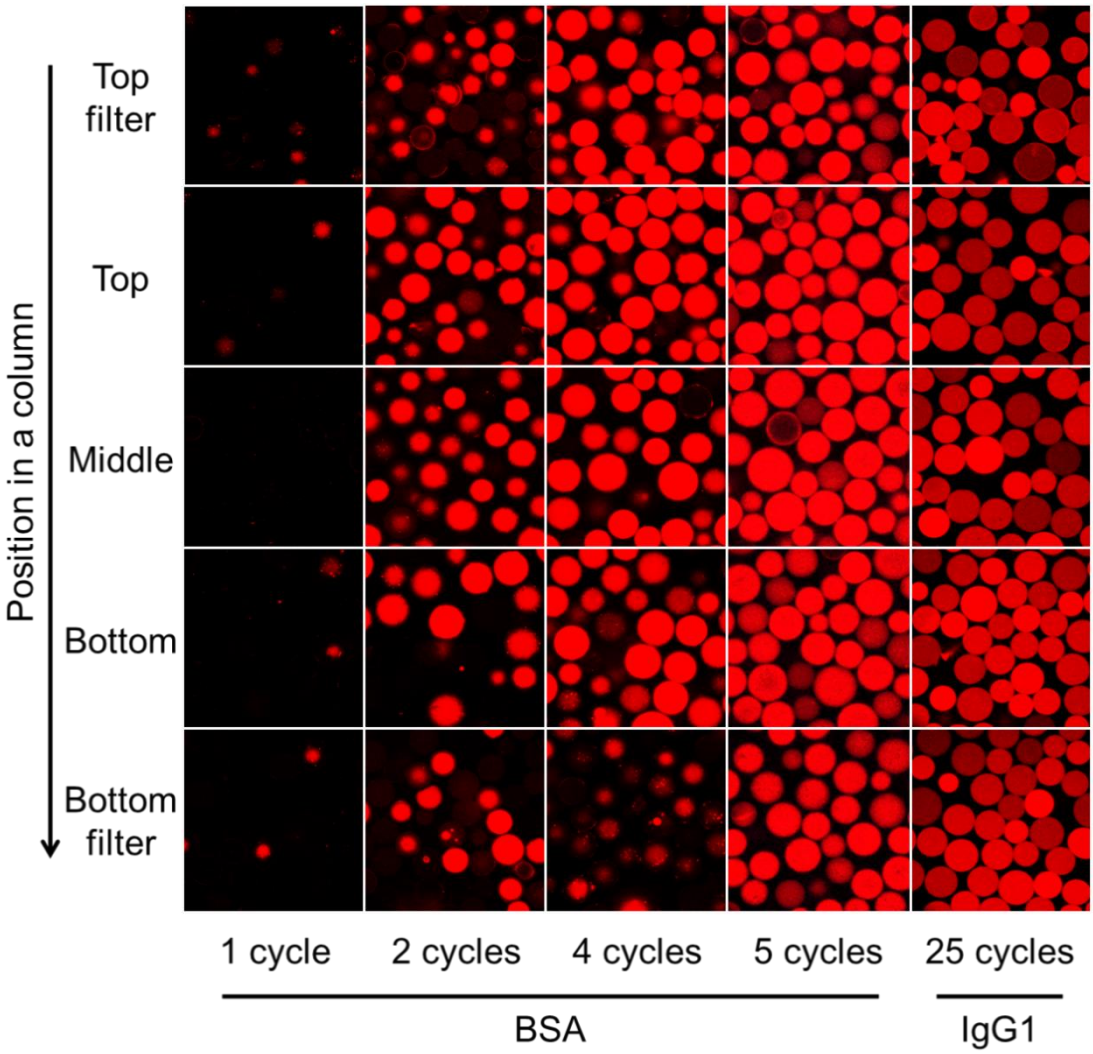

Figure 5-11. CLSM images of column sections after exposure to an increasing number of cycles. CLSM of fluorescence, transmitted light and their overlay are presented. At least three images were taken of top filter (0.2 cm), top (1.5 cm), middle (1.5 cm), bottom (1.5 cm) and bottom filter (0.2 cm) parts of the column and one representative example is shown. CLSM laser intensity was 40%, excitation wavelength was 550 nm and emission wavelength was 600 nm.

The fouling pattern seen for the IgG1 cycles was similar to that seen for the experiments with BSA. The aggregate concentration was similar throughout the different parts of the column, where the overall fluorescence intensity was reasonably low and comparable to that of BSA after 2 cycles **(Figure 5-11, Figure 5-12)**. The fluorescence may have been reduced or eliminated if additional CIP cycles had been performed, which has been shown to improve resin recovery (Siu et al., 2006). Furthermore, there was a clear sample heterogeneity that can be attributed to the spatial bead location and flow properties in that particular sample (Close et al., 2013; Corbett et al., 2013; Zhang et al., 2016b). The hypothesis that small resin beads were fouled first was rejected because the fluorescence was comparable for larger resin beads **(Figure 5-11)**. In addition, residual protein was distributed throughout the entire column length, which can be expected due to a high number of cycles. Nevertheless, no particular areas were found to be affected by round aggregate formation apart from the evidence of bead-to-bead contact once the laser intensity was reduced to 20% for IgG1 samples. This is in contrast to the 'spotting' pattern in BSA samples seen after 2 cycles throughout the whole column **(Figure 5-11)**. Such behaviour indicated that sodium hydroxide caused BSA proteins to form lumps, which then obstructed smaller pores.

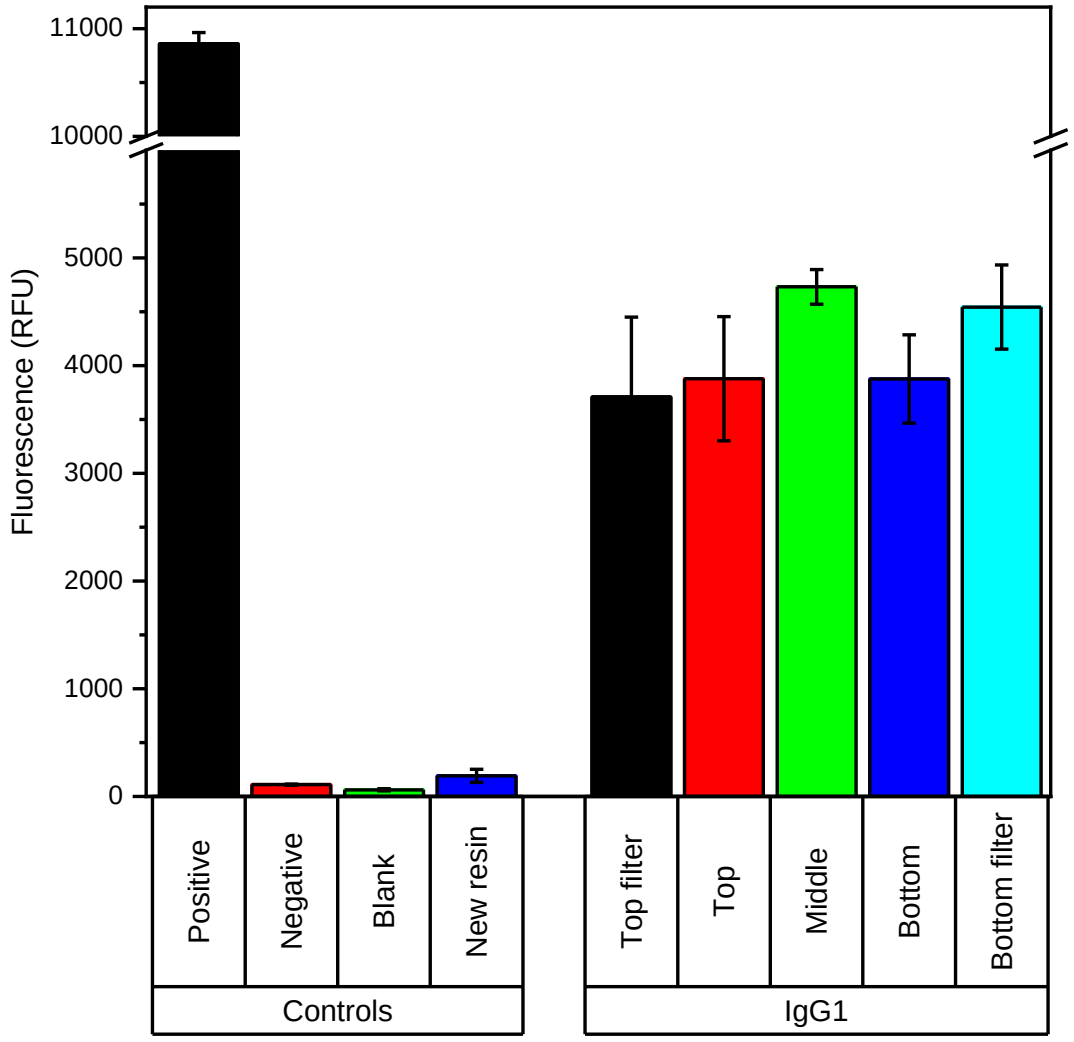

Figure 5-12. Fluorescence intensity measurements of controls and different column sections with IgG1. DBC runs at 10% breakthrough were performed at 50 cm/h with 25 mg of IgG1 per cycle, without a CIP step, only a strip. After 25 cycles resin was separated into sections such as top, middle, bottom, etc., and was subjected to incubation with the Proteostat dye for 20 min. The samples were quantified using a 96-well plate Tecan reader: Excitation wavelength was 550 nm, emission wavelength was 600 nm. Samples were prepared in triplicate, and averages with ± 1SD are shown. Columns of 5 cm height, 1 mL were used. “Top filter” and “bottom filter” reflected 0.2 cm height, whilst “top”, “middle” and “bottom” each had 1.5 cm height. The same controls were used for BSA samples in **Figure 5-9**. Controls: positive, negative and blank were provided by the manufacturer.

5.2.3.3. Fouling heterogeneity is present at bead level

Whilst the dye assay demonstrated an application for resin lifetime studies, it has also revealed a high sensitivity towards spatial foulant distribution patterns at a bead level. Protein deposits were identified in different parts of the bead: surface **(Figure 5-13 i, ii)**, core **(iii)** and intraparticle voids **(iv, v)**.

Two foulant arrangements were identified on bead surfaces using the dye assay **(Figure 5-13 i**, **ii)**. Firstly, foulants were primarily deposited on the surface of the beads forming large interacting structures that caused pore blockage and reduced the rate of protein uptake **(Figure 5-13 i)**, an observation which has been noted in other reports (Close et al., 2013; Corbett et al., 2013; Zhang et al., 2016a; b; Lintern et al., 2016; Pathak and Rathore, 2016). Moreover, fluorescence patterns were comparable to the heat-denatured BSA control **(Figure 5-3 ii)** further supporting the dye's selectivity for the aggregates. Secondly, gaps in bead surface fluorescence were detected **(Figure 5-13 ii)**, which were indicative of particle-particle contact in a packed column resulting in uneven protein uptake (Hubbuch et al., 2002; Close et al., 2013; Corbett et al., 2013; Siu et al., 2007). Residual surface protein build-up was shown to be dependent on the spatial hierarchy in the column and proximity to other beads.

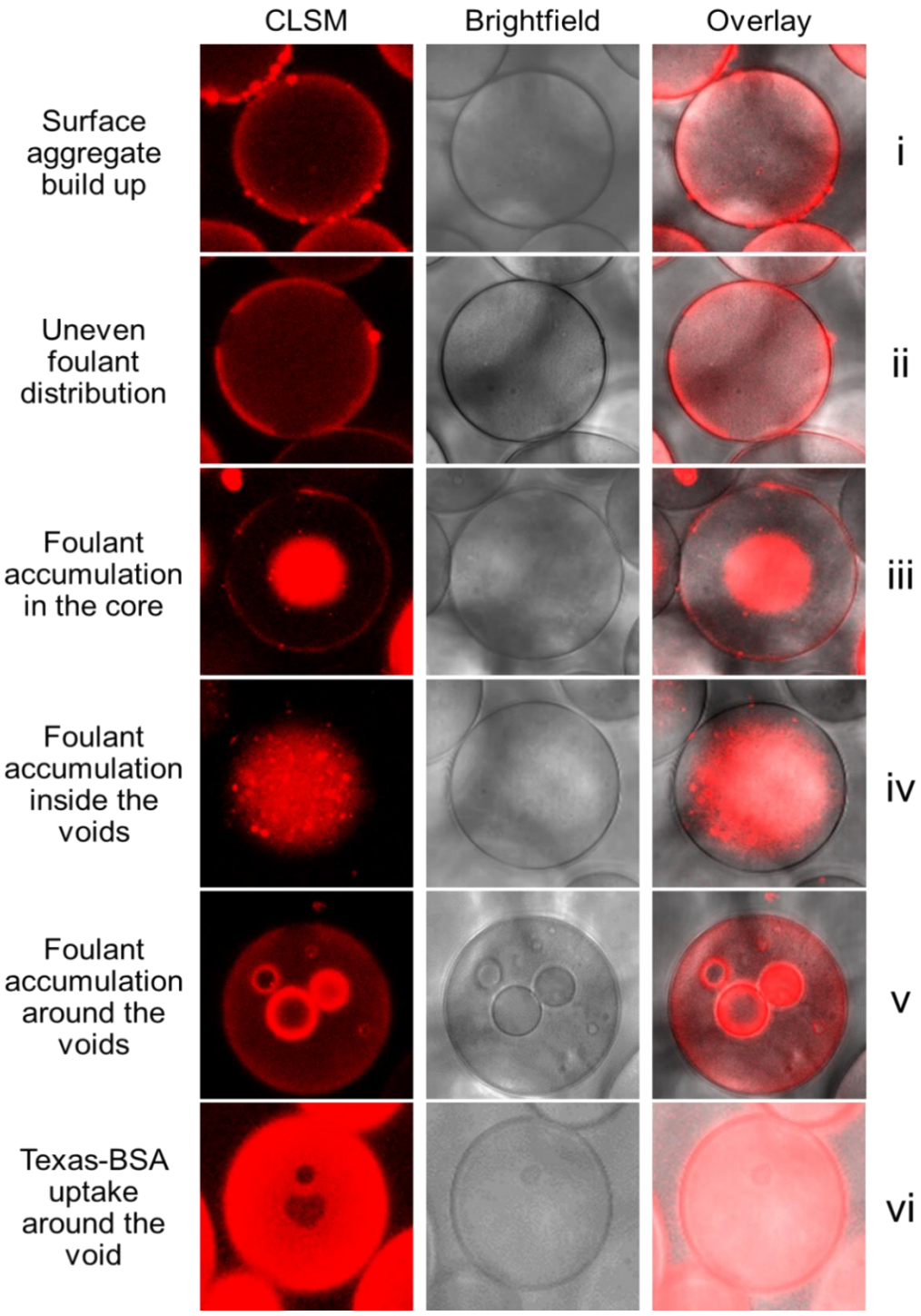

Figure 5-13. Fouling heterogeneity at bead level. CLSM images of fluorescence, transmitted light and their overlay are presented. At least three images were taken and one representative example is shown. Images (i)–(v) were generated using different cleaning conditions and taken from different locations in the column. Image (vi) was generated using Texas Red-labelled BSA in a flow cell during a real time loading step. Laser intensity was 40%, excitation wavelength was 550 nm and emission wavelength was 600 nm.

An overlay of CLSM and transmitted light displayed a fluorescent bead core and a 'halo' surface lining **(Figure 5-13 iii)**. Residual aggregated proteins may have primarily collected in the core rather than the surface, which was much more accessible to the flow of cleaning reagents (Zhang et al., 2016b). Providing chromatography columns are saturated to <70% instead of 100% as in this study, the effect to the core may not be as significant. This is especially true for biologics capture steps using Protein A resin at high linear velocity and short residence time, as proteins may not have sufficient time to utilise the full volume of the bead (Hahn et al., 2003, 2005). Otherwise, consecutive rounds of hold and wash cycles using 1 M NaOH could provide a more effective clean that would allow to reach the centre of the bead once each layer of residual protein had been washed off.

Another area of significant aggregate deposition was observed inside and around the intra-particle voids **(Figure 5-13 iv, v)**. These voids were detected by transmitted light and confocal microscopy, and previously by SEM, TEM, and X-ray computed tomography (Angelo et al., 2013, 2016; Johnson et al., 2018). Whilst the intra-particle voids did not facilitate protein uptake during the loading step **(Figure 5-13 vi)**, they had a distinct affinity towards the fluorescent dye suggesting high aggregate presence **(Figure 5-13 iv, v)**. Despite having minimal role in protein uptake, the voids proved to be highly fluorescent during the elution step as discussed by (Angelo et al., 2016). It was hypothesized that particularly low ligand density in the voids and surrounding narrow channels played a role in both binding and elution steps. I support this hypothesis, as such large empty spaces can act as isolated entities by either having very few or no connections to other channels. Consequently, the flow to and from the voids would be limited leading to uneven or poor diffusion resulting in increased amount of foulant build up. Although voids on the surface of the bead were more accessible to the flow, cleaning reagents were ineffective for both types of voids: present inside and outside of the beads **(Figure 5-13 iv, v)**.

These results demonstrate that contrary to prevailing understanding, voids can play a significant role in a chromatography process (Angelo et al., 2013, 2016). Such intra-particle structures often form during the bead emulsification process, and are a result of oil-in-water-in-oil double emulsions (Garti and Bisperink, 1998). Agarose droplets (water phase) are formed with the help of surfactants (oil phase), which can get trapped inside the agarose droplets causing the appearance of intra-particle inclusions. An increase in intra-particle inclusion formation could alter the effective protein binding area resulting in reduced dynamic binding capacity. In addition, the inclusions could lead to an increase in residual protein accumulation, as it could not be removed using traditional cleaning reagents due to spatial channel constraints. Similar hypotheses have been presented, whereby small intra-particle granules were thought to hinder access to other channels and ligands (Lintern et al., 2016; Pathak and Rathore, 2016). Nevertheless, the process of intra-particle void formation can be controlled by reducing the stirrer speed and slowing down agarose addition into the oil phase (Okushima et al., 2004; Nisisako et al., 2005). The introduced changes could potentially eliminate this type of fouling phenomenon.

5.2.4. Assay validation: Case 2

Fluorescent dye assay was used to confirm whether the drop in DBC for Q45 jetted, Q45, Q65 and Q90 resins with varying ligand densities seen in **Figure 5-1** was in fact caused by the accumulation of aggregated remaining protein.

5.2.4.1. High ligand density causes more fouling

The results showed that particle fluorescence increased with increasing ligand density for all resins **(Figure 5-14, Figure 5-15)**. Any level of fluorescence whether low or high indicated some degree of remaining bound protein, which could not be removed with strip and CIP cycles. Resins containing the lowest ligand density produced no fluorescence meaning that no remaining protein after being exposed to 10 chromatography cycles could be detected **(Figure 5-14)**. Particles with medium and high ligand densities were mostly fully fluorescent suggesting that there was a lot of residual protein which could not be removed with current cleaning procedures. These results agree with the DBC reduction patterns seen at higher ligand densities **(Figure 4-1, Chapter 4)**. Consequently, the remaining aggregated protein in the particles proved that the reduction in DBC during the resin lifetime study **(Figure 5-1)** was caused by increasing levels of biological foulants.

5.2.4.2. Larger particles retain more proteins

As speculated previously, particles of larger size were found to be more affected by fouling compared to the smaller ones. Q90 resins containing both medium and high ligand densities were strongly fluorescent after only 5 chromatography cycles **(Figure 5-15B)**. In contrast, Q65 resins were less affected after the same number of cycles: Medium ligand density resin was only slightly fluorescent, whilst high ligand density had a slightly broader variation in fluorescence **(Figure 5-15A)**.

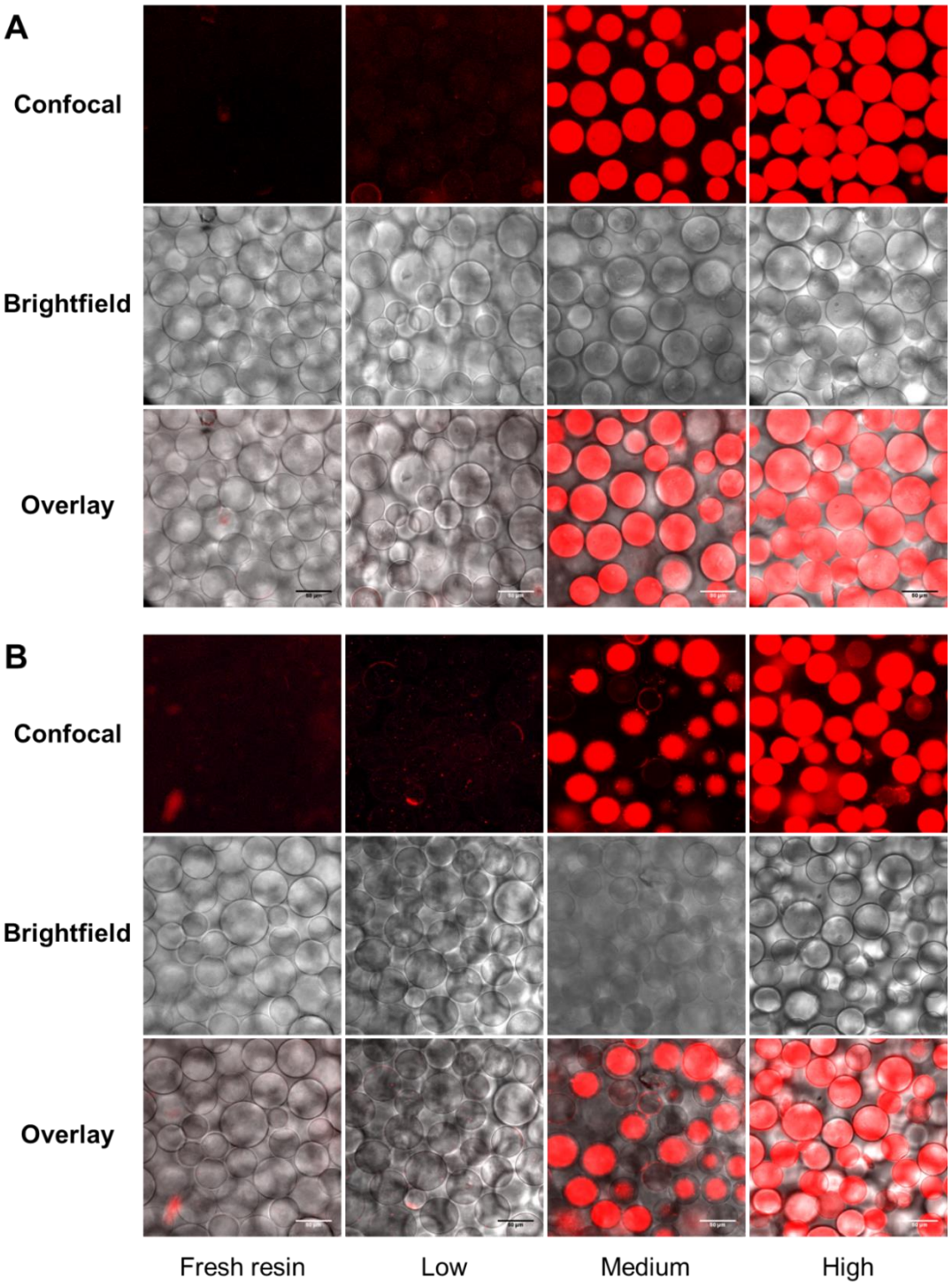

Figure 5-14. Detection of remaining aggregated BSA after 10 chromatography cycles. A – Q45 non-jetted and B – Q45 jetted resins with low, medium and high ligand densities were imaged under CLSM after the Proteostat dye application. CIP was performed after each chromatography cycle using 1 M NaOH for 30 min including the final cycle 10. Fresh resin was a negative control with no protein. Excitation and emission wavelengths were 550 and 600 nm, respectively. Other microscopy parameters: 40x magnification lens with oil immersion, 40% laser intensity and 1024x1024 image resolution.

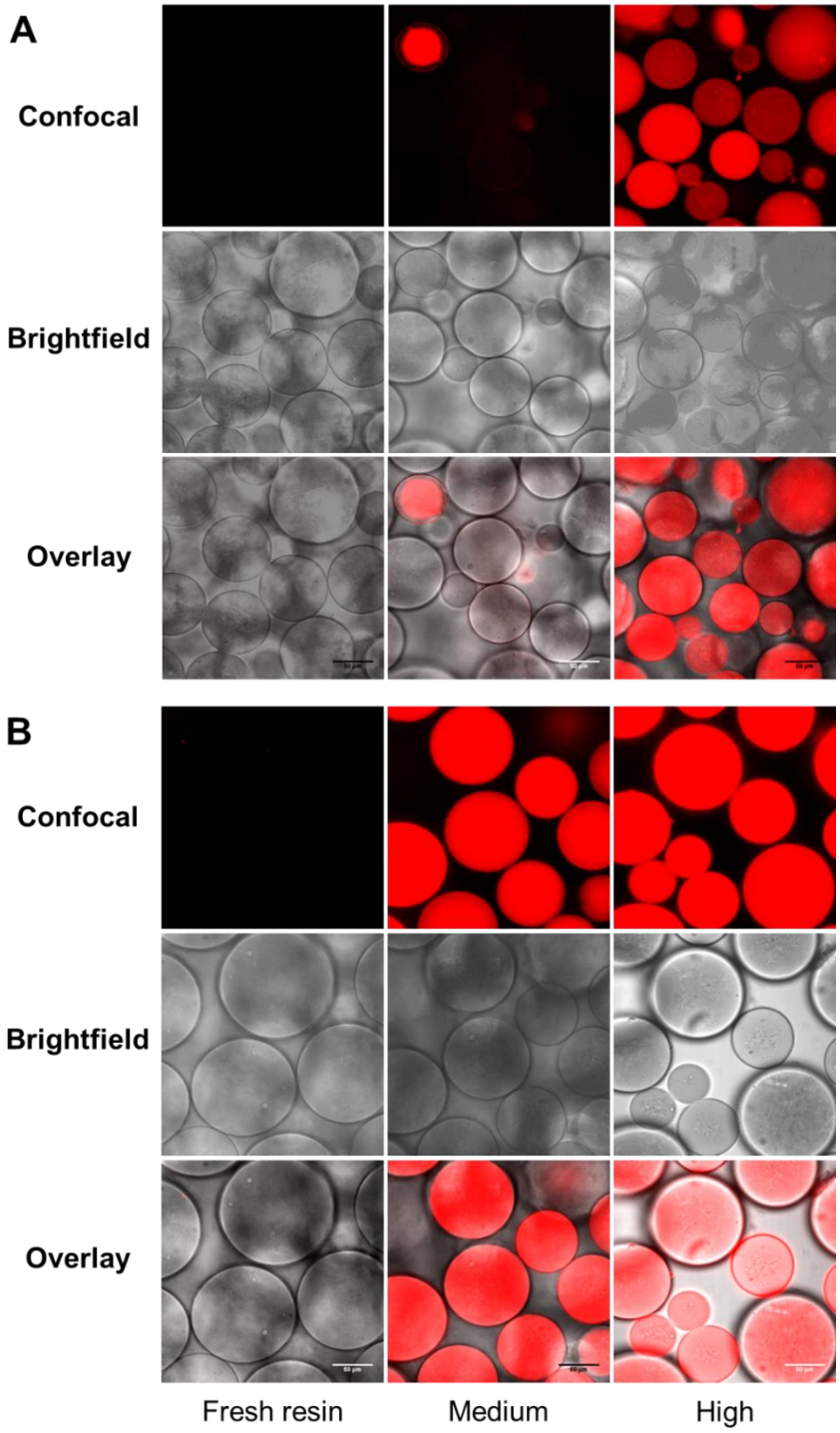

Figure 5-15. Detection of remaining aggregated BSA after 5 chromatography cycles. A – Q65 and B – Q90 resins with medium and high ligand densities were imaged under CLSM after the Proteostat dye application. CIP was performed after each chromatography cycle using 1 M NaOH for 30 min including the final cycle 5. Fresh resin was a negative control with no protein. Excitation and emission wavelengths were 550 and 600 nm, respectively. Other microscopy parameters: 40x magnification lens with oil immersion, 40% laser intensity and 1024x1024 image resolution.

The differences between the two resins Q90 and Q65 may have arisen due to variation in immediate pore accessibility. The distance that the cleaning reagent had to travel to access the core of the bead was shorter for the smaller particles than the larger ones, and was reached quicker within the same time frame. Equally, the same principle would apply for the protein exit, whereby it would be removed quicker from the smaller beads. The theory would only work if the residence time was above 6 minutes so that the particles would have reached near equilibrium saturation. Foulant accumulation was shown to be concentrated in the core of the particles, and would thus require additional rounds of CIP to reach it, thereby proving the importance of particle size **(Figure 5-14)**.

5.2.4.3. Narrow PSD has a potential to reduce fouling

In regards to the particle size distribution and foulant accumulation for the Q45 jetted and non-jetted resins, only small differences could be observed. Medium ligand density containing jetted Q45 resin showed a smaller number of fully fluorescent particles compared to the non-jetted resin **(Figure 5-14)**. This is in agreement with the resin lifetime study in which medium ligand density containing jetted resin had a lower reduction in DBC of up to 30% compared to the non-jetted resin of up to 50% **(Figure 4-1, Chapter 4)**. It, therefore, provides evidence that this resin could be slightly more robust than the medium of the non-jetted resin. However, both low and high ligand density containing jetted and non-jetted resins showed the same patterns: either none or very high levels of fluorescence **(Figure 5-14)**.

5.3. Conclusions

Resin reuse over consecutive chromatography cycles resulted in a reduction in DBC, which was hypothesised to be a cause of residual protein accumulation inside the columns. With the aid of the Proteostat dye and confocal laser scanning microscopy, not only was the hypothesis confirmed, but it also unveiled a number of additional fouling patterns and their causes.

- Fouling patterns were found to be non-uniform across the entire column length, whereby the upper part of the column was most affected as it was in constant contact with the load material.
- Differences across the bead populations were specific to radial sections, possibly due to variation in liquid flow and access to the bead.
- The assay provided evidence to support the concept of changes in protein conformation due to protein-ligand interaction, as the outer bead areas were particularly fluorescent.
- Different cleaning reagents had varying modes of interaction with the bound protein proving that a salt strip was key in the resin regeneration process.
- Resin lifetime was influenced by flow rate: Low flow rate (or long residence time) caused an increase in fouling, whereas high flow rate resulted in minor changes to DBC.
- The extent of fouling was influenced by structural features of the resin including bead size, presence of voids and ligand density.
    - Smaller particle size improved resins' lifetime, whilst the use of larger particles caused earlier deterioration of dynamic binding capacity and higher fluorescence levels.
    - Possession of multiple voids and dead-end channels resulted in higher amounts of residual protein due to obstructed protein and liquid accessibility and manoeuvrability throughout.

- Resins with high ligand density were the first ones to reach the highest loss in DBC, which was linked to an increase in aggregated protein accumulation inside the particles.

6. Chapter: Resin resolution capabilities

The quality of the purified biopharmaceutical product is judged by its structural and functional characteristics as well as impurity profiles and stability. Product- or process-derived effects on quality attributes can lead to changes in pharmacokinetics and pharmacodynamics of the drug product as well as immunogenicity, often stalling product submission and approval or batch release. Here, the effects of process conditions such as resin ligand density and buffer pH on purity and stability of the three different products including ovalbumin, IgG1 and IgG4 were studied. AEX and CEX resins of 45 µm with ligand densities ranging from 0.05 to 0.28 mol/L were developed. Eluates were evaluated for changes in their higher order structure including aggregates, isoforms and degradation profile under thermal stress. High ligand density of >0.20 mol/L was found to be effective in improving ovalbumin isoform separation, whilst lower ligand density of <0.10 mol/L was deemed more practical for both immunoglobulins. Ligand densities above the threshold caused particular instability for the IgG4 molecule resulting in aggregate formation-induced peak splitting, and 60% loss in product recovery. These effects were exaggerated further with the reduction in buffer pH from 5.5 to 4.5. Increased ligand density provided an increased number of protein-ligand interaction points allowing for a stronger connection compared to the lower ligand density resins. In turn, it led to in-column unfolding and irreversible aggregation detected with the Proteostat dye. IgG1 was found to be more thermally and chemically stable than IgG4 as its high pI provided supportive intermolecular repulsions at reduced buffer pH resulting in high step yield of ≥80%. The effect of ligand density and buffer pH on product recovery, purity and stability were heavily dependent on the chosen molecule, and should be carefully optimised for unstable products.

6.1. Introduction

Effective protein separation from its conformation or charge variants is of high importance for the intermediate and polishing steps of process chromatography. The key determinants of that step's success are the compositions of stationary and mobile phases. The pI and stability of the protein determine operating buffer pH range and any excipients needed to prevent aggregation and other non-specific interactions with columns or membranes. The selection of resins is based on their particle and pore sizes, base matrix and ligand type whilst often overlooking the effects of ligand density.

Ligand density is an important factor that determines peak resolution. High ligand density has been found to improve peak separation efficiency when compared to lower ligand densities tested (Kopaciewicz et al., 1985; Wu and Walters, 1992; DePhillips and Lenhoff, 2001; Pessela et al., 2004; Huang et al., 2006, 2010; Dismer and Hubbuch, 2010; Fogle et al., 2012; Lang et al., 2015). This effect has been suggested to arise from a more diverse and, in some instances, stronger multi-point attachment enabled between the protein and the high amount of available ligand. In order to disrupt the stronger connections, higher ionic strength is required, whilst weaker bonds could be easily disturbed with lower ionic strength buffers, thereby providing specific elution times for different species.

The effects of stronger protein-ligand interactions can also result in undesirable protein conformational changes. Unfolding followed by irreversible aggregate formation of various proteins including monoclonal antibodies have been observed due to protein-resin surface contact (Huang et al., 2006; McCue et al., 2009; Huang et al., 2010; Gillespie et al., 2012a; Guo and Carta, 2015; Chen et al., 2016; Guo et al., 2016; Farys et al., 2018). In some cases, it manifested as peak splitting with higher molecular weight formation and a reduction in product recovery. The appearance of

the split peak was also found to escalate due to the use of acidic buffers (Gillespie et al., 2012a; Guo et al., 2014; Guo and Carta, 2015). Low pH tends to facilitate solvent exposure to previously hidden amino acids resulting in weaker intermolecular repulsion and thus increased aggregation (Guo and Carta, 2015). However, occasionally both eluting peaks can be comprised of entirely monomeric species and are believed to form as a result of weak and strong binding sites on the resin that possess fast and slow binding kinetics (Guo et al., 2016).

The extent of the ligand density and buffer pH effect depends on protein net charge and its structural features. Some monoclonal antibodies such as IgG4 are known to be vulnerable to aggregation, whilst others such as IgG1 are prone to fragmentation at acidic pH levels (<5.0) due to differences in their CH2 domain and hinge region length (Garber and Demarest, 2007; Ishikawa et al., 2010; Ito and Tsumoto, 2013; Tian et al., 2014; Skamris et al., 2016). Glycosylation was also found to play an important role in protection against resin surface-induced aggregation (Gillespie et al., 2012a). In addition, charge variants possessing a different apparent pI that arises from various post-translational modifications and degradation events can lead to the split peak phenomenon (Luo et al., 2015).

Considering that protein-ligand interaction has a significant impact on numerous factors in bioprocessing, it is of interest to study whether product quality, e.g. stability and presence of HMWs, can be improved by altering the binding strength to the resin by changing to the amount of ligand density available.

Aim

To understand what effect ligand density has on product purity and stability.

Objectives

- Employ a model protein, ovalbumin, in order to separate its isoforms using jetted and batch-emulsified AEX resins with three ligand densities (0.08-0.28 mol/L).
- Use a solution consisting of two monoclonal antibodies, IgG1 and IgG4, as a model representing a product of interest and an impurity with jetted CEX resins with five ligand densities (0.05 – 0.15 mol/L) within buffer pH range of 5.5 – 4.5.
- Compare IgG1 and IgG4 separation by visually evaluating peak shape, calculating recovery, detecting fouling with Proteostat dye, measuring conformational changes with analytical SEC and CEX, and stability under thermal stress.
- Investigate additional means such as buffer components and additives in order to further increase step yield and protein stability.

6.2. Results and Discussion

6.2.1. Ovalbumin isoform separation

Narrow particle size distribution has been found to be beneficial for column packing efficiency by reducing the HETP value (Liekens et al., 2011; Gritti et al., 2011), and likely improving resolution. Therefore, a comparison study was carried out using jetted and non-jetted Q45 resins with three ligand densities to investigate whether the separation of ovalbumin isoforms could be improved **(Figure 6-1)**. Ovalbumin, as a model protein, was chosen because it contains numerous variants: a total of 151 (Füssl et al., 2019) the majority of which are post-translational modifications such as phospho- and glyco- variants. In the past, only four major peaks could be successfully resolved by both batch and continuous AEX chromatography representing a complex separation system (Hodder et al., 1990; Pacáková et al., 2001; Hsieh et al., 2006; Hirsh and Tsonev, 2017; Wayne, 2018).

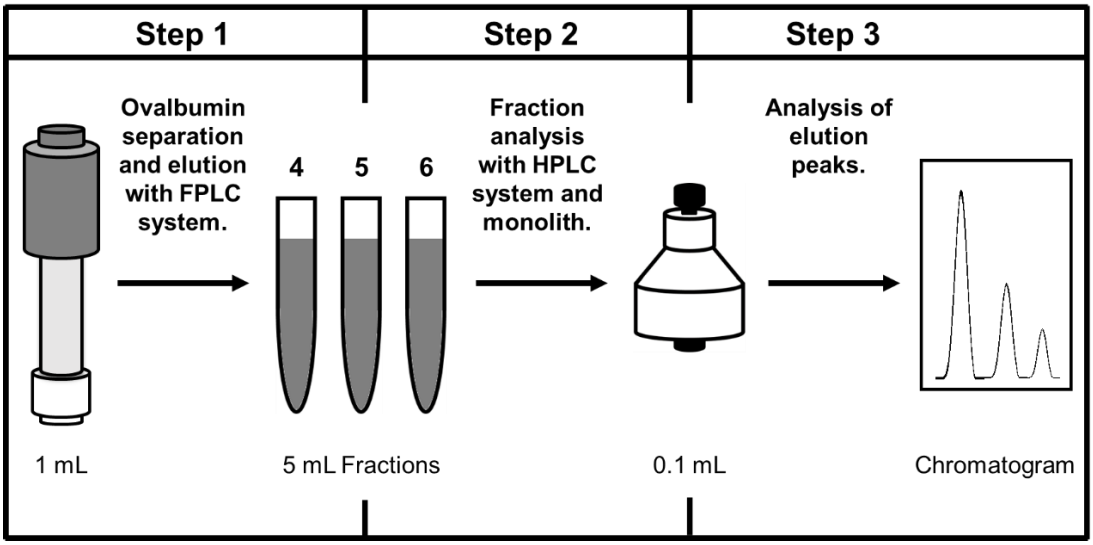

Figure 6-1. Ovalbumin purification and analysis method.

6.2.1.1. Ovalbumin isoforms more retained with higher ligand density

Runs on the preparative chromatography system confirmed that the separation of ovalbumin isoforms was indeed a difficult case. Four poorly separated peaks could be identified: peaks number 1 and 3 being the most resolved, and peaks 2 and 4 being left and right shoulders of the main ones **(Figure 6-2)**, which were representative of the peaks seen elsewhere (Hodder et al., 1990; Pacáková et al., 2001; Hsieh et al., 2006; Hirsh and Tsonev, 2017; Wayne, 2018).

Despite unsatisfactory resolution quality, the chromatograms revealed differences in ovalbumin peak retention times. The use of jetted Q45 resins resulted in narrower peaks, which is in agreement with previous data by (Li et al., 2015), but longer retention times compared to the non-jetted resins **(Figure 6-2)**. In addition, peak 1 was resolved slightly better with the jetted resin. It has been suggested that wider particle distribution could cause band broadening as a result of smaller particles blocking the flow through the pores of the larger beads (Liekens et al., 2011). Therefore, it is likely that jetted material could be beneficial for challenging separations.

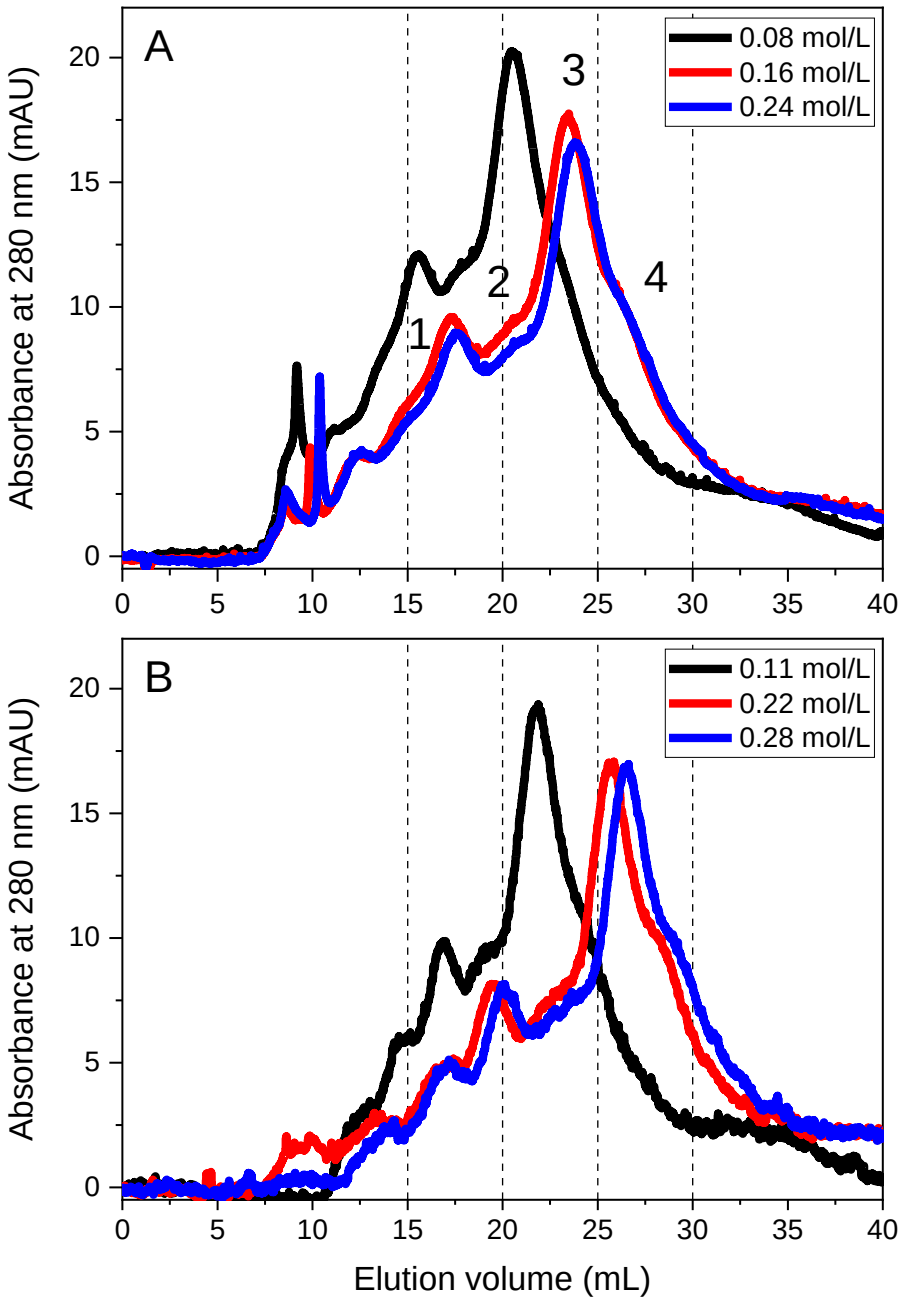

Figure 6-2. Ovalbumin isoform separation on a preparative chromatography column. A – non-jetted and B – jetted Q45 anion exchange resins with low, medium and high ligand densities. Column was equilibrated with 50 mM Tris, pH 9, and eluted with a salt gradient of 100-300 mM over 50 CV. Two milligrams of ovalbumin were loaded onto the 1 mL, 5 cm height columns. Numbers 1-4 represent ovalbumin isoforms. Vertical dashed lines represent a collection of 5 mL fractions.

Ligand density also had a big impact on retention times for both jetted and non-jetted resins. Resins with the lowest ligand densities of 0.08 mol/L (non-jetted) and 0.11 mol/L (jetted) showed the earliest elution time of 41.0 min and 43.8 minutes, respectively, for peak 3 **(Figure 6-3)**. Interestingly, 0.16 and 0.24 mol/L ligand density containing non-jetted resins behaved the same, whereas jetted resins with 0.28 mol/L ligand density had a slightly longer retention time than the 0.22 mol/L resin. Differences in retention time caused by ligand density have been noticed by other researchers (Kopaciewicz et al., 1985; Wu and Walters, 1992; DePhillips and Lenhoff, 2001; Huang et al., 2006, 2010; Dismer and Hubbuch, 2010; Fogle et al., 2012; Lang et al., 2015), whereby retention time increased with increasing ligand density and then plateaued after reaching a high point. An increase in ligand density would cause stronger multipoint protein-ligand interactions, and would thus need a higher salt concentration for dissociation resulting in longer retention times. Nevertheless, a combination of both particle size distribution and ligand density seemed to be responsible for the changes to retention time as seen in **Figure 6-3**.

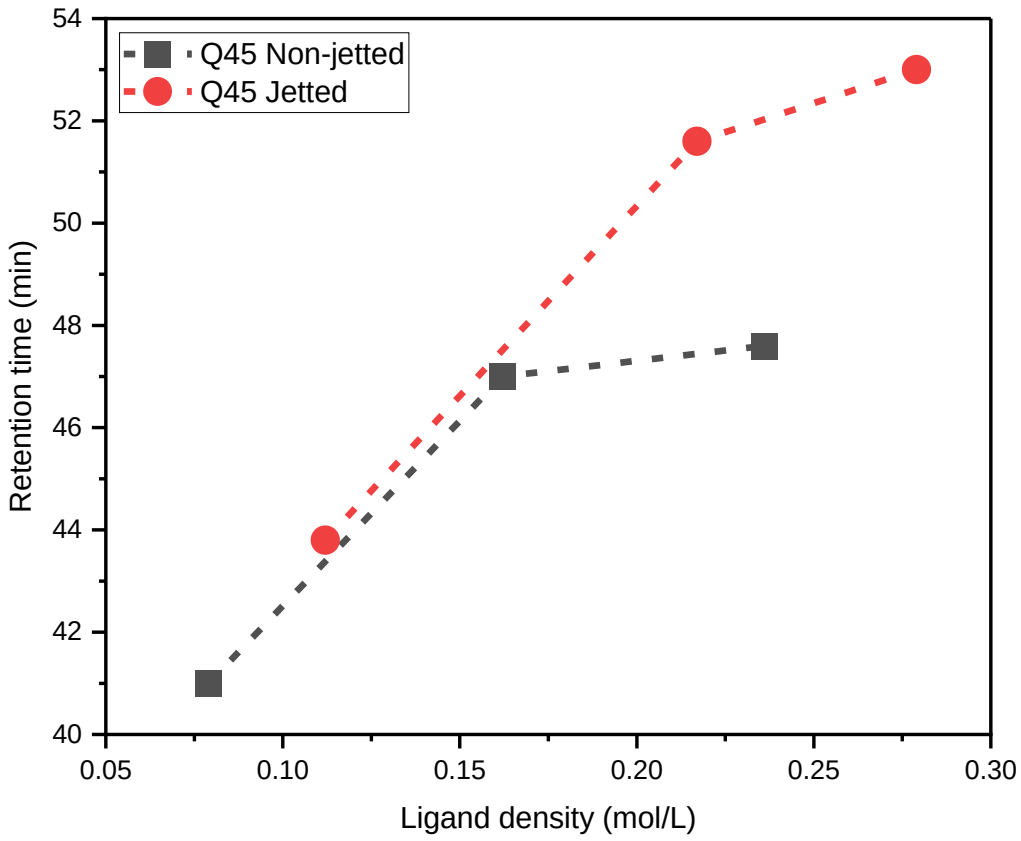

Figure 6-3. Effect of ligand density on retention time of peak 3, ovalbumin. Elution volume was converted to retention time was converted seen in FPLC chromatograms. Dotted line guides the reader's eye through data rather than expresses dependence between variables.

6.2.1.2. Jetted resin and higher ligand density resolve more isoforms

Preparative chromatography fractions were further analysed using an HPLC system to provide a better insight into the effects of both particle size distribution and ligand density **(Figure 6-1)**. Original ovalbumin feed was run first to generate an understanding of the HPLC-monolith separation efficiency **(Figure 6-4)**. The resolution of the four peaks was much better compared to the preparative chromatography performed earlier **(Figure 6-2)** and even some other reports (Hodder et al., 1990; Pacáková et al., 2001; Hsieh et al., 2006; Hirsh and Tsonev, 2017).

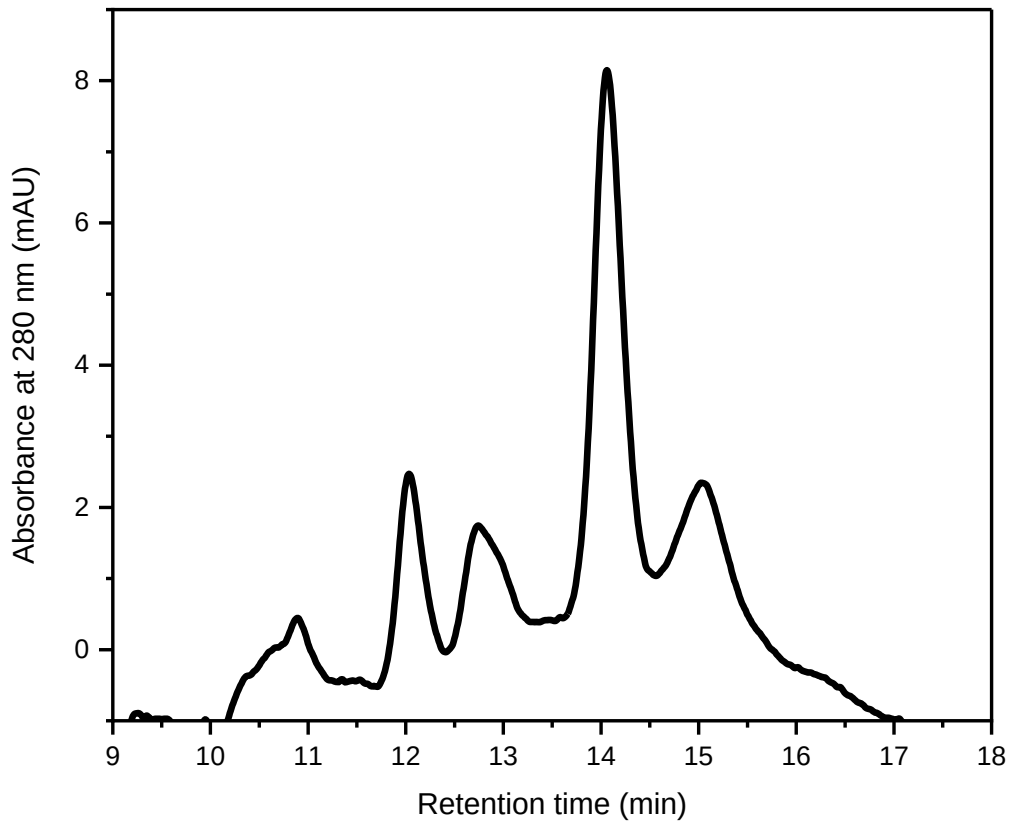

Figure 6-4. Ovalbumin isoform separation on an analytical column. A strong AEX monolith column was equilibrated with 50 mM Tris, pH 9. Ovalbumin was eluted with 100-275 mM NaCl gradient over 20 min.

Due to differences in retention time observed in FPLC chromatograms, the collected fractions were found to be difficult to compare. Therefore, a composite representation that accounted for all the peaks together was chosen (i.e., all fractions were analysed separately and their respective absorbance values were added together to create a composite signal) **(Figure 6-5)**. It revealed that jetted resins with 0.22 and 0.28 mol/L ligand densities were able to resolve an additional peak to the four observed with all non-jetted resins. The separation closely resembled published data, whereby the five peaks were very well resolved in a 10 µm particle size strong AEX column (Perati et al., 2009). Such outcome could only be achieved through a narrow particle size distribution (or smaller average particle size) and higher ligand density.

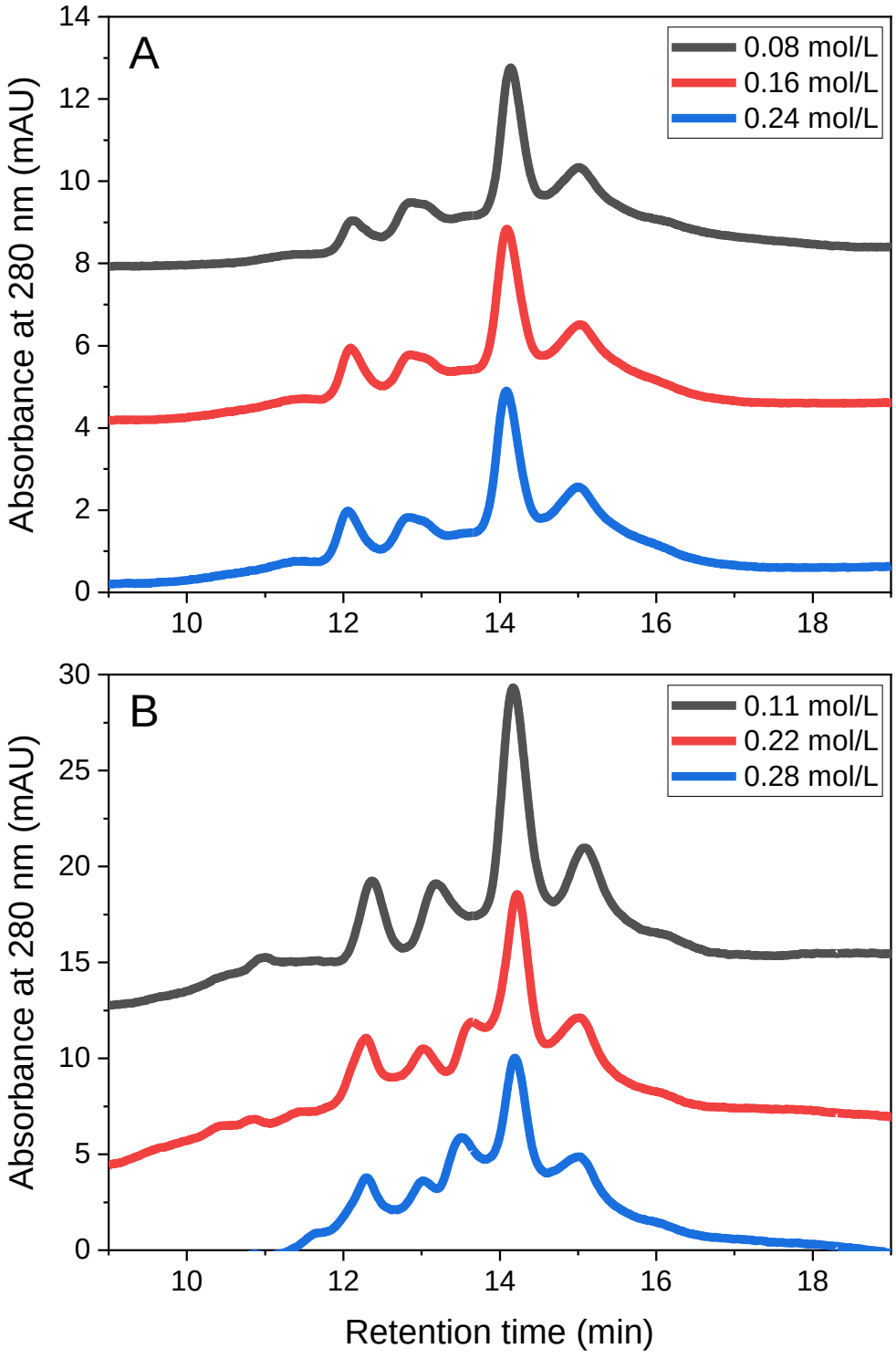

Figure 6-5. Post-CEX ovalbumin fraction analysis on a monolith column. A – non-jetted and B – jetted Q45 resins with low, medium and high ligand densities. A composite signal was generated from fractions collected post-preparative chromatography steps. An AEX monolith column was equilibrated with 50 mM Tris at pH 9, and ovalbumin was recovered with a 100 to 275 mM salt gradient over 20 min.

Overall, changes in resolution were primarily affected by the changes in retention time. Retention time increased with increasing ligand density **(Figure 6-3)**, which may have been a result of multipoint protein-ligand interactions requiring higher salt concentrations to disrupt these bonds. However, the increased retention time could not always be directly translated to improvements in resolution. Jetted resins, for example, were able to enhance ovalbumin resolution with an increase in ligand density, whilst additional ligand density was not beneficial for the non-jetted resins **(Figure 6-5)**.

6.2.2. Monoclonal antibody separation

Having seen changes in ovalbumin variant resolution influenced by different ligand densities, it was interesting to test whether it could be effective for the separation of monoclonal antibodies such as IgG1 and IgG4. Since initial ligand densities of above 0.20 mol/L were considered unnecessarily harsh due to strong protein-ligand interactions, the following work focussed on the lower end range. Results with jetting technology also hinted towards a potential benefit in terms of improved protein resolution when using lower ligand densities. Therefore, cation exchange resins with ligand densities of 0.05, 0.09, 0.12, 0.13, and 0.15 mol/L were manufactured using jetting.

6.2.2.1. Protein A load challenge dictates CEX elution peak recovery

In order to generate material suitable for the CEX experiments, IgG1 and IgG4 clarified cell culture lysates were pooled and loaded onto a Protein A column. Column was heavily overloaded (70 mg IgG/mL resin) during the first cycle with the flow through collected for re-processing. Two more cycles were performed with the adjusted lower load challenges (30 mg IgG/mL resin) as MabSelect SuRe™ is known to have a capacity of around 35 mg *h*IgG/mL resin. Protein A eluates were then subjected to buffer exchange using Vivaspin™ 20 columns prior to loading onto 10 ± 0.2 cm height CEX columns.

CEX chromatograms revealed two IgG1 and IgG4 representing peaks whose retention time / elution volume and peak size were affected by buffer pH **(Figure 6-6)**. As the pH became more acidic, both peaks emerged more retained, whilst the first peak appeared wider and smaller. Prolonged retention time indicated that an increase in the mAbs' net charge allowed them to form stronger attachments to the ligands. However, some of those ligand-protein connections may have been irreversible

causing a reduction in the first peak ('peak 1') that could not be recovered in the 1 M sodium chloride strip step. The area of peak 1 shrunk by 94% with decreasing pH, whilst the area of peak 2 remained the same **(Figure 6-7)**.

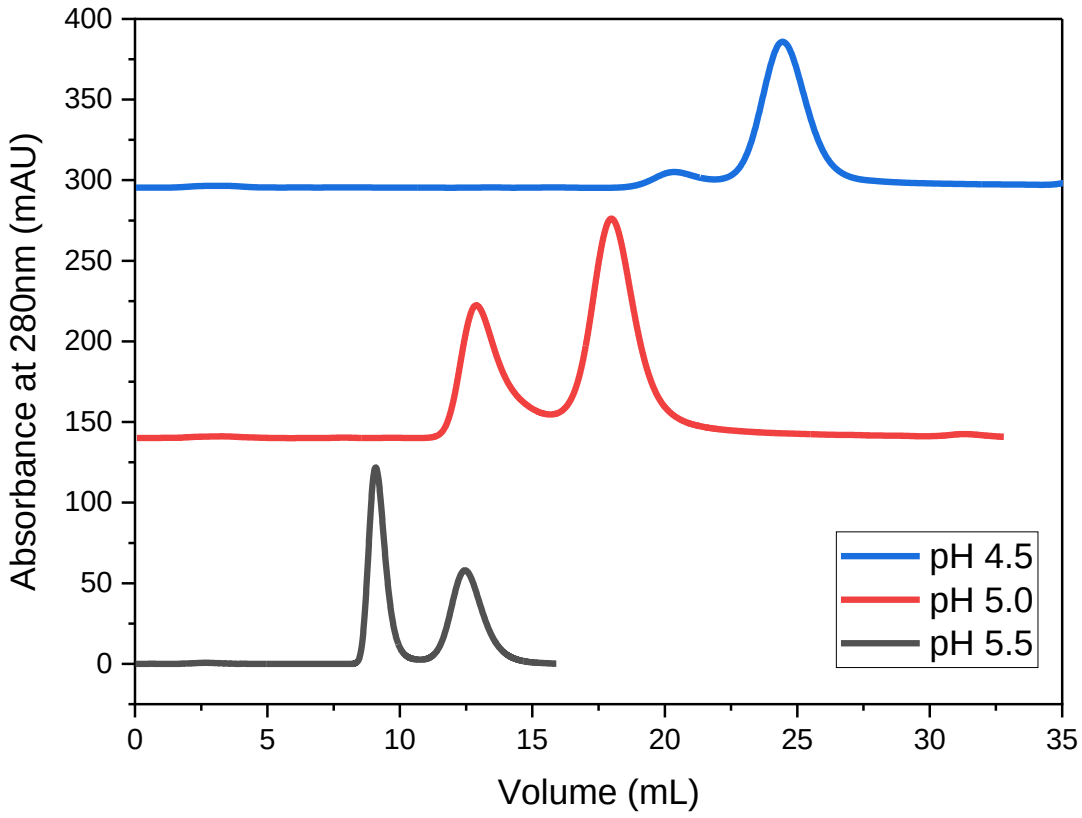

Figure 6-6. Separation of the mAb mixture under different buffer pH conditions. The mAb mixture containing IgG1 and IgG4 was purified with Protein A and exchanged into 20 mM sodium acetate buffer of different pH 4.5-5.5 prior to CEX. CEX resin with 0.12 mol/L ligand density was used with the elution gradient from 100 to 500 mM NaCl. Two milligrams of the feed were loaded onto the 2 mL, 10 ± 0.2 cm height column. Runs were performed in triplicate and the most representative profiles are shown.

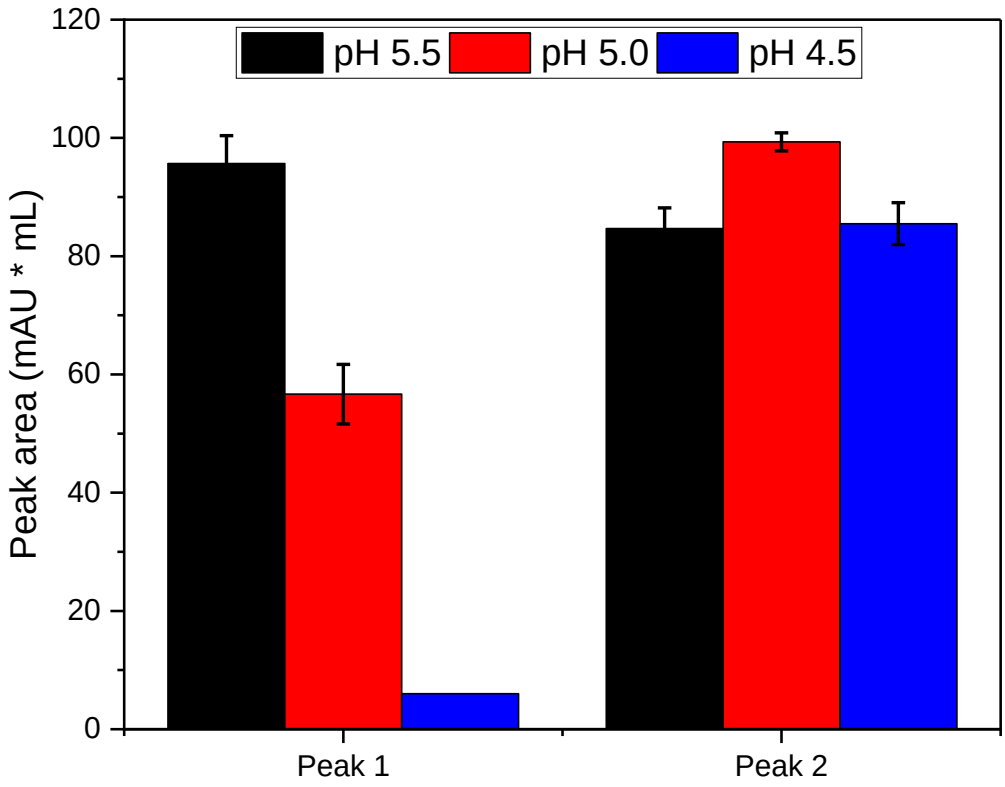

Figure 6-7. Elution peak area taken up by either Peak 1 or Peak 2 at different pH conditions. Peak areas were derived from the CEX mAb separation each representing either IgG1 and IgG4. The mAb mixture was purified with Protein A and exchanged into 20 mM sodium acetate buffer of different pH 4.5-5.5 prior to CEX. CEX resin with 0.12 mol/L ligand density was used with the elution gradient from 100 to 500 mM NaCl. Two milligrams of the feed were loaded onto the 2 mL, 10 ± 0.2 cm height column. Runs were performed in triplicate resulting in ± 1SD.

The area of peak 1 was identified to be affected by the amount of Protein A load challenge. Cycle with the highest load challenge (70 mg/mL resin) had the lowest percentage of peak 1 eluent, whilst cycle with the recycled flow through material (35 mg/mL resin) had the highest amount of peak 1 with respective 25% and 53% at pH 5.5 **(Figure 6-8)**. The other two cycles that were loaded to capacity (30 mg/mL resin), resulted in peak percentage values in between the former two runs.

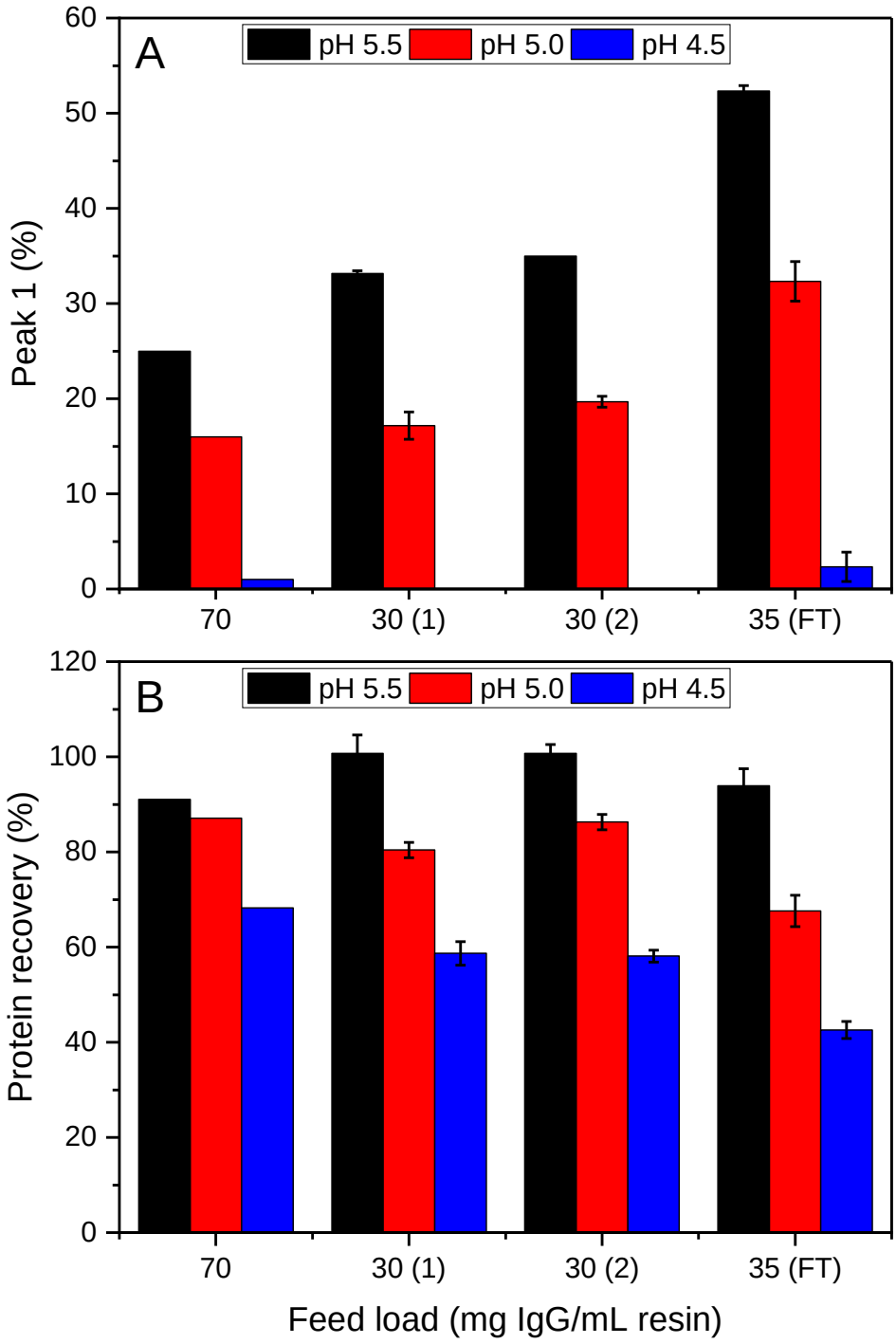

Figure 6-8. Effect of Protein A load on CEX performance. A – amount of Peak 1 in the elution, B – total protein recovery based on the feed load: 70 mg, 30 mg (2 replicates of the same condition) and 35 mg (recycled flow through from 70 mg load) of clarified mAb mixture per 1 mL of Protein A resin. Protein A purified mAbs were subjected to buffer exchange into 20 mM sodium acetate pH 4.5-5.5 prior to CEX with 0.12 mol/L ligand density. Runs were performed in triplicate resulting in ± 1SD; runs with 70 mg IgG/mL resin were carried out once.

In turn, the total protein recovery was dictated by the amount of peak 1, which was heavily affected by buffer pH. The two comparable cycles of 30 mg/mL resin load resulted in 100% recoveries at pH 5.5, which was 10% higher than for the other two cycles **(Figure 6-8)**. In contrast, the recovery plummeted from 100% to 59% when pH was reduced to 4.5, whereas the cycle with the highest load challenge had a better recovery of 64% and its flow through had only 40%. Peak 1 might have been less stable under acidic pH conditions, which would explain why the flow through sample with the highest percentage of peak 1 had the lowest recovery, and why the opposite was true for the cycle with the highest load challenge.

The effects of Protein A load challenge can be explained through competitive binding events between mAbs IgG1 and IgG4 and Protein A ligands as the matrix was being challenged with double the recommended load amount. The mAb in peak 2 was likely to be more strongly bound to the matrix and displaced peak 1 containing mAb, which came out in the flow through. Competitive binding effects of human polyclonal antibodies have been documented with Protein A resins suggesting that IgG1 sub-class antibodies exhibit stronger binding strength due to secondary Fab interactions, and thus bind more strongly to Protein A resins (Weinberg et al., 2017). Consequently, here, peak 1 was expected to consist of weakly bound IgG4, whereas peak 2 was thought to contain strongly bound IgG1 sub-class antibodies.

6.2.2.2. Effects of ligand density on re-processed flow through

Flow through of the cycle with the highest load challenge was most susceptible to pH changes as it had the highest amount of peak 1 (IgG4) in comparison to other cycles **(Figure 6-8)**, and thus was chosen for further investigation with CEX resins. Results showed that the use of lower ligand densities contributed to increased peak 1 percentage **(Figure 6-9)**. This was particularly evident at pH 4.5, whereby a mere 3% of peak 1 was recovered with the highest ligand density resin instead of 38% achieved with the lowest ligand density resin **(Figure 6-9 A)**. As a result, total protein recovery increased by 20% for both pH 4.5 and 5.0 when ligand density was lowered from 0.15 mol/L to 0.05 mol/L **(Figure 6-9 B)**. Ligand density was not influential on the protein solutions with pH 5.5 resulting in >90% recovery. The higher the percentage of peak 1, the higher the overall recovery, suggesting that peak 1 (IgG4) was less stable and more susceptible to process changes than peak 2 (IgG1).

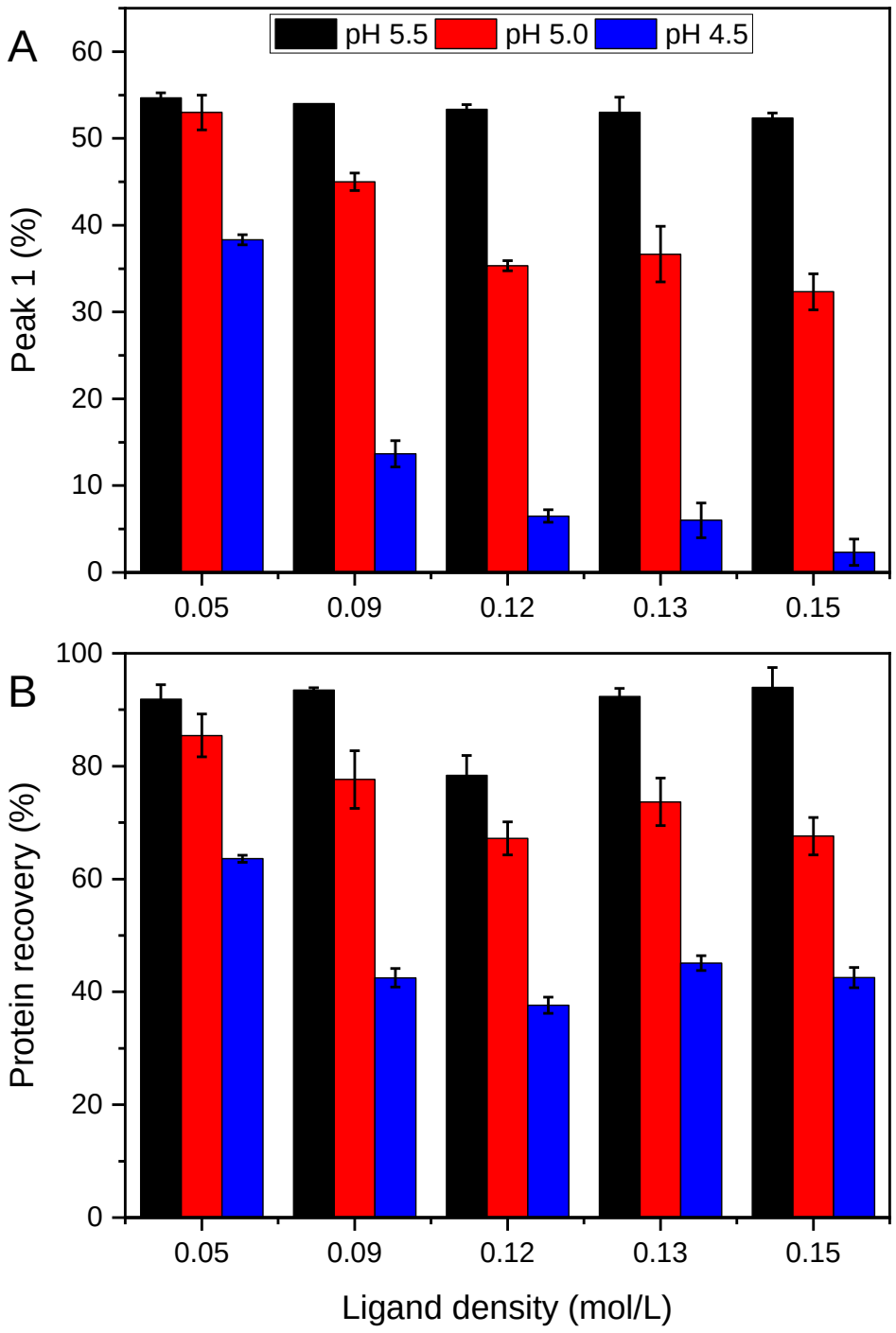

Figure 6-9. Effect of ligand density on both mAb recovery. A – amount of Peak 1 in the elution, and B – total protein recovery. Protein A purified mAbs were subjected to buffer exchange into 20 mM sodium acetate pH 4.5-5.5 prior to CEX. Two milligrams of the 35 mg IgG/mL resin (FT) Protein A feed were loaded onto the 2 mL, 10 ± 0.2 cm height column and eluted with the salt gradient from 100 to 500 mM. Runs were performed in triplicate resulting in ± 1SD.

6.2.2.3. IgG4 - more susceptible to changes in buffer pH and ligand density than IgG1

The next step was to identify which peak corresponded to which antibody by loading pure IgG1 and IgG4 on to the CEX columns. IgG4 eluted first followed by IgG1 thereby corresponding to initially predicted peaks 1 and 2, respectively **(Figure 6-10)**. In alignment with the earlier data, mAb purification heavily depended on buffer pH. As the pH was reduced from 5.5 to 4.5, the initial sharp IgG4 elution peak became wider and more distorted splitting into three smaller peaks, whilst IgG1 peak remained intact throughout **(Figure 6-10)**. In addition, both IgG1 and IgG4 saw up to 11% and 54% reduction in their respective recoveries due to the pH change **(Table 6-1)**.

Antibody-specific pH-dependent peak splitting on cation exchange resins has been observed in several occasions (Guo et al., 2014; Guo and Carta, 2014, 2015; Luo et al., 2014, 2015; Chen et al., 2016). In most cases, IgG1 has been shown to be more stable than IgG4 under the same pH conditions, which is in agreement with this work (Luo et al., 2015; Guo and Carta, 2015; Farys et al., 2018).

Protein recovery and retention time were also influenced by ligand density. All peaks were more retained with high rather than low ligand density resin, with the most significant retention at pH 4.5 for both antibodies **(Figure 6-10)**. Higher ligand density was expected to provide an increased number of interaction points with the target protein resulting in stronger affinity, and hence longer retention time (Kopaciewicz et al., 1985; Wu and Walters, 1992; DePhillips and Lenhoff, 2001; Pessela et al., 2004; Huang et al., 2006, 2010; Dismer and Hubbuch, 2010; Fogle et al., 2012; Lang et al., 2015). In fact, IgG4 was mostly affected by the strong binding kinetics causing peak splitting at pH 5.0 and 4.5 as well as resulting in the most significant reduction in recovery with up to 17% difference between the low and high ligand density resins **(Table 6-1)**. Unexpectedly, the recovery of IgG1 was positively influenced by high ligand density with up to 11% improvement.

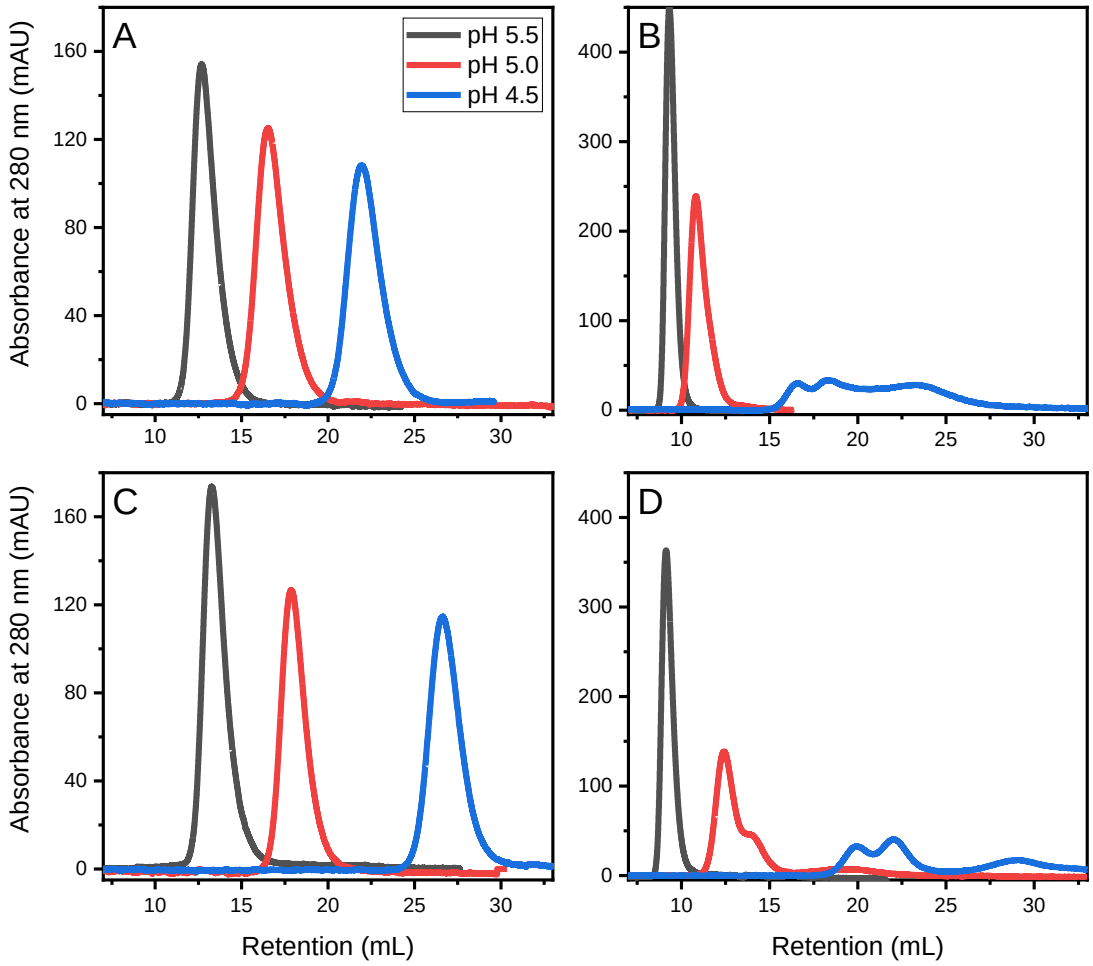

Figure 6-10. Individual IgG1 and IgG4 elution profiles with varying ligand density and buffer pH. A and C represent IgG1 with respective 0.05 and 0.15 mol/L ligand density resins, whilst B and D – IgG4. Pure individual IgG1 and IgG4 were subjected to buffer exchange into 20 mM sodium acetate pH 4.5-5.5 prior to CEX. Two milligrams of each were loaded onto the 2 mL, 10 ± 0.2 cm height column and eluted with the salt gradient from 100 to 500 mM. Runs were performed in triplicate resulting in ± 1SD.

Table 6-1. Comparison of IgG1 and IgG4 recovery post-CEX.

Ligand density (mol/L)	**mAb**	**Average protein recovery (%)**		
		pH 5.5	pH 5.0	pH 4.5
0.05	IgG1	85 ± 5.0*	83 ± 1.0	77 ± 4.0
	IgG4	94 ± 6.0	85 ± 5.0	52 ± 6.0
0.15	IgG1	94 ± 5.0	82 ± 9.0	83 ± 4.0
	IgG4	89 ± 4.0	77 ± 2.0	35 ± 2.0

** Runs performed in triplicate with ± 1SD error bars.*

Two- or three-peak elution generation has been observed for CEX resins with particular pore size and distribution, high surface hydrophobicity and polymer-grafts (Gillespie et al., 2012a; Guo et al., 2014; Luo et al., 2014, 2015; Guo and Carta, 2015; Guo et al., 2016; Farys et al., 2018). Polymer-grafted resins were found to have a more substantial effect than the traditional ones due to an increased number of attachment points (Gillespie et al., 2012a; Guo et al., 2014; Guo and Carta, 2015; Farys et al., 2018). This often encouraged the formation of strongly-bound unfolded intermediates leading to irreversible aggregate formation representing a high percentage of the second and third elution peaks. Similarly, resins with higher ligand density would also offer more interaction sites that could promote conformational changes of the molecule that would manifest in the form of the additional elution peaks.

6.2.2.4. Three-peak elution - not a result of charge variants

An initial hypothesis explaining the peak splitting seen for the IgG4 molecule **(Figure 6-10)** was the presence of charged mAb variants having either a stronger or a weaker affinity for the ligands. Therefore, an analytical CEX - HPLC set up was used to investigate whether there were any differences in charge variants amongst the fractions. The pH gradient of 3.6 to 9.4 carried over 30 min showed that all IgG4 fractions consisted of the same distribution of charge variants: first main peak of pI 6.90 and a smaller second peak of pI 7.04 **(Figure 6-11 B, Table 6-2).** Three-peak eluate of pH 4.5 with high ligand density resin displayed only minor differences in the main peak pI with 6.88, 6.83 and 6.84, respectively **(Table 6-2)**. Hence, peak splitting observed in the IgG4 chromatograms was not a result of charge variant separation.

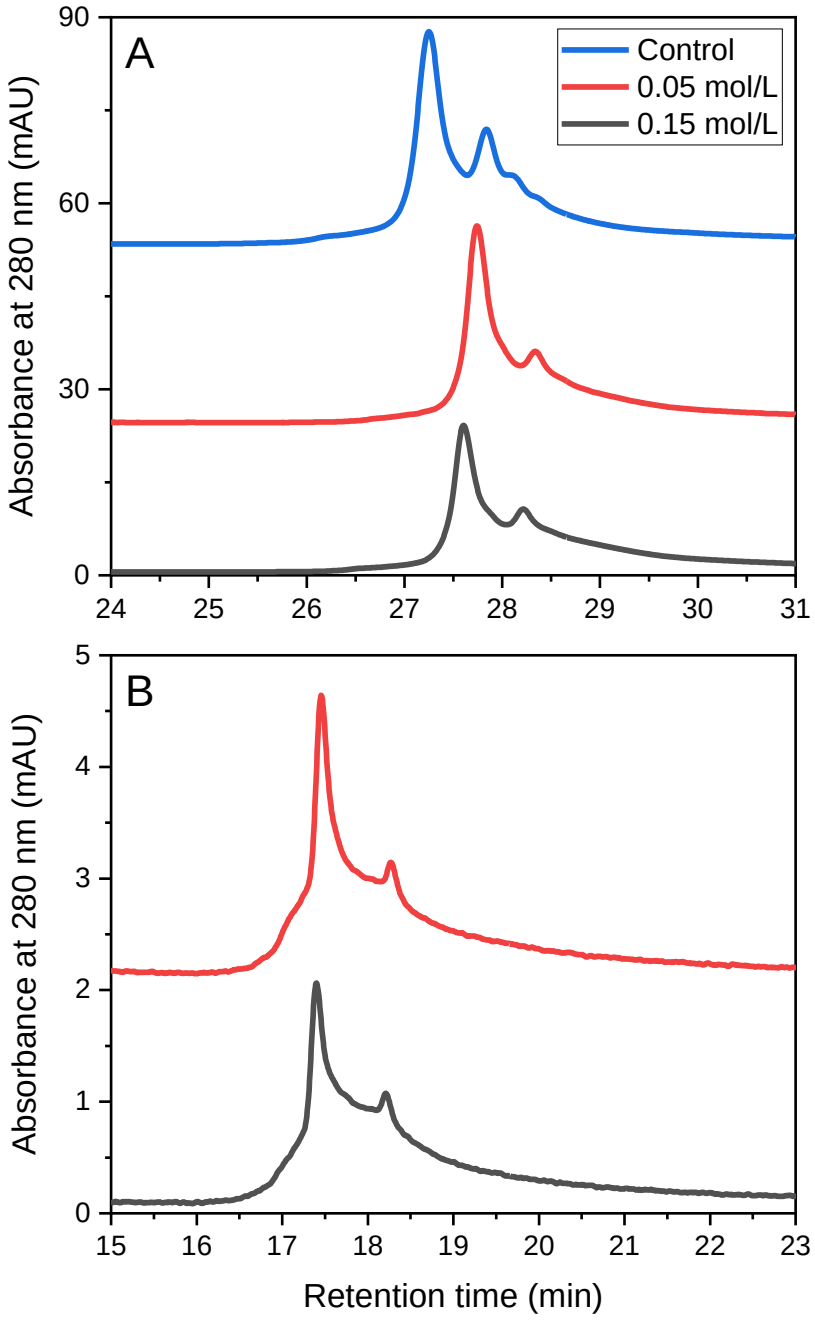

Figure 6-11. Post-CEX fraction analysis of IgG1 and IgG4 charge distribution. A – IgG1 and B – IgG4 charge variant analysis with a pH gradient 3.6 to 9.4 over 30 min. A composite signal was generated from fractions collected post-preparative chromatography step. Buffer composition: 10 mM borate, 10 mM citrate, 10 mM sodium phosphate.

IgG1 was also analysed for the presence of charged variants. The pH gradient resolved the main peak of pI 8.85 followed by the three smaller peaks of pI 8.97, 9.02 and 9.07 **(Figure 6-11 A, Table 6-2)**. The main peak in all fractions had a pI of 8.95 except for the fraction at pH 5.5 with low ligand density resin that had a more acidic pI of 8.86, and resembled the control sample at pH 4.5 **(Table 6-2)**. It suggested that the other eluents had become more basic after contacting chromatography matrix. Although the interaction with high ligand density may have caused a slight change in product pI (by 0.1), it had no negative effect on the product recovery. However, it was not clear whether such change would be significant for the pharmacodynamics of IgG1 molecule.

Table 6-2. Charge / pI evaluation of CEX elution fractions.

pH	Ligand density (mol/L)	IgG1	IgG4
5.5	0.05	8.86	6.90
	0.15	8.95	6.88
5.0	0.05	8.95	6.79
	0.15	8.93	6.88
4.5	0.05	8.95	6.89
	0.15	8.93	6.88, 6.83, 6.84*
	Control	8.85	No data

* *IgG4 pH 4.5 elution produced three peaks.*

6.2.2.5. IgG4 - more prone to aggregate formation than IgG1

Analytical size exclusion chromatography was employed to explain the reasons for the additional CEX peaks, i.e. likely aggregate formation caused by acidic buffer pH and high ligand density. IgG1 feed (control) samples and CEX elution fractions had no presence of dimers **(Figure 6-12 A, C, E)**. In contrast, IgG4 control samples had a pH-dependent increase in dimers and trimers with 1.3%, 3.5%, and 35.4% at pH 5.5, 5.0 and 4.5, respectively **(Figure 6-12 B)**. Similarly, an increasing percentage of IgG4 dimers were detected at pH 4.5 of the low ligand density resin **(Figure 6-12 D)**. The first of the three peaks consisted of monomers, whereas the second and third peaks had 35% and 70% dimers, respectively. Interestingly, this was not the case for the three-peak elution with high ligand density resin **(Figure 6-12 F)**. Large pellets were seen in the tubes after centrifugation of these samples and prior to loading onto the SEC column, which might explain why no dimers were seen in the elution. Overall, the data informed that IgG4 was less stable when exposed to chemical stress and likely more prone to in-column aggregation than IgG1.

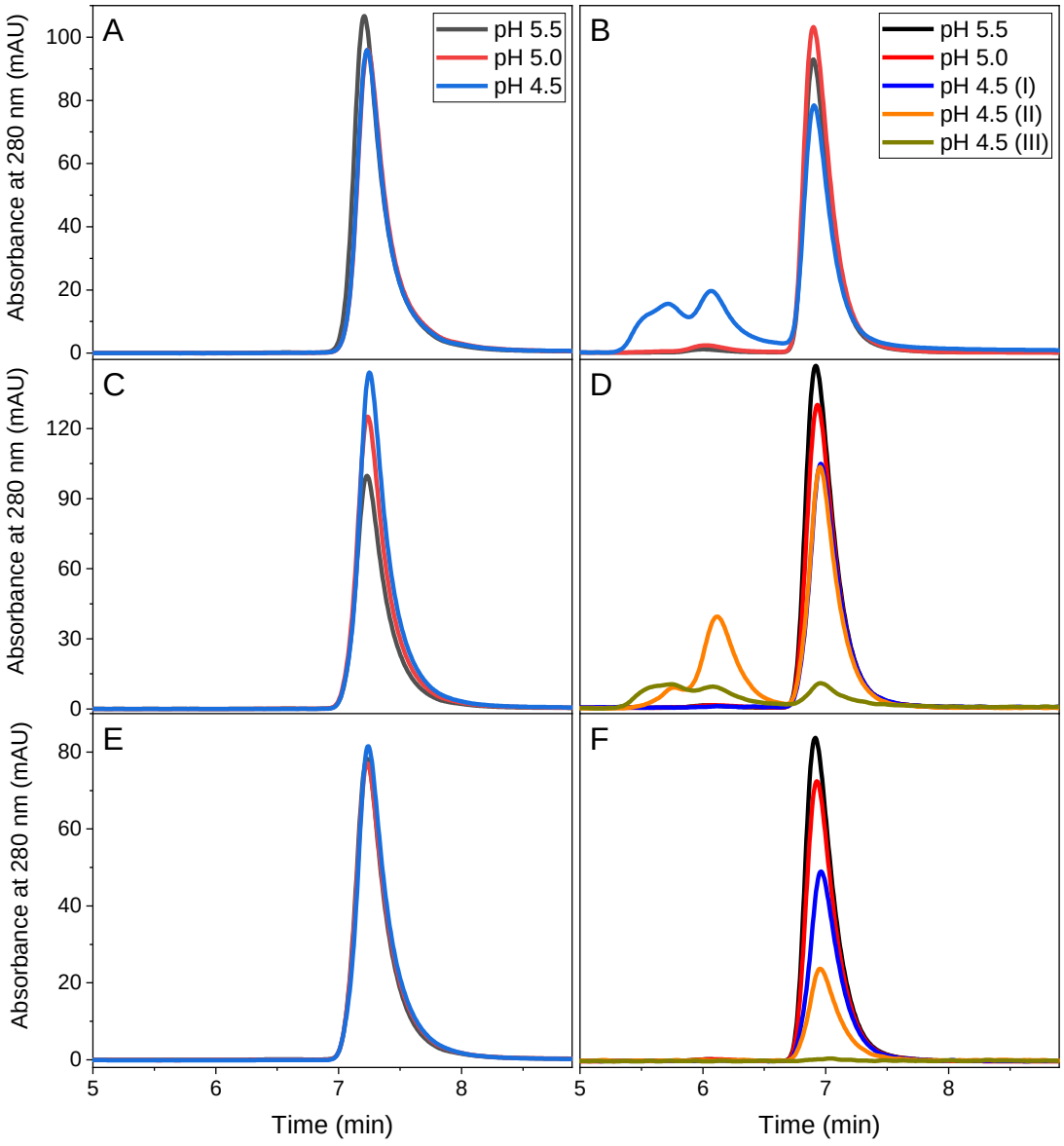

Figure 6-12. Post-CEX fraction analysis of IgG1 and IgG4 molecular size. A, C, E – IgG1, B, D, F – IgG4. First row of graphs represents pure feed material prior to CEX, second and third rows show results with 0.05 and 0.15 mol/L ligand density CEX resins. Analysis was conducted at 0.2 mL/min using mobile phase formulated of 100 mM sodium phosphate and 100 mM sodium chloride at pH 7.0. Samples were centrifuged at 18,000 g for 10 min prior to 20 µL injections. Proteins were quantified using a wavelength absorbance at 280 nm with a reference at 550 nm.

Both IgG4 and IgG1 were subjected to thermal stress in order to confirm that IgG4 was vulnerable to in-column aggregation. As suspected, overall IgG4 aggregation temperature of 60ºC was found to be lower than that of IgG1 - 70ºC making it more prone to aggregation, and thus less stable **(Table 6-3)**. However, IgG1 feed (control) was found to be progressively less stable as the pH decreased from 5.5 to 4.5, something that was also evident from the CEX eluates. The difference in all of the IgG4 elution fractions was not as significant.

Table 6-3. Thermal stability of mAbs expressed as aggregation temperature.

pH	Ligand density (mol/L)	IgG1 (ºC)	IgG4 (ºC)
5.5	0.05	71.4 ± 0.1*	60.6 ± 0.6
	0.15	72.8 ± 0.5	61.4 ± 1.2
	Control	70.4 ± 0.2	61.0 ± 0.9
5.0	0.05	70.6 ± 0.1	60.2 ± 0.7
	0.15	70.4 ± 0.3	60.7 ± 1.2
	Control	71.7 ± 0.2	65.3 ± 0.5
4.5	0.05	67.7 ± 0.6	60.1 ± 0.5
	0.15	67.5 ± 0.2	61.1 ± 0.1
	Control	68.8 ± 0.9	60.6 ± 0.6

** Runs performed in triplicate with ± 1SD error bars.*

It was evident that the two monoclonal antibodies behaved very differently under the same pH and ligand density conditions. IgG4 contained higher levels of dimers and trimers at acidic pH conditions, and had a lower thermal stability making it more susceptible to aggregation than IgG1, which was in agreement with other reports (Garber and Demarest, 2007; Ishikawa et al., 2010; Ito and Tsumoto, 2013; Neergaard et al., 2014; Tian et al., 2014; Skamris et al., 2016; Jin et al., 2019). In addition, the stability of IgG1 was supported by its high pI **(Table 6-2)** that allowed to maintain pronounced intermolecular charge-charge repulsions and greater net charge in the chosen buffer environment than IgG4.

6.2.2.6. Aggregated mAbs remain bound to chromatography matrix

CEX chromatography runs demonstrated that IgG4 was more sensitive to changes in process buffer pH and matrix ligand density than IgG1. Analytical SEC study suggested that pH- and ligand density-induced HMWS might be left bound to the column causing a reduction in recovery. Residual protein detection method consisting of a fluorescent dye Proteostat and confocal laser scanning microscopy was employed to explore this hypothesis. Resins containing low (0.05 mol/L) and high (0.15 mol/L) ligand densities were packed into a miniature flow cell, equilibrated and loaded with the IgG1 or IgG4 prior to adding the dye to obtain the initial images ("Feed application"). The resins were then subjected to wash and elution steps before imaging with the dye again ("Post-elution").

Higher levels of fluorescence were detected for high ligand density resins and acidic buffer pH in the elution steps **(Figure 6-13)**. These conditions were particularly unfavourable for IgG4 as the dye was distinctly bound to the outer edges of the resin particles possibly representing oligomers not seen for the other samples. Results confirmed the hypothesis that the reduction in CEX yield at low pH and / or with high ligand density resin was due to aggregated species remaining irreversibly bound to the matrix.

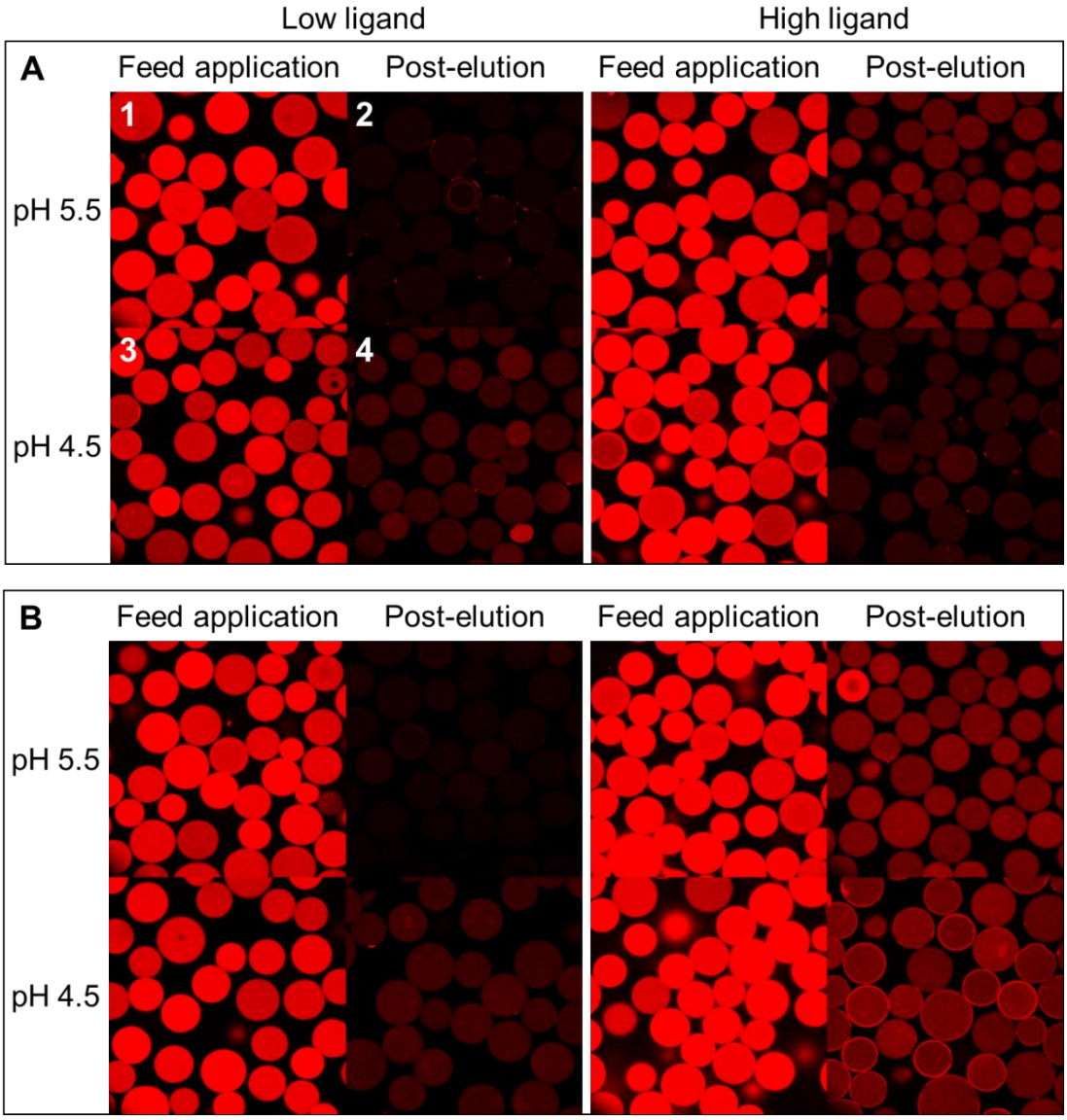

Figure 6-13. Effect of ligand density on foulant accumulation. Confocal laser scanning microscopy images were taken of low ligand density (0.05 mol/L) and high ligand density (0.15 mol/L) CEX resins after loading and post-elution of A – IgG1 and B – IgG4. One milligram of each mAb was loaded into the miniature flow cell packed with 0.02 mL resin under the following buffer conditions: 20 mM sodium acetate pH 5.5 and 4.5. Proteostat dye was added after each step of loading / elution and at least three images were taken with one representative shown. CLSM excitation wavelength was 550 nm, emission wavelength was 600 nm, and laser intensity was 20%.

6.2.2.7. Efforts to improve mAb recovery

Reduction in mAb recovery with high ligand density resins was suspected to be a result of conformational changes that resulted in pronounced protein-protein and / or protein-ligand attraction. Such behaviour has been previously observed (Gillespie et al., 2012a; Guo and Carta, 2015; Guo et al., 2016; Chen et al., 2016; Farys et al., 2018) and mediated with the addition of arginine (Gillespie et al., 2012a; Guo and Carta, 2015; Guo et al., 2016). Arginine has been shown to improve protein recovery and reduce aggregation by protecting proteins from unfolding and sticking to chromatography matrices (Ejima et al., 2005; Arakawa et al., 2007; Gillespie et al., 2012a; Hirano et al., 2014; Guo and Carta, 2015).

To test the hypothesis that protein loss was caused by ligand-induced strong protein-resin interactions, 40 mM arginine was added to the CEX equilibration and elution buffers. The addition of arginine was highly beneficial for the mixed IgG1 and IgG4 solution as visibly higher amount of peak 1 (IgG4) could be recovered at both pH 5.0 and 4.5 **(Figure 6-14)**. In addition, both peaks consisting of IgG1 and IgG4 were seen to be sharper and better resolved from one another. The results confirmed that protein loss was associated with strong protein-matrix interactions that could be alleviated via the addition of arginine.

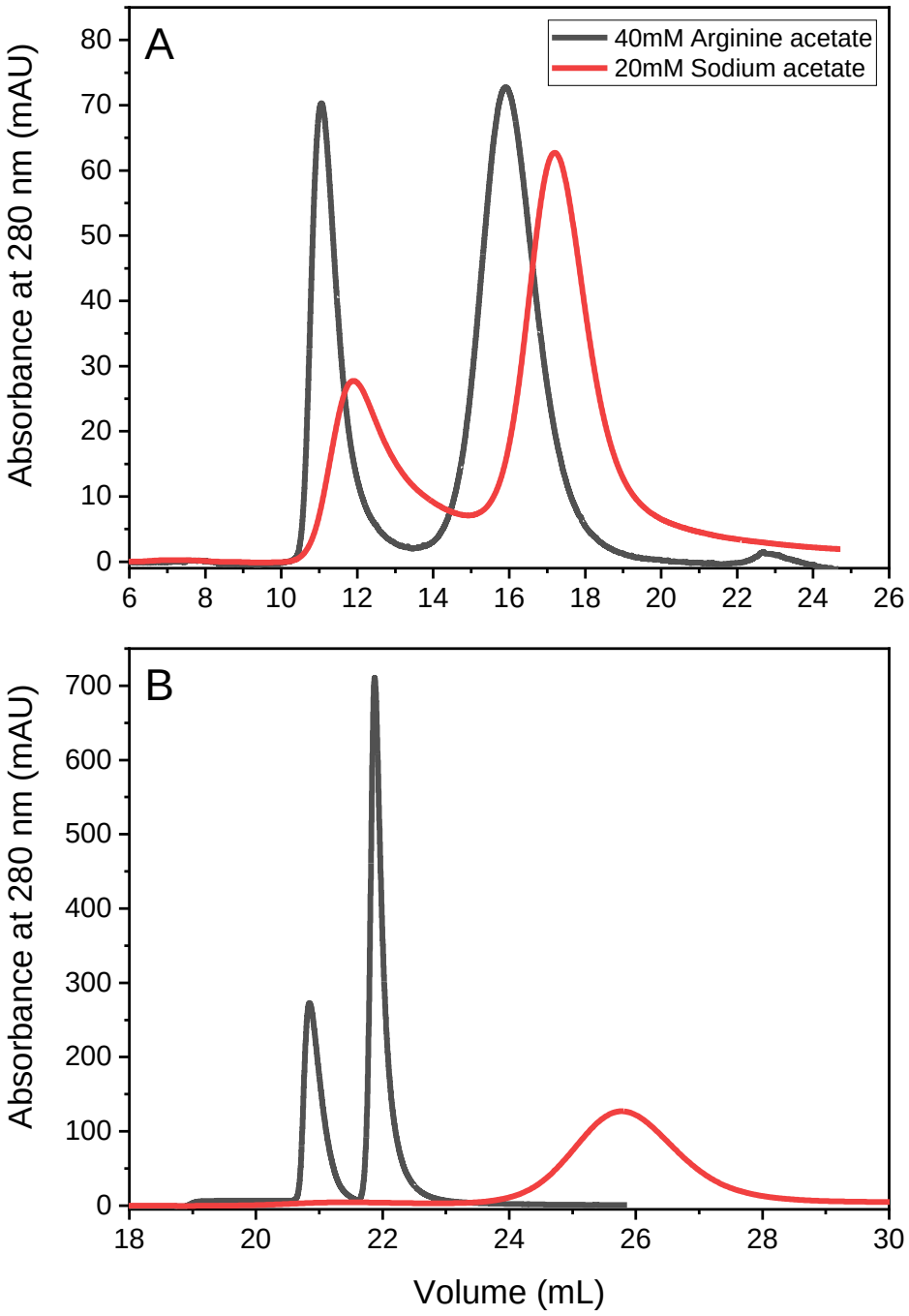

Figure 6-14. Effect of arginine addition to the CEX buffers. A – sodium and arginine acetate buffers at pH 5.0 and B – pH 4.5. CEX resin with 0.15 mol/L ligand density was used with the elution gradient of 100-500 mM NaCl. Two milligrams of the feed were loaded onto the 2 mL, 10 ± 0.2 cm height column.

An alternative buffering salt – sodium citrate was also explored in the efforts to increase IgG1 and IgG4 recovery in solution. Data showed that citrate buffer behaved similarly to the acetate buffer with no benefits in terms of total protein recovery for the pH 5.5 condition, but up to 10% improvement at pH 4.5 **(Table 6-4)**. Unfortunately, experiments with sodium citrate buffer confirmed the initial results whereby increasing ligand density had increasingly undesirable effects on the recovery at both pH 5.0 and 4.5.

Table 6-4. Comparison of sodium acetate and citrate buffers' effects on protein recovery.

Ligand density (mol/L)	**Buffer**	**Average Peak 1 (%)**			**Average protein recovery (%)**		
		pH 5.5	pH 5.0	pH 4.5	pH 5.5	pH 5.0	pH 4.5
0.05	Acetate	55 ± 0.6*	53 ± 2.0	38 ± 0.6	92 ± 2.5	85 ± 3.8	64 ± 0.6
	Citrate	53 ± 2.0	54 ± 1.0	42 ± 1.0	94 ± 3.0	88 ± 0.7	74 ± 2.6
0.15	Acetate	52 ± 0.6	32 ± 2.0	2 ± 1.5	94 ± 3.5	68 ± 3.3	43 ± 1.8
	Citrate	54 ± 0.0	37 ± 3.0	7 ± 1.0	98 ± 2.1	77 ± 5.6	47 ± 1.8

** Runs performed in triplicate with ± 1SD.*

6.2.3. Conclusions

The aim of this chapter was to investigate whether high ligand density would allow to completely separate a mixture of proteins consisting of ovalbumin isoforms and two mAbs: IgG1 and IgG4. Whilst high ligand density provided improved separation capacity for ovalbumin isoforms, the opposite was true for the two mAbs. Diminishing separation quality and reduction in recovery were noticed as the ligand density increased and buffer pH became more acidic. Most effective separation and highest yield of >90% was achieved with pH 5.5 with all ligand densities, whilst poor separation and lowest recovery of 40% was generated with ligand densities above 0.09 mol/L **(Figure 6-9)**. The reduction in yield was linked to the loss of IgG4 consisting peak 1 prompting a closer examination of both mAbs separately.

Upon a closer investigation, it was revealed that IgG1 and IgG4 behaved differently under the same process conditions. Differences in ligand density and buffer pH had no effect on the shape of the IgG1 elution peak, and a comparatively small variation of 77% to 94% in yield **(Table 6-1)**. In contrast, IgG4 had a substantial loss of 60% yield as the ligand density increased and pH decreased as well as significant changes to the shape of the elution peak **(Table 6-1, Figure 6-10)**. The originally single sharp peak at pH 5.5 turned into a wider split peak at more acidic pH and high ligand density.

The composition of the three-peak IgG4 elution was examined using analytical CEX and SEC. Analytical CEX showed that the additional peaks were not a separation of charged variants **(Figure 6-11, Table 6-2)**. SEC revealed that the first peak consisted of monomers, whilst the second and third peaks had an increasing amount of dimers (35% and 70%) when run at pH 4.5 with low ligand density resin **(Figure 6-12)**. Dimers, however, were not present in the samples produced with high ligand density resin suggesting that they may have been irreversibly bound to the resin as the yield decreased by 17% **(Table 6-1)**.

In order to confirm that the significant loss in IgG4 yield during the CEX step was a result of in-column aggregation, Proteostat dye was employed. The images confirmed that the aggregate formation was particularly present in the high ligand density resin during both feed application and post-elution as the dye was highly fluorescent and accumulated on the outer edge of the beads at pH 4.5 **(Figure 6-13)**. Moreover, when arginine, an amino acid that reduces binding strength to the resins, was added to the process buffers, the size of the peaks and, thus, their recovery were improved **(Figure 6-14)**. Two orthogonal data sets confirmed that product loss was a result of high binding strength promoted by high ligand density and low buffer pH.

In-column unfolding, reversible and irreversible aggregate formation may have been encouraged by the increased number of attachment points provided by the high ligand density (Gillespie et al., 2012b; Guo and Carta, 2014, 2015; Chen et al., 2016; Guo et al., 2016; Farys et al., 2018). Less strongly bound monomers would elute first followed by more strongly bound intermediates that can either reverse to monomers or remain as dimers. In addition, some aggregates would stay irreversibly bound to the ligands and fail to elute if the protein-ligand affinity was too strong. Consequently, the protein recovery would be affected negatively, and promote resin fouling.

The selection of appropriate ligand density was of particular importance to molecules that were less stable. IgG4 is known to be more susceptible to aggregation (Garber and Demarest, 2007; Ishikawa et al., 2010; Ito and Tsumoto, 2013; Neergaard et al., 2014; Tian et al., 2014; Skamris et al., 2016; Jin et al., 2019), and here was also found to be less chemically and thermally stable than IgG1 **(Table 6-2)**. The lower pI of 6.9 for IgG4 reduced its colloidal stability in the chosen buffer pH range of 5.5 - 4.5, whilst IgG1 could maintain a higher net charge and intermolecular repulsions with the pI of 8.9. Therefore, IgG4 was more prone to aggregation at acidic pH and high ligand density than IgG1 resulting in lower recoveries. Target product, buffer pH and ligand density played an important role in dictating process yield and resin lifetime.

7. Chapter: Conclusions and Future work

7.1. Conclusions

The aim of this thesis was to identify the most important resin design features for the intensified purification of biopharmaceuticals, and utilise them to create custom designs suitable for meeting different process needs such as high flow rates, high product concentrations, and poor product stability.

Average particle size, particle size distribution and ligand density were identified as the determining factors in dynamic binding capacity, protein uptake rate, product separation, and resin's lifetime; thus, they were implemented in the design of the resins as described in Chapter 3. It was found that particle size and process flow rate had the most significant effects on DBC with the smallest particles and low flow rate providing the best results (Chapter 4). The role of ligand density became progressively important as particle size decreased. Reduction in protein uptake rate could be noticed due to steric hindrance effects manifesting at high flow rates and feed concentration.

A novel analytical aggregate detection assay was developed to confirm the hypothesis that reduction in DBC was a result of foulant accumulation inside the resins (Chapters 5). The assay demonstrated sensitivity, selectivity and robustness for different feed materials including BSA and IgG1 as well as for different types of resins. The usage of a fluorescence plate reader and a confocal microscope facilitated the detection of aggregation and explained the loss in product recovery. The assay could be optimised through an implementation of a high-throughput liquid handling robot to permit an accurate and rapid screening of multiple samples.

The analytical method was further employed to facilitate the understanding of IgG4 yield loss when processed under low pH conditions and high resin ligand density (Chapter 6). It was confirmed that strong multipoint protein-ligand attachment led to irreversible aggregate adherence to resins as well as dimer and trimer formation manifesting as additional elution peaks, all of which caused a reduction in product's yield and contributed to resin's longevity.

The effects of narrow particle size distribution were in most cases deemed insignificant except for the resolution of ovalbumin isoforms. Jetted resin and high ligand density enabled the resolution of an additional peak not seen otherwise (Chapter 6). Therefore, this area should be explored in future studies as more advantages may be revealed.

Finally, it is evident that custom resin designs should be considered for different products, bioprocess steps and their needs. A chromatography resin with an average particle size of 45-65 µm, and low ligand density would be most valuable for the crude feed and high flow rate capture step. In contrast, resin with ligand density above 0.16 mol/L with a particle size of 45 µm would be beneficial for a polishing step, whereby high binding capacity and good product separation are required, and can be achieved at a lower flow rate of 50 cm/h. Nonetheless, ligand density above 0.10 mol/L was deemed undesirable for products such as IgG4 with impaired stability leading to significant yield losses.

7.2. Future work

This chapter considers future development related to chromatography resin design and fluorescent dye assay utilisation. Future work is split into sections that consider short-term, mid-term and long-term activities. Short-term objectives would require up to 6 months of work, mid-term around a year, and long-term plans would take up to several years of research.

7.2.1. Short-term

7.2.1.1. Effects of ligand density on host cell protein and residual DNA clearance

In order to fully understand what effect ligand density has on the bioprocess, host cell protein (HCP) and residual DNA clearance would have to be investigated. Having seen what effect different ligand densities have on model and biological product separation, one can assume that the effects would be similar for the host cell proteins and DNA as well. High ligand density is expected to retain more HCPs and DNA than the lower ligand density. A design of experiment (DoE) study could be performed to establish an optimum ligand density window enabling to achieve desirable recovery of the product of interest and elimination of the impurities. This would aid in developing a process that relies on the quality by design principles.

7.2.1.2. Stability studies

Chromatography purification cycle can sometimes take up to 6 hours due to long feed application times. This arises due to high volume and low product titres that are present in the viral vector production industry but have been resolved in the antibody field. The stability of the product may be influenced by the prolonged product-ligand interactions as the molecules are known to change their conformation upon the

contact. Generation of higher molecular species or reduction in recovery may follow. Therefore, the risk to product stability at prolonged loading times needs to be evaluated with the process conditions established accordingly.

A proposed experimental plan would consist of ligand densities between 0.05 and 0.20 mol/L and loading times spanning 30 minutes to 10 hours. The analytical methods would include HPLC-SEC, dynamic light scattering, Proteostat® dye assay as well as AAV vector genome titre estimation with qPCR and vector capsid titre with the ELISA assay. The results would provide an insight into the viral vector stability when exposed to prolonged contact with charged ligands, and inform about the effects of ligand density.

7.2.2. Mid-term

7.2.2.1. Investigation of molecules that could benefit from custom ligand densities

Chromatography resins are used for the purification of numerous products including small proteins and molecules, fusion proteins, antibodies, antibody-drug conjugates, viral vectors and mRNA. This thesis has studied only several model proteins including BSA and ovalbumin as well as biopharmaceutical products such as IgG1 and IgG4. The work could be expanded further to understand how other molecules behave in the presence of varying ligand densities. This would be particularly beneficial for unstable or difficult to purify molecules such as adeno-associated viral (AAV) vectors. High recovery of >90% has been limited by the strong capsid-ligand interactions, whilst full versus empty capsid separation has been challenging due to their similarities in size and charge causing both factors to become the biggest bottlenecks of the industry. Lower ligand density could increase recovery, whilst higher ligand density might be able to improve the full capsid separation.

7.2.2.2. Evaluation of jetted versus batch-emulsified resins

Uniform resins can be manufactured via a novel jetting technology that employs membrane emulsification rather than the traditional stirred tank batch emulsification. Monodisperse particles are expected to provide improved column packing quality and thus separation efficiency compared to the alternative. Although this work revealed that jetted resins could provide improved product resolution with the aid of higher ligand densities, it was not enough to establish their superiority. In order to understand their benefits or drawbacks when compared to traditional polydispersed resins, additional experiments would have to be carried out.

Maximum flow pressure and packing quality in terms of HETP and asymmetry would be tested using intermediate process scale, for example, XK26 column with 15-20 cm bed height. Peak resolution efficiency would be analysed using several different molecules with the ligand densities above 0.20 mol/L. In order to confirm that jetted resins could have a positive impact on improved resin lifetime, prolonged cycling studies of 50-100 cycles with the most representative feed would have to be performed.

7.2.3. Long-term

7.2.3.1. Modelling of protein-ligand interactions

The knowledge gained in this thesis could provide a bigger picture if the protein-ligand interactions were better understood. Experimental data showed that higher ligand density was responsible for increased retention time, yield loss, and in some cases led to aggregate formation. The hypothesis that molecules formed stronger bonds with the ligands due to the increased number of interaction points was established. However, these interactions could not be visualised and confirmed through laboratory-based experiments. *In-silico* modelling would be able to solve this issue by

focusing on the molecular structure of the protein, its charge distribution, and flexibility upon interaction with ligands.

Sequences and tertiary structures of hundreds of molecules including BSA and mAbs are readily available in the public domains such as the protein data bank. Knowing the sequence of the molecule will help to identify which charged amino acid clusters are most likely to interact with the ligands at a particular buffer pH. The clusters can then be visualised using PyMOL, and subjected to real time simulations with a varying number of ligands using molecular dynamics.

7.2.3.2. Fluorescent dye assay optimisation

Fluorescent dye assay that was successfully developed to detect residual protein in used resin samples could be further optimised for high throughput screening. Liquid handling robots together with <1 mL columns have enabled the industry to perform screening methods at a very small scale and short timelines. The assay could be implemented in the early stage chromatography process optimisation, i.e. screening for the cleaning conditions or resins' lifetime.

Currently the method requires to unpack a column in order to collect the sample, which can be limiting. An alternative solution would be to apply the fluorescent dye onto the <1 mL packed column, incubate for 20 minutes and elute the dye with the equilibration buffer. The eluate would then be collected and the fluorescence would be measured on a plate reader. The difference of fluorescence intensity of the dye before and after the application would determine the amount of residual dye molecules bound to the remaining foulants inside the column. The amount of the dye to be applied onto the column and a reference standard curve would have to be established to enable reproducible and accurate calculations.

Furthermore, this method has only been tested on a handful of resins and could also be assessed with other chromatography matrices including monoliths, membranes and nanofibers. Having done several experiments with 0.22 µm filtration membranes, I have observed promising results allowing to visualise protein distribution across the layers of the membrane. It, however, became clear that (i) the specimen had to be kept hydrated in order to preserve any bound protein; (ii) the amount of the dye had to be optimised in order to improve assay's specificity; and (iii) the sample had to be sized correctly in order to fit onto a microscopy slide and be visualised by the confocal microscope as its observation thickness limit was below 100 µm. These improvements could result in a very diverse assay enabling access to additional knowledge about fouling and cleaning procedures as well as processes that are more robust.

8. Chapter: Process validation

8.1. Fluorescent dye assay application

Residual protein detection assay employing a fluorescent dye Proteostat® can be implemented in research and development as an additional method for the evaluation of resin lifetime. Chromatography matrices are sometimes reused when manufacturing various biopharmaceuticals in order to reduce associated costs and time spent packing / unpacking columns. Traditionally, resin lifetime studies involve subjecting a column to numerous binding cycles (50-150 cycles), and measuring changes in pressure, binding capacity and product recovery. The fluorescent dye would offer benefits in quantifying the residual protein inside the chromatography matrix and predicting its remaining capacity and longevity.

The assay entails applying the fluorescent dye on the used matrix sample and measuring the intensity of the emitted signal under a fluorescence plate reader. Alternatively, this method could be used in the high throughput small scale process development whereby the dye is added onto the stationary phase post-chromatography runs, and the amount of the unbound dye is quantified. The dye that has been bound would translate to the amount of remaining protein inside the matrix.

8.2. Requirements for the validation of the assay

Novel analytical assay implementation and validation requires a good understanding and proof of the assay's specificity, accuracy, precision, limit of detection, limit of quantification, linearity and range. If the fluorescent dye assay developed in this work was to be introduced into the analysis of resin lifetime, and used as part of the validation for resin reusability at any chromatography stage including capture, intermediate and polishing, then all those factors would have to be established.

The assay would have to be able to identify the analyte of interest, i.e. residual impurities bound to the resins in the presence of other components. Chromatography matrix such as beads, monoliths, membranes, nanofibers, and their ligands all have different surface composition and charge that may interfere with the assay's signal. The assay would have to be developed for the specific matrix and ligand. In addition, presence of buffer reagents such as high concentrations of salts, sugars and detergents will have an impact to the background signal: generally an increase in fluorescence (Enzo Life Sciences, 2017). A dilution factor would have to be established in order to mitigate background fluorescence that will remain within the standard curve.

The accuracy of the dye assay can be measured by spiking the test sample with a known concentration of an analyte standard, and calculating spike recovery in percentage. In this case, the stability of the fluorescent dye is important as it goes through the freeze and thaw cycles, and can be exposed to light during application. Variation in the amount of matrix sample, for example, the number of resin particles would also result in a significant error in assay's accuracy.

The analytical method has to be precise meaning that the results can be repeatable and reproducible. The particular amount of dye to test sample is required to improve the repeatability of the assay as the main error arises from the manual pipetting. Reproducible sample collection is another challenge as the same slurry concentration or membrane area have to be maintained across different samples. Temperature will also have an impact because some samples might be prone to aggregation at lower temperatures than others resulting in higher fluorescence signals. The choice of the 96-well plates, calibration of the liquid handling robot (instead of manual pipetting), mixing time and speed could all have an impact on the fluorescence signal, and would have to evaluated in order to gain reproducibility.

Detection and quantification limits of the lowest analyte concentration would have to be established for this assay. Depending on the commonly captured fluorescence values amongst the process samples, the amount of the dye added can be adjusted to alter the sensitivity of the assay towards the lower end of the standard curve.

Linearity and working range can be easily determined as different amounts of aggregated protein from 0 to 100% are used to create a standard curve. The standard curve would have to be specific to the product of interest as each protein has a different degree of thermal sensitivity and can produce aggregates that will elicit different numeral fluorescence responses. Furthermore, the stage of the chromatography process plays an important role. The capture step is exposed to the highest amount of impurities such as host cell proteins and DNA that can clog the pores more readily resulting in an overall higher signal meaning that the range of the assay would have to be moved to the upper limit, whilst the intermediate and polishing steps would contain a smaller amount of impurities leading to a lower fluorescence signal.

9. References

Amersham Biosciences Ab, 2003. *A method of producing hierarchical porous beads*. WO 2003055597.

Angelo, J.M., Cvetkovic, A., Gantier, R. and Lenhoff, A.M., 2013. Characterization of cross-linked cellulosic ion-exchange adsorbents: 1. Structural properties. *Journal of Chromatography A*, 1319, pp.46–56.

Angelo, J.M., Cvetkovic, A., Gantier, R. and Lenhoff, A.M., 2016. Characterization of cross-linked cellulosic ion-exchange adsorbents: 2. Protein sorption and transport. *Journal of Chromatography A*, 1438, pp.100–112.

Arakawa, T., Tsumoto, K., Nagase, K. and Ejima, D., 2007. The effects of arginine on protein binding and elution in hydrophobic interaction and ion-exchange chromatography. *Protein Expression and Purification*, 54(1), pp.110–116.

Athalye, A.M., Gibbs, S.J. and Lightfoot, E.N., 1992. Predictability of chromatographic protein separations. Study of size-exclusion media with narrow particle size distributions. *Journal of Chromatography A*, 589, pp.71–85.

Baker, M.R., 1993. Droplet breakup using in-line mixers located in recirculation loops around batch vessels. *Chemical Engineering Science*, 48(22), pp.3829–3833.

Basova, E.Y. and Foret, F., 2014. Droplet microfluidics in (bio)chemical analysis. *Analyst*, 140(1), pp.22–38.

Baur, D., Angelo, J.M., Chollangi, S., Xu, X., Müller-Späth, T., Zhang, N., Ghose, S., Li, Z.J. and Morbidelli, M., 2018. Model assisted comparison of Protein A resins and multi-column chromatography for capture processes. *Journal of Biotechnology*, 285, pp.64–73.

Van Beers, M.M.C. and Bardor, M., 2012. Minimizing immunogenicity of biopharmaceuticals by controlling critical quality attributes of proteins. *Biotechnology Journal*, 7, pp.1473–1484.

Bell, D. and Santeufemio, C., 2006. Cryo field emission scanning electron microscopy examination of the ultrastructures of agarose based chromatography beads. *Microscopy and Microanalysis*, 12(S02), pp.1124–1125.

Bengtsson, S. and Philipson, L., 1964. Chromatography of animal viruses on pearl-

condensed agar. *BBA - Specialised Section On Biophysical Subjects*, 79(2), pp.399–406.

Bergander, T., Nilsson-Välimaa, K., Öberg, K. and Lacki, K.M., 2008. High-throughput process development: Determination of dynamic binding capacity using microtiter filter plates filled with chromatography resin. *Biotechnology Progress*, 24(3), pp.632–639.

Borzova, V.A., Markossian, K.A., Chebotareva, N.A., Kleymenov, S.Y., Poliansky, N.B., Muranov, K.O., Stein-Margolina, V.A., Shubin, V. V., Markov, D.I. and Kurganov, B.I., 2016. Kinetics of thermal denaturation andaggregation of bovine serum albumin. *PLoS ONE*, 11(4), p.e0153495.

Boulet-Audet, M., Byrne, B. and Kazarian, S.G., 2015. Cleaning-in-place of immunoaffinity resins monitored by in situ ATR-FTIR spectroscopy. *Analytical and Bioanalytical Chemistry*, 407, pp.7111–7122.

Boulet-Audet, M., Kazarian, S.G. and Byrne, B., 2016. In-column ATR-FTIR spectroscopy to monitor affinity chromatography purification of monoclonal antibodies. *Scientific Reports*, 6, p.30526.

Bousse, L., Mouradian, S., Minalla, A., Yee, H., Williams, K. and Dubrow, R., 2001. Protein sizing on a microchip. *Analytical Chemistry*, 73(6), pp.1207–1212.

Bowen, P., 2002. Particle size distribution measurement from millimeters to nanometers and from rods to platelets. *Journal of Dispersion Science and Technology*, 23(5), pp.631–662.

Burgess, D.J., Duffy, E., Etzler, F. and Hickey, A.J., 2004. Particle size analysis: AAPS workshop report, cosponsored by the food and drug administration and the United States pharmacopeia. *AAPS Journal*, 6(3), p.e20.

Canselier, J.P., Delmas, H., Wilhelm, a. M. and Abismaïl, B., 2002. Ultrasound emulsification — an overview. *Journal of Dispersion Science and Technology*, 23(1–3), pp.333–349.

Carlsson, F., Axelsson, A. and Zacchi, G., 1994. Mathematical modelling and parametric studies of affinity chromatography. *Computers and Chemical Engineering*, 18, pp.S657–S661.

Carta, G. and Jungbauer, A., 2010. *Protein Chromatography: Process Development and Scale-Up*. *Wiley-VCH*.

Carter, D.C., He, X.M., Munson, S.H., Twigg, P.D., Gernert, K.M., Broom, M.B. and Miller, T.Y., 1989. Three-dimensional structure of human serum albumin. *Science*, 244(4909), pp.1195–1198.

Charcosset, C., 2006. Membrane processes in biotechnology: An overview. *Biotechnology Advances*, 24(5), pp.482–492.

Charcosset, C., 2009. Preparation of emulsions and particles by membrane emulsification for the food processing industry. *Journal of Food Engineering*, 92(3), pp.241–249.

Chen, Z., Huang, C., Chennamsetty, N., Xu, X. and Li, Z.J., 2016. Insights in understanding aggregate formation and dissociation in cation exchange chromatography for a structurally unstable Fc-fusion protein. *Journal of Chromatography A*, 1460(2016), pp.110–122.

Chon, J.H. and Zarbis-Papastoitsis, G., 2011. Advances in the production and downstream processing of antibodies. *New Biotechnology*, 28(5), pp.458–463.

Clark, A.H., Saunderson, D.H.P. and Suggett, A., 1981. Infrared and laser-raman spectroscopic studies of thermally-induced globular protein gels. *International Journal of Peptide and Protein Research*, 17(3), pp.353–364.

Close, E.J., Salm, J.R., Iskra, T., Sørensen, E. and Bracewell, D.G., 2013. Fouling of an anion exchange chromatography operation in a monoclonal antibody process: Visualization and kinetic studies. *Biotechnology and Bioengineering*, 110(9), pp.2425–2435.

Corbett, R., Carta, G., Iskra, T., Gallo, C., Godavarti, R. and Salm, J.R., 2013. Structure and protein adsorption mechanisms of clean and fouled tentacle-type anion exchangers used in a monoclonal antibody polishing step. *Journal of Chromatography A*, 1278, pp.116–125.

Cramer, S.M. and Holstein, M.A., 2011. Downstream bioprocessing: Recent advances and future promise. *Current Opinion in Chemical Engineering*, 1(1), pp.27–37.

DePhillips, P. and Lenhoff, A.M., 2000. Pore size distributions of cation-exchange adsorbents determined by inverse size-exclusion chromatography. *Journal of Chromatography A*, 883(1–2), pp.39–54.

DePhillips, P. and Lenhoff, A.M., 2001. Determinants of protein retention

characteristics on cation-exchange adsorbents. *Journal of Chromatography A*, 933(1–2), pp.57–72.

Dewaele, C. and Verzele, M., 1983. Influence of the particle size distribution of the packing material in reversed-phase high-performance liquid chromatography. *Journal of Chromatography A*, 260, pp.13–21.

Dismer, F. and Hubbuch, J., 2010. 3D structure-based protein retention prediction for ion-exchange chromatography. *Journal of Chromatography A*, 1217(8), pp.1343–1353.

Do, T., Ho, F., Heidecker, B., Witte, K., Chang, L. and Lerner, L., 2008. A rapid method for determining dynamic binding capacity of resins for the purification of proteins. *Protein Expression and Purification*, 60(2), pp.147–150.

Dolomite, 2015. Agarose Bead Synthesis. [online] pp.1–15. Available at: <http://www.dolomite-microfluidics.com/images/stories/PDFs/application_notes/adm_app_applicationnote_agarose.pdf> [Accessed 8 Jan. 2017].

Dolomite, 2017. *Telos droplet manufacture system*. [online] Available at: <http://www.dolomite-microfluidics.com/webshop/telos_system> [Accessed 8 Jan. 2017].

Dziennik, S.R., Belcher, E.B., Barker, G.A., DeBergalis, M.J., Fernandez, S.E. and Lenhoff, A.M., 2003. Nondiffusive mechanisms enhance protein uptake rates in ion exchange particles. *Proceedings of the National Academy of Sciences of the United States of America*, 100(2), pp.420–425.

Dziennik, S.R., Belcher, E.B., Barker, G.A. and Lenhoff, A.M., 2005. Effects of ionic strength on lysozyme uptake rates in cation exchangers. I: Uptake in SP sepharose FF. *Biotechnology and Bioengineering*, 91(2), pp.139–153.

Egorov, A.M., Vakhabov, A.K. and Chernyak, V.Y., 1970. Isolation of agarose and granulation of agar and agarose gel. *Journal of Chromatography A*, 46(C), pp.143–148.

Ejima, D., Yumioka, R., Tsumoto, K. and Arakawa, T., 2005. Effective elution of antibodies by arginine and arginine derivatives in affinity column chromatography. *Analytical Biochemistry*, 345(2), pp.250–257.

Elich, T., Iskra, T., Daniels, W. and Morrison, C.J., 2016. High throughput

determination of cleaning solutions to prevent the fouling of an anion exchange resin. *Biotechnology and Bioengineering*, 113(6), pp.1251–1259.

Enzo Life Sciences, 2017. ProteoStat protein aggregation assay: Instruction manual. pp.1–18.

Eon-Duval, A., Broly, H. and Gleixner, R., 2012. Quality attributes of recombinant therapeutic proteins: An assessment of impact on safety and efficacy as part of a quality by design development approach. *Biotechnology Progress*, 28(3), pp.608–622.

Farys, M., Gibson, D., Lewis, A.P., Lewis, W. and Kucia-Tran, R., 2018. Isotype dependent on-column non-reversible aggregation of monoclonal antibodies. *Biotechnology and Bioengineering*, 115, pp.1279–1287.

Fogle, J., Mohan, N., Cheung, E. and Persson, J., 2012. Effects of resin ligand density on yield and impurity clearance in preparative cation exchange chromatography. I. Mechanistic evaluation. *Journal of Chromatography A*, 1225, pp.62–69.

Fogle, J. and Persson, J., 2012. Effects of resin ligand density on yield and impurity clearance in preparative cation exchange chromatography. II. Process characterization. *Journal of Chromatography A*, 1225, pp.70–78.

Franke, A., Forrer, N., Butté, A., Cvijetić, B., Morbidelli, M., Jöhnck, M. and Schulte, M., 2010. Role of the ligand density in cation exchange materials for the purification of proteins. *Journal of Chromatography A*, 1217(15), pp.2216–2225.

Füssl, F., Criscuolo, A., Cook, K., Scheffler, K. and Bones, J., 2019. Cracking proteoform complexity of ovalbumin with anion-exchange chromatography-high-resolution mass spectrometry under native conditions. *Journal of Proteome Research*, 18(10), pp.3689–3702.

Gagnon, P., Nian, R., Lee, J., Tan, L., Latiff, S.M.A., Lim, C.L., Chuah, C., Bi, X., Yang, Y., Zhang, W. and Gan, H.T., 2014. Nonspecific interactions of chromatin with immunoglobulin G and protein A, and their impact on purification performance. *Journal of Chromatography A*, 1340, pp.68–78.

Garber, E. and Demarest, S.J., 2007. A broad range of Fab stabilities within a host of therapeutic IgGs. *Biochemical and Biophysical Research Communications*, 355(3), pp.751–757.

Garti, N. and Bisperink, C., 1998. Double emulsions: Progress and applications. *Current Opinion in Colloid and Interface Science*, 3(6), pp.657–667.

Ghose, S., Hubbard, B. and Cramer, S.M., 2007. Binding capacity differences for antibodies and Fc-fusion proteins on protein A chromatographic materials. *Biotechnology and Bioengineering*, 96(4), pp.768–779.

Ghosh, R., 2002. Protein separation using membrane chromatography: Opportunities and challenges. *Journal of Chromatography A*, 952(1–2), pp.13–27.

Gijsbertsen-Abrahamse, A.J., Van Der Padt, A. and Boom, R.M., 2004. Status of cross-flow membrane emulsification and outlook for industrial application. *Journal of Membrane Science*, 230(1–2), pp.149–159.

Gillespie, R., Nguyen, T., Macneil, S., Jones, L., Crampton, S. and Vunnum, S., 2012a. Cation exchange surface-mediated denaturation of an aglycosylated immunoglobulin (IgG1). *Journal of Chromatography A*, 1251, pp.101–110.

Gillespie, R., Nguyen, T., Macneil, S., Jones, L., Crampton, S. and Vunnum, S., 2012b. Cation exchange surface-mediated denaturation of an aglycosylated immunoglobulin (IgG1). *Journal of Chromatography A*, 1251, pp.101–110.

Gospodarek, A.M., Hiser, D.E., O'Connell, J.P. and Fernandez, E.J., 2014. Unfolding of a model protein on ion exchange and mixed mode chromatography surfaces. *Journal of Chromatography A*, 1355, pp.238–252.

Goto, M. and McCoy, B.J., 2000. Inverse size-exclusion chromatography for distributed pore and solute sizes. *Chemical Engineering Science*, 55(4), pp.723–732.

Gramer, M.J., 2014. Product quality considerations for mammalian cell culture process development and manufacturing. *Advances in biochemical engineering/biotechnology*, 139, pp.123–166.

Grilo, A.L. and Mantalaris, A., 2019. The increasingly human and profitable monoclonal antibody market. *Trends in Biotechnology*, 37(1), pp.9–16.

Gritti, F., Farkas, T., Heng, J. and Guiochon, G., 2011. On the relationship between band broadening and the particle-size distribution of the packing material in liquid chromatography: Theory and practice. *Journal of Chromatography A*, 1218(45), pp.8209–8221.

Groenning, M., Norrman, M., Flink, J.M., van de Weert, M., Bukrinsky, J.T.,

Schluckebier, G. and Frokjaer, S., 2007a. Binding mode of Thioflavin T in insulin amyloid fibrils. *Journal of Structural Biology*, 159(3), pp.483–497.

Groenning, M., Olsen, L., van de Weert, M., Flink, J.M., Frokjaer, S. and Jørgensen, F.S., 2007b. Study on the binding of Thioflavin T to β-sheet-rich and non-β-sheet cavities. *Journal of Structural Biology*, 158(3), pp.358–369.

Grönberg, A., Eriksson, M., Ersoy, M. and Johansson, H.J., 2011. A tool for increasing the lifetime of chromatography resins. *mAbs*, 3(2), pp.192–202.

Guo, J. and Carta, G., 2014. Unfolding and aggregation of a glycosylated monoclonal antibody on a cation exchange column. Part II. Protein structure effects by hydrogen deuterium exchange mass spectrometry. *Journal of Chromatography A*, 1356, pp.129–137.

Guo, J. and Carta, G., 2015. Unfolding and aggregation of monoclonal antibodies on cation exchange columns: Effects of resin type, load buffer, and protein stability. *Journal of Chromatography A*, 1388, pp.184–194.

Guo, J., Creasy, A.D., Barker, G. and Carta, G., 2016. Surface induced three-peak elution behavior of a monoclonal antibody during cation exchange chromatography. *Journal of Chromatography A*, 1474, pp.85–94.

Guo, J., Zhang, S. and Carta, G., 2014. Unfolding and aggregation of a glycosylated monoclonal antibody on a cation exchange column. Part I. Chromatographic elution and batch adsorption behavior. *Journal of Chromatography A*, 1356, pp.117–128.

Hagel, L., Jagschies, G. and Sofer, G., 2008. *Handbook of Process Chromatography*. *2nd Edition*.

Hahn, R., Bauerhansl, P., Shimahara, K., Wizniewski, C., Tscheliessnig, A. and Jungbauer, A., 2005. Comparison of protein A affinity sorbents: II. Mass transfer properties. *Journal of Chromatography A*, 1093(1–2), pp.98–110.

Hahn, R., Schlegel, R. and Jungbauer, A., 2003. Comparison of protein A affinity sorbents. *Journal of Chromatography B: Analytical Technologies in the Biomedical and Life Sciences*, 790(1–2), pp.35–51.

Han, N. -W, Bhakta, J. and Carbonell, R.G., 1985. Longitudinal and lateral dispersion in packed beds: Effect of column length and particle size distribution. *AIChE Journal*, 31(2), pp.277–288.

Hardick, O., Dods, S., Stevens, B. and Bracewell, D.G., 2013. Nanofiber adsorbents

for high productivity downstream processing. *Biotechnology and Bioengineering*, 110(4), pp.1119–1128.

Hardin, A.M., Harinarayan, C., Malmquist, G., Axén, A. and van Reis, R., 2009. Ion exchange chromatography of monoclonal antibodies: Effect of resin ligand density on dynamic binding capacity. *Journal of Chromatography A*, 1216(20), pp.4366–4371.

Harinarayan, C., Mueller, J., Ljunglöf, A., Fahrner, R., Van Alstine, J. and Van Reis, R., 2006. An exclusion mechanism in ion exchange chromatography. *Biotechnology and Bioengineering*, 95(5), pp.775–787.

Henry, R.A., 2014. Impact of particle size distribution on HPLC column performance. *LC-GC North America*, 32(4), pp.12–19.

Hirano, A., Arakawa, T. and Kameda, T., 2014. Interaction of arginine with Capto MMC in multimodal chromatography. *Journal of Chromatography A*, 1338, pp.58–66.

Hirsh, A.G. and Tsonev, L.I., 2017. Multiple, simultaneous, independent gradients for a versatile multidimensional liquid chromatography. Part II: Application 2: Computer controlled pH gradients in the presence of urea provide improved separation of proteins: Stability influenced anion and. *Journal of Chromatography A*, 1495, pp.22–30.

Hodder, A.N., Aguilar, M.I. and Hearn, M.T.W., 1990. High-performance liquid chromatography of amino acids, peptides and proteins. XCVII. The influence of the gradient elution mode and displacer salt type on the retention properties of closely related protein variants separated by high-performance anion-exc. *Journal of Chromatography A*, 506(C), pp.17–34.

Holdich, R.G., Dragosavac, M.M., Vladisavljević, G.T. and Kosvintsev, S.R., 2010. Membrane emulsification with oscillating and stationary membranes. *Industrial and Engineering Chemistry Research*, 49(8), pp.3810–3817.

Holm, N.K., Jespersen, S.K., Thomassen, L. V., Wolff, T.Y., Sehgal, P., Thomsen, L.A., Christiansen, G., Andersen, C.B., Knudsen, A.D. and Otzen, D.E., 2007. Aggregation and fibrillation of bovine serum albumin. *Biochimica et Biophysica Acta - Proteins and Proteomics*, 1774(9), pp.1128–1138.

Horváth, K., Lukács, D., Sepsey, A. and Felinger, A., 2014. Effect of particle size distribution on the separation efficiency in liquid chromatography. *Journal of*

Chromatography A, 1361, pp.203–208.

Hsieh, Y.L., Chen, T.H. and Liu, C.Y., 2006. Capillary electrochromatographic separation of proteins on a column coated with titanium dioxide nanoparticles. *Electrophoresis*, 27(21), pp.4288–4294.

Huang, Y., Bi, J., Zhao, L., Ma, G. and Su, Z., 2010. Regulation of protein multipoint adsorption on ion-exchange adsorbent and its application to the purification of macromolecules. *Protein Expression and Purification*, 74(2), pp.257–263.

Huang, Y., Bi, J., Zhou, W., Li, Y., Wang, Y., Ma, G. and Su, Z., 2006. Improving recovery of recombinant hepatitis B virus surface antigen by ion-exchange chromatographic supports with low ligand density. *Process Biochemistry*, 41(11), pp.2320–2326.

Hubbuch, J. and Kula, M.R., 2008. Confocal laser scanning microscopy as an analytical tool in chromatographic research. *Bioprocess and Biosystems Engineering*, 31(3), pp.241–259.

Hubbuch, J., Linden, T., Knieps, E., Ljunglöf, A., Thömmes, J. and Kula, M.R., 2003a. Mechanism and kinetics of protein transport in chromatographic media studied by confocal laser scanning microscopy: Part I. The interplay of sorbent structure and fluid phase conditions. *Journal of Chromatography A*, 1021(1–2), pp.93–104.

Hubbuch, J., Linden, T., Knieps, E., Thömmes, J. and Kula, M.R., 2002. Dynamics of protein uptake within the adsorbent particle during packed bed chromatography. *Biotechnology and Bioengineering*, 80(4), pp.359–368.

Hubbuch, J., Linden, T., Knieps, E., Thömmes, J. and Kula, M.R., 2003b. Mechanism and kinetics of protein transport in chromatographic media studied by confocal laser scanning microscopy: Part II. Impact on chromatographic separations. *Journal of Chromatography A*, 1021(1–2), pp.105–115.

Ioannidis, N., 2009. Manufacturing of agarose-based chromatographic media with controlled pore and particle size. *PhD Thesis*, p.214.

Ioannidis, N., Bowen, J., Pacek, A. and Zhang, Z., 2012. Manufacturing of agarose-based chromatographic adsorbents - Effect of ionic strength and cooling conditions on particle structure and mechanical strength. *Journal of Colloid and Interface Science*, 367(1), pp.153–160.

Ishikawa, T., Ito, T., Endo, R., Nakagawa, K., Sawa, E. and Wakamatsu, K., 2010. Influence of pH on heat-induced aggregation and degradation of therapeutic monoclonal antibodies. *Biological and Pharmaceutical Bulletin*, 33(8), pp.1413–1417.

Iskra, T., Bolton, G.R., Coffman, J.L. and Godavarti, R., 2013. The effect of protein a cycle number on the performance and lifetime of an anion exchange polishing step. *Biotechnology and Bioengineering*, 110(4), pp.1142–1152.

Ito, T. and Tsumoto, K., 2013. Effects of subclass change on the structural stability of chimeric, humanized, and human antibodies under thermal stress. *Protein Science*, 22, pp.1542–1551.

Jin, J., Chhatre, S., Titchener-Hooker, N.J. and Bracewell, D.G., 2010. Evaluation of the impact of lipid fouling during the chromatographic purification of virus-like particles from Saccharomyces cerevisiae. *Journal of Chemical Technology and Biotechnology*, 85(2), pp.209–215.

Jin, W., Xing, Z., Song, Y., Huang, C., Xu, X., Ghose, S. and Li, Z.J., 2019. Protein aggregation and mitigation strategy in low pH viral inactivation for monoclonal antibody purification. *mAbs*, 11(8), pp.1479–1491.

Johnson, T.F., Bailey, J.J., Iacoviello, F., Welsh, J.H., Levison, P.R., Shearing, P.R. and Bracewell, D.G., 2018. Three dimensional characterisation of chromatography bead internal structure using X-ray computed tomography and focused ion beam microscopy. *Journal of Chromatography A*, 1566, pp.79–88.

Jungbauer, A., 2013. Continuous downstream processing of biopharmaceuticals. *Trends in Biotechnology*, 31(8), pp.479–492.

Kaplon, H., Muralidharan, M., Schneider, Z. and Reichert, J.M., 2020. Antibodies to watch in 2020. *mAbs*, 12(1), p.e1703531.

Kim, H.B., Hayashi, M., Nakatani, K., Kitamura, N., Sasaki, K., Hotta, J. and Masuhara, H., 1996. In situ measurements of ion-exchange processes in single polymer particles: laser trapping microspectroscopy and confocal fluorescence microspectroscopy. *Analytical chemistry*, 68(3), pp.409–414.

Kopaciewicz, W., Rounds, M.A. and Regnier, F.E., 1985. Stationary phase contributions to retention in high-performance anion-exchange protein chromatography: ligand density and mixed mode effects. *Journal of Chromatography A*, 318, pp.157–172.

Lang, K.M.H., Kittelmann, J., Pilgram, F., Osberghaus, A. and Hubbuch, J., 2015. Custom-tailored adsorbers: A molecular dynamics study on optimal design of ion exchange chromatography material. *Journal of Chromatography A*, 1413, pp.60–67.

Langer, E. and Rader, R., 2015. Biopharmaceutical Manufacturing: Historical and Future Trends in Titers, Yields, and Efficiency in Commercial-Scale Bioprocessing. *BioProcessing Journal*, 13(4), pp.47–54.

Langford, J.F., Xu, X., Yao, Y., Maloney, S.F. and Lenhoff, A.M., 2007. Chromatography of proteins on charge-variant ion exchangers and implications for optimizing protein uptake rates. *Journal of Chromatography A*, 1163(1–2), pp.190–202.

Li, X.Q., Li, Q., Gong, F.L., Lei, J. Du, Zhao, X., Ma, G.H. and Su, Z.G., 2015. Preparation of large-sized highly uniform agarose beads by novel rotating membrane emulsification. *Journal of Membrane Science*, 476, pp.30–39.

Liekens, A., Billen, J., Sherant, R., Ritchie, H., Denayer, J. and Desmet, G., 2011. High performance liquid chromatography column packings with deliberately broadened particle size distribution: Relation between column performance and packing structure. *Journal of Chromatography A*, 1218(38), pp.6654–6662.

Linden, T., Ljunglöf, A., Hagel, L., Kula, M.R. and Thömmes, J., 2002. Visualizing patterns of protein uptake to porous media using confocal scanning laser microscopy. *Separation Science and Technology*, 37(1), pp.1–32.

Linden, T., Ljunglöf, A., Kula, M.R. and Thömmes, J., 1999. Visualizing two-component protein diffusion in porous adsorbents by confocal scanning laser microscopy. *Biotechnology and Bioengineering*, 65(6), pp.622–630.

Lintern, K., Pathak, M., Smales, C.M., Howland, K., Rathore, A. and Bracewell, D.G., 2016. Residual on column host cell protein analysis during lifetime studies of protein A chromatography. *Journal of Chromatography A*, 1461, pp.70–77.

Ljunglöf, A. and Hjorth, R., 1996. Confocal microscopy as a tool for studying protein adsorption to chromatographic matrices. In: *Journal of Chromatography A*. pp.75–83.

Ljunglöf, A. and Thömmes, J., 1998. Visualising intraparticle protein transport in porous adsorbents by confocal microscopy. *Journal of Chromatography A*, 813(2), pp.387–395.

Lu, H.L., Lin, D.Q., Zhu, M.M. and Yao, S.J., 2012a. Effects of ligand density and pore size on the adsorption of bovine IgG with DEAE ion-exchange resins. *Journal of Separation Science*, 35(16), pp.2131–2137.

Lu, H.L., Lin, D.Q., Zhu, M.M. and Yao, S.J., 2012b. Protein adsorption on DEAE ion-exchange resins with different ligand densities and pore sizes. *Journal of Separation Science*, 35(22), pp.3084–3090.

Luo, H., Cao, M., Newell, K., Afdahl, C., Wang, J., Wang, W.K. and Li, Y., 2015. Double-peak elution profile of a monoclonal antibody in cation exchange chromatography is caused by histidine-protonation-based charge variants. *Journal of Chromatography A*, 1424, pp.92–101.

Luo, H., Macapagal, N., Newell, K., Man, A., Parupudi, A., Li, Y. and Li, Y., 2014. Effects of salt-induced reversible self-association on the elution behavior of a monoclonal antibody in cation exchange chromatography. *Journal of Chromatography A*, 1362, pp.186–193.

Maaloum, M., Pernodet, N. and Tinland, B., 1998. Agarose gel structure using atomic force microscopy: Gel concentration and ionic strength effects. *Electrophoresis*, 19(10), pp.1606–1610.

Matlschweiger, A., Fuks, P., Carta, G. and Hahn, R., 2019. Hindered diffusion of proteins in mixture adsorption on porous anion exchangers and impact on flow-through purification of large proteins. *Journal of Chromatography A*, 1585, pp.121–130.

Matthew S. Grasso & Philip M. Lintilhac, 2016. Microbead encapsulation of living plant protoplasts a new tool for the handling of single plant cells. *Applications in Plant Sciences*, pp.1–5.

McCue, J.T., Engel, P. and Thömmes, J., 2009. Effect of phenyl sepharose ligand density on protein monomer/aggregate purification and separation using hydrophobic interaction chromatography. *Journal of Chromatography A*, 1216(6), pp.902–909.

Millipore Corporation, 2010. *Method and apparatus for making porous agarose beads*. US 20100227015.

Mohanty, K. and Purkait, M.K., 2012. Membrane technologies and applications. In: *Membrane technologies and applications*, 1st ed. Boca Raton: Taylor & Francis Group, pp.192–195.

Mu, Y., Lyddiatt, A. and Pacek, A.W., 2005. Manufacture by water/oil emulsification of porous agarose beads: Effect of processing conditions on mean particle size, size distribution and mechanical properties. *Chemical Engineering and Processing: Process Intensification*, 44(10), pp.1157–1166.

Naefe, M. and Halász, I., 1972. Influence of column parameters on peak broadening in high pressure liquid chromatography. *Analytical Chemistry*, 44(1), pp.76–84.

Nakanishi, K., Yamamoto, S., Matsuno, R. and Kamikubo, T., 1978. Effect of particle size distribution on column efficiency in gel chromatography. *Agricultural and Biological Chemistry*, 42(10), pp.1943–1945.

Nazir, A., Schroën, K. and Boom, R., 2010. Premix emulsification: A review. *Journal of Membrane Science*, 362(1–2), pp.1–11.

Neergaard, M.S., Nielsen, A.D., Parshad, H. and De Weert, M. Van, 2014. Stability of monoclonal antibodies at high-concentration: Head-to-head comparison of the IgG1 and IgG4 subclass. *Journal of Pharmaceutical Sciences*, 103(1), pp.115–127.

Nelson, R., Sawaya, M.R., Balbirnie, M., Madsen, A., Riekel, C., Grothe, R. and Eisenberg, D., 2005. Structure of the cross-β spine of amyloid-like fibrils. *Nature*, 435, pp.773–778.

Nisisako, T., Okushima, S. and Torii, T., 2005. Controlled formulation of monodisperse double emulsions in a multiple-phase microfluidic system. *Soft Matter*, 1, pp.23–27.

Nweke, M.C., 2017. *Chromatography resin characterisation to analyse fifetime and performance during biopharmaceutical manufacture*. University College London.

Nweke, M.C., McCartney, R.G. and Bracewell, D.G., 2017a. Mechanical characterisation of agarose-based chromatography resins for biopharmaceutical manufacture. *Journal of Chromatography A*, 1530, pp.129–137.

Nweke, M.C., Rathore, A.S. and Bracewell, D.G., 2018. Lifetime and aging of chromatography resins during biopharmaceutical manufacture. *Trends in Biotechnology*, 36(10), pp.992–995.

Nweke, M.C., Turmaine, M., McCartney, R.G. and Bracewell, D.G., 2017b. Drying techniques for the visualisation of agarose-based chromatography media by scanning electron microscopy. *Biotechnology Journal*, 12(3), p.1600583.

Okushima, S., Nisisako, T., Torii, T. and Higuchi, T., 2004. Controlled production of

monodisperse double emulsions by two-step droplet breakup in microfluidic devices. *Langmuir*, 20(23), pp.9905–9908.

Oshinbolu, S., Shah, R., Finka, G., Molloy, M., Uden, M. and Bracewell, D.G., 2018. Evaluation of fluorescent dyes to measure protein aggregation within mammalian cell culture supernatants. *Journal of Chemical Technology & Biotechnology*, 93(3), pp.909–917.

Pacáková, V., Hubená, S., Tichá, M., Madra, M. and Stulík, K., 2001. Effects of electrolyte modification and capillary coating on separation of glycoprotein isoforms by capillary electrophoresis. *Electrophoresis*, 22(3), pp.459–463.

Paredes, J.I., Martínez-Alonso, A. and Tascón, J.M.D., 2003. Application of scanning tunneling and atomic force microscopies to the characterization of microporous and mesoporous materials. *Microporous and Mesoporous Materials*, 65(2–3), pp.93–126.

Pathak, M., Lintern, K., Chopda, V., Bracewell, D.G. and Rathore, A.S., 2017. Fluorescence based real time monitoring of fouling in process chromatography. *Scientific Reports*, 7, p.45640.

Pathak, M. and Rathore, A.S., 2016. Mechanistic understanding of fouling of protein A chromatography resin. *Journal of Chromatography A*, 1459, pp.78–88.

Pathak, M. and Rathore, A.S., 2017. Implementation of a fluorescence based PAT control for fouling of protein A chromatography resin. *Journal of Chemical Technology and Biotechnology*, 92(11), pp.2799–2807.

Pathak, M., Rathore, A.S., Lintern, K. and Bracewell, D.G., 2018. Protein A chromatography resin lifetime—impact of feed composition. *Biotechnology Progress*, 34(2), pp.412–419.

Perati, P., Hanko, V. and Rohrer, J., 2009. High-performance ion-exchange chromatography for analysis of protein phosphorylation. *LC GC North America*, 214, pp.3–5.

Pernodet, N., Maaloum, M. and Tinland, B., 1997. Pore size of agarose gels by atomic force microscopy. *Electrophoresis*, 18(1), pp.55–58.

Persson, P., Gustavsson, P.E., Zacchi, G. and Nilsson, B., 2006. Aspects of estimating parameter dependencies in a detailed chromatography model based on frontal experiments. *Process Biochemistry*, 41(8), pp.1812–1821.

Pessela, B.C.C., Munilla, R., Betancor, L., Fuentes, M., Carrascosa, A. V., Vian, A., Fernandez-Lafuente, R. and Guisán, J.M., 2004. Ion exchange using poorly activated supports, an easy way for purification of large proteins. *Journal of Chromatography A*, 1034(1–2), pp.155–159.

Purolite Corporation, 2014. *Method of producing uniform polymer beads of various sizes*. US 20140264984.

Rader, R. and Langer, E., 2018. Biopharma Market: An Inside Look. *Pharma Manufacturing*. [online] Available at: <https://www.pharmamanufacturing.com/articles/2018/biopharma-market-an-inside-look/>.

Rajamanickam, V., Herwig, C. and Spadiut, O., 2015. Monoliths in bioprocess technology. *Chromatography*, 2(2), pp.195–212.

Rathore, A.S. and Sofer, G., 2005a. Examples of scale down models. In: *Process validation in manufacturing of biopharmaceuticals*. Boca Raton: Taylor & Francis Group, pp.75–82.

Rathore, A.S. and Sofer, G., 2005b. Experimental approaches to determine and validate chromatography media life span. In: *Process validation in manufacturing of biopharmaceuticals*. Boca Raton: Taylor & Francis Group, pp.180–193.

Roque, A.C.A., Pina, A.S., Azevedo, A.M., Aires-Barros, R., Jungbauer, A., Di Profio, G., Heng, J.Y.Y., Haigh, J. and Ottens, M., 2020. Anything but conventional chromatography approaches in bioseparation. *Biotechnology Journal*, 15(8), p.1900274.

Rovnyagina, N.R., Sluchanko, N.N., Tikhonova, T.N., Fadeev, V. V., Litskevich, A.Y., Maskevich, A.A. and Shirshin, E.A., 2018. Binding of thioflavin T by albumins: An underestimated role of protein oligomeric heterogeneity. *International Journal of Biological Macromolecules*, 108, pp.284–290.

Schultz, S., Wagner, G., Urban, K. and Ulrich, J., 2004. High-pressure homogenization as a process for emulsion formation. *Chemical Engineering and Technology*, 27(4), pp.361–368.

Sen, P., Fatima, S., Ahmad, B. and Khan, R.H., 2009. Interactions of thioflavin T with serum albumins: Spectroscopic analyses. *Spectrochimica Acta - Part A: Molecular and Biomolecular Spectroscopy*, 74(1), pp.94–99.

Serra, C.A. and Chang, Z., 2008. Microfluidic-assisted synthesis of polymer particles. *Chemical Engineering and Technology*, 31(8), pp.1099–1115.

Shembekar, N., Chaipan, C., Utharala, R. and Merten, C.A., 2016. Droplet-based microfluidics in drug discovery, transcriptomics and high-throughput molecular genetics. *Lab Chip*, 16, pp.1314–1331.

Shen, D., Coleman, J., Chan, E., Nicholson, T.P., Dai, L., Sheppard, P.W. and Patton, W.F., 2011. Novel cell- and tissue-based assays for detecting misfolded and aggregated protein accumulation within aggresomes and inclusion bodies. *Cell Biochemistry and Biophysics*, 60(3), pp.173–185.

Shukla, A.A., Wolfe, L.S., Mostafa, S.S. and Norman, C., 2017. Evolving trends in mAb production processes. *Bioengineering & Translational Medicine*, 2(1), pp.58–69.

Siu, S.C., Boushaba, R., Liau, J., Hjorth, R. and Titchener-Hooker, N.J., 2007. Confocal imaging of chromatographic fouling under flow conditions. *Journal of Chemical Technology and Biotechnology*, 82(10), pp.871–881.

Siu, S.C., Boushaba, R., Topoyassakul, V., Graham, A., Choudhury, S., Moss, G. and Titchener-Hooker, N.J., 2006. Visualising fouling of a chromatographic matrix using confocal scanning laser microscopy. *Biotechnology and Bioengineering*, 95(4), pp.714–723.

Skamris, T., Tian, X., Thorolfsson, M., Karkov, H.S., Rasmussen, H.B., Langkilde, A.E. and Vestergaard, B., 2016. Monoclonal antibodies follow distinct aggregation pathways during production-relevant acidic incubation and neutralization. *Pharmaceutical Research*, 33(3), pp.716–728.

Sofer, G. and Yourkin, J., 2007. Cleaning and cleaning validation in process chromatography. Current industry practices and future. *BioProcess Technical*, pp.72–82.

Sörensen, M.H., Valle-Delgado, J.J., Corkery, R.W., Rutland, M.W. and Alberius, P.C., 2008. AFM-porosimetry: Density and pore volume measurements of particulate materials. *Langmuir*, 24(13), pp.7024–7030.

Staby, A., Jacobsen, J.H., Hansen, R.G., Bruus, U.K. and Jensen, I.H., 2006. Comparison of chromatographic ion-exchange resins. V. Strong and weak cation-exchange resins. *Journal of Chromatography A*, 1118(2), pp.168–179.

Staby, A. and Jensen, I.H., 2001. Comparison of chromatographic ion-exchange resins - II. More strong anion-exchange resins. *Journal of Chromatography A*, 908(1–2), pp.149–161.

Staby, A., Jensen, R.H., Bensch, M., Hubbuch, J., Dünweber, D.L., Krarup, J., Nielsen, J., Lund, M., Kidal, S., Hansen, T.B. and Jensen, I.H., 2007. Comparison of chromatographic ion-exchange resins. VI. Weak anion-exchange resins. *Journal of Chromatography A*, 1164(1–2), pp.82–94.

Staby, A., Sand, M.B., Hansen, R.G., Jacobsen, J.H., Andersen, L.A., Gerstenberg, M., Bruus, U.K. and Jensen, I.H., 2004. Comparison of chromatographic ion-exchange resins: III. Strong cation-exchange resins. *Journal of Chromatography A*, 1034(1–2), pp.85–97.

Staby, A., Sand, M.B., Hansen, R.G., Jacobsen, J.H., Andersen, L.A., Gerstenberg, M., Bruus, U.K. and Jensen, I.H., 2005. Comparison of chromatographic ion-exchange resins: IV. Strong and weak cation-exchange resins and heparin resins. *Journal of Chromatography A*, 1069(1), pp.65–77.

Stang, M., Schuchmann, H. and Schubert, H., 2001. Emulsification in High-Pressure Homogenizers. *Engineering in Life Sciences*, 1(4), pp.151–157.

Steinebach, F., Coquebert de Neuville, B. and Morbidelli, M., 2017. Relating saturation capacity to charge density in strong cation exchangers. *Journal of Chromatography A*, 1507, pp.95–103.

Stickel, J.J. and Fotopoulos, A., 2001. Pressure-flow relationships for packed beds of compressible chromatography media at laboratory and production scale. *Biotechnology Progress*, 17(4), pp.744–751.

Stone, M.C., Tao, Y. and Carta, G., 2009. Protein adsorption and transport in agarose and dextran-grafted agarose media for ion exchange chromatography: Effect of ionic strength and protein characteristics. *Journal of Chromatography A*, 1216(20), pp.4465–4474.

Tian, X., Langkilde, A.E., Thorolfsson, M., Rasmussen, H.B. and Vestergaard, B., 2014. Small-angle X-ray scattering screening complements conventional biophysical analysis: Comparative structural and biophysical analysis of monoclonal antibodies IgG1, IgG2, and IgG4. *Journal of Pharmaceutical Sciences*, 103(6), pp.1701–1710.

Tran, R., Joseph, J.R., Sinclair, A., Bracewell, D., Zhou, Y. and Titchener-Hooker,

N.J., 2007. A framework for the prediction of scale-up when using compressible chromatographic packings. *Biotechnology Progress*, 23(2), pp.413–422.

Urban, K., Wagner, G., Schaffner, D., Röglin, D. and Ulrich, J., 2006. Rotor-stator and disc systems for emulsification processes. *Chemical Engineering and Technology*, 29(1), pp.24–31.

Vladisavljevic, G.T., 2015. Structured microparticles with tailored properties produced by membrane emulsification. *Advances in Colloid and Interface Science*, 225, pp.53–87.

Wahome, J., Zhou, W. and Kundu, A., 2008. Impact of lot-to-lot variability of cation exchange chromatography resin on process performance. *BioPharm International*, 21(5), pp.48–56.

Wang, S., Li, X. and Sun, Y., 2019. Poly(N,N-dimethylaminopropyl acrylamide)-grafted Sepharose FF: A new anion exchanger of very high capacity and uptake rate for protein chromatography. *Journal of Chromatography A*, 1597, pp.187–195.

Wayne, C.J., 2018. *Theoretical Analysis and Experimental Investigation of Simulated Moving Bed Chromatography for the Purification of Protein Mixtures*. University College London.

Weinberg, J., Zhang, S., Crews, G., Healy, E., Carta, G. and Przybycien, T., 2017. Polyclonal and monoclonal IgG binding on protein A resins—Evidence of competitive binding effects. *Biotechnology and Bioengineering*, 114(8), pp.1803–1812.

Wen, J., Arakawa, T. and Philo, J.S., 1996. Size-exclusion chromatography with on-line light-scattering, absorbance, and refractive index detectors for studying proteins and their interactions. *Analytical Biochemistry*, 240(2), pp.155–166.

Wilson, L.J., Lewis, W., Kucia-Tran, R. and Bracewell, D.G., 2019. Identification of upstream culture conditions and harvest time parameters that affect host cell protein clearance. *Biotechnology Progress*, 35(3), p.e2805.

Wrzosek, K., Gramblička, M. and Polakovič, M., 2009. Influence of ligand density on antibody binding capacity of cation-exchange adsorbents. *Journal of Chromatography A*, 1216(25), pp.5039–5044.

Wu, D. and Walters, R.R., 1992. Effects of stationary phase ligand density on high-performance ion-exchange chromatography of proteins. *Journal of Chromatography*

A, 598(1), pp.7–13.

Yan, Y., Zhang, Z., Stokes, J.R., Zhou, Q.Z., Ma, G.H. and Adams, M.J., 2009. Mechanical characterization of agarose micro-particles with a narrow size distribution. *Powder Technology*, 192(1), pp.122–130.

Yang, K., Bai, S. and Sun, Y., 2008. Protein adsorption dynamics in cation-exchange chromatography quantitatively studied by confocal laser scanning microscopy. *Chemical Engineering Science*, 63(16), pp.4045–4054.

Yang, K. and Sun, Y., 2008. Optics-intrinsic double-circle phenomenon in protein adsorption visualized by confocal laser scanning microscopy. *Biochemical Engineering Journal*, 39(2), pp.258–266.

Yao, Y. and Lenhoff, A.M., 2004. Determination of pore size distributions of porous chromatographic adsorbents by inverse size-exclusion chromatography. *Journal of Chromatography A*, 1037(1–2), pp.273–282.

Yao, Y. and Lenhoff, A.M., 2006. Pore size distributions of ion exchangers and relation to protein binding capacity. *Journal of Chromatography A*, 1126(1–2), pp.107–119.

Yigzaw, Y., Piper, R., Tran, M. and Shukla, A.A., 2006. Exploitation of the adsorptive properties of depth filters for host cell protein removal during monoclonal antibody purification. *Biotechnology Progress*, 22(1), pp.288–296.

Yu, J., Song, Y. and Tian, W., 2020. How to select IgG subclasses in developing anti-tumor therapeutic antibodies. *Journal of Hematology and Oncology*, 13(1), pp.1–10.

Zhang, J., Xu, S. and Li, W., 2012. High shear mixers: A review of typical applications and studies on power draw, flow pattern, energy dissipation and transfer properties. *Chemical Engineering and Processing: Process Intensification*, 57–58, pp.25–41.

Zhang, S., Daniels, W., Salm, J., Glynn, J., Martin, J., Gallo, C., Godavarti, R. and Carta, G., 2016a. Nature of foulants and fouling mechanism in the Protein A MabSelect resin cycled in a monoclonal antibody purification process. *Biotechnology and Bioengineering*, 113(1), pp.141–149.

Zhang, S., Xu, K., Daniels, W., Salm, J., Glynn, J., Martin, J., Gallo, C., Godavarti, R. and Carta, G., 2016b. Structural and functional characteristics of virgin and

fouled Protein A MabSelect resin cycled in a monoclonal antibody purification process. *Biotechnology and Bioengineering*, 113(2), pp.367–375.

Zhao, X., Wu, J., Gong, F.L., Cui, J.M., Janson, J.C., Ma, G.H. and Su, Z.G., 2014. Preparation of uniform and large sized agarose microspheres by an improved membrane emulsification technique. *Powder Technology*, 253, pp.444–452.

Zhou, Q.Z., Ma, G.H. and Su, Z.G., 2009. Effect of membrane parameters on the size and uniformity in preparing agarose beads by premix membrane emulsification. *Journal of Membrane Science*, 326(2), pp.694–700.

Zhou, Q.Z., Wang, L.Y., Ma, G.H. and Su, Z.G., 2007. Preparation of uniform-sized agarose beads by microporous membrane emulsification technique. *Journal of Colloid and Interface Science*, 311(1), pp.118–127.

Zhou, Q.Z., Wang, L.Y., Ma, G.H. and Su, Z.G., 2008. Multi-stage premix membrane emulsification for preparation of agarose microbeads with uniform size. *Journal of Membrane Science*, 322(1), pp.98–104.

Zhou, X.P., Li, W., Shi, Q.H. and Sun, Y., 2006. Analysis of mass transport models for protein adsorption to cation exchanger by visualization with confocal laser scanning microscopy. *Journal of Chromatography A*, 1103(1), pp.110–117.

Appendix A

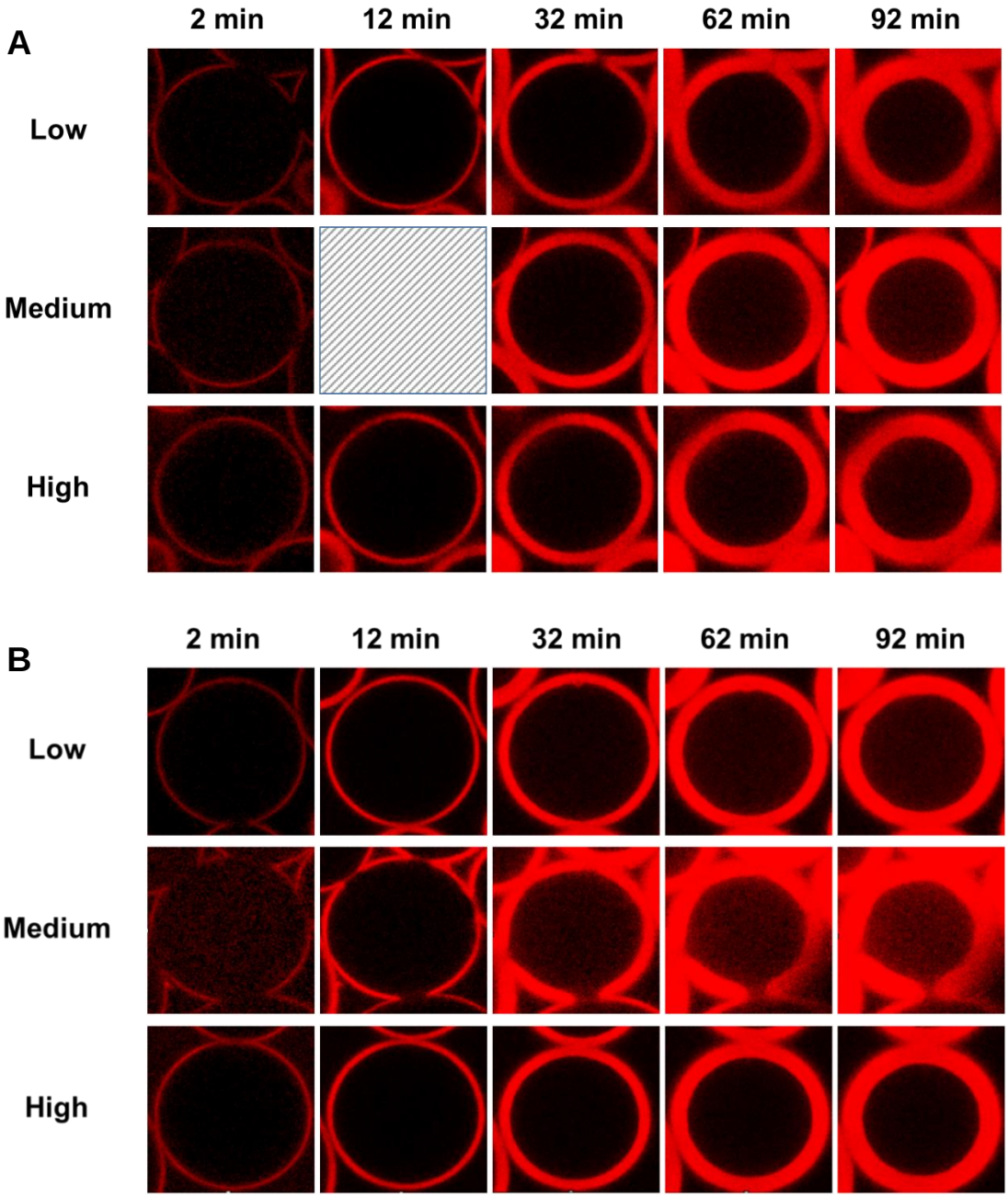

Figure 0. CLSM images of 3 g/L Texas Red-labelled BSA uptake for Q65 and Q90 resins over time. A – Q65 and B – Q90 resins with low, medium and high ligand densities. They were packed in a flow cell and equilibrated with 50 mM Tris, pH 8.5 at 380 cm/h flow. Total of 5 particles each were analysed and the most representative profiles are shown. Excitation and emission wavelengths were 550 and 600 nm, respectively. Other microscopy parameters: 40x magnification lens with oil immersion, 40% laser intensity and 512x512 image resolution.

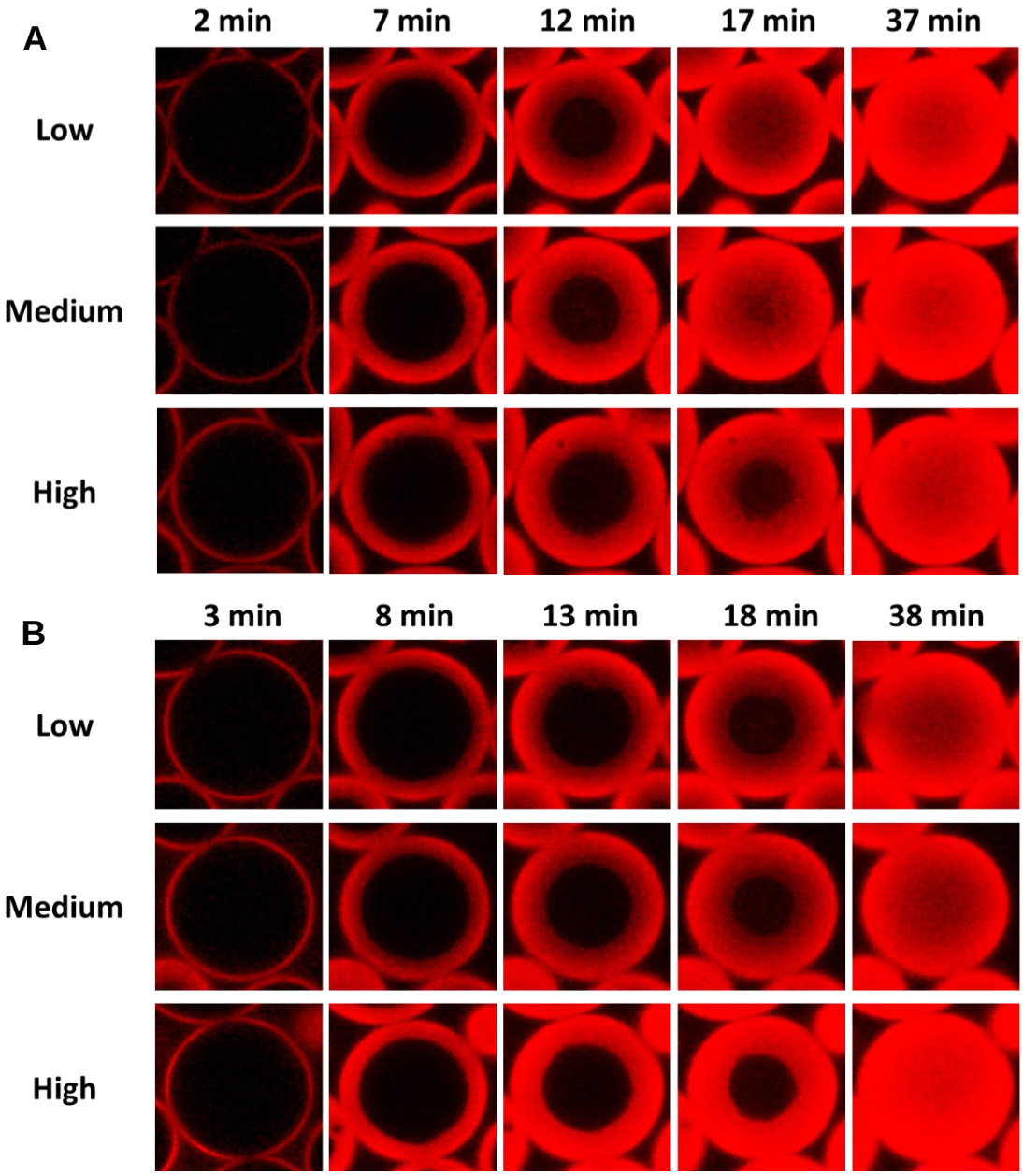

Figure 1. CLSM images of 10 g/L Texas Red-labelled BSA uptake for Q65 and Q90 resins over time. A – Q65 and B – Q90 resins with low, medium and high ligand densities. They were packed in a flow cell and equilibrated with 50 mM Tris, pH 8.5 at 380 cm/h flow. Total of 5 particles each were analysed and the most representative profiles are shown. Excitation and emission wavelengths were 550 and 600 nm, respectively. Other microscopy parameters: 40x magnification lens with oil immersion, 40% laser intensity and 512x512 image resolution.

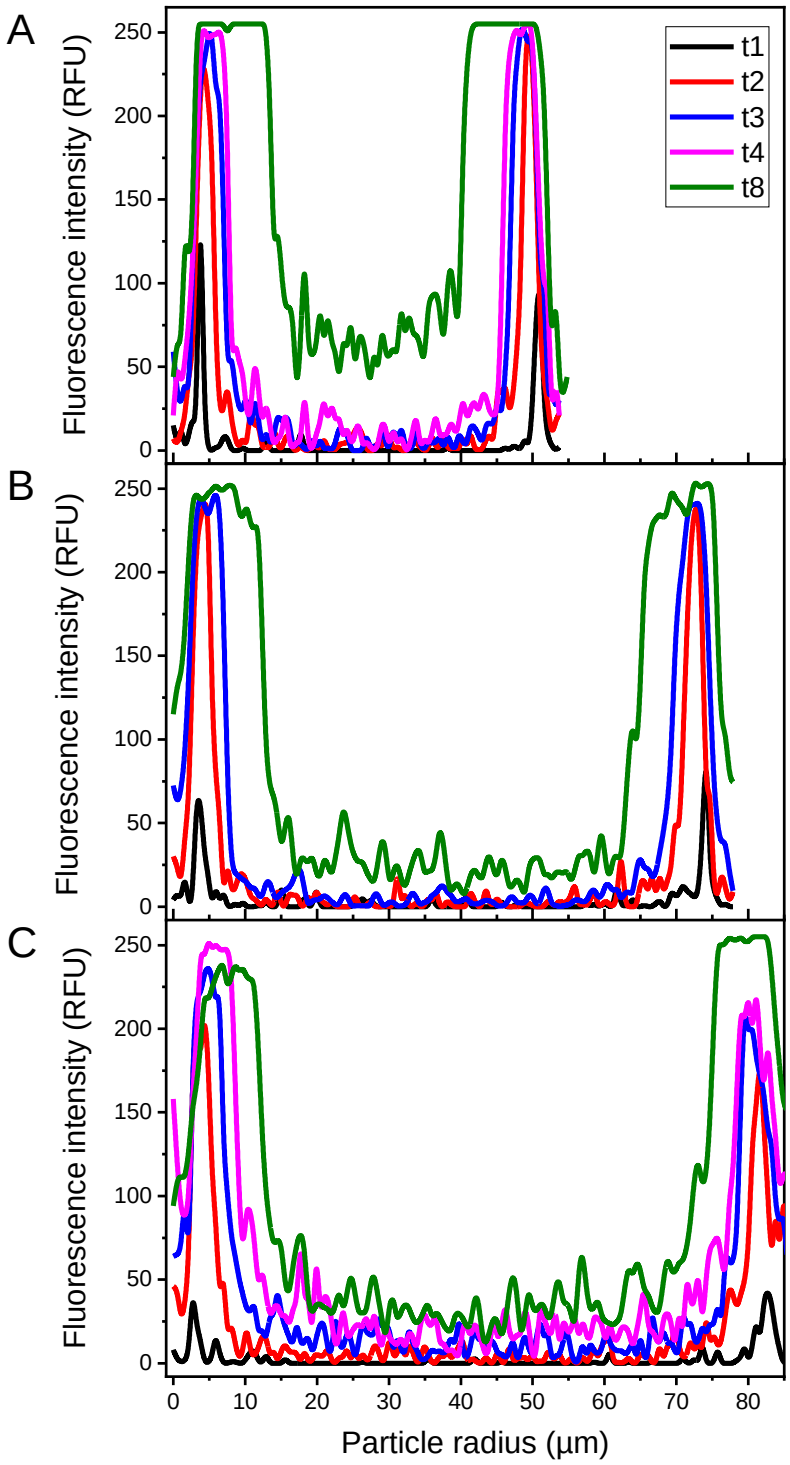

Figure 2. Fluorescence intensity data comparison for three bead sizes at 3 g/L feed conc. A – Q45 non-jetted, B – Q65 and C – Q90 resins were packed in a flow cell and equilibrated with 50 mM Tris, pH 8.5 at 380 cm/h flow. Images of Texas Red-labelled BSA solution uptake rate obtained from CLSM were analysed with ImageJ tool to extrapolate fluorescence intensity values. Time points t1 to t8 were taken every 5-10 minutes for a single particle over its diameter. Total of 5 particles each were analysed and the most representative profiles are shown.

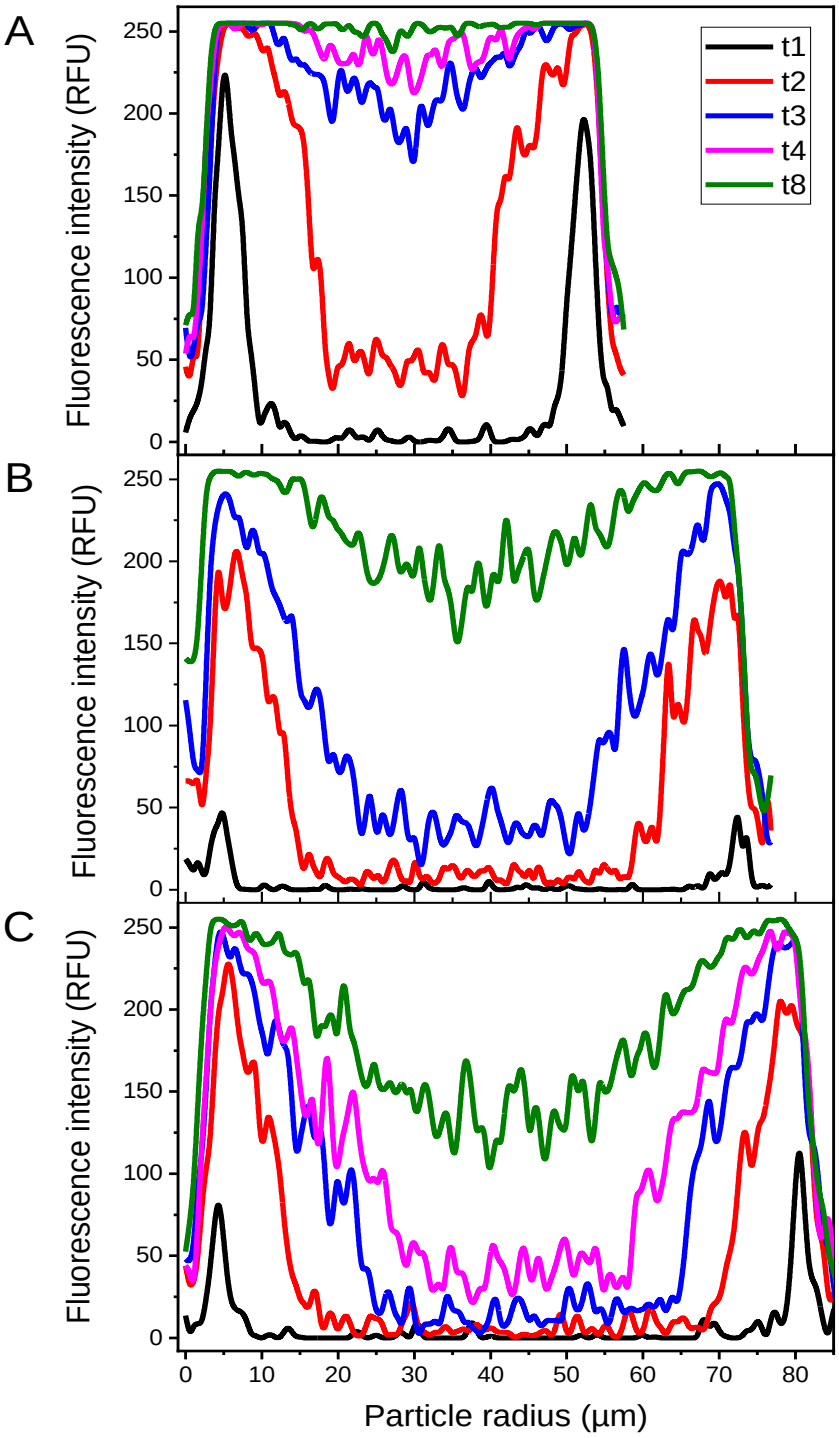

Figure 3. Fluorescence intensity data comparison for three bead sizes at 10 g/L feed conc. A – Q45 non-jetted, B – Q65 and C – Q90 resins were packed in a flow cell and equilibrated with 50 mM Tris, pH 8.5 at 380 cm/h flow. Images of Texas Red-labelled BSA solution uptake rate obtained from CLSM were analysed with ImageJ tool to extrapolate fluorescence intensity values. Time points t1 to t8 were taken every 5-10 minutes for a single particle over its diameter. Total of 5 particles each were analysed and the most representative profiles are shown.

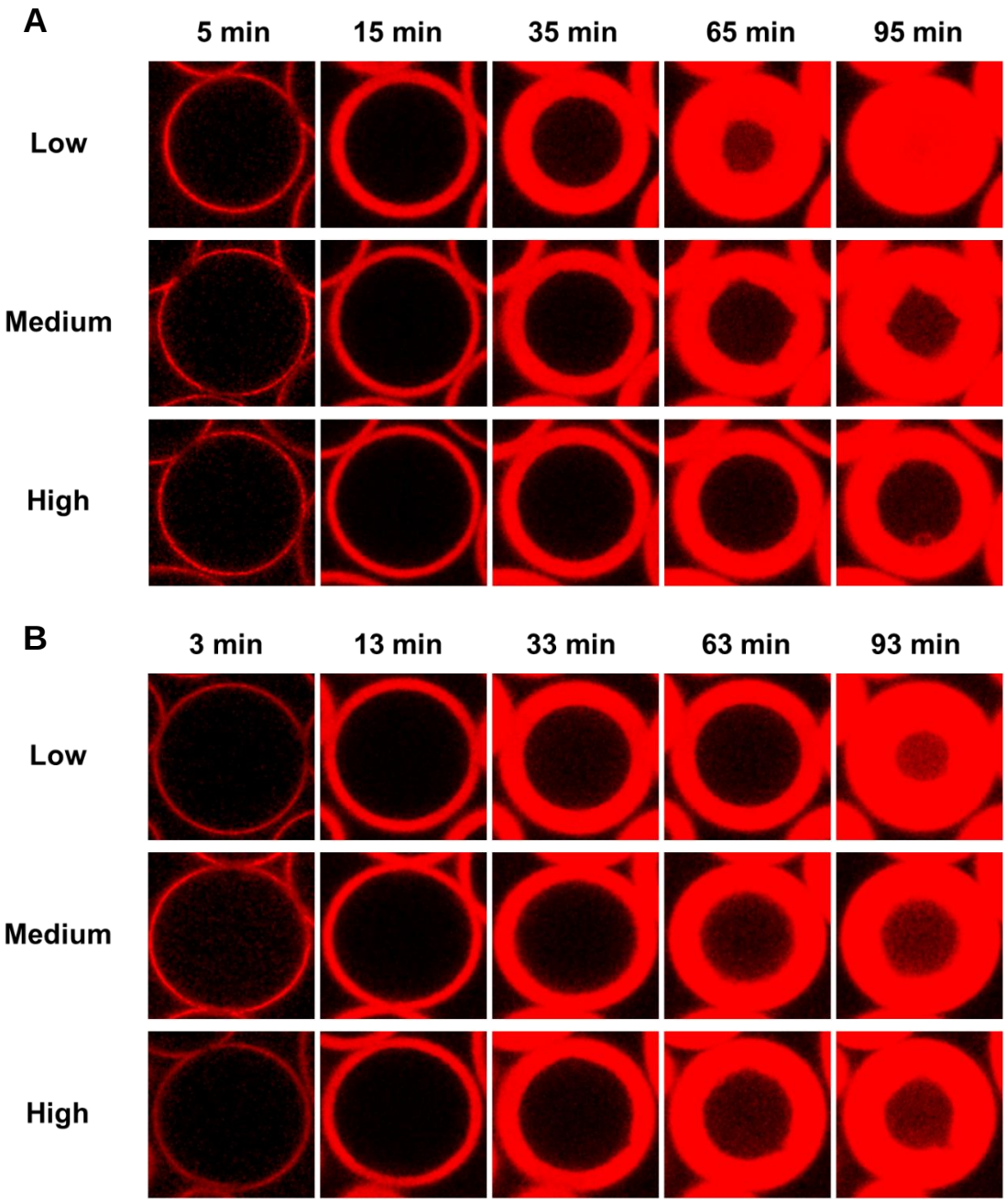

Figure 4. CLSM images of 3 g/L Texas Red-labelled BSA uptake at varying flow rates. A – 255 cm/h and B – 380 cm/h flow rate with Q45 non-jetted resins of low, medium and high ligand densities. They were packed in a flow cell and equilibrated with 50 mM Tris, pH 8.5 prior to loading. Total of 5 particles each were analysed and the most representative profiles are shown. Excitation and emission wavelengths were 550 and 600 nm, respectively. Other microscopy parameters: 40x magnification lens with oil immersion, 40% laser intensity and 512x512 image resolution.

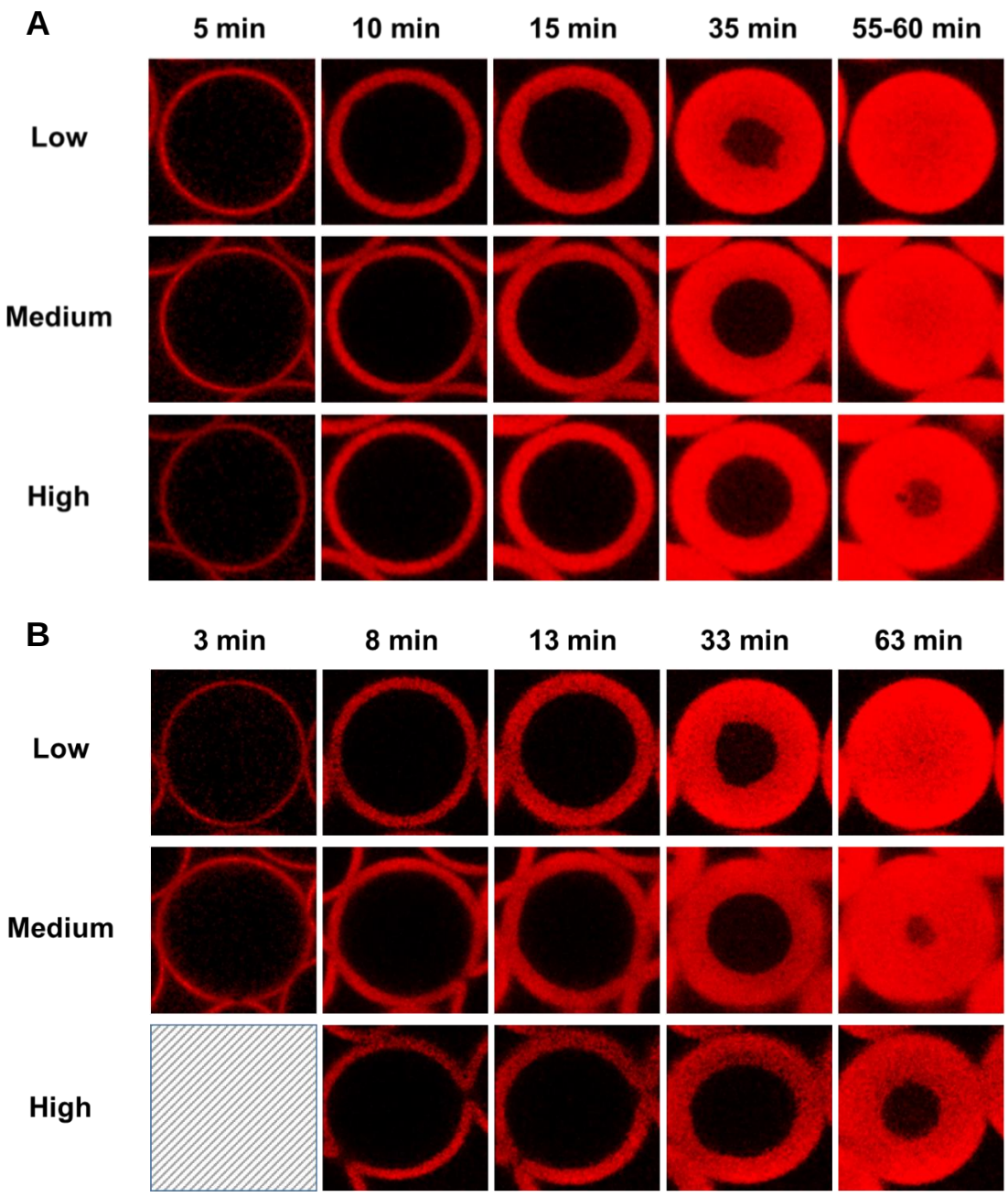

Figure 5. CLSM images of 5 g/L Texas Red-labelled BSA uptake at varying flow rates. A – 255 cm/h and B – 380 cm/h flow rate with Q45 non-jetted resins of low, medium and high ligand densities. They were packed in a flow cell and equilibrated with 50 mM Tris, pH 8.5 prior to loading. Total of 5 particles each were analysed and the most representative profiles are shown. Excitation and emission wavelengths were 550 and 600 nm, respectively. Other microscopy parameters: 40x magnification lens with oil immersion, 40% laser intensity and 512x512 image resolution.

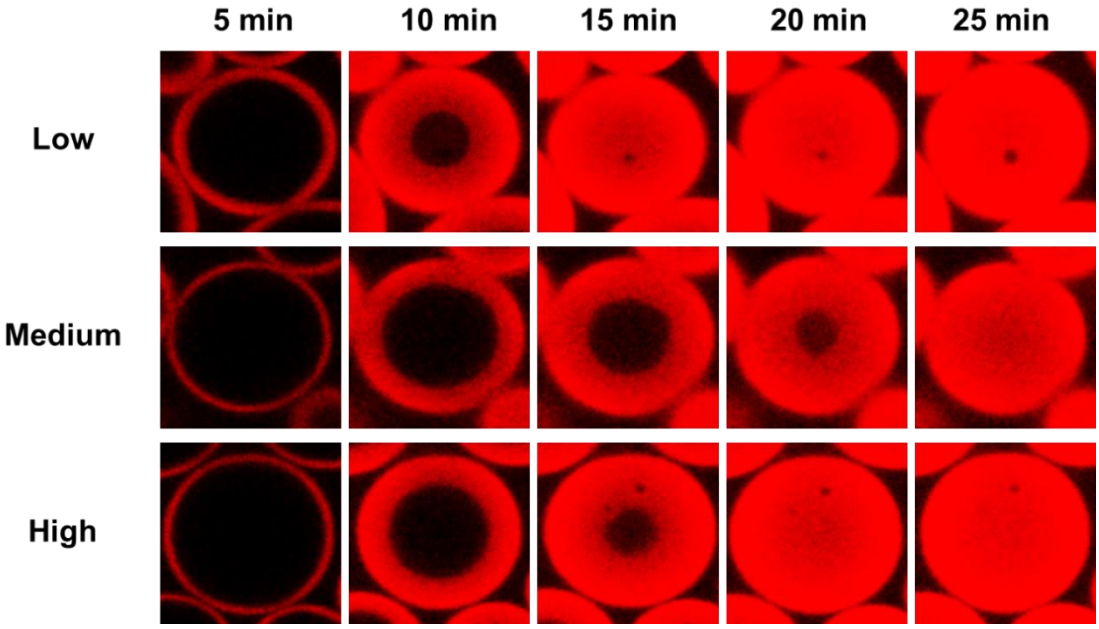

Figure 6. CLSM images of 10 g/L Texas Red-labelled BSA uptake at 380 cm/h flow. Q45 non-jetted resins with low, medium and high ligand densities. They were packed in a flow cell and equilibrated with 50 mM Tris, pH 8.5 prior to loading. Total of 5 particles each were analysed and the most representative profiles are shown. Excitation and emission wavelengths were 550 and 600 nm, respectively. Other microscopy parameters: 40x magnification lens with oil immersion, 40% laser intensity and 512x512 image resolution.